

---

# First principles investigations of layered materials and their interaction with support

---

A thesis

submitted in partial fulfillment of the requirements

of the degree of

Doctor of Philosophy

by

Niharika JOSHI

Roll No. 20143294



Department of Chemistry

INDIAN INSTITUTE OF SCIENCE EDUCATION AND RESEARCH, PUNE

PUNE 411008, MAHARASHTRA, INDIA

December 2020

# Certificate

Certified that the work incorporated in the thesis entitled “First principles investigation of layered materials and their interaction with support” submitted by **Niharika Joshi** was carried out by the candidate, under my supervision. The work presented here or any part of it has not been included in any other thesis submitted previously for the award of any degree or diploma from any other University or institution.



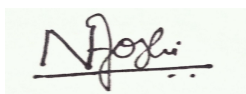
Date: 10/12/2020

(Dr. Prasenjit Ghosh)

Thesis supervisor

# Declaration

I, Niharika Joshi, declare that this thesis titled, “First principles investigations of layered materials and their interaction with support”, written submission represents my ideas in my own words and where others’ ideas have been included, I have adequately cited and referenced the original sources. I also declare that I have adhered to all principles of academic honesty and integrity and have not misrepresented or fabricated or falsified any idea/data/fact/source in my submission. I understand that violation of the above will be cause for disciplinary action by the Institute and can also evoke penal action from the sources which have thus not been properly cited or from whom proper permission has not been taken when needed.

A handwritten signature in black ink on a light green rectangular background. The signature appears to be 'N. Joshi' with a horizontal line underneath.

Niharika Joshi  
Roll No. 20143294  
Date: April 2020

# Synopsis

Since the discovery of graphene, there has been a surge in research activity (both experimental and theoretical) related to the study of a monolayer or a few layers of different layered materials. In addition to studying pristine layered materials, there have been efforts to tune their properties by chemical modifications. While in most of the experimental studies, the experiments are performed by depositing these materials on a support (active or passive), the computational studies are performed on the free standing material. However, the support might significantly alter the properties of these materials through chemical (like bond formation) and physical (eg. strain) interactions. Hence in an effort to understand the role of support and their influence on the pristine and modified layered materials, in this thesis, using density functional theory (and its variants) based calculations, we have studied layered materials on lattice matched supports. In particular, in Chapter 3 to 5 we have studied modified graphene monolayer (chemical modification through hydrogenation or oxygen intercalation and single C vacancy creation) on lattice matched ferromagnetic Ni(111) substrates. Additionally, we have also studied the effect of doping a layered semiconductor, namely, GaSe doped with Mn atoms in Chapter 6.

The thesis is divided into seven chapters.

The **first chapter** of the thesis contains an introduction to layered materials, their classification and their importance in various applications. Additionally we have briefly discussed the role of substrates in modifying the properties of two-dimensional materials. At the end we have provided short summaries of all other remaining chapters included in the thesis.

In **Chapter 2** we have briefly discussed the underlying theory and computational techniques used in our study to determine the total energy of a many-body system efficiently. These include: (i) Born-Oppenheimer approximation and density functional theory which reduces many-body problem to essentially solving one-body problem, (ii) periodic boundary conditions (PBC) and plane-wave basis set that are useful to handle infinitely large but periodic systems, (iii) pseudopotential method which not only allows us to neglect the core electrons in our calculations but also enables us to approximate the ion-electron interactions and the valence electron wavefunction near the atomic nucleus with a smoother pseudo potential and pseudo wavefunction so as to reduce the size of plane-wave basis set required for our calculations and (iv) supercell method, which is helpful in handling aperiodic systems within a PBC framework.

In **Chapter 3** we have investigated the possibility to tune the electronic and magnetic properties of uniformly semihydrogenated graphene (graphone)/Ni(111) interface through oxygen (O) intercalation. Our study shows that the interaction of graphone becomes stronger with the Ni(111) surface as the coverage of intercalating O atoms is increased. Moreover, we find that as a function of O coverage, there is an interplay between the energy gained by O intercalation and the instability in the graphene sheet due to the presence of unsaturated C atoms which drives the reconstruction of the Ni surface at O coverages below 0.5 ML. With the increase in O coverage we find that there is huge enhancement in the magnetic moments on the Ni atoms at the interface. Most interestingly, for the interface at half a monolayer O coverage, we find that there is a significant enhancement in the magnetic moment of the graphone sheet that otherwise is quenched when adsorbed on Ni(111) surface in absence of oxygen.

Freestanding graphone has been predicted to be a ferromagnetic semiconductor, thereby making it an interesting material for spintronic applications. However, graphone is known to be highly unstable due to large chemical imbalance between the sublattices of the bipartite graphene lattice. One can stabilise the semihydrogenated graphene sheet by changing the H-adsorption pattern such that the chemical imbalance between the sublattices is nullified. This gives rise to three other adsorption pattern, in addition to the uniformly semihydrogenated graphene sheet (UGrH), namely, rectangular graphone

(RGrH), zigzag graphone (ZGrH) and armchair graphone (AGrH). In **Chapter 4**, we have studied the stability of these four H-adsorption patterns when they are supported on lattice matched (111) surfaces of Co, Ni and Cu. Our calculations show that the highly unstable UGrH can be stabilised by placing it on these substrates. Moreover, depending on the substrate, we find that either all the H adsorption patterns are equally stable or there energy differences are very small. Our computed C 1s core-level shifts (CLS) of these four semihydrogenated graphene on the (111) surfaces shows that the change in the CLS from one pattern to another is less than 0.2 eV, which is typically the resolution in experimental X-ray Photoelectron spectroscopy (XPS) measurements. Thus it is highly unlikely that one can discern the four different semihydrogenated structures on Ni(111), Co(111) and Cu(111) surfaces from XPS measurements. Further, with variations in the H adsorption pattern, variations in electronic and magnetic properties of the interface is observed. We find that of all the structures only UGrH on Cu(111) shows higher possibility for spin-polarised conduction at the interface.

It is desirable to have materials with high magnetic anisotropy energy (MAE) for use in data storage devices. A large value of MAE suggests stabilization of the magnetization vector, thereby preventing loss of stored data due to thermal fluctuations. Usually bulk ferromagnets have MAEs that are of the order of micro eV, thereby making the devices made out of them thermally unstable even at room temperature. Hence there are efforts to find novel systems with MAEs that are greater than  $k_B T$ . One such class of systems are transition metal adatoms on oxide support. However, in many of these cases the adatoms bind very weakly to the substrate thereby diffusing easily at device operational temperature and coalesce to form larger clusters that have low values of MAE. In our effort to find novel systems where such problems can be circumvented, in **Chapter 5** we have studied three single C vacancies and Co adatom complexes when they are freestanding and supported on Ni(111) surface. The three different structures are Co adatom adsorbed at : (1) undecorated single C vacancy, (2) N-decorated and (3) B-decorated single C vacancies. For (1), in the free standing case, we find the MAE to be about 0.03 meV. In contrast the Co atoms bound to the B and N decorated C-vacancy has MAEs of about 3.80 and 1.49 meV. Upon placing these on Ni(111) substrates, the MAEs are significantly enhanced. For each of the three systems the MAE on the Co

atom is about 40 meV, that is about 15 meV higher than the thermal energy at room temperature.

In **Chapter 6** we have studied the effect of doping magnetic atom (Mn) in gallium selenide which belongs to III-VI semiconductor group and is also a layered material. Their layered structure makes them unique compared to the conventional III-V and II-VI class of semiconductors, which have been extensively studied as possible host material for dilute magnetic semiconductor. The main aim of our study was to understand experimental results where using soft X-ray techniques there have been study of the diffusion of Mn into the host GaSe. For 5.5% Mn doping, we find that Mn prefers to substitute surface Ga atom (thermodynamically the most stable configuration). Additionally, we find that the replaced Ga atom moves to the GaSe(0001) surface and adsorbs at the Se-Se bridge site. The density of states computed for this configuration matches well with the experimental valence band photoemission spectra. We also observe strong hybridization between Mn *s* and *p* states with *p* states of Ga and Se. In contrast, the hybridization between Mn-*d* states with the Se-*p* states are rather weak. Further, unlike conventional DMS, we find that the dopant Mn-*d* states interact only with symmetric Ga-*s* states. As a consequence we do not observe notable crystal-field effects on Mn atom, which is in accordance with the experimental studies.

Finally, we summarize the results from all chapters in this thesis in **Chapter 7** wherein we provide few future directions for pursuing this work further.

*To my family*



# Acknowledgement

At first, I would like to extend my sincere thanks to my thesis supervisor, Dr. Prasenjit Ghosh, for his guidance, immense support and constant encouragement throughout my research. Because of his diligent and thoughtful efforts in teaching me have resulted in accomplishing different projects undertaken during my research tenure as a research fellow in Indian Institute of Science Education and Research, Pune (IISER Pune). Truly, this thesis would not have been possible without his valuable support and guidance.

I would like to thank and dedicated my research work to my family. My parents, Mrs. Chandana Joshi and Mr. Hemant Joshi, my elder sister, Ms. Malvika and my adorable niece, Ms. Spruha are my backbone. Their rock-solid support have boosted me up at my every challenging instances. My parents-in-law, Mrs. Surekha Deshmukh and Mr. Rajeev Deshmukh, my sister-in-law, Ms. Sayali Deshmukh and my husband, Mr. Gaurav Deshmukh have beautifully accepted me and my research job. All thanks to their caring and supportive nature that my research was never hampered after my marriage in the middle of the research tenure.

I am grateful to the Research Advisory Committee (RAC) members, Dr. Mukul Kabir and Dr. Nirmalya Ballav, for their valuable suggestions and comments during RAC meetings held every year from 2016 to 2019. Their critical examinations and advices have always helped in directing me toward more appropriate paths in my research work. I am also very thankful to our in-house collaborators, Dr. Nirmalya Ballav and Dr. Angshuman Nag, and Dr. Luigi Sangaletti from University of Cattolica for giving me opportunities to work with different materials posing different challenges which was indeed very helpful.

I would like to express my sincere gratitude to Indian Institute of Science Education and Research (IISER), Pune for funding, for providing excellent research facilities and for an outstanding and healthy research environment. I take this opportunity to thank the whole staff of IT section, academic section, administration section, Srinivas Ramanujan Library and house-cleaning of IISER Pune for their co-operation. Additionally, I would like to acknowledge Center for Development of Advanced Computing, Pune (CDAC-Pune), Center for Modelling and Simulation of University of Pune and Center for Computational Materials Science, Institute for Materials Research, Tohoku University for computing facility and DST-Nanomission Project No. SR/NM/NS-15/2011 and SR/NM/NS-1285/2014 for funding.

A special thanks to my friends and labmates Dr. Indu Kaul, Dr. Nandha Kumar V., Dr. Subrahmanyam Sappati, Ms. Ashwathi Mohan, Ms. Aarti Shukla, Mr. Unmesh Mondal, Mr. Vineet Kumar Panday, Ms. Kanika Kohli, Mr. Gautam Sharma, Mr. Mujjafir Hossain, Ms. Sarika, Mr. Prajjwal, Mr. Raghavendra, Mr. Aseem Kshirsagar, Mr. Amit Sahu, Mr. C. Gaurav, Mr. Debnath Talukdar, Dr. Saikat Chattopadhyay, Dr. Rahul Hardikar, Dr. Krishnakanth Mondal, and Dr. Nishamol Kurkoise. The number of discussions with them and their suggestions were always fruitful and have worked positively towards the betterment of my research work. Further, last but not the least I would also like thank all my friends outside IISER and to all my dear relatives for their inextinguishable encouragement and support.

# List of Figures

1.1	Schematic diagram showing special features of 2-D materials and their applications . . . . .	4
2.1	Flowchart showing self-consistent field cycle to solve Kohn-Sham equations.	15
2.2	Pictorial diagram of periodic supercells for (a) surface, (b) vacancy in crystal and (c) dimer molecule. . . . .	23
3.1	Variation in the Ni- <i>d</i> occupation in (a) NiO bulk, (b) Ni bulk and (c) Ni(111)-O surface as a function of the perturbing potential ( $\alpha$ ). . . . .	31
3.2	Density of states projected on to (a) Ni- <i>d</i> states of surface Ni atom, (b) O- <i>p</i> states and (c) graphone in Ni(111)-O/GrH interface with 1 ML O coverage. The blue, green and red lines show plots for U=0 eV, U=4.67 eV and U=9.18 eV, respectively. The vertical dotted line shows the Fermi energy which is set at 0 eV. . . . .	33
3.3	(a) Top-view and (b) side veiw of top-fcc configuration of Ni(111)/1ML-O/GrH. Ni, C, O, H atoms are denoted by purple, green, red and magenta colors, respectively. In (a) for better visualization the Ni atoms forming hcp and fcc sites are denoted by pink and cyan colors. Distance marked in the figures are in Å. . . . .	34
3.4	Side-view top-fcc configuration of (b) Ni(111)/0.5 ML-O/GrH and (c) Ni(111)/0.25 ML-O/GrH. Ni, C, O, H atoms are denoted by purple, green, red and magenta colors, respectively. Distances marked in the figures are Å. . . . .	35
3.5	Magnetization density ( $\Delta m = n^\uparrow - n^\downarrow$ ) at the interface of graphone and Ni(111) surface with (a) 1 ML, (b) 0.50 ML and (c) 0.25 ML O coverages. The yellow and blue isosurfaces represents positive (spin-up) and negative (spin-down) net magnetization ( $\Delta m$ ). The isovalue is around $0.02 \text{ e}^-/\text{\AA}^3$ . . . . .	38
3.6	Spin-resolved and total charge transfer at the interface of graphone and Ni(111) surface with 1.0, 0.5 and 0.25 ML O coverage. The red and blue isosurface represents charge accumulation and depletion, respectively. The isovalue is around $0.02 \text{ e}^-/\text{\AA}^3$ . . . . .	39

3.7	(a) Macroscopic average of the electrostatic potential of Ni(111)-O surface when (i) with the adsorbed graphone (black), (ii) fully relaxed (red) and (iii) in the geometry as with graphone (blue) with different oxygen coverages. The two dotted vertical black lines show $z$ value of bulk and vacuum chosen to determine $V(\text{bulk})$ and $V(\text{vacuum})$ . In the same plot the magenta dashed line shows the approximate position of top Ni(111) layer and the zero of X-axis denotes the bottom most Ni(111) layer. (b) Macroscopic average of the electrostatic potential of freestanding graphone in the geometry as on Ni(111)-O surface with different O coverages. The magenta vertical lines in (b) show the $z$ values chosen to determine $V(\pm\infty)$ .	40
3.8	(Color online) Plot of the variation of surface dipole density (and its components) and net magnetic moment on the surface Ni atom as a function of O coverage. The Y-axis on the left hand side of the figure is for the dipole density while that on the right is for magnetic moment. . . . .	41
3.9	(Color online) Spin-resolved density of states (a, d, g) and integrated local density of states in the energy range of $E_f - 0.5$ to $E_f + 0.5$ eV in spin-up channel (b, e, h) and spin-down channel (c, f, i) for Ni(111)/O/GrH interface at 1 ML (top row), 0.5 ML (middle row) and 0.25 ML (bottom row) O coverage. In DOS plots the states of Ni- $3d$ (black and green), O- $2p$ (red) and sum of C- $2s$ , C- $2p$ and H- $1s$ (blue) are plotted. The vertical dotted line denotes the Fermi level. The energies are shifted with respect to vacuum energy. . . . .	43
4.1	(a) Structure of freestanding graphene sheet. The black dashed box denotes the orthorhombic unit cell. (b, c, d) Structure (in panel [I]) and charge transfer plot (in panel [II]) for hydrogenated graphene with one, two and three H atoms in the orthorhombic unit cell of graphene, respectively. Charge transfer is determined using eq. (3). The red and blue isosurfaces show accumulation and depletion of charge, respectively. (e) Optimised structure of hydrogenated graphene sheet with four H atoms in the orthorhombic unit cell. (f, g) DOS for C atoms in structures (b) and (d), respectively. In this and the subsequent figures the C and H atoms are denoted by orange and blue colored spheres, respectively. . . . .	53
4.2	(a)-(d) Side and top-view geometry of the uniform, rectangular, zigzag and armchair hydrogen patterns on the graphene sheet, respectively. The black dotted box is the orthorhombic cell containing 8 C atoms. The distances displayed in the figures are in angstrom units. . . . .	55
4.3	Binding energy of H on freestanding graphene and its constituent energy terms. $\Delta E^{int}$ is the sum of $E_{Gr-H}^{int}$ and $E_{H-H}^{int}$ . . . . .	57
4.4	(a)-(d) PDOS plot of semihydrogenated graphene in uniform, rectangular, zigzag and armchair H-patterns, respectively. The red, blue and green curve shows total DOS, DOS projected on the $2p$ states of the unhydrogenated and hydrogenated carbon atoms, respectively. In (a), (b) and (d) the vertical dashed lines denote valence band maxima (VBM) and conduction band minima (CBM). The energy gap between VBM and CBM is also given in the plot in eV. In (c) the vertical dashed line denotes the Fermi energy. . . . .	58

4.5	(a)-(d) Charge transfer plots for U-GrH, R-GrH, Z-GrH and A-GrH, respectively. The charge transfer is evaluated as: $\Delta n(r) = n_{GrH} - n_{Gr} - n_{4H}$ , where, $n_{GrH}$ is the charge density of semihydrogenated graphene in different H-patterns, $n_{Gr}$ charge density of clean graphene in the same geometry as in the presence of H and $n_{4H}$ is the charge density of four H atoms in the same geometry as they are in the semihydrogenated graphene structures. The C-C bond lengths (in Å) between the unhydrogenated C atoms are also shown. . . . .	59
4.6	Topview (in top panel) and side-view (in bottom panel) of configurations of uniformly hydrogenated graphone (UGrH) (a), rectangular graphone (RGrH) (b), zigzag graphone (c) and armchair graphone (d) on Ni(111) surface. In top-view the bigger dark (brown) colored atoms are surface Ni atoms and lighter ones are the Ni atoms that resides below the surface. The blue rectangular box denotes the unit cell. The distances shown in side-view figures are in angstrom units. . . . .	60
4.7	Topview (in top panel) and side-view (in bottom panel) of configurations of uniformly hydrogenated graphone (UGrH) (a), rectangular graphone (RGrH) (b), zigzag graphone (c) and armchair graphone (d) on Co(111) surface. In top-view the bigger dark (blue) colored atoms are surface Co atoms and lighter ones are the Co atoms that resides below the surface. The red rectangular box denotes the unit cell. The distances shown in side-view figures are in angstrom units. . . . .	61
4.8	Topview (in top panel) and side-view (in bottom panel) of configurations of uniformly hydrogenated graphone (UGrH) (a), rectangular graphone (RGrH) (b), zigzag graphone (c) and armchair graphone (d) on Cu(111) surface. In top-view the bigger dark (red) colored atoms are surface Cu atoms and lighter ones are the Cu atoms that resides below the surface. The blue rectangular box denotes the unit cell. The distances shown in side-view figures are in angstrom units. . . . .	62
4.9	(a) Strain energy, (b) interaction energy and (c) binding energy of H on graphene supported on Ni(111) (black), Co(111) (red) and Cu(111) (blue) surfaces. . . . .	63
4.10	Corelevel shifts of C 1s of the unhydrogenated carbon (C) and hydrogenated carbon (HC) in the semihydrogenated graphene sheet supported on Ni(111) surface. The dotted and solid curves corresponds to C and HC, respectively. The peaks are shifted with respect to the experimental peak of the unhydrogenated C atom at 284.96 eV. The experimental data is obtained from the XPS studies performed by Zhao <i>et al.</i> [1]. The difference in the binding energy are noted above the plot. . . . .	66
4.11	Corelevel shifts of C 1s of the unhydrogenated carbon (C) and hydrogenated carbon (HC) in the semihydrogenated graphene sheet supported on (a)Co(111) surface and (b) Cu(111) surface. C and HC are denoted by dotted and solid curves, respectively. The peaks are shifted with respect to the peak of unhydrogenated carbon atom at 0 eV. The differences in the binding energies are noted above the plot. . . . .	67
4.12	Net magnetic moment on (a) surface Ni (black) and Co (red) atoms and (b) on graphene sheet in four semihydrogenated structures supported on Ni(111) (black) and Co(111) (red) surfaces. . . . .	68

4.13	Projected DOS of surface TM atom (shaded grey), unhydrogenated C (red) and hydrogenated C (blue) in (a, e, i) UGrH, (b, f, j) RGrH, (c, g, k) ZGrH and (d, h, l) AGrH supported on TM(111) surface. The energies are shifted with respect to vacuum energy. The vertical dashed line denotes Fermi energy. . . . .	70
5.1	Linear response of Co- <i>d</i> occupation with respect to varying perturbing potential ( $\alpha$ ) in (a) Co-SVG, (b) Co-SVNG and (c) Co-SVBG . . . . .	75
5.2	Structure of a single C vacancy in (a) freestanding graphene (SVG) and (b, c) graphene with single vacancy supported on Ni(111) surface (Ni/SVG). (b) and (c) shows top-view and side-view of Ni/SVG, respectively. Golden and pale blue colored atoms denote C and Ni atoms, respectively. The C atoms around the vacancy and the displaced Ni atom below the vacancy are marked differently with blue and pink color, respectively. (d) and (e) show projected density of states (PDOS), projected on the atomic orbitals of the C atoms and Ni atom at the vacancy site in SVG and Ni/SVG, respectively. The states are shifted with respect to Fermi energy. . . . .	78
5.3	Structure of (a) freestanding graphene with B-decorated single vacancy (SVBG). (b, c) top-view and side-view of B-decorated single vacancy in graphene supported on Ni(111) surface (Ni/SVBG). Golden and pale blue colored atoms denote C and Ni atoms, respectively. The B atoms around the vacancy and the displaced Ni atom below the vacancy are denoted with green and pink color, respectively. (d) and (e) show PDOS of states of atoms at the vacancy site in SVBG and Ni/SVBG, respectively. The states are shifted with respect to Fermi energy. . . . .	81
5.4	Structure of (a) freestanding graphene with N-decorated single vacancy (SVNG). (b, c) top-view and side-view of N-decorated single vacancy in graphene supported on Ni(111) surface (Ni/SVNG) after removing C atom from fcc site. Golden and pale blue colored atoms denote C and Ni atoms, respectively. The N atoms around the vacancy and surface Ni atoms that interact with N atoms are denoted with magenta and pink color, respectively. (d) and (e) show PDOS of states of atoms at the vacancy site in SVNG and Ni/SVNG. The states are shifted with respect to Fermi energy. . . . .	82
5.5	(a) Top-view and (b) side-view of single vacancy-Co complex in free-standing graphene sheet. C and Co atoms are denoted with golden and purple color while the C atoms around the vacancy are highlighted with blue color. The distance mentioned in the figures are in Å.(c) shows the magnetization density plot in which the yellow and cyan colored surfaces denote spin-up and spin-down magnetic moment, respectively. (d) DOS plots for Co (top panel) and C (bottom panel) states. The dashed vertical line represents Fermi energy. . . . .	85
5.6	(a) Side-view geometry of Ni/Co-SVG. The distance marked are in Å. C atoms away from vacancy, C atoms surrounding vacancy, Ni and Co atoms are denoted with golden, blue, pale blue and purple colored spheres. (b) Magnetization density plot with yellow and cyan colored isosurface representing spin-up and spin-down magnetic moment. The isovalue is 0.02 (No. of electron)/(bohr <sup>3</sup> ). (c) Density of states for Co (top panel), C atoms around the vacancy (middle panel) and Ni atom below the vacancy (bottom panel). The vertical dotted line represents Fermi energy. . . . .	86

5.7	(a) Top-view and (b) side-view of single vacancy-Co complex with N-decoration in freestanding graphene sheet. C, N and Co atoms are denoted with golden, magenta and purple color. The distance mentioned in the figures are in Å.(c) shows the magnetization density plot in which the yellow and cyan colored surfaces denote spin-up and spin-down magnetic moment, respectively. (d) DOS plots for Co (top panel) and N (bottom panel) states. The dashed vertical line represents Fermi energy. . . . .	88
5.8	(a) Top-view and (b) side-view of single vacancy-Co complex with B-decoration in freestanding graphene sheet. C, B and Co atoms are denoted with golden, green and purple color. The distance mentioned in the figures are in Å.(c) shows the magnetization density plot in which the yellow and cyan colored surfaces denote spin-up and spin-down magnetic moment, respectively. (d) DOS plots for Co (top panel) and B (bottom panel) states. The dashed vertical line represents Fermi energy. . . . .	89
5.9	(a) Side-view geometry of Ni/Co-SVNG. The distance marked are in Å. C, N, Ni and Co atoms are denoted with golden, magenta, pale blue and purple colored spheres. (b) Magnetization density plot with yellow and cyan colored isosurface representing spin-up and spin-down magnetic moment. The isovalue is 0.02 (No. of electron)/(bohr <sup>3</sup> ). (c) Density of states for Co (top panel), N atom (middle panel) and Ni atom below the vacancy (bottom panel). The vertical dotted line represents Fermi energy.	90
5.10	(a) Side-view geometry of Ni/Co-SVBG. The distance marked are in Å. C, B, Ni and Co atoms are denoted with golden, green, pale blue and purple colored spheres. (b) Magnetization density plot with yellow and cyan colored isosurface representing spin-up and spin-down magnetic moment. The isovalue is 0.02 (No. of electron)/(bohr <sup>3</sup> ). (c) Density of states for Co (top panel), N atom (middle panel) and Ni atom below the vacancy (bottom panel). The vertical dotted line represents Fermi energy. . . . .	91
5.11	Isosurface showing difference between charge density when the magnetization axis is along X and Z direction for (a) Co-SVG, (b) Co-SVNG and (c) Co-SVBG, respectively. The isovalues are $1 \times 10^{-5}$ , $1.5 \times 10^{-4}$ and $1.5 \times 10^{-3}$ (No. of electrons/bohr <sup>3</sup> ), respectively for Co-SVG, Co-SVNG and Co-SVBG. . . . .	92
5.12	Total DOS of Co- <i>d</i> in (a) Co-SVG and (b)Ni/Co-SVG. The bottom panel showing contour plots in each figure are ILDOS corresponding to the energy ranges marked as ‘E1’ and ‘E2’ and ‘E3’. In (b) the red dotted inset box at the right corner contains energy level diagram. . . . .	94
5.13	Color map of strain (in %) in bonds experienced by atoms in Co-SVG complex as it is placed on Ni(111) surface. The color codes for different amount of strain is displayed at the right-hand corner. The small filled black circle represents the center of the bond, the bigger filled black circle denote C atoms while the biggest circle filled with grid pattern denotes Co adatom. . . . .	96

5.14	Density of states for (a)Co-SVG→Ni and (b)Co-SVG-Ni. In (a) top and bottom panel corresponds to C' atom (with shorter Co-C bond length) and C'' atom (with greater Co-C bond length), respectively and middle panel corresponds to Co. In (b) top and bottom panel corresponds to Co and Ni atoms while middle panel corresponds to C atoms. The magenta shaded region and bold green lines shows DOS of $p_z$ and $sp^2$ states of C' atom while the dotted line in magenta and green shows DOS of $p_z$ and $sp^2$ states of C'' atom. The vertical black dotted line represents Fermi energy. . . . .	97
5.15	(a)Top and (b) side view of structure of bulk $\epsilon$ -GaSe. The dashed parallelogram in (a) shows the unit cell of bulk $\epsilon$ -GaSe. The dashed horizontal lines in (b) denote the periodically repeated unit along the z axis. The blue and orange spheres denote Se and Ga atoms, respectively. In (a) the purple spheres denotes Ga atoms from the bottom sandwich. (c) The slab model of GaSe(0001) surface. . . . .	105
5.16	Linear response of Mn- $d$ occupation with respect to varying perturbing potential ( $\alpha$ ) . . . . .	106
5.17	(a) The isosurfaces showing the difference between the computed charge density and that obtained from superposition of atomic charge density for bulk $\epsilon$ -GaSe. The yellow (cyan) surfaces show accumulation (depletion) of charge. Bandstructure and density of states (total, Ga- $s, p$ and Se- $s, p$ ) for (b) bulk $\epsilon$ -GaSe and (c) GaSe(0001) surface. The horizontal dashed line represents the valence band maxima while the vertical dashed lines marks the high symmetry points in the Brillouin zone. The red solid (dashed) arrow denotes the direct (indirect) bandgap. . . . .	107
5.18	Two adsorption geometries of Mn atom on GaSe(0001) surface: (a) Mn atop surface Se atom in monolayer GaSe(0001) and Mn at Se-Se bridge site in (b) monolayer GaSe(0001) and (c) bilayer GaSe(0001) slab. The distances shown in the figures are in Å. The purple closed surface denotes the distorted tetrahedra around the Mn dopant. Se, Ga and Mn are denoted with blue, orange and purple colored spheres. . . . .	110
5.19	Geometries of Mn-doped (a)monolayer and (b) bilayer GaSe(0001) surface with Mn present at the interstitial site. The distances shown in the figures are in Å. The purple closed surface in the monolayer structure denotes the trigonal prism around the Mn dopant. Se, Ga and Mn are denoted with blue, orange and purple colored spheres. . . . .	111
5.20	Geometries of Mn intercalated between two GaSe(0001) sandwiches. (a) Mn is atop Se atom and (b) atop Ga atom of the bottom sandwich. Se, Ga and Mn are denoted with blue, orange and purple colored spheres. The distances shown in the figures are in Å. . . . .	113
5.21	Structures of Mn substituting Ga atom from Ist layer where in (a) the replaced Ga is pushed to a interstitial site and in (b) the replaced Ga atom is moved to the surface. Se, Ga and Mn are denoted with blue, orange and purple colored spheres. The distances shown in the figures are in Å. . . . .	114
5.22	Structures of Mn substituting Ga atom from IInd layer where in (a) the replaced Ga is pushed to a interstitial site and in (b) the replaced Ga atom is moved deeper to intercalate between the two sandwiches. Se, Ga and Mn are denoted with blue, orange and purple colored spheres. The distances shown in the figures are in Å. . . . .	115



---

5.23	Density of states of <i>s</i> and <i>p</i> states of Ga and Se (top panel), <i>s</i> and <i>p</i> states of Mn (middle panel) and <i>d</i> states of Mn (bottom panel) for Mn-doped GaSe(0001) where (a) Mn replaces Ga atom from 1st layer and (b) Mn intercalates between two sandwiches. . . . .	117
5.24	Valence-band spectra of the clean GaSe (thin line) and the reacted Mn-GaSe surface (thick line) (a). Spin-projected DOS calculated for Mn adsorbed on the surface (b), Mn replacing Ga in the first Ga layer below the surface (c), Mn replacing Ga in the second Ga layer below the surface (d), Mn intercalated between the two Se layers (e), and Mn interstitial (f). The Mn partial DOS is represented by shaded areas. The vertical dashed lines represent the calculated highest occupied states. Reprinted with permission from ref.[2] Copyright2016, APS . . . . .	119
5.25	Magnetization density plot for Mn-doped GaSe(0001) bilayer structure of (a)-(c)type I and (d)-(e) type II. (a), (b) and (c) correponds to strutcules where Mn is adsorbed, Mn is present intertitially and Mn is intercalated, respectively, while (b) and (c) corresponds to strutures where Mn replaces Ga from 1st and 2nd layers, respectively. The red and blue isosurface denotes spin-up and spin-down magnetization, repectively. In each figures atoms interacting with Mn are marked with their atomic symbol. . . . .	122
26	Dipole corrected electrostatic potential for all the Mn-doped GaSe(0001) surfaces . . . . .	132
27	Density of states of <i>s</i> and <i>p</i> states of Ga and Se (top panel), <i>s</i> and <i>p</i> states of Mn (middle panel) and <i>d</i> states of Mn (bottom panel) for Mn-doped GaSe(0001) where (a) Mn is adsorbed on the surface at Se-Se bridge site, (b) Mn is present interstitially and (c) Mn replaces Ga atom from 2st layer with the replaced Ga intercalating between two sandwiches. . . . .	134

# List of Tables

3.1	Formation energy of the interface ( $E_f$ ) and binding energy of H ( $E_b$ ) on graphone supported on Ni(111)-O surface at different O coverages and for different possible configurations. . . . .	36
3.2	Work function ( $\phi$ ) and surface dipole density ( $p$ ) of Ni(111)-O surface before (with subscript “0”) and after adsorption of graphone. The positive and negative values of surface dipole densities indicates outwards and inwards orientation, respectively. . . . .	41
4.1	The cell parameters of freestanding semihydrogenated graphene sheet in different H adsorption patterns and transition metal surfaces . . . . .	49
4.2	Interaction energy of graphene (column 2) and semihydrogenated graphene in different H patterns (column 3-6) with its transition metal substrate in eV/Å <sup>2</sup> . . . . .	64
5.1	Formation energy of single C vacancy in graphene ( $E_f$ ) and binding energy of graphene with vacancy on Ni(111) surface ( $E_b$ ). $V_{top/fcc}$ stands for vacancy at the top/fcc site. . . . .	80
5.2	Magnetic anisotropy energies (MAE) along easy axis of magnetization are listed for Co-vacancy complexes in freestanding graphene and graphene supported on Ni(111) surface. . . . .	91
5.3	Formation energy for Mn-doped GaSe(0001) bilayer surface in different configurations. Formation energy of adsorption and interstitial configuration for monolayer GaSe(0001) are also included. FM and AFM represents structures where Mn-Mn coupling is ferromagnetic and antiferromagnetic, respectively. . . . .	116
5.4	Magnetic moment on Mn and bandgap obtained each of the five Mn-doped GaSe(0001) structures. The magnetic moment values in the paranthesis are contribution from Mn- $d$ orbital. . . . .	121

# Contents

<b>Certificate</b>	<b>i</b>
<b>Declaration</b>	<b>ii</b>
<b>Synopsis</b>	<b>iii</b>
	<b>vii</b>
<b>Acknowledgement</b>	<b>viii</b>
<b>List of Figures</b>	<b>x</b>
<b>List of Tables</b>	<b>xvii</b>
<b>Contents</b>	<b>xviii</b>
<b>1 Introduction</b>	<b>1</b>
1.1 Layered materials . . . . .	2
1.2 Technological importance of 2-D layered materials . . . . .	3
1.3 Interface with substrate . . . . .	5
1.4 Outline of thesis . . . . .	7
<b>2 Theoretical background for computational methods</b>	<b>10</b>
2.1 Born-Oppenheimer Approximation . . . . .	11
2.2 Density functional theory . . . . .	12
2.2.1 Local density approximation . . . . .	15
2.2.2 Generalised gradient approximation . . . . .	16
2.2.3 Correction to exchange-correlation functional . . . . .	16
2.3 Periodic supercells . . . . .	19
2.4 Electron-ion interaction . . . . .	24
2.5 Summary . . . . .	27
<b>3 Tuning of electronic and magnetic properties at Ni(111)/graphene interface by intercalation of atomic oxygen</b>	<b>29</b>
3.1 Introduction . . . . .	29
3.2 Methodology . . . . .	30
3.2.1 Computational Details . . . . .	30

3.2.2	Determination of U . . . . .	31
3.2.3	Determination of energetics . . . . .	33
3.3	Results . . . . .	34
3.3.1	Structure and energetics . . . . .	34
3.3.2	Magnetic properties at Ni(111)/O/graphene interface . . . . .	38
3.3.3	Charge transfer at the Ni(111)/O/graphene interface . . . . .	39
3.3.4	Electronic properties at the Ni(111)/O/graphene interface . . . . .	44
3.3.5	Experimental outlook for the synthesis of Ni(111)/O/GrH interface . . . . .	45
3.4	Conclusion . . . . .	45
<b>4</b>	<b><i>Ab initio</i> study of semihydrogenated graphene on lattice-matched transition metal surfaces</b> . . . . .	<b>47</b>
4.1	Introduction . . . . .	47
4.2	Computational methods . . . . .	49
4.3	Results and discussion . . . . .	52
4.3.1	Determining stable structure of freestanding semihydrogenated graphene . . . . .	52
4.3.2	Semihydrogenated graphene sheet on transition metal surfaces . . . . .	59
4.4	Summary . . . . .	71
<b>5</b>	<b>Investigation of vacancy-Co adatom complex in freestanding graphene and graphene supported on Ni(111) surface</b> . . . . .	<b>72</b>
5.1	Introduction . . . . .	72
5.2	Computational Details . . . . .	75
5.3	Results and discussions . . . . .	78
5.3.1	Single C vacancy in freestanding graphene and graphene supported on Ni(111) surface . . . . .	78
5.3.2	B-decorated and N-decorated single vacancy in freestanding graphene and graphene supported on Ni(111) surface . . . . .	80
5.3.3	Co adsorption at undecorated single vacancy in freestanding graphene and graphene supported on Ni(111) surface . . . . .	84
5.3.4	Co adsorption at B-decorated and N-decorated single vacancy in freestanding graphene and graphene supported on Ni(111) surface . . . . .	87
5.3.5	Magnetic anisotropy energy of different vacancy-Co adatom structures . . . . .	90
5.4	Summary . . . . .	99
	<b>Effect of doping on the structure and electronic properties of GaSe(0001) surface</b> . . . . .	<b>102</b>
5.5	Introduction . . . . .	102
5.6	Computational details . . . . .	104
5.7	Results . . . . .	107
5.7.1	Properties of GaSe bulk and (0001) surface . . . . .	107
5.7.2	Structure and stability of Mn-doped GaSe(0001) surface . . . . .	108
5.7.2.1	Structures of type I Mn-doped GaSe(0001) surface . . . . .	110
5.7.2.2	Structures of type II Mn-doped GaSe(0001) surface . . . . .	113
5.7.3	Electronic properties of Mn-doped GaSe(0001) surface: Elucidating interaction between Mn dopant and host atoms . . . . .	117

---

5.7.4	Magnetism in Mn-doped GaSe(0001) . . . . .	120
5.8	Summary . . . . .	123
<b>Summary and outlook</b>		<b>124</b>
<b>Appendix A</b>		<b>131</b>
.1	Dipole-corrected electrostatic potential for different Mn-doped GaSe(0001) structures . . . . .	131
.2	Density of states of Mn-doped GaSe(0001) surface . . . . .	133
<b>Bibliography</b>		<b>135</b>

# Chapter 1

## Introduction

The current trend in the material science research involve studies in nanoscale regime to a larger extent. However, even with highly advanced experimental techniques probing a material at nanoscale is a major challenge. Under these circumstances computational modelling and simulations play an important role in material science research. With the availability of enhanced computational power, advanced theories and improved algorithms, computational studies of materials (at different length and time scale) have evolved as a strong tool for not only to understand properties of materials but also to design novel materials with improved functionalities.

In this thesis, using density functional theory based calculations, we have explored the effects of chemical functionalization and defects (such as doping, vacancy and substitutional defects) on the electronic and magnetic properties of two-dimensional (2-D) layered materials. In order to understand their feasibility in electronic nanodevice applications, we have studied the effects of interactions of these chemically modified 2-D materials with its transition metal substrates.

In Section 1.1 we have given a brief introduction to layered materials and their types. Further in Section 1.2 we have discussed novel features of the layered materials and how these features have resulted into using them in a range of applications. Next in Section 1.3 we have briefly elucidated the effects of the substrates on the properties of the layered materials. Finally, in Section 1.4 we have presented the outline of the chapters in this thesis.

## 1.1 Layered materials

A layered material consists of anisotropic bonds; strong covalent bonds are present within the plane of the material while weak van der Waals bonds are present along the direction perpendicular to the plane. Every layered material thus can be thinned down to few layers or even to a single layer forming what is commonly referred as “two-dimensional (2-D) materials”. These 2-D materials exhibit novel properties which are absent in their parent bulk material. It was the discovery of graphene, the monolayer of graphite, in 2004 which triggered a surge of interest in 2-D materials. [3] Graphene shows exceptional electrical, thermal and mechanical properties but due to the semimetallic behaviour its application in semiconducting devices is limited. There are various approaches, like chemical modifications [4–6] or applying electric field [7, 8], for opening bandgap in graphene. However, these methods either degrade the carrier mobility in graphene or result in insufficient bandgap opening. Therefore, 2-D materials from other layered materials were explored. The 2-D materials can be distinguished as single-component material, binary material or ternary materials, depending upon the number of elements present in its one layer. For example, graphene, silicene, germanene, phosphorene, etc. are classified as single-component material because in each of these cases the 2-D material is made up of only one chemical component.[9–12] However unlike graphene, other single-component materials form a puckered atomic layer suggesting weaker  $\pi - \pi$  interaction between the neighbouring atoms. Among the single-component materials silicene, germanene and stanene show zero-bandgap in their bandstructure, as also seen for graphene. But in contrary with graphene, these three 2-D materials exhibit small bandgap opening upon inclusion of spin-orbit coupling (SOC). [9], [10], [13] This suggests better SOC strengths in these materials which is helpful in experimentally realising topological insulator phase. Another single-component 2-D material is phosphorene which is a semiconductor with a bandgap of around 2.0 eV. [11] Apart from graphene, phosphorene is the only other single-component 2-D material which can be synthesized by mechanical exfoliation. However, it is more sensitive to the ambient gases and hence needs special attention during experiments.

The binary materials which can form 2-D materials include nitrides (BN,  $\text{Ca}_2\text{N}$ ), carbides ( $\text{Y}_2\text{C}$ ), oxides ( $\text{MO}_3$ , where M can be Mo, Ta, W), chalcogenides (MCh,  $\text{MCh}_2$ ,  $\text{MCh}_3$ , where M stands for transition metals like Mo, W, Pd, Pt, etc. or post transition metals like Pb, Ga, In, etc. and Ch for chalcogens like S, Se, Te) and halides.[14] BN is found to be a suitable gate insulator with bandgap of about 5.9 eV. [15]  $\text{Ca}_2\text{N}$  and  $\text{Y}_2\text{C}$  are electron donating 2-D materials which are known to form another class of metals with very low work functions. Chalcogenides form larger class of compounds which

consists of mono-, di-, and tri-chalcogenides. The interlayer interaction in 2-D chalcogenides are relatively stronger resulting in electronic bandstructure which is dependent on number of layers. Additionally, these materials exhibits various crystal structures with different electronic properties. For instance, MoS<sub>2</sub> in hexagonal structure (2H-MoS<sub>2</sub>) is semiconducting but Li-intercalated MoS<sub>2</sub> attains octahedral (1T-MoS<sub>2</sub>) or distorted octahedral (1T'-MoS<sub>2</sub>) structure which shows metallic behaviour. [16] Moreover, change in the elemental components results in transition in their electronic properties. To clarify this we quote an example of 1T-TiCh<sub>2</sub>: TiS<sub>2</sub> is a semimetal while TiSe<sub>2</sub> is a semiconductor.[17, 18]

The increased degree of freedom in ternary and quaternary 2-D material (due to an increase in elemental components) results in interesting but at the same time complex properties. To elaborate we note an example of WS<sub>x</sub>Te<sub>2-x</sub>. WS<sub>2</sub> is stable in 2H phase while WTe<sub>2</sub> is stable in 1T phase. It is expected that WS<sub>x</sub>Te<sub>2-x</sub> should be stable in 2H and 1T phases for S-rich and Te-rich compositions, respectively. [19] This further implies that there should exist a specific composition where the two phases are very close in energy. Thus the structure of WS<sub>x</sub>Te<sub>2-x</sub> is highly sensitive to the concentration of S and Te. Ternary materials like CrSiTe<sub>3</sub> [20] and CrSnTe<sub>3</sub> [21], are ferromagnetic semiconductors. Magnetism in semiconductors is intriguing from the point-of-view of applications for spin-related devices. While in semiconducting single-component and binary 2-D materials one needs to use doping or other artificial modifications to bring in the magnetic behaviour, these ternary materials are naturally magnetic.

## 1.2 Technological importance of 2-D layered materials

2-D materials are not just intriguing but they also show potentials for applications in various field. In figure 1.1 we have shown a schematic diagram displaying special features of 2-D materials as well as different fields where their use is beneficial. As discussed in the preceding section, in a layered material the bonds between atoms along the plane of the surface are strong covalent while those between atoms of consecutive layers are weak van der Waals in nature. It is this anisotropic bonding which give rise to interesting features in the material. To start with, these layered materials can be exfoliated to form thin sheets containing few layers or even a single layer which are defect-free (in principle). The electrons in 2-D materials are confined naturally to the atomically thin layer of the material and hence they are stable in ambient conditions. This is unlike the thin sheets of a 3-D bulk material which terminate with dangling bonds. Hence, in field-effect transistors 2-D materials have started replacing the thin films of 3-D semiconductors to avoid scattering of charge due to dangling bonds.[22] Another instance of integration



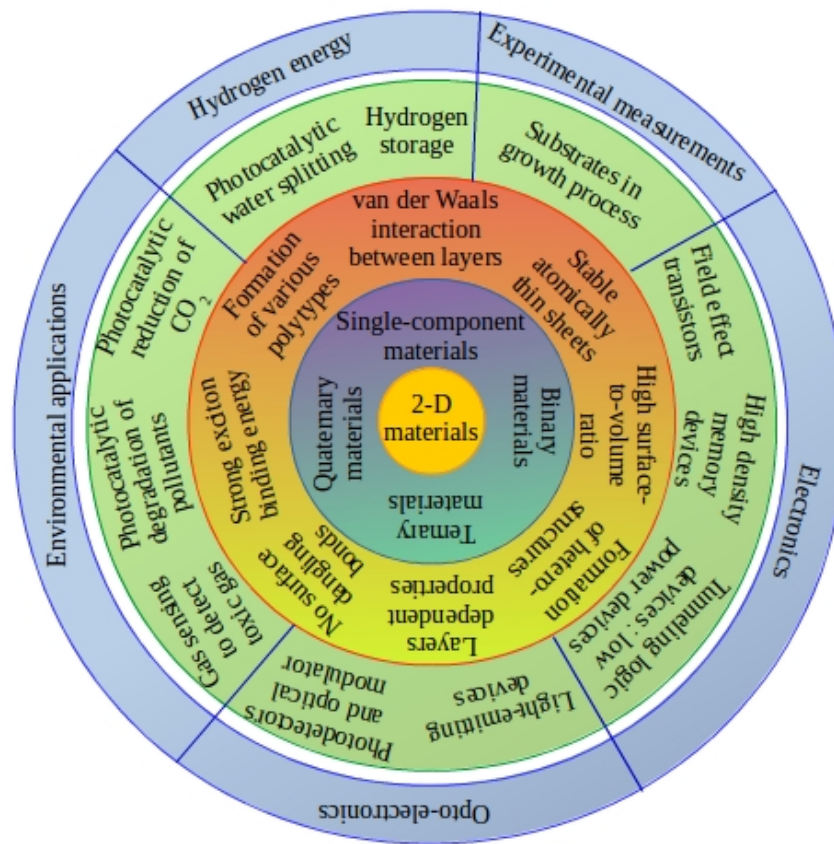


FIGURE 1.1: Schematic diagram showing special features of 2-D materials and their applications

of 2-D material in electronic devices is in flash memory devices. The thick metallic floating gate in transistor is replaced by thin layers of graphene so that the size of the transistor is reduced and more number of transistors can be used to give greater storage density.[23]

Eventually it was realised that by thoughtful stacking of monolayers of different 2-D materials one can achieve novel properties. To mention a few instances, heterostructure of direct bandgap semiconducting monolayers of  $\text{MoS}_2$  and  $\text{WSe}_2$  shows type-II band alignment.[24] Thus the conduction band minima and valence band maxima are located on either of the monolayers. As a consequence free electrons and holes pairs are spatially separated which is useful for solar energy conversion and optoelectronics applications.  $\text{MoS}_2/\text{WS}_2$  heterostructure shows ultrafast transfer of holes from  $\text{MoS}_2$  to  $\text{WS}_2$  which is interesting from the point-of-view of photodetector applications.[25] One can thus obtain desired application specific properties in these engineered heterostructures.[26–28]

Another optoelectronics application where 2-D materials are realised to be useful is light emitting devices. An unbalanced charge in 3D-bulk material is screened by atoms and

electrons around it in all three directions. However, in 2-D material screening is strong only within the plane of the material while it is weak along the out-of-plane direction. As a result Coulomb interactions are enhanced which give rise to stronger exciton binding energy resulting in interesting optoelectronic applications. ZnO shows large exciton binding energy (about 60 meV) which resulted in successful fabrication of ZnO base UV photodetectors.[29] One more interesting example is of electrically biased freely suspended graphene sheet showing bright white light emission due to Joule heating.[30] Similar emission is also observed from freely suspended MoS<sub>2</sub> sheet.[31]

A 2-D material has a large surface-to-volume ratio. As a consequence, it provides more opportunities for tuning and controlling its properties by chemical functionalization, like doping with foreign atoms or adsorption of atoms or molecules on the surface. The pre-requisite of bandgap opening for graphene can be achieved by doping with small molecules or metal or non-metal atoms. For instance, hydrogenation of graphene is the simplest chemical modification to change and tune electronic and magnetic properties of graphene.[32] Additionally, hydrogenation of graphene is reversible and hence it is one of the suggested routes for hydrogen storage. Further, NO<sub>2</sub> adsorption causes hole doping in graphene due to charge transfer from graphene to the molecule.[33] Thus graphene shows p-type behaviour. Substitutional doping of B also results in p-type behaviour while N-doping in n-type behaviour in graphene.[34] N-doped graphene was fabricated in FET which rendered lower conductivity, lower mobility and high on/off current ratio.[35] Besides graphene, N-doped MoS<sub>2</sub> shows better photocatalytic activity due to narrow bandgap induced by N-doping.[36] Upon irradiation of light N-doped MoS<sub>2</sub> generates excitons such that the electrons react with oxygen and form superoxides while holes react with water forming hydroxyl and hydrogen ions. The hydroxyl ions and oxides react with water pollutants and degrade them. Similarly, F-doped phosphorene is also realised as a visible light photocatalyst.[37] Moreover, co-doping of N and B increases sensitivity and selectivity of MoS<sub>2</sub> towards the most toxic Hg<sup>+2</sup> ions.[38] Vacancies and doping in stanene have also shown enhanced gas sensing ability towards hazardous SO<sub>2</sub> and H<sub>2</sub>S gas molecules.[39] Additionally, transition-metal dichalcogenides, like MoS<sub>2</sub> and WSe<sub>2</sub>, show impressive CO<sub>2</sub> reduction performance which is comparable with that of the expensive noble metal catalyst.[40, 41]

### 1.3 Interface with substrate

To conduct experiments and also to realise potential applications of nanomaterials, one needs to support the nanomaterial on a substrate. Unlike in 1-D or 0-D materials, the whole surface of 2-D materials is in contact with its substrate, either just through

physical interaction or through stronger chemical interaction. Thus interaction with substrate strongly influences the properties of the epitaxial 2-D materials. To explain the influence of substrate we again state the example of electrically biased freely suspended graphene which shows light emission in visible region. While graphene supported on SiO<sub>2</sub> substrate emits light in mid-infrared region with low efficiency.[30, 42]

Substrates can be identified as (1) those which just provide support and does not disturb the properties of the epitaxial 2-D materials and (2) those which does bring significant variation in the properties of the epitaxial 2-D materials. However, whether the substrate is of type (1) or type (2) depends upon the adsorbate. For example, h-BN is type (1) substrate for transition metal dichalcogenides. h-BN is chemically inert and thermally stable. Thus it does not chemically interact with the adsorbate surface and change its properties. But interestingly for graphene, h-BN is a type (2) substrate. This is because h-BN not only has a similar lattice as that of graphene but also the lattice parameters of h-BN and graphene have just less than 2% mismatch.[43] The most favourable configuration of graphene on h-BN is when C lie on top of B with N atoms at the center of hexagonal ring of epitaxial graphene. Graphene lattice has to slightly stretch in order to achieve this most favourable configuration. But due to the high Young modulus of graphene it is difficult for graphene to maintain this configuration throughout the lattice. Thus the most favourable configuration is only observed locally such that in between two such regions there exist regions where graphene lattice shows different orientations with respect to the lattice of the h-BN substrate. This gives rise to Moirè patterns in graphene which modifies its electronic properties.

For any 2-D material, terminated surfaces of 3-D materials are impartially of type(2) due to the surface dangling bonds. Like graphene supported on Ni(111) (Gr/Ni), Pt(111) (Gr/Pt) or Ru(0001) (Gr/Ru) surface show major changes in its original properties. Gr/Ni shows no surface corrugation due almost matching lattice parameter. But Gr/Pt shows small corrugation along with domains that are oriented with different angle of rotations and Gr/Ru shows only single domain but with large corrugations. These are evidenced from LEED patterns for three interfaces reported in Ref. [44]. Therefore, graphene on different metal surfaces show different electronic properties. Due to almost perfect matching of lattice parameters of graphene and Ni(111) surface, every alternating C atom in graphene overlaps on surface Ni atom which results in charge transfer of electrons from Ni-*d* to graphene sheet. Thus graphene on Ni(111) surface is electron-rich and shows n-type behaviour. In Gr/Ru, it is observed that there is charge transfer from the elevated region to the depressed region of graphene. Thus the elevated region shows p-type behaviour while the depressed region shows n-type behaviour. Graphene on Pt(111) is found to have p-type behaviour.

Not only does the interaction with different substrates induce different behaviour in the 2-D materials, but also their different growth processes on the same substrate. Different morphologies was observed for  $\text{WS}_2$  as well as  $\text{MoS}_2$  which were as-grown on  $\text{SiO}_2$  substrate and those transfered to  $\text{SiO}_2$  substrate.[45] Additionally, difference was also noted in temperature shifts for in-plane and out-of-plane vibration modes. As a result, variation in electronic as well as transport properties that are dependent on electron-phonon coupling is expected. Further, different polytypes of the 3-D substrate have different effects on the 2-D adsorbate. This can be seen from graphene grown on different polytypes of SiC substrate, namely 4H-SiC(0001), 6H-SiC(0001) and 3C-SiC(111). [46] Thus from all the above examples it is very clear that substrates can significantly influence the properties of the adsorbate materials.

## 1.4 Outline of thesis

The thesis is organised in the following manner:

**Chapter 2:** In this chapter we have briefly discussed the computational techniques, like density functional theory, pseudopotential method, periodic boundary conditions and plane-wave basis set and supercell, to determine total energy of a many-body system efficiently.

**Chapter 3:** Though graphene shows exceptional properties its application in device fabrication is restricted due to zero bandgap in its electronic structure. Therefore various ways are investigated to induce a bandgap in graphene which can tune the bandgap of graphene according to the required device application. One of the ways is to place graphene on transition metal surfaces like Ni(111) surface. From our earlier study we found that not only small bandgap but a small magnetic moment is also induced in the epitaxial graphene sheet when supported on Ni and Co surfaces.[47, 48] Thus the epitaxial graphene is feasible for electronic device applications. We further noticed that the induced magnetic moment and bandgap can be tuned by hydrogenating the epitaxial graphene. The maximum hydrogen coverage possible on the epitaxial graphene is when alternating C atom is hydrogenated. This hydrogenated graphene is named as graphone. In freestanding condition, graphone is a ferromagnetic semiconductor. However on Ni(111) surface we observe that the magnetic moment on graphone is highly quenched. Moreover the magnetic moment on Ni(111) surface is also quenched significantly. Therefore in this chapter we make an attempt to enhance the magnetic moment at this interface by intercalation of a layer of atomic O. We observe that the stability of the interface depends upon the balance between energy gained due to O

intercalation and energy cost due to instabilities occurring as a result of unsaturated C atoms in the graphene sheet. Furthermore we find that the magnetic moment at the interface increases with increase in O coverage. Not only is the magnetic moment at the interface increased but the interface at 1 ML O coverage shows spin polarised conduction of electrons at the Fermi energy. But only at 0.50 ML O coverage the magnetic moment on graphone sheet shows enhancement while at 1 ML and 0.25 ML O coverages the magnetic moment on the graphone sheet is highly quenched. Therefore we suggests that Ni(111)/graphone interfaces with 1 ML and 0.50 ML intercalating O coverages should be interesting from the point of view of spintronic device applications.

**Chapter 4:** Graphone, uniformly semihydrogenated graphene sheet, though unstable in freestanding condition due to sublattice imbalance but is found to be stable on Ni(111) surface. Other hydrogenation patterns, at the same H coverage, has been investigated in the freestanding condition and are observed to be stable. In this chapter we have studied and compared four such different H adsorption patterns, including the uniform pattern (graphone), on semihydrogenated graphene sheet supported on three different transition metal surfaces (Ni(111), Co(111) and Cu(111)) in order to understand the following: (1) Whether hydrogenation patterns, other than the uniform pattern, are stable on the semihydrogenated graphene sheet supported on transition metal surface and (2) The role of transition metal substrates in stabilizing the hydrogenation pattern on the graphene sheet. From binding energy analysis and calculated C-1s corelevel shifts we have shown that though the four different H adsorption patterns on graphene supported on these transition metal surfaces display different electronic and magnetic properties but they are difficult to discern experimentally. Especially on Ni(111) surface, we find all four H patterns are equally stable and the core-level shifts between C-1s peaks corresponding to hydrogenated and unhydrogenated shows small variation with change in H pattern. The largest difference in the core-level shift noted between two semihydrogenated graphene structures on Ni(111) surface is around 0.05 eV which is much less than the resolution of the XPS instrument (0.20 eV). Similarly, the largest difference in core-shifts for structures on Co(111) and Cu(111) are noted to be around 0.15 eV and 0.19 eV. We further find that in order stablize different hydrogenation patterns the graphene sheet chooses different structural configurations on its transition metal substrates.

**Chapter 5:** In this chapter we have investigated complex structures of Co adatom at undecorated single C vacancy and decorated single C vacancies with N and B in graphene. This study intends to find out whether or not a single magnetic atom adsorbed on the planar graphene can act as a magnetic bit. These structures are studied in freestanding graphene as well as graphene supported on Ni(111) surface. We have computed magnetic anisotropy energy for each complex structure in freestanding and

supported conditions and find that the decorated structures of freestanding graphene shows better magnetic moment on Co and MAE ( $\sim 10^{-3}$  eV) than the undecorated structure ( $10^{-5}$  eV). However, the highlight of the study is the huge enhancement in MAE, about 40 meV, obtained for three complex structures when supported on Ni(111). So far such large MAE has not been reported for single metal adatom on graphene.

**Chapter 6:** Inducing magnetism in semiconducting materials is intriguing as well as important from the point of view of spintronic device applications. This chapter discusses the effects of doping magnetic impurity (Mn) on the electronic and magnetic properties of GaSe(0001) surface. We have considered different possible doping sites for Mn in order to predict whether the dopant moves within the layers of surface or stays on the surface of the host material. Further, we have noted magnetic and electronic properties of each possible doped structures. In here, we observe that rather than Mn-*d* states, the empty Mn-*s,p* states are involved in the interaction with host material. Thus we obtain unperturbed magnetic moment on the Mn atom ( $5\mu_B$ ) in each doped structures. Though the doping site shows high local magnetism in all five doped structures, we observe notable magnetic coupling only in few of the doped structures.

**Chapter 7:** In this final chapter we have summarised our work and we suggest future scope for the different studies undertaken in this thesis.

## Chapter 2

# Theoretical background for computational methods

It will not be overrated if one states that almost all the physical properties can be computationally determined from the total energies or difference of the total energies of materials. [49] Some of the few examples include lattice constants, bulk moduli, bondlengths, force constants, polarizabilities, and many more. With decreasing cost of computers and increasing computational efficiency over the years the *ab initio* total energy calculation tools have proved to be more cost-effective than experimental measurements. Where for every measurement a new set of experimental apparatus is required only a single computational tool is sufficient to predict more than one physical properties of the material. The current-age computational tools can handle systems of hundreds and thousands of atoms and hence they are proved to be useful in solving range of interesting real-world problems in different field of science.

Computational predictions involve calculation of quantum mechanical total energy of the system and its minimization with respect to the coordinates of electrons and nuclei. For the calculation of quantum mechanical total energy of a system one needs to use a number simplifications and approximations. The first approximation described in this chapter is Born-Oppenheimer approximation which reduces the many-body problem to solving dynamics of electrons with frozen nuclear coordinates. Further simplification involve iterative minimization technique to relax electronic coordinates, density functional theory to model electron-electron interaction, pseudopotential theory to model the electron-ion interaction, supercells are used to model aperiodic systems. Below, in each section, we have described these techniques.

## 2.1 Born-Oppenheimer Approximation

For a system of  $N$  nuclei and  $n$  electrons the exact solution is determined by solving the following Schrödinger equation.

$$\mathbf{H}\Psi(\{R_I, r_i\}) = E\Psi(\{R_I, r_i\}) \quad (2.1)$$

where  $E$  and  $\Psi$  are energy and many body wavefunction of the system.  $\mathbf{H}$  is the Hamiltonian which consists of the following terms:

$$\begin{aligned} \mathbf{H} = & - \sum_I \frac{\hbar^2}{2M_I} \nabla_{R_I}^2 - \sum_i \frac{\hbar^2}{2m_i} \nabla_{r_i}^2 + \sum_{i,j;i>j} \frac{1}{4\pi\epsilon_0} \frac{e^2}{|r_i - r_j|} \\ & - \sum_{i,I} \frac{1}{4\pi\epsilon_0} \frac{Z_I e^2}{|R_I - r_i|} + \sum_{I,J;I>J} \frac{1}{4\pi\epsilon_0} \frac{Z_I Z_J e^2}{|R_I - R_J|} \end{aligned} \quad (2.2)$$

In the above equation the upper case and lower case letters corresponds to nuclear and electronic coordinates. Thus  $M_I$  and  $R_I$  are mass and position of  $I$ th nucleus, respectively. Similarly  $m_i$  and  $r_i$  are mass and position of  $i$ th electron, respectively.  $Z_I$  is the atomic number or number of protons in  $I$ th nucleus. Hence  $eZ_I$  and  $e$  are charges of nucleus and electron, respectively.  $\epsilon_0$  is permittivity of free space and  $\hbar = h/2\pi$ , where  $h$  is the Planck's constant. The first and the second term in equation 2.2 are nuclear and electronic kinetic energy operators, respectively. The rest three terms are electron-electron, electron-ion and ion-ion potential energy operators, respectively. The total wavefunction of the system depends on both, nuclear as well as electronic coordinates. This makes solving the above Hamiltonian extremely difficult, even for few tens of atoms.

To simplify the problem, separating nuclear and electronic degrees of freedom will be helpful. However motion of nuclei and electrons in the system are correlated by the electron-ion interaction term which has significantly large contribution to the total energy. But nuclei are much heavier particles and move very slowly than electrons. Hence for a current nuclear configuration electrons can easily secure their lowest energy positions before the nuclei arrange in another minimum energy configuration. The electrons can thus be approximated to be present in a static field of nuclei and one can separate nuclear and electronic degrees of freedom. As a result the total wavefunction ( $\Psi(\{R_I, r_i\})$ ) can be expressed as a product of electronic wavefunction ( $\psi(r_i; R_I)$ ), which is only parametrically dependent on nuclear coordinates, and nuclear wavefunction ( $\chi(R_I)$ ).



This approximation of separating nuclear and electronic degrees of freedom is Born-Oppenheimer (BO) approximation.[50] Within BO approximation one can define the electronic Hamiltonian ( $\mathbf{H}_e$ ) as follows,

$$\mathbf{H}_e = - \sum_i \frac{\hbar^2}{2m_i} \nabla_{r_i}^2 + \sum_{i,j;i>j} \frac{1}{4\pi\epsilon_0} \frac{e^2}{|r_i - r_j|} - \sum_{i,I} \frac{1}{4\pi\epsilon_0} \frac{Z_I e^2}{|R_I - r_i|} \quad (2.3)$$

where the motion of nuclei are neglected. The total electronic energy will be the sum of total energy of electrons, obtained by solving the electronic Schrödinger equation, and electrostatic energy of nuclei. However, the electronic wavefunction is dependent on  $r_i$  which is again a large number. To explain this let us take an example of a single  $\text{Cl}_2$  molecule which consists of 34 electrons. To define position of each electron one requires 3 coordinates which amount to 102 variables.

A more critical issue than solving the electronic Schrödinger equation for large number of variables is the Coulombic electron-electron interactions which are not negligible and has infinite range of interaction. Infact, these interactions are very strong for shorter electron-electron separations, like in  $d$  states of transition-metal atoms. The form of the interaction suggests that in order to determine a single electron wavefunction one needs to determine wavefunctions of all other electrons present in the system making the Schrödinger equation a many-body problem. In the next section we have discussed a first principles method, density functional theory, which reduces the many-body problem to solving single-particle Hamiltonians without neglecting electron-electron interaction term from the electronic Hamiltonian.

## 2.2 Density functional theory

Density functional theory originated from the two theorems which were stated and proved P. Hohenberg and W. Kohn.[51] The first theorem states that, “*The external potential is determined, within a trivial additive constant, by the electron density.*” Alternatively, “*For a many-body system the total energy of the system is a unique functional of the electron density;  $E \equiv E[\rho(\mathbf{r})]$ .*” The second theorem gives energy variational principle and it states: “*For a trial electron density, such that  $\tilde{\rho}(\mathbf{r}) \geq 0$  and  $\int \tilde{\rho}(\mathbf{r})d\mathbf{r} = n$ , the ground state total energy,  $E_0 \leq E[\tilde{\rho}(\mathbf{r})]$ .*” Therefore the ground state energy can be obtained by minimising the energy functional,  $E[\rho(\mathbf{r})]$ . With these two theorem W. Kohn and L. Sham developed an iterative method to convert many-electron problem into a set of one-electron equations. They defined the energy functional for an interacting

system containing  $N$  nuclei and  $n$  electrons as sum of two terms:

$$E[\rho(\mathbf{r})] = \int \rho(\mathbf{r}) \cdot v(\mathbf{r}) \cdot d\mathbf{r} + F[\rho(\mathbf{r})], \quad (2.4)$$

The first term gives the potential energy due to electron-ion interaction while the second term ( $F[\rho(\mathbf{r})]$ ) is sum of the remaining energy terms (kinetic energy and electron-electron interaction energy). The electronic density for the interacting system,  $\rho(\mathbf{r})$ , is given as:

$$\rho(\mathbf{r}) = \sum_i^n f_i |\psi_i(\mathbf{r})|^2 \quad (2.5)$$

where,  $f_i$  are the occupation of each single-particle state such that  $0 \leq f_i \leq 1$ . The kinetic energy,  $T[\rho(\mathbf{r})]$ , can also be expressed in terms of single-particle wavefunction as:

$$T = \sum_i^n f_i \langle \psi_i | -\frac{1}{2} \nabla^2 | \psi_i \rangle \quad (2.6)$$

Suppose if one considers a non-interacting electron system with same electron density,  $\rho(\mathbf{r})$ , whose Hamiltonian is defined as follows:

$$\mathbf{H}_s = \sum_i^n -\frac{1}{2} \nabla_i^2 + \sum_i^n v_s(\mathbf{r}) = \sum_i^n \mathbf{h}_s \quad (2.7)$$

where,  $\mathbf{h}_s$  is the one-electron Hamiltonian. There is no electron-electron interaction term and so the electron density and kinetic energy is then expressed as:

$$\rho(\mathbf{r}) = \sum_i^n |\psi_i(\mathbf{r})|^2 \quad (2.8)$$

and

$$T_s = \sum_i^n \langle \psi_i | -\frac{1}{2} \nabla^2 | \psi_i \rangle \quad (2.9)$$

where  $f_i = 1$  for  $n$  orbitals and  $f_i = 0$  for rest number of orbitals. The solution of  $\mathbf{H}_s$  will then have determinantal form;  $\Psi_s = \frac{1}{\sqrt{(n!)}} \det[\psi_1 \psi_2 \dots \psi_n]$ , where  $\psi_i$  are  $n$  lowest eigenstates of one-electron Hamiltonian:

$$\mathbf{h}_s \psi_i = [-\frac{1}{2} \nabla_i^2 + v_s(\mathbf{r})] \psi_i = \epsilon_i \psi_i \quad (2.10)$$

$v_s(\mathbf{r})$  is electron-ion potential.

The kinetic energy of non-interacting system,  $T_s[\rho]$ , is uniquely defined for electron density,  $\rho(\mathbf{r})$ . However, it is not equal to kinetic energy of the interacting system,  $T[\rho]$ . This is because the motion of a electron in the interacting system is correlated

with all other electrons in the system. The missing electron-electron interaction in non-interacting system consists of Coulombic repulsion between electrons. This repulsion energy is reduced when electrons with same spin state move away from each other. The reduction in repulsion energy is known as exchange energy which results from the antisymmetric nature of the wavefunction. A further reduction in the Coulomb energy takes place when electrons of different spins are also spatially separated. This reduction in energy is known as correlation energy which reduces Coulomb energy but by increasing the kinetic energy of electrons. Hence  $F[\rho(\mathbf{r})]$  is given as,

$$F[\rho] = T[\rho] + V_{ee}[\rho] = T_s[\rho] + J[\rho] + E_{xc}[\rho] \quad (2.11)$$

where,

$$E_{xc}[\rho] = T[\rho] - T_s[\rho] + V_{ee}[\rho] - J[\rho] \quad (2.12)$$

$E_{xc}$  is the energy term which incorporates the exchange and correlation energies. It is defined by sum of two differences: 1) kinetic energy of interacting system and kinetic energy of non-interacting system which accounts for correlation energy and 2) potential energy due total electron-electron interaction ( $V_{ee}[\rho]$ ) and electron-electron Coulomb repulsion ( $J[\rho]$ ) which gives the exchange energy. Thus the one-electron Hamiltonian for an interacting system can be defined similarly to that defined for non-interacting system as follows:

$$\mathbf{h}\psi_i = \left[-\frac{1}{2}\nabla_i^2 + v_{eff}(\mathbf{r})\right]\psi_i = \epsilon_i\psi_i \quad (2.13)$$

such that

$$v_{eff} = v(\mathbf{r}) + \int \frac{\rho(\mathbf{r}')}{|\mathbf{r} - \mathbf{r}'|} d\mathbf{r}' + v_{xc}(\mathbf{r}) \quad (2.14)$$

and

$$\rho(\mathbf{r}) = \sum_i^n f_i |\psi_i(\mathbf{r})|^2 \quad (2.15)$$

$v_{xc}$  is functional derivative of exchange-correlation energy;  $v_{xc}(\mathbf{r}) = \frac{\delta E_{xc}[\rho(\mathbf{r})]}{\delta \rho(\mathbf{r})}$

In the above set of equations we can observe cyclic dependence among them such that in order to solve the set of equation 2.13 we need to determine  $v_{eff}$  which in-turn is determined using  $\rho(\mathbf{r})$  (equation 2.14). Moreover  $\rho(\mathbf{r})$  is evaluated by  $\psi_i$  (equation 2.15), which are solutions of one-electron Hamiltonian defined in equation 2.13. Therefore Kohn and Sham suggested to solve these equations iteratively or self-consistently as shown in the flowchart in figure 2.1.

Equation 2.13 is referred as Kohn-Sham equations and the corresponding solutions,  $\psi_i$ , are known as Kohn-Sham orbitals. Kohn-Sham equation is obtained by mapping the interacting electron system onto non-interacting electron system. Though these

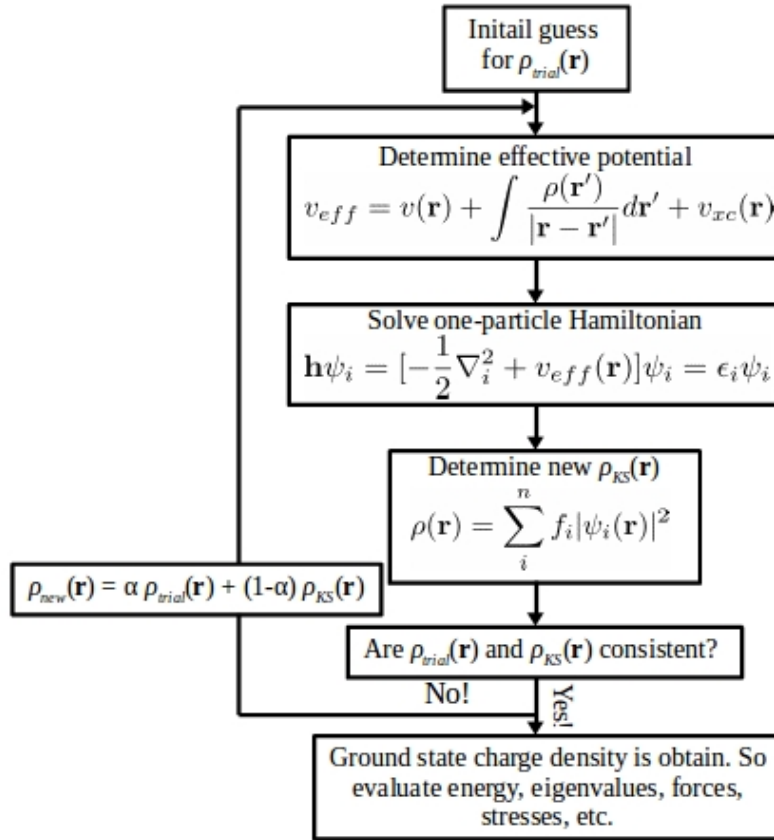


FIGURE 2.1: Flowchart showing self-consistent field cycle to solve Kohn-Sham equations.

equations provide an exact approach to solve many-electron system but evaluation of  $E_{xc}$  requires some approximations as its exact mathematical expression is unknown. Another note, the sum of eigenvalues obtained from Kohn-Sham equations does not result in total energy of the system. This is because the electron-electron interaction is over-counted in Hartree potential as well as in exchange-correlation potential. This overcounting error is called self-interaction error.

### 2.2.1 Local density approximation

The exact Kohn-Sham procedure faces problem while evaluating exchange-correlation energy which is a functional of electron density. One way to determine the exchange-correlation energy is to consider homogeneous electron gas for which the electron density is constant at all points. Thus the exchange-correlation energy depends on local density

around a point  $\mathbf{r}$  and is given by the following equation. [52]

$$E_{xc}[\rho(\mathbf{r})] = \int \epsilon_{xc}[\rho(\mathbf{r})] \cdot \rho(\mathbf{r}) \cdot d\mathbf{r} \quad (2.16)$$

where  $\epsilon_{xc}$  is exchange-correlation energy per particle of a homogeneous electron gas in which at each point  $\mathbf{r}$  local density is  $\rho(\mathbf{r})$ . This approximation is known as local density approximation (LDA) which works well for systems with slowly varying density.

### 2.2.2 Generalised gradient approximation

For practical systems the exchange-correlation energy depends not only on the local density but also on the variation of local density. It is the variation in density which defines the chemical bonding. Hence taking into account the derivative of density around each point  $\mathbf{r}$  while calculating the exchange-correlation energy has proved to be an improvement over local density approximation.[52] This approximation is known as generalised gradient approximation (GGA) which alters equation 2.16 as follows:

$$E_{xc}[\rho(\mathbf{r})] = \int \epsilon_{xc}[\rho(\mathbf{r}), \nabla\rho(\mathbf{r})] \cdot \rho(\mathbf{r}) \cdot d\mathbf{r} \quad (2.17)$$

In many complex systems it is observed that the simple GGA also fails. A number of other functionals has been developed such that exchange and correlation energies are evaluated separately under different approximations (Hartree-Fock or LDA or GGA) and then their linear combination is given as the total exchange-correlation energy functional. Such functionals are called hybrid functionals which are derived from more than one approximations. Another improvement in simple GGA or LDA functional is by rectifying the self-interaction error which is discussed in the following subsection.

### 2.2.3 Correction to exchange-correlation functional

Both, LDA and GGA, functionals are usually seen to fail for strongly correlated materials which are materials with partially filled  $d$  or  $f$  valence shell. In these, electrons spend more time around ions and thus they experience strong electron-electron repulsion compared to electrons in simple metals. Thus there are two competing factors: (i) kinetic energy which when stronger than the on-site Coulomb repulsion delocalizes the electron and hence gives rise to metallic behaviour and (ii) correlation which is stronger when electrons are present in narrow bands resulting in localization of electron. The system with strong correlation thus usually prefers insulating behaviour. These two extreme scenarios are not distinguished well by the simpler exchange and correlation functionals defined

above. This is because in the simpler functionals every electron is treated in a mean field of other electrons which naturally fails to describe the strong correlation. One of the way to rectify the interactions is by including Hubbard U correction which we have used in our work. Such a method was first formulated by Anisimov *et al.* [53, 54] and which was revised later by W. Pickett *et al.* [55] The elementary form of the energy functional with the U correction is expressed as follows:

$$E = E_0 + E_{hub} - E_{dc} \quad (2.18)$$

$$E = E_0 + \sum_I \left[ \frac{U}{2} \sum_{m,\sigma \neq m',\sigma'} n_m^{I\sigma} n_{m'}^{I\sigma'} - \frac{U}{2} n^I (n^I - 1) \right] \quad (2.19)$$

where  $n^I = \sum_{m,\sigma} n_{m,\sigma}^I$  is occupation of atom at site  $I$  at each state defined by the magnetic quantum number ( $m$ ) and spin ( $\sigma$ ).  $U$  is the Hubbard U correction parameter. The first term ( $E_0$ ) is the simple total energy obtained using either from LDA or GGA. The second term ( $E_{hub}$ ) contains the correct on-site correlation energy while the inaccurate correlations from GGA or LDA functional are included in the last term ( $E_{dc}$ ). By differentiating equation 2.19 with respect to orbital occupation ( $n_{m,\sigma}^I$ ) one obtains the corresponding orbital energy ( $\epsilon_{m,\sigma}^I$ ).

$$\epsilon_{m,\sigma}^I = \epsilon_{m,\sigma}^{0I} + U \left( \frac{1}{2} - n_{m,\sigma}^I \right) \quad (2.20)$$

Further we can express  $n_{m,\sigma}^I$  as  $n_{m,\sigma}^I = \sum_i \langle \psi_i^\sigma | P_{m\sigma}^I | \psi_i^\sigma \rangle$  so that the potential entering in the Kohn-Sham equations can be written as given in the following equation:

$$V | \psi_i^\sigma \rangle = V_0 | P_{m,\sigma}^I \psi_i^\sigma \rangle + \sum_{I,m} U \left( \frac{1}{2} - n_{m,\sigma}^I \right) P_{m,\sigma}^I | \psi_i^\sigma \rangle \quad (2.21)$$

$P^I$  is the projection operator on atomic orbitals at site  $I$ . The above expression for potential implies that if initially an orbital is more (less) than partially filled then the Hubbard contribution to the potential is attractive (repulsive) and the electrons in these orbitals are localised (delocalised). A gap of width around  $U$  is thus opened between states with  $n_m^I \approx 1$  and  $n_m^I \approx 0$ .

A significant flaw in the above scheme is that the expression of energy functional with U correction (equation 2.19) is not invariant under rotation of atomic orbital basis set. This problem was corrected by Anisimov *et al.* [56] with the following scheme which is similar to Hatree-Fock formalism:

$$E_{hub}[n_{mm'}^I] = \left\{ \frac{1}{2} \sum_{m,\sigma,I} \langle m, m'' | V_{ee} | m', m''' \rangle n_{mm'}^{I\sigma} n_{m''m'''}^{I-\sigma} \right. \\ \left. + (\langle m, m'' | V_{ee} | m' m''' \rangle - \langle m, m'' | V_{ee} | m''' m' \rangle) n_{mm'}^{I\sigma} n_{m''m'''}^{I-\sigma} \right\} \quad (2.22)$$

$$E_{dc}[n^I] = \sum_I \frac{U}{2} n^I (n^I - 1) - \frac{K}{2} [n^{I\sigma} (n^{I\sigma-1} + n^{I\sigma'} n^{I\sigma'-1})] \quad (2.23)$$

where  $U$  and  $K$  represents Coulomb and exchange parameters. A more simplified scheme is suggested by M. Cococcioni and S. Gironcoli [57] which expresses the correction term as follows:

$$E_{hub}[n_{mm'}^I] - E_{dc}[n^I] = \frac{U}{2} \sum_{I,\sigma} Tr[n_{\sigma}^I (1 - n_{\sigma}^I)] \quad (2.24)$$

Additionally M. Cococcioni and S. Gironcoli have also devised a simple procedure for determining the value of  $U$  parameter in such a way that it takes into account the physical behaviour of the system. Therefore the  $U$  parameter correctly estimates the tendency of the system towards strong correlation and hence its effects like electron localization and bandgap opening. But before describing the procedure for calculating  $U$  one should understand what exactly the  $U$  parameter corrects in the total energy functional. The mean-field approach used in LDA and GGA formalism gives rise to incomplete self-interaction energy which results in unphysical non-linear contribution, rather than an expected linear contribution, of total energy with respect to orbital occupation. As a consequence of the spurious curvature of the total energy, fractional occupations of valence states describe incorrect electronic behaviour especially for the case of strongly correlated materials. The issue can be solved if the valence atomic orbital occupations are restricted to integer values. This is achieved in LDA+ $U$  (or GGA+ $U$ ) method by including  $U$  correction which acts like a constraining parameter on the occupation of orbitals. The  $U$  parameter is hence the spurious curvature in total energy.

In order to evaluate  $U$  a large supercell is chosen in which occupation only at a single site is varied. However the curvature of total energy arising due to the variation of occupation does not directly give the value for  $U$ . This is because change in occupation results in rehybridization of the localised orbitals which occurs even under non-interacting condition. The rehybridization effect is eliminated by taking the difference between the curvature of the total energy in non-interacting condition ( $\frac{d^2 E}{d(n^I)^2}$ ) and the curvature of total energy in interacting condition ( $\frac{d^2 E_{KS}}{d(n^I)^2}$ ).

$$U = \frac{d^2 E}{d(n^I)^2} - \frac{d^2 E_{KS}}{d(n^I)^2} \quad (2.25)$$

Rather than constraining orbital occupations, a better way to vary the occupation of strongly correlated orbitals is by adding a perturbing potential of varying amplitude  $\alpha$  at a single site,  $I$ , as given by the following equation:

$$V^{constr} = V_0 + \alpha_I P^I \quad (2.26)$$

where  $V_0$  is the potential used in LDA or GGA calculation and  $P^I$  is the projector operator on atomic states at site  $I$  and is given as:  $P^I = \sum_m |\phi_m^I\rangle \langle \phi_m^I|$ . It can be easily shown that curvature of total energy is variation of the potential shift ( $\alpha_I$ ) with respect to variation in occupation of atomic orbitals at a particular site when occupation on other sites are same.

$$\frac{d^2 E[n^J]}{dn^I} = -\frac{d\alpha_I(n^J)}{dn^I} \quad (2.27)$$

However from calculations the quantity that is easily obtained is the inverse of quantity on the RHS of equation 2.27 which is the response function ( $\chi_{IJ}$ ). Thus we redefine the expression for  $U$  as:

$$U = -\frac{d\alpha^I}{dn^I} + \frac{d\alpha^I}{dn_0^I} = (\chi_0^{-1} - \chi^{-1})_{II} \quad (2.28)$$

## 2.3 Periodic supercells

So far it was discussed in this chapter that using density functional theory one can drastically reduce the computational efforts for solving many-body problem. However there still remains two difficulties while treating infinite number of electrons which move in a static potential of infinite ions in a solid. The first difficulty is to calculate wavefunction for each of the infinite number of electrons and the second difficulty is of infinitely large basis set which is required to define each wavefunction. Both these difficulties can be solved if one takes into account periodicity of the solid and build our wavefunction using Bloch's theorem.[49, 58] Every periodic solid is defined by three primitive lattice vectors ( $\mathbf{a1}$ ,  $\mathbf{a2}$  and  $\mathbf{a3}$ ) and position of atoms inside a primitive unit cell, also known as basis. The linear combination of these primitive lattice vectors is defined as translational lattice vector which is given as:

$$\mathbf{P} = p_1 \mathbf{a1} + p_2 \mathbf{a2} + p_3 \mathbf{a3}, \quad (2.29)$$

where  $p_1, p_2$  and  $p_3$  are integers. All the equivalent points connected by these lattice vectors in real space forms a Bravais lattice whose volume is defined as,  $\Omega = |\mathbf{a1} \cdot (\mathbf{a2} \times \mathbf{a3})|$ . For any Bravais lattice value of any function at point  $\mathbf{r}$ , which lies in a primitive



unit cell is same at another equivalent point in other unit cell which is reached by a translation of  $\mathbf{P}$ . Thus one needs to determine value of a function only within a single primitive unit cell. One can prove this mathematically by constructing a reciprocal space. The reciprocal primitive lattice vectors can be determined from the primitive lattice vectors of real space as follows:

$$\mathbf{b1} = \frac{2\pi(\mathbf{a2} \times \mathbf{a3})}{\mathbf{a1} \cdot (\mathbf{a2} \times \mathbf{a3})}, \mathbf{b2} = \frac{2\pi(\mathbf{a3} \times \mathbf{a1})}{\mathbf{a1} \cdot (\mathbf{a2} \times \mathbf{a3})}, \mathbf{b3} = \frac{2\pi(\mathbf{a1} \times \mathbf{a2})}{\mathbf{a1} \cdot (\mathbf{a2} \times \mathbf{a3})} \quad (2.30)$$

These equation imply

$$\mathbf{a_i} \cdot \mathbf{b_j} = 2\pi \cdot \delta_{ij} \quad (2.31)$$

and volume of the reciprocal unit cell is,

$$\Omega' = |\mathbf{b1} \cdot (\mathbf{b2} \times \mathbf{b3})| = \frac{2\pi^3}{\Omega} \quad (2.32)$$

Like in real-space, in reciprocal space all the equivalent points are connected by translational reciprocal lattice vectors ( $\mathbf{G}$ ) which is defined as:  $\mathbf{G} = m_1\mathbf{b1} + m_2\mathbf{b2} + m_3\mathbf{b3}$  where  $m_i$  are inetgers. By construction, the relation between  $\mathbf{P}$  and  $\mathbf{G}$  is the following:

$$\mathbf{P} \cdot \mathbf{G} = 2\pi l, \quad (2.33)$$

where  $l = p_1m_1 + p_2m_2 + p_3m_3$ , is integer. Or another relation holds true,

$$e^{i\mathbf{G} \cdot \mathbf{P}} = 1 \quad (2.34)$$

Now suppose a function at  $\mathbf{r}$ ,  $f(\mathbf{r})$ , in a primitive unit cell. The Fourier transform of  $f(\mathbf{r})$  is given by the following equation:

$$f(\mathbf{r}) = \sum_{\mathbf{G}} e^{i\mathbf{G} \cdot \mathbf{r}} \cdot f(\mathbf{G}) \quad (2.35)$$

At another point in real space which is away from  $\mathbf{r}$  by  $\mathbf{P}$  the above equation can be written as follows:

$$f(\mathbf{r} + \mathbf{P}) = \sum_{\mathbf{G}} e^{i\mathbf{G} \cdot (\mathbf{r} + \mathbf{P})} \cdot f(\mathbf{G}) \quad (2.36)$$

$$f(\mathbf{r} + \mathbf{P}) = \sum_{\mathbf{G}} e^{i\mathbf{G} \cdot \mathbf{r}} \cdot e^{i\mathbf{G} \cdot \mathbf{P}} \cdot f(\mathbf{G}) \quad (2.37)$$

From equation 2.34 one gets,

$$f(\mathbf{r} + \mathbf{P}) = \sum_{\mathbf{G}} e^{i\mathbf{G} \cdot \mathbf{r}} \cdot f(\mathbf{G}) = f(\mathbf{r}) \quad (2.38)$$

Thus from the relation between real space and reciprocal space lattice vectors one can find that the value of a function at a point in one primitive unit cell in real space is same at an equivalent point in other unit cell which is away by  $\mathbf{P}$ . This statement is applied to the wavefunction of a periodic system which essentially is the Bloch's theorem which states: "When the potential in the single particle Hamiltonian has the translational periodicity of the Bravais lattice such that,  $V(\mathbf{r} + \mathbf{P}) = V(\mathbf{r})$ , the single particle wavefunction have same symmetry up to a phase factor:

$$\psi_{\mathbf{k}}(\mathbf{r} + \mathbf{P}) = e^{i\mathbf{k}\cdot\mathbf{P}} \psi_{\mathbf{k}}(\mathbf{r}) \quad (2.39)$$

Alternatively,

$$\psi_{\mathbf{k}}(\mathbf{r}) = e^{i\mathbf{k}\cdot\mathbf{P}} u(\mathbf{r}) \quad (2.40)$$

such that  $u(\mathbf{r}) = u(\mathbf{r} + \mathbf{P})$ , where  $u(\mathbf{r})$  is a function with periodicity of the Bravais lattice." Therefore from Bloch's theorem one needs to determine wavefunction only within a single primitive unit cell or in other words only for ions and electrons enclosed within a single primitive unit cell. This thus solves the first problem of determining wavefunction for infinite electrons.

In equation 2.39 and 2.40, the subscript  $\mathbf{k}$  represents a vector in reciprocal space which is defined as:

$$\mathbf{k} = h_1\mathbf{b}_1 + h_2\mathbf{b}_2 + h_3\mathbf{b}_3 \quad (2.41)$$

where  $h_i$  are integers.  $\mathbf{k}$  is defined by reciprocal lattice vectors and hence can be thought of as a wave-vector. Under Born-von Karman periodic boundary conditions one can state that,

$$\psi_{\mathbf{k}}(\mathbf{r}) = \psi_{\mathbf{k}}(\mathbf{r} + S_j\mathbf{a}_j) \quad (2.42)$$

where,  $S_j$  are number of unit cells along  $a_j$ ,  $j=1,2$  and  $3$ . From equations 2.39 and 2.42 one obtains the following:

$$e^{i\mathbf{k}\cdot(S_j\mathbf{a}_j)} = 1 \quad (2.43)$$

Using equation 2.41 in equation 2.43 one finds the following:

$$e^{i\mathbf{k}\cdot(S_j\mathbf{a}_j)} = 1 = e^{i2\pi h_j S_j} \quad (2.44)$$

$$\Rightarrow h_j = \frac{S_j}{S_j} \quad (2.45)$$

where,  $s_j$  are integers. Therefore  $h_j$  is real which implies  $\mathbf{k}$  is also real from equation 2.41 and hence is continuous. Thus  $e^{i\mathbf{k}\cdot\mathbf{r}}$  represents a plane wave of wave-vector,  $\mathbf{k}$  which implies that the wavefunction,  $\psi_{\mathbf{k}}(\mathbf{r})$  does not decay within the crystal but extends over the entire crystal and shows variations according to the periodic function,  $u(\mathbf{r})$ . The periodic function can be expanded using plane-wave basis set as follows:

$$u(\mathbf{r}) = \sum_{\mathbf{G}} c_{\mathbf{G}} e^{i\mathbf{G}\cdot\mathbf{r}} \quad (2.46)$$

Therefore each electronic wavefunction can be written as a sum of plane waves as given in the following equation,

$$\psi_{\mathbf{k}+\mathbf{G}}(\mathbf{r}) = \sum_{\mathbf{G}} e^{i(\mathbf{k}+\mathbf{G})\cdot\mathbf{r}} c_{\mathbf{k}+\mathbf{G}} \quad (2.47)$$

where,  $c_{\mathbf{k}+\mathbf{G}}$  are coefficients to the basis function such that  $\sum_{\mathbf{G}} |c_{\mathbf{k}+\mathbf{G}}|^2 = 1$ . From equation of Bloch state and from equation 2.33 and 2.34 we can easily conclude that the wavefunction at  $\mathbf{k}$  and at  $\mathbf{k} + \mathbf{G}$  in reciprocal space are same since the translation by  $\mathbf{G}$  gives rise to difference of factor of  $2\pi i$  in the argument of exponential in equation 2.43 which equals 1. Thus the number of values of  $\mathbf{k}$  are restricted to only those inequivalent values which lie within a volume in the reciprocal space which is known as the Brillouin Zone (BZ). BZ is analogous to primitive unit cell of real space. However the number of  $G$  vectors are still infinite which makes the basis set infinitely large. This can be resolved by using a condition for truncating the infinite series. Typically those electronic wavefunctions are important which give rise to small kinetic energy. So if we operate the kinetic energy operator ( $\hat{T} = \frac{\hbar^2}{2m} \nabla^2$ ) on the electronic wavefunction defined in equation 2.47 we obtain kinetic energy ( $T$ ) as,

$$T = \frac{\hbar^2}{2m} |\mathbf{k} + \mathbf{G}|^2 \quad (2.48)$$

Thus the plane-wave basis set or the number of  $\mathbf{G}$  can be truncated so as to include only those kinetic energy values which are less than or equal to a certain cutoff energy ( $E_{cut}$ ).

$$\frac{\hbar^2}{2m} |\mathbf{k} + \mathbf{G}|^2 \leq E_{cut} \quad (2.49)$$

The value of cutoff energy is fixed by checking its convergence with total energy. More elaborately, the value of  $E_{cut}$  is increased till we notice that the values of total energies are consistent upto minimum order of error.

Next, while studying an aperiodic system using periodic boundary conditions, as has been done in this thesis, we note that the basis set is discrete along those directions which shows periodicity of lattice while it is continuous along the directions where the periodicity is broken. Thus along directions where the periodic boundary conditions do not hold true, infinite number of plane-wave basis states are needed to be included. For such aperiodic systems one needs to use periodic supercells.[49]

A supercell is a cell which consists of more than one unit cell. Figure 2.2 demonstrates periodic supercells for three such aperiodic systems: (a) a surface where the perpendicular direction to the plane of the surface shows aperiodicity. (b) vacancy in a crystal where periodicity is broken after certain number of periodic units and (c) dimer molecule which does not have periodicity along any direction.

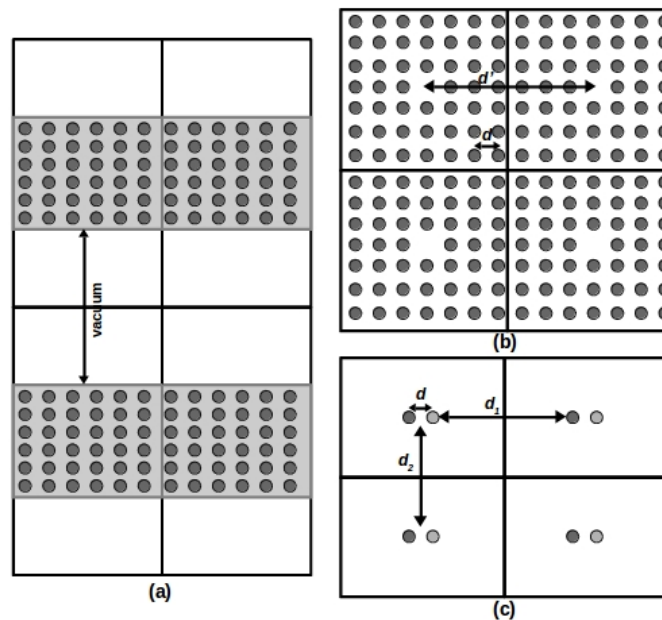


FIGURE 2.2: Pictorial diagram of periodic supercells for (a) surface, (b) vacancy in crystal and (c) dimer molecule.

In figure 2.2(a) vacuum of sufficient thickness separates the two periodic images of the slab generated due to periodic boundary conditions. The vacuum ensures minimum interaction between the periodic images. In a crystal with vacancy, figure 2.2(b), sufficient number of periodic units inbetween the periodic images of the vacancy site reduces vacancy-vacancy interactions. The width of one unit ( $d$ ) is significantly smaller than the distance between two vacancy centers. For the last example of dimer, vacuum along all directions isolates the dimer from its periodic image. The vacuum thickness in different directions ( $d_1, d_2$ ) is much larger than bondlength of dimer ( $d$ ).

## 2.4 Electron-ion interaction

In the last section it was discussed that by using periodic boundary conditions and plane-wave basis states one can significantly reduce computational efforts. However this is true only for  $\mathbf{r}$  away from the core region of an atom. In the core region electrons experience strong potential of the massive nucleus. The atomic wavefunctions are eigenstates of the atomic Hamiltonian and thus are mutually orthogonal to each other. The core states are mostly localised in the region close to the nucleus. Therefore, the valence states oscillate rapidly in the core region so as to satisfy the orthogonality with the core states. These large number oscillations in the wavefunction requires larger basis set making the computation highly expensive. The large oscillations results in large kinetic energy which nearly compensates the strong Coulomb potential of the nucleus. Thus it is a good approximation to replace the strong potential in the core region with a weaker potential, known as pseudopotential, such that the potential outside the core region matches with the actual true potential. Consider an atom with Hamiltonian  $\mathbf{H}$ , core states  $|\chi_n\rangle$  with core energy eigenvalue  $E_n$ . Let us suppose one valence state  $|\psi\rangle$  with energy eigenvalue  $E$ . We can construct a smoother pseudo-state  $|\phi\rangle$  which is given as,

$$|\psi\rangle = |\phi\rangle + \sum_n \alpha_n |\chi_n\rangle \quad (2.50)$$

where,  $n$  runs over all core states. As the valence states must be orthogonal core states,

$$\langle \chi_m | \psi \rangle = 0 = \langle \chi_m | \phi \rangle + \alpha_m \quad (2.51)$$

Thus the orthogonality condition fixes the expansion coefficient ( $\alpha_n$ ).

The pseudopotential acts on pseudowavefunctions and not on actual valence wavefunction.<sup>[52]</sup> However the pseudowavefunction after a particular value of radial distance from the center of the nucleus merges into the true wavefunction. The radial distance ( $r_c$ ) from nucleus after which the pseudowavefunction and true all-electron wavefunction become equal is chosen so that the last node of the all-electron wavefunction lies within it. If larger value of  $r_c$  is chosen one requires less number of plane-wave states in the valence region. But the pseudopotential thus generated is less transferable. A pseudopotential is said to transferable if it can be used for the same atom in different environments.

There are two ways of obtaining pseudopotential:

1. Empirical potential where the parameters defining the potentials are obtained by fitting to atomic or solid state data using experiments. These potentials are generally found to be less transferable.

2. *Ab initio* potentials which are generated using the calculations on atoms and are found to be transferable.

The *ab initio* pseudopotentials further have two types: (a) norm-conserving and (b) ultrasoft. The norm-conserving pseudopotential is constructed using the following set of requirements:

1. For a chosen atomic configuration the all-electron and pseudo-valence eigenvalues are in agreement.
2. Beyond the core radius ( $r_c$ ) the all-electron and pseudo-valence wavefunction are in agreement.
3. At  $r_c$  the logarithmic derivative of all-electron and pseudo-wavefunctions are in agreement.
4. Within  $r_c$  the integrated charge corresponding to all-electron and pseudo-wavefunctions are in agreement.
5. At  $r_c$  the first derivative of all-electron and pseudo-wavefunctions with respect to energy are in agreement.

Condition 1 and 2 are implied from the fact that there is a unique potential corresponding to a given wavefunction and energy. Thus these conditions guarantee that the generated pseudopotential matches with the atomic potential beyond  $r_c$ . Condition number 3 is satisfied only when wavefunction and its radial derivative are continuous at  $r_c$ . The next condition conserves the total core charge when the actual strong potential is replaced with a weaker potential in the core region of the atom. Finally condition 5 is important because change in the environment of an atom results in changes in wavefunction and eigenvalues. The condition ensures that the change in wavefunction and eigenvalues produces change in the self-consistent potential.

Norm-conserving pseudopotentials have a good level of accuracy and transferability for which the core radius cutoff is quite small. A smaller  $r_c$  demands for a larger basis set making the calculations expensive. The potential is hence called “hard” potential. The reason for using pseudopotentials is to minimize the cost of calculations. Thus it is desired that the pseudopotentials are as “smooth” as possible but accurate at the same time. Increasing smoothness of the potential implies that the range in Fourier space required to define valence wavefunction is reduced with necessary level of accuracy. One practical approach to achieve smoother pseudopotential is by relaxing the

norm-conserving condition (condition 4) with a constraint that the all-electron wavefunction and pseudo-wavefunction matches at  $r_c$ . The core radius cutoff can thus be chosen larger. The required accuracy can be maintained by adding an auxiliary charge density to the core charge density defined by the pseudo-wavefunction inside  $r_c$ . Such pseudopotentials are known as ultrasoft pseudopotentials.

Further as the number of protons in the nucleus of an atom increases the attraction between electrons and nucleus increases. Thus in order to avoid falling into the nucleus, electrons, especially in the inner orbits, revolve around the nucleus with increased speed which is comparable to the speed of light. Hence relativistic effects for core electrons becomes important which can change the self-consistent potential seen by the valence electrons. The Hamiltonian which incorporates relativity effects is derived from Dirac equation and is defined as follows,

$$\mathbf{H}^{\mathbf{R}} = \mathbf{H}^{\mathbf{NR}} + \mathbf{H}^{\mathbf{SR}} + \mathbf{H}^{\mathbf{SO}} \quad (2.52)$$

where  $\mathbf{H}^{\mathbf{NR}}$  is the non-relativistic Hamiltonian which is same as that defined in equation 2.3.  $\mathbf{H}^{\mathbf{SR}}$  and  $\mathbf{H}^{\mathbf{SO}}$  are scalar relativistic term and spin-orbit coupling term, respectively, which are defined below.

$$\mathbf{H}^{\mathbf{SR}} = -\frac{\mathbf{p}^4}{8c^2} + \frac{\nabla v}{8c^2} \quad (2.53)$$

$$\mathbf{H}^{\mathbf{SO}} = \frac{1}{2c^2} \frac{1}{r} \frac{dv}{dr} \mathbf{l} \cdot \mathbf{s} \quad (2.54)$$

where, the  $\mathbf{p}$  is momentum operator and  $c$  is speed of light. The first term in equation 2.53 is the mass-shift term which takes into account the variation in mass with velocity. The second term in equation 2.53 is Darwin correction to the non-local electron-nucleus interaction. In equation 2.54 the spin-orbit coupling includes the interaction of electron spin with the magnetic field generated due to its motion around the nucleus. These relativity effects are incorporated into the pseudopotential as potential shift due to scalar relativistic effects ( $V_l^{SR}$ ) and due to spin-orbit coupling ( $V_l^{SO}$ ) which are expressed in the following equations.

$$V_l^{SR} = \frac{l}{2l+1} [(l+1)V_{l+1/2} + lV_{l-1/2}] \quad (2.55)$$

$$V_l^{SO} = \frac{2}{2l+1} [V_{l+1/2} - V_{l-1/2}] \quad (2.56)$$

## 2.5 Summary

The chapter describes quantum mechanical method to compute the total energy of a system from which most of the physical properties can be derived. The total energy consists of following contributions: (1) kinetic energy of ions and electrons (2) electron-electron interaction (3) electron-ion interaction and (4) ion-ion interaction. Since the heavy nucleus moves much slowly in comparison to the fast moving electrons around it, the electronic configuration immediately adjusts itself for any change in the ionic configuration. Thus by dropping the kinetic energy term of ions and considering ion-ion interaction as constant in the expression for total energy one can obtain total energy which explicitly depends only on the electronic degrees of freedom. This is the Born-Oppenheimer approximation. The second contribution of electron-electron interaction involves not only Coulomb repulsion between electrons but also exchange and correlation interactions which are extremely difficult to determine. Kohn and Sham devised a method which takes into account all the components of electron-electron interaction. By using electronic density rather than electronic wavefunction as a variable entity, Kohn-Sham method is proved to be significantly computationally efficient. The Kohn-Sham method is an iterative method which includes the following steps for determining the total energy: (a) Initially charge density is given a guess value. (b) Hartree and exchange-correlation potentials, combinedly known as effective potential, are derived from the guess charge density. The exchange and correlation potentials are constructed using local density approximation or generalised gradient approximation or by a hybrid functional depending upon the nature of the system. Additionally one needs to include correct correlation effect for strongly correlated material. One way is to use LDA+U or GGA+U method where a constraining parameter ( $U$ ) is included to correct the occupation of valence atomic orbitals. (c) With the effective potential, single-particle eigenvalue equations are solved at each  $\mathbf{k}$ -point included in the calculation to obtain Kohn-Sham eigenstates. (d) The new charge density obtained from the Kohn-Sham eigenstates is compared with the initial charge density used to construct the electronic potentials. (e) If the charge densities are inconsistent then a new electronic potential is constructed from the new charge density which give rise to new eigenstates. The procedure is repeated till consistency is achieved.

For solid the number of electrons are infinite and thus one needs to determine infinite number of wavefunctions. This is simplified by Bloch's theorem which says that wavefunction at point  $\mathbf{r}$  is equivalent to wavefunction at point  $\mathbf{r} + \mathbf{P}$ , where  $\mathbf{P}$  is the translation vector of the real space lattice. Thus only those wavefunctions are needed to be determined which are within a unit of the system. Further each for defining electronic wavefunction one needs to use infinitely large basis set. Plane wave basis set is usually



preferred for solid systems because of the periodic nature of their lattice. The number of terms included in the plane-wave basis set depends on the number of reciprocal lattice vector,  $\mathbf{G}$ . The number of  $\mathbf{G}$  are restricted by a convergence condition which compares the kinetic energy with a cutoff energy.

The last interaction of electron-ion faces troubles due to the strong attractive potential experienced by the electrons near the nucleus. The strong potential give rise to large number oscillations in the wavefunction which can be represented by larger basis set. This issue is resolved by replacing the strong potential with a weak potential, known as pseudopotential, in the core-region such that the potential outside the core region matches with the actual true potential. Hence core states are excluded from the calculations of total energy. Therefore rather than total energy, difference of total energies between different ionic configuration is more important.

The theories discussed in this chapter were referred from [49–52, 58].

## Chapter 3

# Tunning of electronic and magnetic properties at Ni(111)/graphone interface by intercalation of atomic oxygen

### 3.1 Introduction

Despite possessing several interesting properties like long mean free path of electrons, high electron mobility, [3] etc., the use of graphene in electronic devices is greatly limited by the fact that it is a semimetal with zero band gap. Hence, there are efforts towards controllable band gap opening. One plausible way to achieve band gap opening is through chemical functionalization of the graphene sheet. For example, it has been shown that functionalizing graphene with a varying coverage of H atoms helps in achieving controllable band gap opening.[59] Moreover, it has also been predicted that when one side of the graphene sheet is completely hydrogenated (*graphone*) it becomes a ferromagnetic semiconductor with each unhydrogenated C atom having a magnetic moment of  $1.0 \mu_B$ . [60] The origin of the magnetic moment is attributed to the presence of localized unpaired  $p_z$  electrons that results from the breaking of the highly delocalised  $\pi$ -electron cloud of graphene due to the formation of -CH bonds.[60]

In spite of the intriguing properties of graphone (GrH), its main drawback is that free standing GrH is unstable due to a huge sublattice imbalance, which arises due to the adsorption of hydrogen atoms on the carbon atoms of one sublattice of the graphene sheet.[61, 62] Recently W. Zhao *et al.* have experimentally synthesized GrH on Ni(111)

substrate suggesting that graphone can be stabilised on transition metal surfaces. [63] Nevertheless, they did not study the magnetic properties of the supported graphone sheet. From our previous theoretical study of GrH supported on the Ni(111) surface (Ni(111)/GrH), we find that GrH strongly interacts with Ni(111) that results in quenching of the interface magnetic moments. Not only are the magnetic moments on the C atoms quenched to  $0.04 \mu_B$ , but also those on the surface Ni atoms are reduced to  $0.16 \mu_B$  from  $0.71 \mu_B$  for the clean surface.[47] Retaining magnetic moment of Ni(111) surface is essential in order to design spintronic nanodevices, using Ni(111)/GrH interface.

Oxygen intercalation between an adsorbate and substrate is shown to be an useful way to tune the interactions (both in terms of electronic properties and magnetic couplings) between them. For example, Bernien *et al.* [64] have shown that intercalating O between Fe-porphyrin molecules and ferromagnetic substrates results in an antiferromagnetic coupling between them. Studies of oxygen intercalation between graphene and its transition metal (TM) substrate show that the graphene sheet moves away and decouples from the substrate.[65–67] These results motivated us to study the effect of O intercalation between GrH and Ni(111) surface.

The rest of the paper is organised as follows: In section 3.2 we have described the details of the computational methods used in our calculations. The results from our calculations are presented and discussed in section 3.3. In this section we also provide a plausible way of experimentally synthesizing these interfaces. Finally we conclude in Section 3.4.

## 3.2 Methodology

### 3.2.1 Computational Details

We have performed *ab initio* density functional theory (DFT) calculations using the plane-wave based Quantum ESPRESSO software. [68] The electron-ion interactions have been described using ultrasoft pseudopotentials. [69] The energy cutoffs used for wavefunction and charge density are 35 Ry and 360 Ry, respectively. The electron-electron exchange-correlation potential is described by Perdew, Burke and Ernzerhof parametrization of the generalised gradient approximation. [70] The Brillouin zone integrations are performed on a  $12 \times 12 \times 1$  shifted Monkhorst Pack k-point grid per ( $1 \times 1$ ) Ni(111) surface unit cell.[71] To accurately calculate the small magnetic moments on the supported graphone we have used a denser k-point grid of  $36 \times 36 \times 1$  per ( $1 \times 1$ ) Ni(111) surface unit cell. To speed up the convergence we have used Marzari-Vanderbilt smearing of width 0.005 Ry. [72]

The Ni(111) surface unit cell is modelled by an asymmetric slab of 6 layers, of which the bottom 3 layers are kept fixed at the bulk interplanar distance while the top 3 layers are relaxed. The periodic images in the direction perpendicular to the surface are separated by a vacuum of 12 Å to minimize the spurious interaction between them. Additionally we have included dipole correction to remove the spurious long range dipole interaction between the periodic images of the slab along the direction perpendicular to the surface.

In order to test the pseudopotentials we have computed the lattice parameter and magnetic moment of bulk Ni, the bond length and magnetic moment of oxygen molecule in gas phase, and the lattice parameter and C-C bond length in freestanding graphene. We have obtained the lattice parameter of bulk Ni to be 3.52 Å with magnetic moment of 0.64  $\mu_B$  per Ni atom. From our calculations we find that the oxygen molecule is in a triplet ground state with an O-O bond length of 1.22 Å. For freestanding graphene, we have obtained the lattice parameter to be 2.46 Å with C-C bond length of 1.43 Å. All these results are in excellent agreement with the previous reports [58, 60, 73, 74].

### 3.2.2 Determination of $U$

Since conventional GGA functionals do not correctly account for the exchange and correlation interactions between the Ni- $d$  electrons, particularly when they are interacting with O- $2p$  states (eg. NiO), we have performed GGA+ $U$  calculations to determine the structure and electronic properties of this interface. In order to determine the value of  $U$  we have used the linear response approach proposed by M. Cococcioni and S. Gironcoli [57] which we have discussed in chapter 2. In this method the value of the on-site Coulomb ( $U$ ) correction is given by the difference of the inverse of the interacting ( $\chi$ ) and non-interacting ( $\chi_0$ ) response of the occupation of the Ni- $d$  states to a small perturbing potential. The response function and  $U$  is given by equation 2.28:

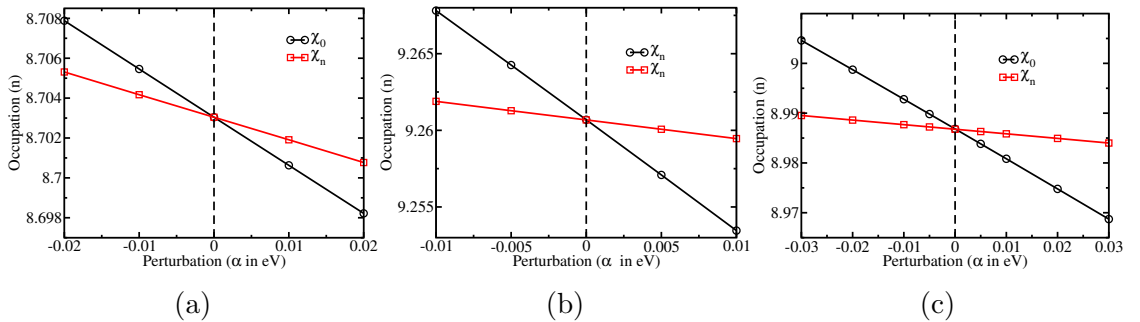


FIGURE 3.1: Variation in the Ni- $d$  occupation in (a) NiO bulk, (b) Ni bulk and (c) Ni(111)-O surface as a function of the perturbing potential ( $\alpha$ ).

In our system, the Ni atoms are in two different types of environment. The ones at the surface of the slab are interacting with both the Ni and O atoms, while those below the

surface Ni layer, are interacting with neighbouring Ni atoms only. Hence, to understand for which atoms the effect of U will be important, we have computed U for three cases: (i) bulk Ni, (ii) bulk NiO and (iii) the surface Ni atom in Ni(111)/1ML-O system using the linear response method described above. To determine the U for bulk Ni and bulk NiO, we used  $(3 \times 3)$  supercells. For the Ni(111)/1ML-O we have used a  $(2 \times 2)$  supercell. Fig. 3.1 shows the change in the Ni-*d* occupation as a function of perturbing potential in the interacting and non-interacting cases for bulk NiO, bulk Ni and Ni(111)/1ML-O surface. The values of U obtained for these systems are 4.67 eV, 6.84 eV and 9.18 eV respectively. Our obtained value of U for NiO is in excellent agreement with that reported by Coccocini *et al.*[57]

The lattice parameters obtained for bulk Ni with and without U (3.48 Å vs. 3.52 Å) are similar but the magnetic moments are significantly different. While with GGA the magnetic moment on each Ni atom is about  $0.64 \mu_B$ , upon incorporating U it reduces to about  $0.48 \mu_B$ . We find that for bulk Ni the results without U correction are in excellent agreement with experiments. For the systems studied in this work, the Ni atoms from the second layer of the slab onwards are in an environment that is similar to the bulk. Since from our test calculations we find that the GGA+U correction does not correctly describe the Ni-bulk environment, for our system, we have applied GGA+U only for the surface Ni atoms that are interacting with O.

For the Ni(111)/1ML-O, since our obtained value of U=9.18 eV is quite large, we also did the calculations for this system with U=4.67 eV. Fig. 3.2 shows the density of states (DOS) projected on Ni-*d* states of the Ni atoms at the interface, O-*p* and graphene electronic states computed with U=0, 4.67 and 9.18 eV for Ni(111)/1ML-O/GrH. We find that the localization effect due to the U correction results in a shift of the density of Ni-*d* states towards lower energy compared to those obtained from GGA. In contrast, the shift in the DOS for O *p*-states and that of graphene are much smaller. Additionally we also observe a depletion in the contribution to the DOS at the Fermi energy from not only the Ni-*d* and O-*p* states but also for the graphene. In particular, for the Ni-*d* spin down states the decrease in DOS is quite significant. While the states around the Fermi energy are due to hybridization between Ni-*d* and O-*p*, the ones that are occupied (empty) have a predominantly O-*p* (Ni-*d*) character. We note that both values of U give a qualitatively same picture. Hence, we have used U=9.18 eV for our calculations, which is the value of U obtained from the linear response calculations.

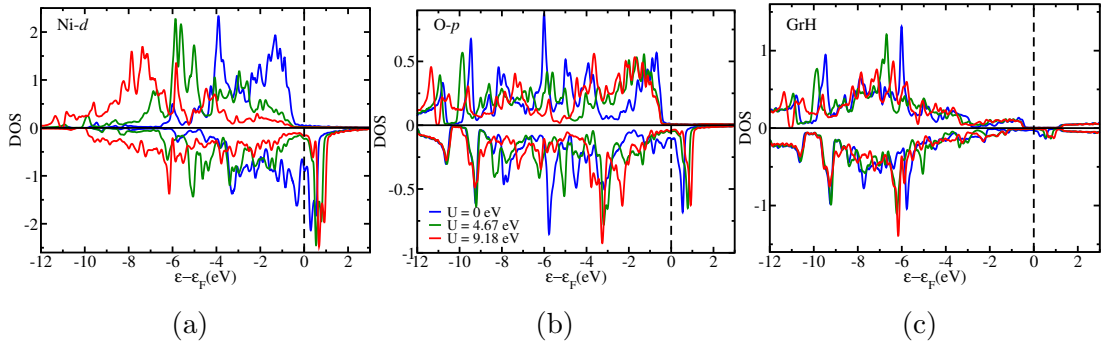


FIGURE 3.2: Density of states projected on to (a) Ni- $d$  states of surface Ni atom, (b) O- $p$  states and (c) graphene in Ni(111)-O/GrH interface with 1 ML O coverage. The blue, green and red lines show plots for  $U=0$  eV,  $U=4.67$  eV and  $U=9.18$  eV, respectively. The vertical dotted line shows the Fermi energy which is set at 0 eV.

### 3.2.3 Determination of energetics

To determine the stability of the O-intercalated Ni-GrH interface compared to that in the absence of oxygen we have computed the formation energy ( $E_f$ ), which is given by:

$$E_f = \frac{E_{Ni(111)-O/GrH} - E_{Ni(111)/GrH} - \frac{N}{2} \times E_{O_2}}{A} \quad (3.1)$$

In the above equation  $E_{Ni(111)-O/GrH}$  and  $E_{Ni(111)/GrH}$  are the total energies of the interface with and without O respectively.  $E_{O_2}$  is the total energy of an oxygen molecule in the gas phase,  $N$  is the number of O atoms at the interface and  $A$  is the area of the interface. A negative value of  $E_f$  implies that the O intercalated interface is more stable than the one without O.

Further, in order to understand how the interaction between the intercalated O atoms and C atoms of the graphene sheet affects the C-H bond strength in graphene we have also computed the H binding energy ( $E_b$ ) that is given as:

$$E_b = \frac{E_{Ni(111)-O/GrH} - E_{Ni(111)-O/Gr} - n \times E_H}{A} \quad (3.2)$$

In Eqn. 3.2,  $E_{Ni(111)-O/Gr}$  and  $E_H$  are the total energies of the graphene sheet on Ni-O and a H atom in gas phase. Since graphene is prepared by adsorbing atomic H on graphene, we have considered the reference energy for H as that of an isolated H atom.  $n$  is the number of H atoms in the unit cell.

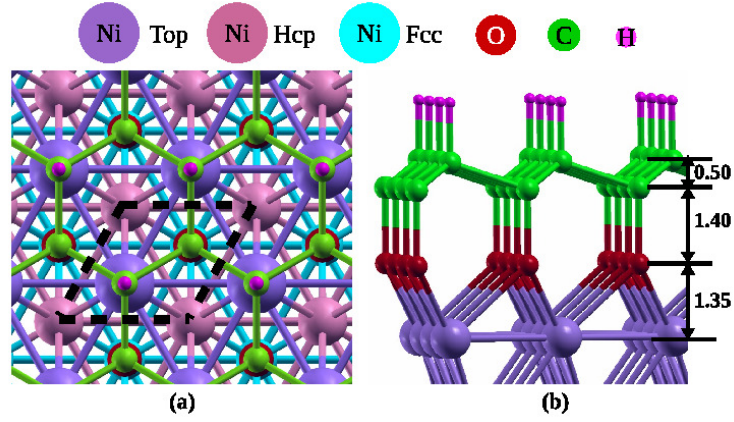


FIGURE 3.3: (a) Top-view and (b) side view of top-fcc configuration of Ni(111)/1ML-O/GrH. Ni, C, O, H atoms are denoted by purple, green, red and magenta colors, respectively. In (a) for better visualization the Ni atoms forming hcp and fcc sites are denoted by pink and cyan colors. Distance marked in the figures are in Å.

### 3.3 Results

#### 3.3.1 Structure and energetics

Previous studies have shown that the oxygen atoms preferably binds at the highly coordinated fcc-site on Ni(111) surface [75]. Hence for all the O coverages, namely, 0.25 ML, 0.50 ML and 1.00 ML we have kept the O atoms on the Ni-fcc hollow site and determined the lowest energy adsorption configuration for GrH.

**1.0 ML O coverage:** In free standing GrH there are two types of C atoms, namely hydrogenated (C1) and unhydrogenated (C2). On Ni(111)/1ML-O surface there are three available sites for the adsorption of carbon atoms in GrH, namely, top, hcp and fcc sites. Therefore there are six possible configurations for the interface of Ni(111)/1ML-O/GrH : i)top-fcc, ii)top-hcp, iii)hcp-top, iv) hcp-fcc, v) fcc-top and vi) fcc-hcp. Throughout this paper we have followed the convention that in the name of the configurations the first (second) label represents the adsorption site of C1 (C2). For example, top-fcc means that the C1 atom is on a site that is directly above the Ni atom while the C2 C atom is occupying an fcc hollow site. In our previous study [47] we have shown that the fcc-top configuration of GrH (C1 at the fcc site and C2 at the top site) is most stable. Since C1 is already hydrogenated, it is unlikely that C1 will bind with the O at the fcc site. Therefore, we have not considered fcc-top and fcc-hcp configurations. Amongst the remaining four configurations we find top-fcc and hcp-fcc configurations to be the most favourable ones with equal formation energies of  $-0.19 \text{ eV}/\text{Å}^2$ . Fig. 3.3 shows the top and side view of the relaxed top-fcc configuration. The H binding energies in Ni(111)/1ML-O/GrH in these two configurations are  $-0.54 \text{ eV}/\text{Å}^2$ . We note that this is more negative

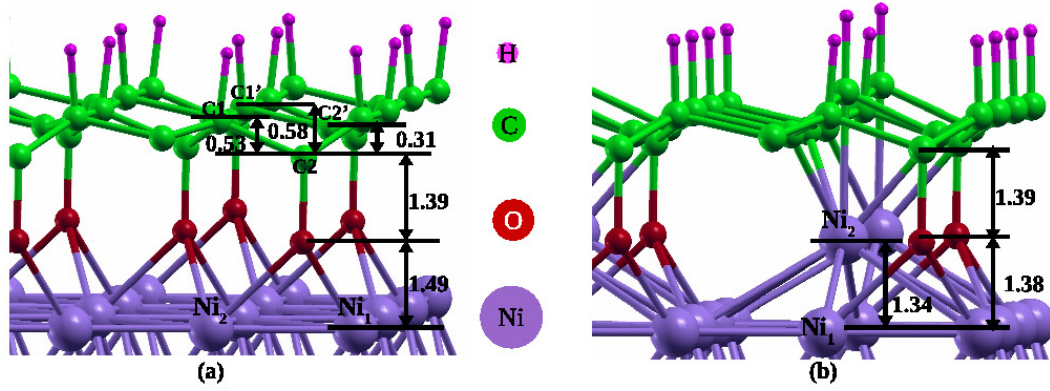


FIGURE 3.4: Side-view top-fcc configuration of (b) Ni(111)/0.5 ML-O/GrH and (c) Ni(111)/0.25 ML-O/GrH. Ni, C, O, H atoms are denoted by purple, green, red and magenta colors, respectively. Distances marked in the figures are Å.

compared to that of  $-0.39 \text{ eV}/\text{\AA}^2$  in absence of O intercalation, thereby indicating that O intercalation strengthens the C-H bond. The strong binding of H to the Gr supported on O covered Ni surface is also reflected in the enhanced buckling of  $0.50 \text{ \AA}$  observed in GrH. The C-O bond length is about  $1.40 \text{ \AA}$  in both, top-fcc and hcp-fcc, configurations. We note that this is larger in comparison to the C-O bond length in CO molecule in gas phase ( $\sim 1.13 \text{ \AA}$ ) and that of CO molecule adsorbed on Ni(111) surface with C atom interacting with the surface ( $\sim 1.20 \text{ \AA}$ ).<sup>[76]</sup> The Ni-O bond length is also increased to  $1.98 \text{ \AA}$  and  $1.97 \text{ \AA}$  in top-fcc and hcp-fcc configurations, respectively, compared to that of  $1.85 \text{ \AA}$  observed in absence of GrH.

**0.50 ML O coverage:** To determine the structure of the interface in presence of 0.5 ML O, we have used a  $(2 \times 2)$  surface unit cell. This results in two O atoms in between the Ni(111) surface and GrH. Graphene can have four possible configurations: (i) two configurations with C1 at top site while C2 either at hcp (top-hcp) or fcc (top-fcc) site and (ii) two configurations with C1 at hcp site and C2 either at top (hcp-top) or fcc site (hcp-fcc). From our calculations we find that graphene prefers to adsorb on Ni(111) surface when oxygen atoms are present at fcc sites alone.

Similar to the interface with 1 ML O coverage, the Ni(111)/0.5 ML O/GrH interface has two configurations, namely top-fcc and hcp-fcc, that are lowest in energy, each having a formation energy of around  $-0.18 \text{ eV}/\text{\AA}^2$ .  $E_f$  is reduced compared to the 1.0 ML O case. At this O coverage the number of inequivalent C atoms in GrH increases to four, namely, those at the top-site (or hcp-site in hcp-fcc) with hydrogen adsorbed on them (C1 and C1'), the unhydrogenated ones at fcc-site (C2') that do not interact with O and the unhydrogenated ones at fcc-site which directly interact with the oxygen atoms (C2), as shown in Fig. 3.4 (a). The buckling between the planes of C1 and C2 is about  $0.53 \text{ \AA}$  and that of C2 and C1' is about  $0.58$  ( $0.57$ ) Å in top-fcc (hcp-fcc) configuration. The



TABLE 3.1: Formation energy of the interface ( $E_f$ ) and binding energy of H ( $E_b$ ) on graphene supported on Ni(111)-O surface at different O coverages and for different possible configurations.

O coverage	O position	C1 position	C2 position	$E_f$ (eV/Å <sup>2</sup> )	$E_b$ (eV/Å <sup>2</sup> )
1 ML	fcc	top	fcc	-0.19	-0.54
		top	hcp	0.16	-0.19
		hcp	fcc	-0.19	-0.54
		hcp	top	0.21	-0.14
0.5 ML	fcc-fcc	top	fcc	-0.18	-0.39
		top	hcp	0.17	-0.04
		hcp	top	0.03	-0.18
		hcp	fcc	-0.18	-0.39
0.25 ML	fcc	top	fcc	-0.05	-0.22
		top	hcp	0.17	0.01
		hcp	top	0.11	-0.06
		hcp	fcc	-0.05	-0.22

buckling between C2 and C2' is about 0.31 Å in top-fcc (0.30 Å in hcp-fcc configuration). Not only the GrH sheet is rumpled but also the Ni surface is slightly distorted due to the interaction with GrH. Out of the four surface Ni atoms in the (2 × 2) unit cell, two bind to one oxygen atom (Ni<sub>1</sub>) and two binds to two oxygen atoms (Ni<sub>2</sub>). This results in a small rumppling of about 0.01 Å (0.02 Å) on the Ni surface in fcc-fcc:top-fcc (fcc-fcc:hcp-fcc) configuration. The binding energy of the H atoms reduces of to -0.39 eV/Å<sup>2</sup> and is comparable with that observed in absence of the O atom.

**0.25 ML O coverage:** Upon further reducing the oxygen coverage to 0.25 ML we again have four possible configurations (top-fcc, top-hcp, hcp-fcc and hcp-top) of Ni(111)/O/GrH interface with O at the fcc site. We have excluded fcc-top and fcc-hcp configurations because placing C1 of GrH over O atoms is not feasible. Similar to the interface with 1 ML and 0.50 ML coverages we find top-fcc and hcp-fcc to be more stable configurations. However, in contrast with the other higher O coverages, at 0.25 ML O coverage we observe that 1/4 of the surface Ni atoms move outward by about 1.34 Å in top-fcc configuration (Fig. 3.4). The shifted Ni atom (Ni<sub>2</sub>) directly interacts with the graphene sheet, as shown in figure 3.4(b) for top-fcc configuration. These pulled out Ni atoms and O atoms (in fcc site) form a rumppled NiO layer with rumppling of 0.04 Å in top-fcc configuration. The graphene sheet is also highly puckered. Therefore, we find that the formation energy of the interface and binding energy of H at 0.25 ML coverage of O are further reduced to -0.05 eV/Å<sup>2</sup> and -0.22 eV/Å<sup>2</sup>, respectively, in both, top-fcc and hcp-fcc configurations.

Table 3.1 summarizes the  $E_b$  and  $E_f$  values of the different configurations at each of the three O coverages. Interestingly we find that the C-H bond strength is modulated by the O coverage at interface. At 1.0 ML O coverage the C-H bonds are stronger compared to that in absence of O. Upon reducing the O coverage to 0.5 ML, the bond strength is reduced and is same as that in absence of O atom. Further reduction of the O-coverage results in weakening of the bond compared to that observed in absence of O. Moreover, in all three O coverages we find that top-fcc and hcp-fcc configurations are equally favourable and the geometry of these two configurations are also similar. The difference in these two configurations is only in the position of the hydrogenated C atom of graphene which does not actively participate in the interaction with the substrate atoms. Hence, we find that both the configurations show similar properties. Therefore, further we have discussed the results obtained for only top-fcc configuration of the Ni(111)/O/GrH interface at different O coverages.

To ascertain whether the surface reconstruction at low O coverages is induced by interactions with the graphene sheet, we took the reconstructed O covered Ni surface in the same geometry as with GrH and relaxed the structure. We find that upon relaxation the surface goes back to the unreconstructed form thereby confirming that the strong interaction between GrH and the surface induces reconstruction of the oxygenated Ni(111) surface. The driving force for this reconstruction can be attributed to the minimization of GrH sublattice imbalance to enhance its stability. On clean Ni(111) surface all the unhydrogenated C atoms of GrH form bonds with Ni atoms. This configuration results in removal of sublattice imbalance making GrH stable. Similarly for the 1.0 ML coverage, each of the unhydrogenated C atoms forms C-O bonds with the interface O. Hence in this case also there is no sublattice imbalance and no reconstruction is observed. However, at 0.25 ML O coverage, at the unreconstructed interface, 3/4 of the unhydrogenated C atoms cannot form bonds either with Ni or O; GrH remains unstable. To minimize this imbalance and thereby enhance its stability, GrH induces reconstruction of the Ni(111) surface such that maximum possible number of unhydrogenated C atoms can form bonds. In this context, it is intriguing that the Ni surface is not reconstructed at 0.5 ML O coverage where there is still unsaturated C atoms in the graphene sheet. To understand this, it is instructive to compare the  $E_b$  between 0 and 0.5 ML O coverage. In absence of any intercalated O (0 ML O coverage), the lattice imbalance in the graphene sheet is zero because each C atom is either bound to a Ni or a H atom. Hence, the  $E_b$  for this case, which is  $-0.39 \text{ eV}/\text{\AA}^2$ , provides a lower bound of the energy that needs to be gained by the system on O intercalation that will stabilize the graphene lattice. For cases where the energy gain is less than above, the lattice instability will drive the reconstruction. For the particular case of 0.5 ML O coverage we find that  $E_b$  is exactly same as that in absence of O. The moment the O coverage is reduced, the

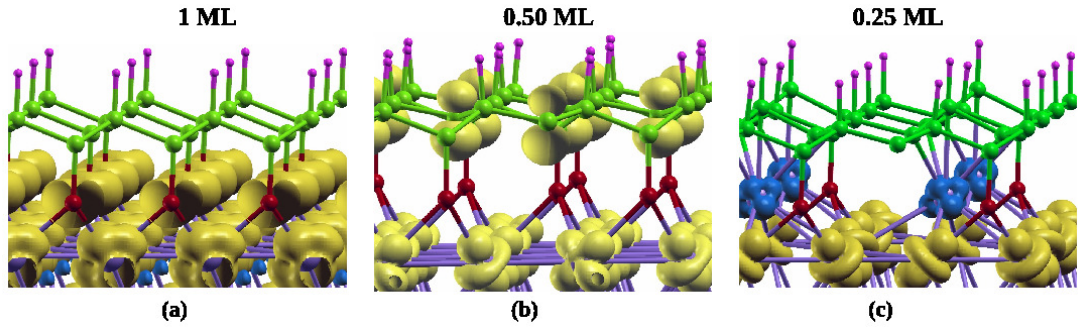


FIGURE 3.5: Magnetization density ( $\Delta m = n^\uparrow - n^\downarrow$ ) at the interface of graphene and Ni(111) surface with (a) 1 ML, (b) 0.50 ML and (c) 0.25 ML O coverages. The yellow and blue isosurfaces represents positive (spin-up) and negative (spin-down) net magnetization ( $\Delta m$ ). The isovalue is around  $0.02 e^-/\text{\AA}^3$ .

instability takes over and induces reconstruction of the Ni(111) surface as observed in case of 0.25 ML coverage.

### 3.3.2 Magnetic properties at Ni(111)/O/graphene interface

Fig. 3.5 shows the magnetization density plots for Ni(111)/O/GrH interface with 1 ML, 0.50 ML and 0.25 ML O coverages, respectively. In Ni(111)/O 1ML/GrH we have obtained a small magnetic moment of about  $0.02 \mu_B/\text{C}$  atoms on GrH, which is contributed by the C1 atoms. The magnetic moment on GrH is aligned parallel with respect to the magnetic moment of the surface Ni atoms. This is in contrast to what we had observed in the absence of the intercalating O atoms where we had found a small magnetic moment of about  $-0.02 \mu_B/\text{C}$  atom orientated antiparallel with respect to the magnetic moments on the surface Ni atoms.[47] The intercalation of oxygen atoms not only modifies the magnetic coupling between the carbon atoms of graphene and surface Ni atoms but also results in more than *seven-fold* enhancement of the magnetic moments on surface Ni atoms. While the magnetic moment on the Ni atoms are quenched upon adsorption of GrH to  $0.16 \mu_B/\text{Ni}$  atom[47] from that of  $0.71 \mu_B/\text{Ni}$  atom for the clean surface, we find that on O intercalation, the magnetic moment of the surface Ni atoms increases to about  $1.13 \mu_B/\text{Ni}$  atom (about 45% enhanced with respect to that in the clean Ni(111) surface). The Ni atoms in the second and third layers below the top one show small reduction of magnetic moment of around 7% and 3%, respectively, with respect to their moments in clean surface. The magnetic moments in the remaining Ni(111) layers are unchanged compared to that in the clean Ni(111) surface.

Upon reducing the O coverage to 0.50 ML and then further to 0.25 ML we notice that the magnetic moments on the surface Ni atoms also decreases. In Ni(111)/O 0.50 ML/GrH

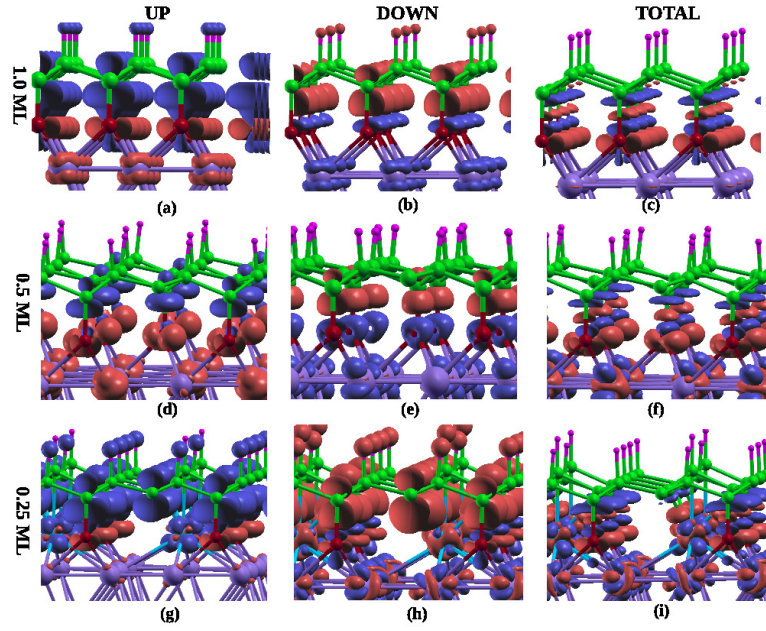


FIGURE 3.6: Spin-resolved and total charge transfer at the interface of graphene and Ni(111) surface with 1.0, 0.5 and 0.25 ML O coverage. The red and blue isosurface represents charge accumulation and depletion, respectively. The isovalue is around  $0.02 \text{ e}^-/\text{\AA}^3$ .

interface the magnetic moments on  $\text{Ni}_1$  and  $\text{Ni}_2$  are nearly same,  $0.98 \mu_B$ . The average magnetic moment ( $0.98 \mu_B/\text{Ni atom}$ ) is slightly smaller than that obtained with 1 ML oxygen coverage but still about six times greater than what is observed in the absence of the intercalating oxygen layer. [47] The magnetic moments on hydrogenated C ( $\text{C}_1$  and  $\text{C}_1'$ ) and  $\text{C}_2$  carbon atoms are about  $-0.06 \mu_B$  and  $0.04 \mu_B$  respectively, while that on  $\text{C}_2'$ , with a dangling bond, is around  $0.72 \mu_B$ . This results in an average moment of about  $0.17 \mu_B$  per C atom in GrH, which is *eight* times greater than the average moment of GrH on clean Ni(111) surface. In Ni(111)/O 0.25 ML/GrH the magnetic moments of the undisplaced Ni ( $\text{Ni}_1$ ) and displaced Ni ( $\text{Ni}_2$ ) atoms have antiparallel orientations and their magnitudes are about  $0.96$  and  $-0.36 \mu_B$  respectively. The magnetic moment on carbon atoms which are hydrogenated or are bound to oxygen atom are negligible. The remaining carbon atoms that interacts with  $\text{Ni}_2$  atoms have a small magnetic moment of about  $-0.06 \mu_B$  aligned ferromagnetically with respect to that of  $\text{Ni}_2$ .

### 3.3.3 Charge transfer at the Ni(111)/O/graphene interface

To understand the enhancement of the magnetic moments of the surface Ni atoms due to O intercalation we have plotted spin-resolved and total charge transfer at different O coverages. The isosurfaces for the same are shown in Fig. 3.6. We find that the direction of charge transfer is dependent on the spin polarisation. While for the spin

up channel we find that electrons are transferred from GrH to Ni, for the spin down channel we find the charge transfer occur in the reverse direction. This results in a net accumulation of spin-up electrons on the surface Ni atoms resulting in seven fold increase in the magnetic moment at 1 ML O coverage. However, this net accumulation of spin-up electrons decreases on Ni(111) surface with decrease in O coverage, thereby resulting in a decrease in the magnetic moment on the Ni atoms at lower O coverages. For the 0.25 ML O coverage the interface with reconstructed Ni(111) surface shows two types of charge transfer. While a charge transfer similar to that described above is seen for the undisplaced Ni<sub>1</sub> atoms, the displaced Ni<sub>2</sub> atoms show charge transfer in reverse direction. Ni<sub>2</sub> atoms accept spin-down electrons and donates spin-up electrons which is similar to the charge transfer observed at the interface of Ni(111) surface and GrH in the absence of oxygen atoms.[47] We note that this particular Ni atom is interacting directly with the C atoms of GrH. Thus our results indicate that varying the O coverage provides a handle to tune the charge transfer at the interface, which thereby gives rise to interesting magnetic and electronic properties of the interface.

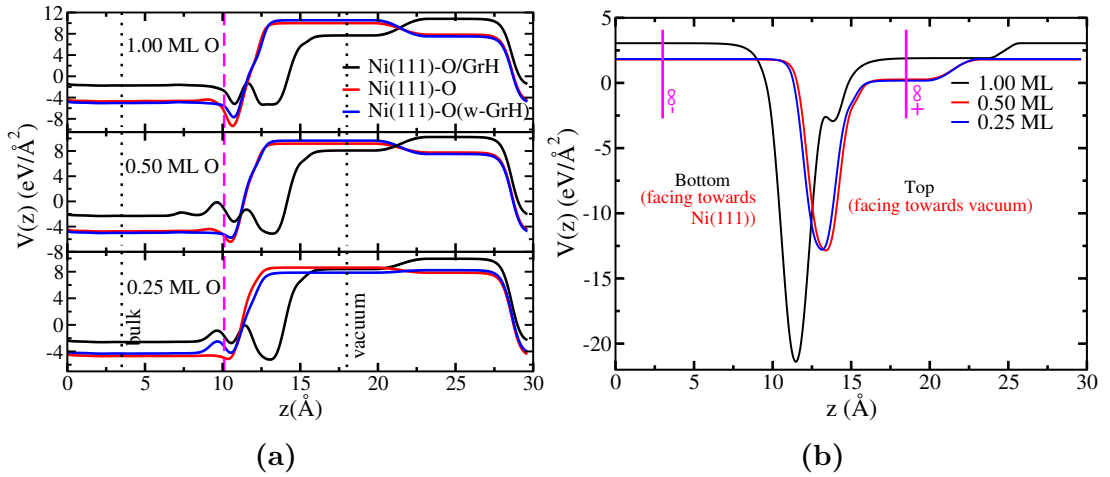


FIGURE 3.7: (a) Macroscopic average of the electrostatic potential of Ni(111)-O surface when (i) with the adsorbed graphene (black), (ii) fully relaxed (red) and (iii) in the geometry as with graphene (blue) with different oxygen coverages. The two dotted vertical black lines show  $z$  value of bulk and vacuum chosen to determine  $V(\text{bulk})$  and  $V(\text{vacuum})$ . In the same plot the magenta dashed line shows the approximate position of top Ni(111) layer and the zero of X-axis denotes the bottom most Ni(111) layer. (b) Macroscopic average of the electrostatic potential of freestanding graphene in the geometry as on Ni(111)-O surface with different O coverages. The magenta vertical lines in (b) show the  $z$  values chosen to determine  $V(\pm\infty)$ .

Table 3.2 shows the changes in the work function of Ni(111) surface for different O coverages, both with ( $\phi$ ) and without ( $\phi_0$ ) graphene. We find that in absence of GrH,  $\phi_0$  increases as the O coverage increases. However, in presence of graphene, we not only find a decrease in the work function (4.0 eV vs. 5.03 eV, with and without GrH at 0 ML O) but also the trends as a function of O coverage is reversed. In contrast to that

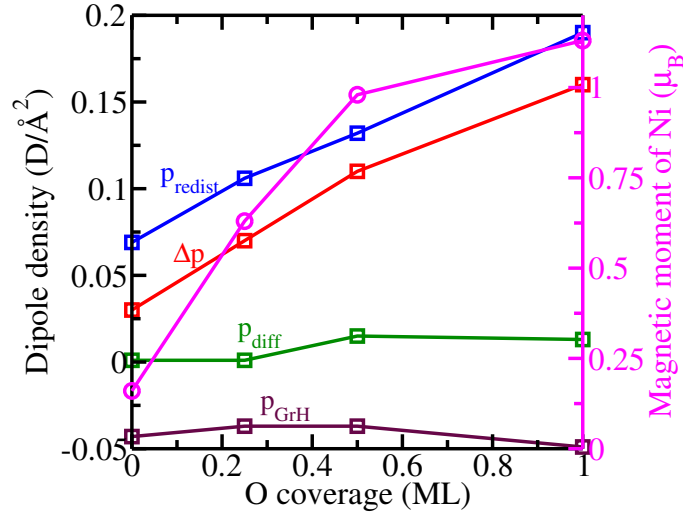


FIGURE 3.8: (Color online) Plot of the variation of surface dipole density (and its components) and net magnetic moment on the surface Ni atom as a function of O coverage. The Y-axis on the left hand side of the figure is for the dipole density while that on the right is for magnetic moment.

TABLE 3.2: Work function ( $\phi$ ) and surface dipole density ( $p$ ) of Ni(111)-O surface before (with subscript “0”) and after adsorption of graphene. The positive and negative values of surface dipole densities indicates outwards and inwards orientation, respectively.

O coverage (ML)	$\phi$ (eV)	$\phi_0$ (eV)	$p$ ( $\text{D}/\text{\AA}^2$ )	$p_0$ ( $\text{D}/\text{\AA}^2$ )
0	4.01	5.03	0.03	0.00
0.25	3.64	6.37	0.07	-0.05
0.50	3.24	7.52	0.11	-0.08
1.00	1.93	8.07	0.16	-0.09

observed without GrH, we find that upon adsorbing GrH,  $\phi$  decreases as the O-coverage increases. The changes in the work function of a material ( $\Delta\phi$ ) is typically related to the changes in the surface dipole density  $\Delta p$  and is given by:

$$\Delta\phi = -\frac{e}{\epsilon_0}\Delta p \quad (3.3)$$

where,  $e$  and  $\epsilon_0$  are charge of an electron and vacuum permittivity, respectively. For our system these changes in the trends and magnitudes of work function implies that not only the magnitude but also the direction of the surface dipole density is changed upon adsorbing GrH. Interaction of an adsorbate with the substrate changes the dipole moment through charge transfer/redistribution ( $p_{redist}$ ) between substrate and adsorbate and through charge redistribution due to changes in the geometry of the substrate ( $p_{sub}$ ) and the adsorbate ( $p_{ads}$ ). Hence, we can write  $\Delta p$  as:

$$\Delta p = p_{redist} + p_{sub} + p_{ads}. \quad (3.4)$$

$p_{redist}$  in the above equation is given by:

$$p_{redist} = \frac{-e}{A} \int_0^c \Delta n(z) z dz \quad (3.5)$$

where,

$$\Delta n(z) = n_{NiOGrH}(z) - n_{NiO}(z) - n_{GrH}(z) \quad (3.6)$$

$A$  and  $c$  in Eqn. 3.5 are the area and height of the unit cell respectively.  $\Delta n(z)$  is the planar average ( $n(z) = \frac{1}{A} \int_0^a dx \int_0^b n(x, y, z) dy$ ) of the charge transfer which is defined in Eqn. 3.6. The three terms in Eqn. 3.6 are the planar averages of the charge density of the oxygenated Ni(111) surface with epitaxial graphene ( $n_{NiOGrH}$ ), oxygenated Ni(111) surface in the same geometry as in the presence of graphene ( $n_{NiO}$ ) and graphene in the same geometry as when deposited on the oxygenated Ni(111) surface ( $n_{GrH}$ ), respectively.

The dipole density due to the structural changes occurring at the surface on adsorption of another material ( $p_{sub}$ ) is given by the difference between the dipole densities of the oxygenated Ni(111) surface when it is in the same geometry as in the presence of graphene ( $p'_{Ni(111)-O}$ ) and when it is fully relaxed ( $p_{Ni(111)-O}$ ) and is expressed as:

$$p_{sub} = p'_{Ni(111)-O} - p_{Ni(111)-O} \quad (3.7)$$

The dipole density in each case is determined as,  $p = \epsilon_0(V_{vacuum} - V(bulk))$  where,  $V$  is the electrostatic potential at vacuum and bulk, respectively, as shown in Figure 3.7(a).

The last term in equation 3.4, i.e., the dipole density of the adsorbate ( $p_{abs}$ ) in the same geometry as when it is deposited on the surface and can be written as

$$p_{abs} = \epsilon_0(V(+\infty) - V(-\infty)). \quad (3.8)$$

$V(\pm\infty)$  is defined in figure 3.7(b).

Fig. 3.8 shows the variation in  $\Delta p$  for Ni(111)-O/GrH and its three components with increase in O coverage. In absence of GrH, the surface dipole of the O covered Ni surface

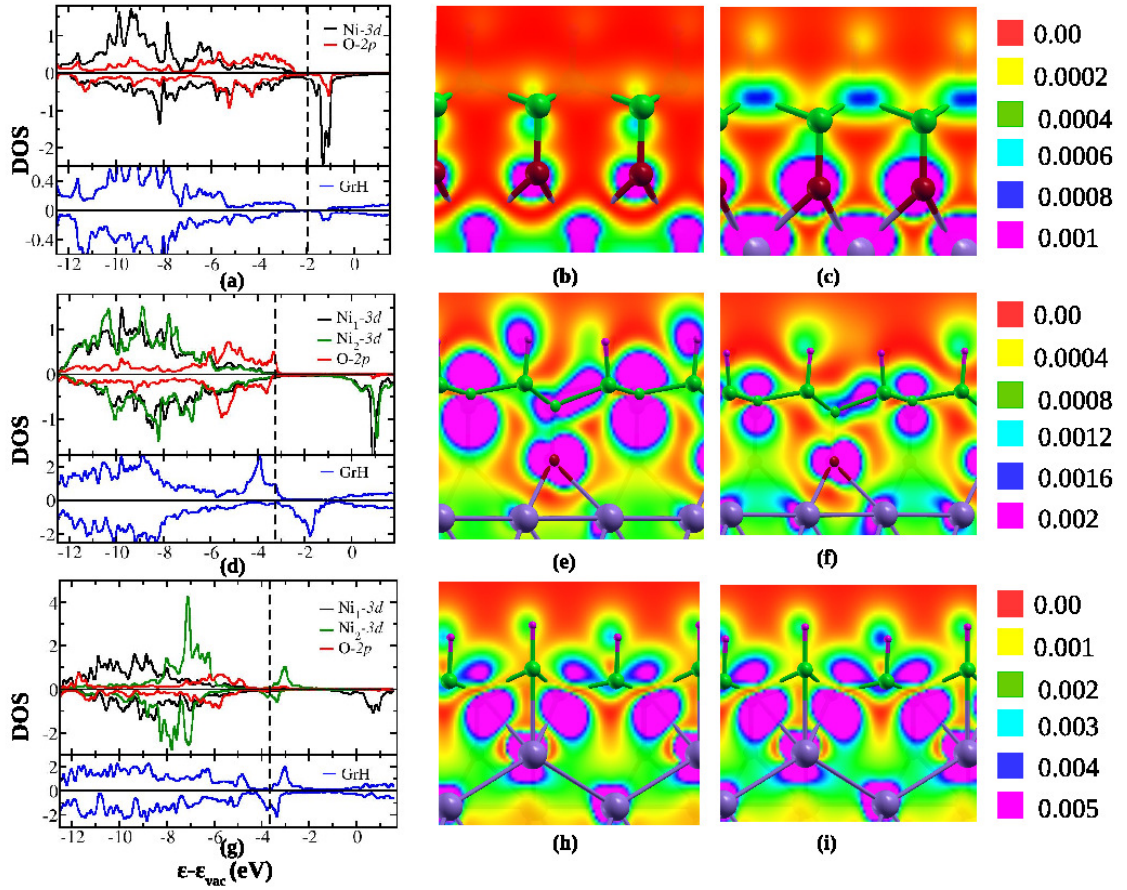


FIGURE 3.9: (Color online) Spin-resolved density of states (a, d, g) and integrated local density of states in the energy range of  $E_f - 0.5$  to  $E_f + 0.5$  eV in spin-up channel (b, e, h) and spin-down channel (c, f, i) for Ni(111)/O/GrH interface at 1 ML (top row), 0.5 ML (middle row) and 0.25 ML (bottom row) O coverage. In DOS plots the states of Ni-3d (black and green), O-2p (red) and sum of C-2s, C-2p and H-1s (blue) are plotted. The vertical dotted line denotes the Fermi level. The energies are shifted with respect to vacuum energy.

points inwards. However, due to the interaction with the graphene sheet, the surface dipole moments reverse their direction and point away from the surface. As a function of O coverage, the magnitude of the surface dipole density increases from  $0.02 \text{ D}/\text{\AA}^2$  to  $0.16 \text{ D}/\text{\AA}^2$ . Among the three constituent terms we find that the largest contribution to the surface dipole density is from  $p_{redist}$ . Additionally, consistent with the direction of charge transfer observed, we find that the magnitude of  $p_{redist}$  is positive.  $p_{abs}$  shows smaller variation with its value lying in the range of  $-0.04 \text{ D}/\text{\AA}^2$  and  $-0.05 \text{ D}/\text{\AA}^2$  as the O coverage is increased.



### 3.3.4 Electronic properties at the Ni(111)/O/graphene interface

Figure 3.9 (a), (d) and (g) show the plots of the DOS projected on GrH, Ni- $d$  of the Ni atoms at the interface and O- $p$  atoms with 1.00, 0.50 and 0.25 ML of O coverage, respectively. At 1.0 ML coverage the interaction between GrH and Ni atoms are mediated through the interfacial O atoms. At the Fermi energy, for the spin up channel we observe that all the surface Ni- $d$  states are below Fermi energy while there is a very small contribution of Ni- $d$  states in the spin down channel. The U shifts the Ni- $d$  states towards lower energy that results in reduction of hybridization with the O states. Between -12 to -6 eV, the contribution to the DOS comes primarily from the Ni- $d$  states. Above -6 eV, there is mixing of the Ni- $d$  with O- $p$ . Above the Fermi energy, we observe empty Ni- $d$  states in the spin down channel only. These are primarily the  $d_{yz}$  and  $d_{zx}$  orbitals with a small contribution also from the  $d_{xy}$  and  $d_{x^2-y^2}$ . These results are consistent with the large magnetic moment observed in our calculations. We do not find any GrH states at the Fermi energy. As the O coverage is reduced to 0.5 ML, the basic feature of the DOS remains similar. However, in contrast with that at 1.0 ML coverage, we don't observe any Ni- $d$  or O- $p$  states at the Fermi energy. Again for the spin-up channel all the Ni- $d$  states are occupied while for the spin down channel, there are empty Ni states, in accordance with the large magnetic moment observed for this case. However here, the two Ni atoms behave differently. While for Ni<sub>1</sub> the empty spin down states are primarily from  $d_{yz}$ , for Ni<sub>2</sub> these are predominantly from  $d_{zx}$ . Additionally we find GrH states at the Fermi energy. For the reconstructed surface at 0.25 ML coverage, the interaction between the Ni<sub>1</sub> atoms (those which are not pulled out of the surface) and the O atoms for the 0.25 ML coverage are similar to that observed for 1.0 and 0.5 ML coverage. In this case empty states in the spin down channel are primarily from the  $d_{yz}$  orbitals. The Ni<sub>2</sub> (those that are pulled out of the surface)  $d$  states are more localized compared to those of Ni<sub>1</sub> and are more or less completely filled in both the spin channel resulting in a reduced magnetic moment observed on these atoms. We also observe some states at the Fermi energy from GrH.

Since the electronic states of the spin up and spin down channel of this interface show different behaviour, there might be a possibility of spin polarized conduction at these interfaces. To explore this we have computed the integrated local density of states (ILDOS) in the energy range of  $E_f - 0.5$  eV to  $E_f + 0.5$  eV for all the three O coverage. The ILDOS plots are shown in Fig. 3.9. In order to have a continuous transport channel the electronic states need to span the whole region between the electrode. For the 1.0 ML coverage we find that the spin up states (Fig. 3.9(b)) are primarily localized along the C-O, O-Ni bonds. In contrast the spin down states are more delocalized throughout the space (Fig. 3.9(c)). This suggests that at this interface there is a possibility

of a spin-polarized current. However, for 0.5 ML (Fig. 3.9(e) and (f)) and 0.25 ML (Fig. 3.9(h) and (i)) the electronic states for both the spin up and spin down channel are delocalized throughout the interface. Hence for these interfaces the probability of having spin polarized transport is less compared to that for 1.0 ML O coverage.

### 3.3.5 Experimental outlook for the synthesis of Ni(111)/O/GrH interface

For realising the viability of the results obtained through computational techniques it is important to relate the computational modelling of a desired system with the latest experimental techniques of material synthesis. In this paper we propose a plausible way to fabricate the proposed Ni(111)-O/GrH interface. The structure and energetics at the interface are hence majorly influenced from the following experimental method for fabricating O-intercalated interface of Ni(111) and GrH. It has been shown earlier that single layer graphene can be successfully grown on Ni thin-film substrate.[77] Also, oxygen-covered Ni substrate can be achieved by so called surfactant-mediated growth method.[64, 78–80] Thus, based on earlier reports, a step-by-step experimental prototype can be proposed as: (i) deposition of, for example, 10 ML of Ni on W(110) single crystal, (ii) dosing of O<sub>2</sub> gas (say 15 Langmuir), (iii) deposition of another 10 ML of Ni, (iv) growth of graphene layer, (v) hydrogenation of the graphene layer i.e. formation of graphone, and (vi) finally, heating-up of the system at elevated temperature, for example, 250°C to make the Ni(111)-O/GrH interface. Notably, the dosing of O<sub>2</sub> gas can be controlled, which will allow us to tune the interfacial coverage of oxygen vis-à-vis magnetic coupling across the interface.

## 3.4 Conclusion

In summary, using GGA+U calculations, we have shown that the properties of Ni(111) surface and GrH interface can be tuned by intercalating O atoms between them. Our results show that there is a subtle balance between the energy gain due to O-intercalation and the instability in the graphene sheet due to sublattice imbalance. From our calculations we show that below 0.5 ML coverage and in particular at 0.25 ML coverage the graphene lattice instability induces reconstruction of the Ni surface. In addition to the structural changes, we also observe significant changes in the magnetic properties of the interface. At 1 and 0.5 ML O coverages, the magnetic moments of the surface Ni atoms at the interface are significantly enhanced compared to the clean Ni(111) surface. Interestingly, for the 0.5 ML O coverage, we find the magnetic moment of the

graphene sheet is also larger by an order of magnitude compared to that observed in absence of O. Our results indicate that the 1 ML and 0.5 ML O coverage interface may be promising candidates for spintronic applications. We hope that our work will motivate experimentalists to prepare these systems.

## Chapter 4

# *Ab initio* study of semihydrogenated graphene on lattice-matched transition metal surfaces

### 4.1 Introduction

One of the most reliable routes to alter properties of graphene is hydrogenation. Zhou *et al.* [81] predicted from their first principles study that a freestanding uniformly semihydrogenated graphene sheet (UGrH) is ferromagnetic. However, the large sublattice imbalance is induced in the graphene lattice as carbon atoms on only one out of the two sublattices are hydrogenated. This makes UGrH highly unstable. The sublattice imbalance is defined as,  $\eta = N_\alpha - N_\beta$ , where  $N_\alpha$  and  $N_\beta$  are number of C atoms at sublattices  $\alpha$  and  $\beta$  in graphene respectively, to which the adsorbing species binds.  $\eta = 0$  hence corresponds to zero sublattice imbalance. From previous investigations it is observed that the sublattice imbalance is minimized for adsorption of H in more closed packed pattern on the graphene sheet. [82],[83] Clustering of H was also observed in experimental studies using scanning tunnelling microscopy (STM) on the epitaxial graphene sheet supported on SiC substrate at both low and high H exposures. [84] Different H adsorption patterns were predicted using first principles studies by studying H diffusion such that the sublattice imbalance is zero and hence are more stable than UGrH. A rectangular H pattern (RGrH) is predicted by Feng *et al.* [85] while a zigzag H pattern is suggested by Šljivančanin *et al.* [86] for H atom in the semihydrogenated

graphene sheet. However none of the studies conclusively state the ground state for freestanding semihydrogenated graphene.

One more way to reduce the chemical imbalance is to grow graphone on a transition metal (TM) surfaces. The TM surfaces are classified according to their interaction with the epitaxial graphene: (i) surfaces on which graphene is chemisorbed like Ni, Co, Rh, Ru and (ii) surfaces on which graphene is physisorbed like Cu, Au, Ag, Ir, Pt. [87]-[88] Further each group can be divided into two subgroups: (1) surfaces having lattice parameter in close agreement with that of graphene (2.46 Å) like Ni(111) (2.49 Å), Co(0001) and Co(111) (2.51 Å) which are from group (i) and Cu (2.60 Å) from group (ii) and (2) surface having large lattice mismatch with graphene (for example Rh(0001) and Ru(111) from group (i) and (111) surfaces of Ir, Pt, Au from group (ii)). On lattice mismatched metal surfaces it is observed that the graphene sheet is ruffled. This is because on these surfaces between two successive top-site C atoms, along the lattice vectors of the metal surface, the positions of the C atoms vary continuously from top site to bridge site to again top site. The top site is right atop of the surface metal atom while bridge site is defined when instead of carbon atom, C-C bond is on the top or hollow site of the metal surface. As a consequence of relative change in the position of C atoms causes periodic buckling in graphene sheet such that some portions of the graphene sheet show binding to metal substrate while some do not. The hydrogenation pattern is found to be sensitive to the interaction of epitaxial graphene with its substrate. For example High Resolution Electron Energy Loss Spectroscopy (HREELS) studies of Kyhl *et al.* [89] have shown that the denser hydrogenated structures (dimer-like structures) are formed where the C atoms in the graphene sheet interact strongly (weakly) with the Ir(111) substrate. Further the degree of hydrogen uptake also varies depending on the substrate. For example, Son *et al.* [90] found that uptake of hydrogen is reduced by 50% when the graphene sheet is on hexagonal boron nitride (almost lattice matched with graphene) compared to that observed when the support is silicon or molybdenum disulphide (MoS<sub>2</sub>). Similarly, among TM surfaces, graphene supported on lattice-mismatched Ir(111) and Pt(111) show large hydrogen uptake of around 67% and 50% while on commensurate Ni(111) surface, it is observed that the H uptake on graphene is only 17% . [91] Only recently Zhao *et al.* [1] have shown from their combined study using X-ray Photoelectron Spectroscopy (XPS) measurements and density functional theory (DFT) calculations that graphene sheet supported on Ni(111) surface can show an uptake of 50% H resulting in GrH. Based on their DFT studies they concluded that the adsorbed hydrogen form an uniform adsorption pattern, i.e. UGrH. The pattern formation observed upon H adsorption on the graphene sheet supported on surfaces of TM such as Ir and Pt are driven by the strain that the graphene sheet experiences due to lattice mismatch. However, on surface of TM like Ni, Co and Cu the C atoms of the graphene sheet is in registry with

the substrate and there is negligible strain on graphene. On lattice matched surfaces the most stable configuration of graphene is where one of the C sublattice is on top of the metal atoms while the second one is at a hollow site. [92]-[93] Based on the concept of sublattice imbalance, it is natural to expect that the adsorbed H atoms form a uniform pattern, i.e. they bind only to the C atoms that are in registry with the hollow site of the metal surface. However, this gives rise to a set of questions such as (1) What happens to the other adsorption patterns, namely the ZGrH and RGrH, that were more stable compared to UGrH for the free standing GrH? (b) Can these or some other novel H adsorption patterns be stabilized for graphene on these substrates and if so, how their properties are affected because of the interaction with the substrates?

To find answers to these questions, we have investigated the relative thermodynamic stability and properties of semihydrogenated graphene with different H adsorption patterns on three transition metal surface, namely Ni(111) and Co(111) from group (i) and Cu(111) from group (ii). The rest of the chapter is organized as follows. The details of the computational methods used in our study are given in section 4.2. Then in section 4.3 we present and discuss our results, first on freestanding and then on TM surface-supported semihydrogenated graphene. We also compare our results with the XPS measurements reported by Zhao *et al.* [1]. Finally, we summarize our results and conclude in section 4.4

## 4.2 Computational methods

TABLE 4.1: The cell parameters of freestanding semihydrogenated graphene sheet in different H adsorption patterns and transition metal surfaces

Structure	Cell parameters (Å)	
	<b>a</b>	<b>b</b>
Gr	4.27	4.93
UGrH	4.38	5.06
RGrH	4.28	5.09
ZGrH	4.29	5.00
AGrH	4.28	4.85
Ni(111)	4.32	4.98
Co(111)	4.35	5.02
Cu(111)	4.50	5.19

We have performed *ab initio* spin polarized DFT calculations using plane-wave based Quantum ESPRESSO software [68] for investigating semihydrogenation of freestanding graphene and graphene supported on Ni(111), Co(111) and Cu(111) surfaces. The electron-ion interactions have been treated with ultrasoft pseudopotentials [69] that are

available on Quantum ESPRESSO website. The pseudopotentials have been generated using Rappe Rabe Kaxiras Joannopoulos (RRKJ) method [94]. The valence configurations used for the generation of pseudopotentials for C, H, Ni, Co and Cu are  $[\text{He}]2s^22p^2, 1s^1$ ,  $[\text{Ar}]4s^13d^9$ ,  $[\text{Ar}]4s^13d^8$  and  $[\text{Ar}]4s^13d^{10}$ , respectively. The kinetic energy cutoffs for wavefunction and charge density used for the calculation in freestanding condition are 35 Ry and 280 Ry, respectively, those on Ni(111) and Cu(111) surface are 35 Ry and 360 Ry, respectively and those on Co(111) surface are 40 Ry and 320 Ry. The electron-electron exchange-correlation potential is described by Perdew, Burke and Ernzerhof parametrization which uses the generalized gradient approximation. [69] The Brillouin zone integrations are performed on a  $12 \times 12 \times 1$  Monkhorst Pack shifted k-point grid per  $(1 \times 1)$  unit cell of graphene. [71] For speeding up the calculations we have used Marzari-Vanderbilt smearing [72] of widths 0.003 Ry and 0.01 Ry for the freestanding and supported semihydrogenated graphene, respectively. Further we have tested the pseudopotentials by computing the following quantities: We have obtained the lattice parameter of Ni bulk to be 3.52 Å with magnetic moment of  $0.64 \mu_B$  per Ni atom; lattice parameter of Co bulk to be 2.50 Å and c/a ratio of around 1.55 with magnetic moment of  $1.69 \mu_B$  per Co atom; lattice parameter of Cu bulk to be 3.67 Å. For freestanding graphene, we have obtained the lattice parameter of 2.46 Å with C-C bond length of 1.43 Å. These preliminary results for TM bulk and pristine graphene are in excellent agreement with the previous reports [58], [81]. Upon uniformly semihydrogenating graphene the sheet becomes buckled with the hydrogenated carbon moving out-of-plane. The buckling is obtained of around 0.32 Å, the C-C bond length increases to 1.50 Å and the C-H bond length is about 1.15 Å. The graphene sheet becomes ferromagnetic semiconductor with total magnetization of  $1 \mu_B / (1 \times 1)$  unit cell, which is majorly contributed by the unhydrogenated carbon atom, and an indirect bandgap of around 0.68 eV. These results for the uniformly semihydrogenated graphene or graphone are in perfect agreement with those reported by Zhou *et al.* [81]. Uniform graphone can be modeled in  $1 \times 1$  hexagonal cell while zigzag, rectangular and armchair requires supercell of size  $1 \times 2$ ,  $2 \times 1$  and  $2 \times 2$ , respectively. In order to investigate all the different H adsorption patterns in the same size of cell we have modeled the graphene sheet in an orthorhombic unit cell whose optimized lattice parameters are  $a = 4.27 \text{ \AA}$  and  $b = 4.93 \text{ \AA}$ . Each unit cell contains 8 carbon atoms. The cell parameters are further optimized upon semihydrogenating the graphene sheet with different H adsorption patterns which are given in Table 4.1. On a substrate, the lattice parameter of graphene will be determined by that of the substrate. Hence, the semihydrogenated graphene supported on TM surfaces is modeled in the orthorhombic unit cell of (i) Ni(111) surface lattice with  $a = 4.32 \text{ \AA}$  and  $b = 4.98 \text{ \AA}$ ; (ii) Co(111) surface lattice with  $a = 4.35 \text{ \AA}$  and  $b = 5.02 \text{ \AA}$  and (iii) Cu(111) surface lattice with  $a = 4.50 \text{ \AA}$  and  $b = 5.19 \text{ \AA}$ . The slab of (111) surface of Ni, Co and Cu are asymmetric and consist of 6, 7, 6 layers, respectively,

of which bottom 3 layers are kept fixed at the bulk interplanar distance while the top 3 layers are relaxed. The periodic images of pristine graphene and clean TM surfaces in the direction perpendicular to the surface are separated by a vacuum of 12 Å thickness to minimize the spurious interaction between them. The interaction between TM surface and graphene is weak chemisorption in case of Ni(111) and Co(111) while physisorption in case of Cu(111) surface. Therefore for obtaining the TM-C interaction correctly at the interface one needs to consider the dispersion interaction between the two surfaces, which otherwise is not included in the DFT based calculations [93]. For this purpose we have used Grimme's van der Waals dispersion (DFT-D2) correction in all our calculations for the supported semihydrogenated graphene. [95],[96] We have checked the validation of the DFT-D2 correction for the case of Ni(111)/graphene interface which is widely studied in comparison with Co(111)/graphene and Cu(111)/graphene interfaces, by comparing our results with previous studies (both experimental and computational) reported in literature. We have obtained the binding energy of graphene on Ni(111) surface ( $\Delta E_{Gr}$ ) to be around -0.17 eV/C atom and the Ni-graphene distance ( $d_{Ni-Gr}$ ) to be around 2.1 Å, which agrees well with those reported in other computational as well as experimental studies. For example, Gamo *et al.* [97] performed low-energy electron diffraction (LEED) experiments to investigate atomic structure of graphene on Ni(111) surface and found  $d_{Ni-Gr}$  to be around  $2.11 \pm 0.07$  Å that is in excellent agreement with our computed value. Zhao *et al.* [98] obtained  $d_{Ni-Gr}$  around 2.2 Å and  $\Delta E_{Gr}$  around -0.12 to -0.14 eV using density functional theory calculations with semiempirical van der Waals correction developed by Ortmann *et al.* [99]. Hamada and Otani [100] studied graphene supported on different metal surfaces using van der Waals density functional (vdW-DF) [101] and its second version, vdW-DF2 [102], with exchange functional developed by Cooper (C09) [103]. Their computed values of  $\Delta E_{Gr}$  and  $d_{Ni-Gr}$  reported with vdW-DF C09x (vdW-DF2 C09x) are around -0.18 (-0.14) eV and 2.06 (2.07) Å, which are in good agreement with those obtained by our calculations. [92] However when compared with ACDF-RPA results we find that DFT-D2 overestimates the binding energy. [93] Nonetheless the binding distance is in close agreement.

For semihydrogenated graphene supported on TM surface we have determined core-level shifts in the C 1s states due to the local environment by calculating the core level binding energy ( $\Delta E^C$ ) using the following equation:

$$\Delta E^C = E^{GS} - E^{CFS} \quad (4.1)$$

where,  $E^{GS}$  and  $E^{CFS}$  is the ground state and full core-hole final state energy of the system, respectively.  $\Delta E^C$  is computed for both, hydrogenated and unhydrogenated carbon atoms of graphene. The computed binding energies are then plotted as a Gaussian



function, as given by equation 4.2, with a width ( $\sigma$ ) of 0.5 eV.

$$I(\epsilon) = \frac{1}{\sigma} \sum_{j=1, N_C} \exp\left[-\frac{(\epsilon - \Delta E^C(j))^2}{2\sigma^2}\right] \quad (4.2)$$

where,  $I(\epsilon)$  is intensity at energy  $\epsilon$  of the incident X-ray.  $N_C$  is the number of carbon atoms whose core-level binding energy is calculated. In the pseudopotential based calculations the information regarding the energies of the core states is not available. Therefore the absolute values of computed and experimental binding energies do not match. Hence we have compared the differences in binding energies of hydrogenated and unhydrogenated carbon atoms obtained from our calculations with that obtained from the experimental study. For the calculation of system with corehole we have used full corehole norm-conserving pseudopotential for the excited carbon atom in order to describe the electron-ion interaction. The pseudopotential with a hole in the 1s core state for C is also taken from the Quantum ESPRESSO website. This pseudopotential had been generated using the Troullier-Martin method. [104] The electronic configuration used for the generation of this pseudopotential is  $1s^1 2s^2 2p^{1.5}$ . The kinetic energy cutoff for wavefunction is increased to 65 Ry. The separation between the periodic images of the C atoms with corehole is around 4.38 Å and 5.06 Å along the **a** and **b** directions. On increasing the separation to around 7.59 Å (by using a 3×3 hexagonal cell) the core-level shifts change by about 0.1 eV, with respect to the previous case with a smaller separation between the periodic images. We note that these changes are smaller than the differences in the binding energy of the C 1s electron between the hydrogenated and unhydrogenated C atoms. Therefore all calculations with corehole are performed with the smaller separation between the core-hole atoms.

## 4.3 Results and discussion

### 4.3.1 Determining stable structure of freestanding semihydrogenated graphene

In pristine graphene sheet the unbalanced  $p_z$  electrons on every carbon atom form a  $\pi - \pi$  bonding network. The electronic structure of graphene shows that the occupied bonding and unoccupied antibonding states of these  $p_z$  electrons cross each other exactly at the Fermi energy. Thus the bandstructure of graphene shows zero bandgap with zero density of states at the Fermi energy. [105] The  $\pi$ -network is however broken locally upon adsorption of H atom. As a result new C- $p_z$  state emerges near Fermi energy which belongs to the carbon atoms that are in close vicinity of the hydrogenated carbon

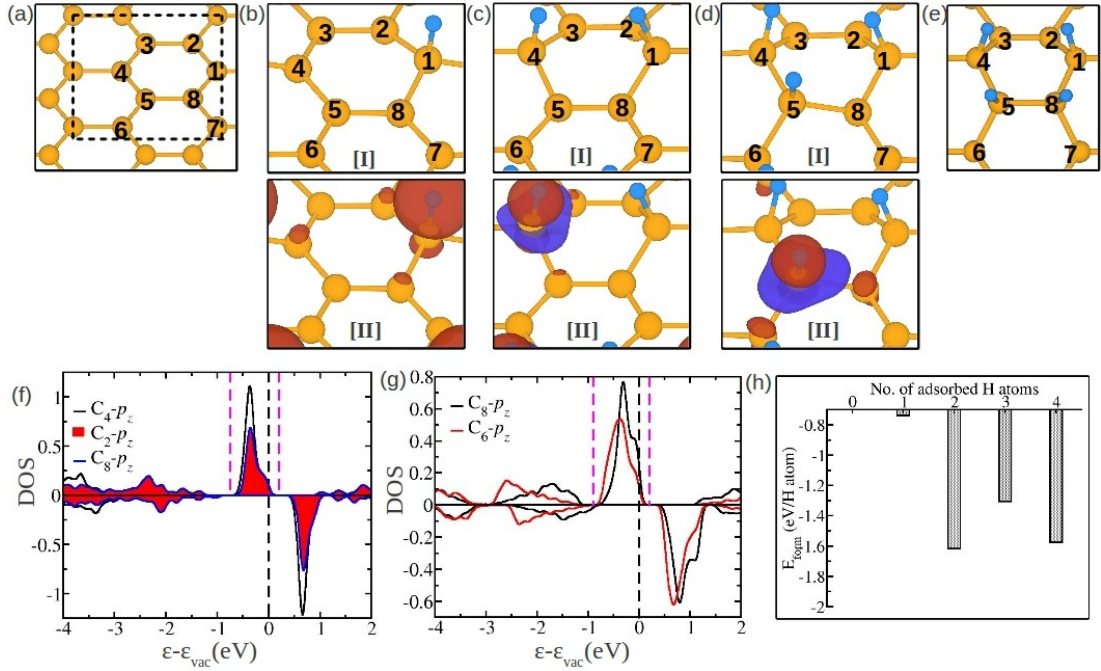


FIGURE 4.1: (a) Structure of freestanding graphene sheet. The black dashed box denotes the orthorhombic unit cell. (b, c, d) Structure (in panel [I]) and charge transfer plot (in panel [II]) for hydrogenated graphene with one, two and three H atoms in the orthorhombic unit cell of graphene, respectively. Charge transfer is determined using eq. (3). The red and blue isosurfaces show accumulation and depletion of charge, respectively. (e) Optimised structure of hydrogenated graphene sheet with four H atoms in the orthorhombic unit cell. (f, g) DOS for C atoms in structures (b) and (d), respectively. In this and the subsequent figures the C and H atoms are denoted by orange and blue colored spheres, respectively.

atoms. Šljivančanin *et al.* [82] demonstrated from their first principles study of H dimer on graphite surface that the second H atom adsorbs selectively at a site, neighboring to the first hydrogenation site, with highest local density of states near the Fermi energy. An increase in the local density of states is a consequence of increased charge localization on the carbon atom due to breaking of the  $\pi - \pi$  bond upon hydrogenation. Therefore the unhydrogenated C atoms closest to the hydrogenated C will show greater charge localization and hence will be more reactive. Thus we observe that the adsorbed H is present in a closed-packed arrangement rather than in scattered or dispersed patterns on graphene. [82]-[84] In the present study we make use of this site selectivity of adsorbing H atom to determine the lowest energy structure of the semihydrogenated freestanding graphene. For this purpose we hydrogenate one carbon atom at a time in an orthorhombic unit cell containing 8 C atoms (figure 4.1 (a)). For each hydrogenation step we have determined the charge localization ( $\Delta n(r)$ ) on unhydrogenated C atoms so as to find out the next preferable H adsorption site. The charge localization is determined using the following equation:

$$\Delta n(r) = n_{H-Gr}^X(r) - n_{H-Gr}^{X-1}(r) - n_H \quad (4.3)$$

In equation 4.3,  $n_{H-Gr}^X$  is the total charge density of graphene sheet with  $X$  number of H adsorbed ( $XH - Gr$ ),  $n_{H-Gr}^{X-1}$  is the total charge density of graphene sheet with one H atom less than in  $XH - Gr$  but in the same geometry as  $XH - Gr$  and  $n_H$  is the charge density of H atom(s) in the same unit cell as that of the hydrogenated graphene sheet.  $X$  takes the minimum value of 1 and maximum value of 4, which corresponds to a minimum H coverage of 0.125 ML and a maximum H coverage of 0.50 ML on graphene sheet, respectively. In the beginning hydrogen is adsorbed at  $C_1$ , on sublattice  $\alpha$ , which gives rise to a non-zero sublattice imbalance. The charge transfer shows that the charge localizes on the neighboring carbon atoms,  $C_2$ ,  $C_4$  and  $C_8$  of sublattice  $\beta$  as shown in figure 4.1 (b). We notice that  $C_2$  and  $C_8$  are equivalent with respect to their local environment and thus they show equal charge localization, which we have confirmed from the exactly same contribution to the density of states (DOS) from these two C atoms near the Fermi energy (in figure 4.1 (f)). Therefore hydrogenating either of these two carbon atoms is thermodynamically equivalent. Unlike  $C_2$  and  $C_8$ ,  $C_4$  has a diagonally opposite hydrogenated carbon atom. So hydrogenating  $C_4$  will form a more denser H cluster than that formed by hydrogenating  $C_2$  or  $C_8$ . Hence we find that  $C_4$  shows slightly greater charge localization relative to  $C_2$  and  $C_8$  as shown by the projected DOS in figure 4.1 (f). As a consequence hydrogenating  $C_4$  is energetically more favourable (by 0.72 eV) than hydrogenating  $C_2$  or  $C_8$ . By taking into account the periodic boundary conditions, we find that the structure in figure 4.1 (c) is similar to that reported for H trimer on graphene [83]. On adding the second H at  $C_4$  the chemical imbalance within the graphene lattice is nullified. With H adsorbed at  $C_1$  the second H adsorbed on  $C_4$  give rise to charge localization on  $C_3$  and  $C_5$  (figure 4.1 (c) [II]).  $C_3$  and  $C_5$  are equivalent with respect to their local environment and hence hydrogenating either of them amounts to equal thermodynamic stability. So we add the third H in the unit cell at  $C_5$  and we find that the charge localizes on  $C_6$  and  $C_8$ , as shown in figure 4.1 (d) [II].  $C_8$  has two neighboring hydrogenated C while  $C_6$  has only one. Therefore similar to the case of adsorption of the second H atom we find that hydrogenating  $C_8$  is more favorable (by around 0.80 eV) because it forms a more compact H cluster on the graphene sheet than that formed upon hydrogenating  $C_6$ . Consistently we find from the DOS of  $C_{6,8} - 2p$  that the charge accumulation is greater on  $C_8$  than that on  $C_6$  (figure 4.1 (g)). Thus we add the fourth and the last H on  $C_8$ . We do not add any more H atoms as we are only interested in studying the hydrogenation of graphene at 0.5 ML H coverage.

An important observation to note here is that every new H atom that is added in the

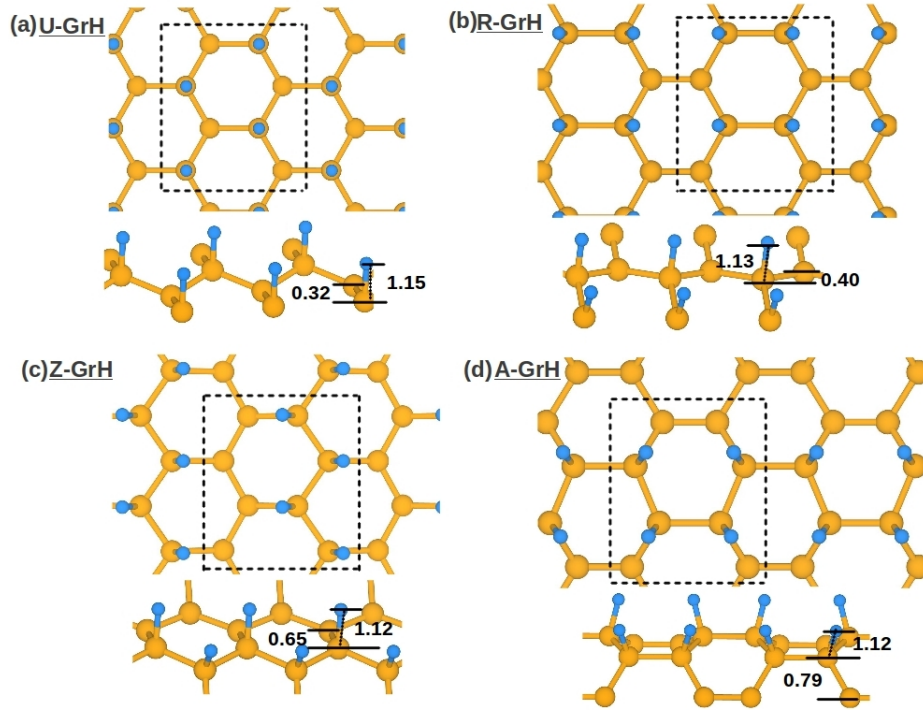


FIGURE 4.2: (a)-(d) Side and top-view geometry of the uniform, rectangular, zigzag and armchair hydrogen patterns on the graphene sheet, respectively. The black dotted box is the orthorhombic cell containing 8 C atoms. The distances displayed in the figures are in angstrom units.

cell is adsorbed on a different sublattice than in the previous step. This shows that the chemical imbalance majorly governs the site selective adsorption of H on graphene. The charge redistribution guides us to the lowest energy structure of semihydrogenated graphene which is shown in figure 4.1 (e). The hydrogenation pattern in this lowest energy structure form strips of hydrogen atoms along the armchair direction of the graphene sheet. Therefore we call this structure as armchair graphone (AGrH) consistent with other nomenclature like rectangular graphone (RGrH) [85] and zigzag graphone (ZGrH) [86]. Further we have compared the stability of AGrH with the other three earlier reported semihydrogenated graphene structures (GrH, RGrH and ZGrH) by determining the binding energy of H,  $\Delta E_H$ , using the following equation:

$$\Delta E_H = \frac{E_{Gr/H} - E_{Gr} - 4 \times E_H}{A} \quad (4.4)$$

The first ( $E_{Gr/H}$ ) and second ( $E_{Gr}$ ) terms on the right hand side (RHS) of equation 4.4 are the total energies of hydrogenated and pristine graphene sheet in freestanding condition, respectively. The third term ( $E_H$ ) is the total energy of an isolated H atom.  $A$  is the unit cell area of the hydrogenated graphene sheet. We find that the hydrogen atoms binds strongest on the graphene sheet in AGrH with  $\Delta E_H$  of around  $-0.30 \text{ eV}/\text{\AA}^2$ . In

RGrH and ZGrH  $\Delta E_H$  is around  $-0.28 \text{ eV}/\text{\AA}^2$  and that in UGrH is around  $-0.12 \text{ eV}/\text{\AA}^2$ . We have shown the optimized structures of all the four semihydrogenated graphene sheets in figure 4.2.

Further in order to understand the stability in AGrH we have decomposed  $\Delta E_H$  into its three contributing factors, namely, the interaction of graphene with H atoms ( $E_{Gr-H}^{int}$ ), the H-H interaction when H atoms are adsorbed over graphene ( $E_{H-H}^{int}$ ) and the strain energy in graphene upon adsorption of H atoms ( $E_{Gr}^{strain}$ ). The decomposition of  $\Delta E_H$  in terms of the above mentioned quantities can be expressed as:

$$\Delta E_H = E_{GrH}^{int} + E_{Gr}^{strain} + E_{H-H}^{int} \quad (4.5)$$

The first term in the RHS of equation 4.5,  $E_{Gr-H}^{int}$ , is given by:

$$E_{Gr-H}^{int} = \frac{E_{Gr/H} - E'_{Gr} - E'_{4H}}{A} \quad (4.6)$$

where,  $E_{Gr/H}$  is the total energy of combined system. The second (third) term in equation 4.6,  $E'_{Gr}$  ( $E'_{4H}$ ), is the total energy of graphene (H atoms) obtained by removing the H (graphene) atoms from the optimised geometry of the combined system. The second term in equation 4.5 ( $E_{Gr}^{strain}$ ) corresponds to the strain arising in graphene due to change in its geometry upon hydrogenation and is determined by the difference between the energy of graphene when present in the same geometry as in the combined system ( $E'_{Gr}$ ) and total energy of completely relaxed pristine graphene ( $E_{Gr}$ ) as given below:

$$E_{Gr}^{strain} = \frac{E'_{Gr} - E_{Gr}}{A} \quad (4.7)$$

The last term in equation 4.5,  $E_{H-H}^{int}$ , is given by:

$$E_{H-H}^{int} = \frac{E'_{4H} - (4 \times E_H)}{a} \quad (4.8)$$

The decomposed energy terms obtained for the freestanding case are plotted in figure 4.3. The stability of a given adsorption pattern is determined by the competition between  $E^{int}$  (sum of  $E_{Gr-H}^{int}$  and  $E_{H-H}^{int}$ ) and  $E_{Gr}^{strain}$ , the former stabilizes the system while the latter destabilizes it. The buckling between unhydrogenated and hydrogenated C in the freestanding semihydrogenated graphene is significantly large in A-GrH (largest) and Z-GrH compared to that in GrH or R-GrH (as shown in figure 4.2). As a consequence we observe that A-GrH has the largest strain energy. The large buckling in A-GrH

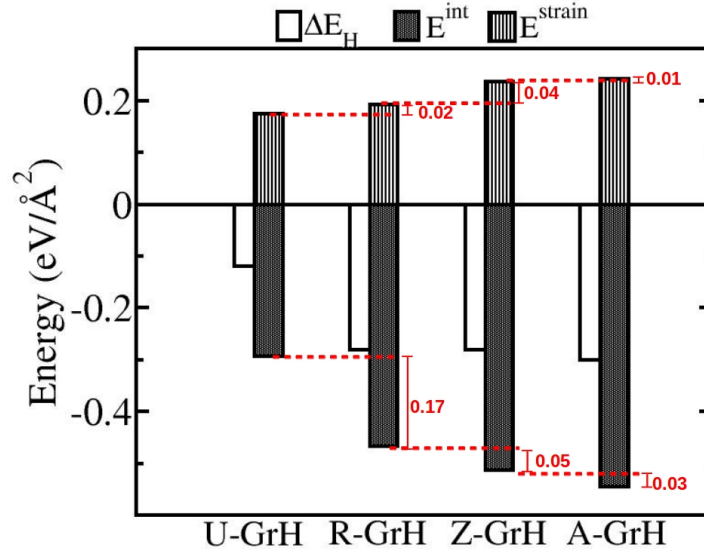


FIGURE 4.3: Binding energy of H on freestanding graphene and its constituent energy terms.  $\Delta E^{int}$  is the sum of  $E_{Gr-H}^{int}$  and  $E_{H-H}^{int}$ .

is induced by the strong interaction between H and graphene. Therefore, we observe that  $E^{int}$  is not only largest for A-GrH amongst all the hydrogen patterns considered in this study, but is also significantly larger than the  $E_{Gr}^{strain}$  in A-GrH, thereby stabilizing A-GrH. To understand why the interaction energy is large in A-GrH we look into the packing of the H atoms amongst the different patterns where there is no sublattice imbalance, namely R-GrH, Z-GrH and A-GrH. For R-GrH, each hydrogenated C atom has one hydrogenated C atom and two unhydrogenated C atoms as nearest neighbours. Thus there are dimers of  $sp^3$  hybridized carbons separated by patches of  $sp^2$  hybridized C atoms. In contrast, for Z-GrH and A-GrH each hydrogenated C atom have two hydrogenated C atoms and one unhydrogenated C atom as nearest neighbours. The second and third nearest hydrogenated C atoms is about 2.56 Å and 2.72 Å, respectively, in A-GrH while that in Z-GrH are 2.49 Å and 3.84 Å, respectively. This suggests that the H atoms are more closely packed in A-GrH than in Z-GrH and hence the interaction energy of H with graphene surface is slightly larger in A-GrH than that in Z-GrH.

In figure 4.4 we have shown the density of states (DOS) projected on the C-2p states of the hydrogenated and unhydrogenated carbon atoms in the semihydrogenated graphene sheet with four different H-patterns, namely, U-GrH, R-GrH, Z-GrH and A-GrH. The DOS for U-GrH and R-GrH obtained with our calculations match well with those reported earlier by Zhou *et al.*[81] and Feng *et al.* [85], respectively. We observe spin-split states only for the case of ferromagnetic U-GrH. We also note that only Z-GrH shows metallic behaviour. U-GrH, R-GrH and A-GrH have band gaps of around 0.70 eV, 2.40

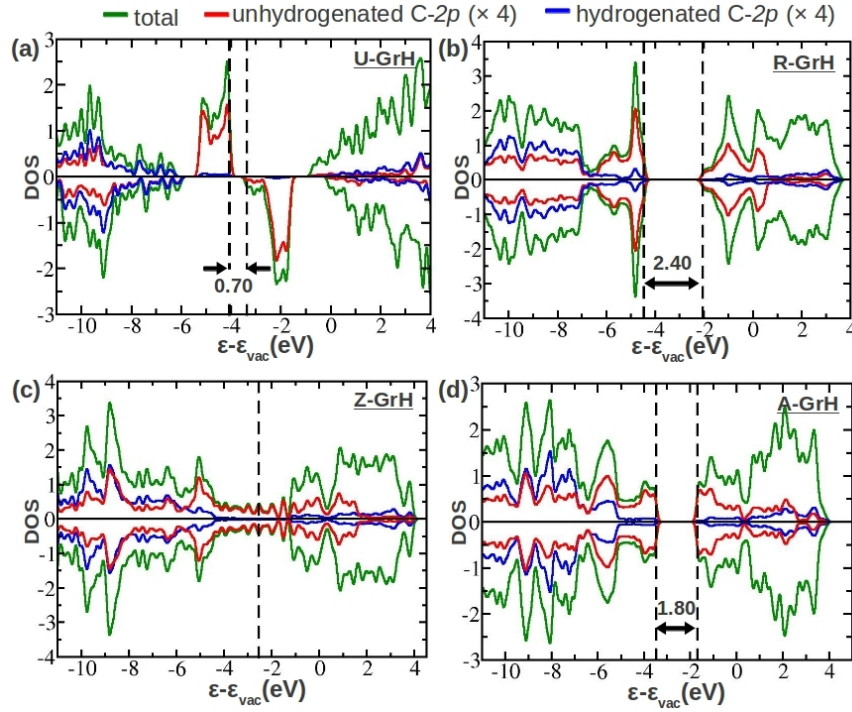


FIGURE 4.4: (a)-(d) PDOS plot of semihydrogenated graphene in uniform, rectangular, zigzag and armchair H-patterns, respectively. The red, blue and green curve shows total DOS, DOS projected on the  $2p$  states of the unhydrogenated and hydrogenated carbon atoms, respectively. In (a), (b) and (d) the vertical dashed lines denote valence band maxima (VBM) and conduction band minima (CBM). The energy gap between VBM and CBM is also given in the plot in eV. In (c) the vertical dashed line denotes the Fermi energy.

eV and 1.80 eV, respectively, with VBM and CBM formed by C- $2p$  states of the unhydrogenated C atom. The varying electronic behaviour with varying H-pattern can be understood in the following way: Hydrogenation of half of the carbon atoms breaks the delocalized  $\pi$  cloud resulting in a varying degree of localization of charge on the unhydrogenated carbon atoms. In U-GrH each unhydrogenated C atom is surrounded by three neighbouring hydrogenated C atoms. Therefore the unpaired electron is completely localised on the unhydrogenated C atoms as shown in figure 4.5 (a). This results in large band gaps (largest amongst the different adsorption patterns) in the individual spin channels. The exchange splitting results in an effective gap of about 0.70 eV. In contrast, on the R-GrH, the electrons are localized on a pair of C atoms (figure 4.5(b)), the C-C bond lengths for this pair is about 1.35 Å and is significantly shortened compared to that of 1.42 Å observed in pristine graphene. However, these pair of C atoms are surrounded by hydrogenated C atoms that prevent hopping of the electron resulting in a band gap of 2.40 eV. For the A-GrH, the unhydrogenated C atoms form a dimerized chain. The electrons are localized on a pair of C atoms that have a bond length of 1.37 Å, while between two such C-C “dimers” the bond lengths are about 1.47

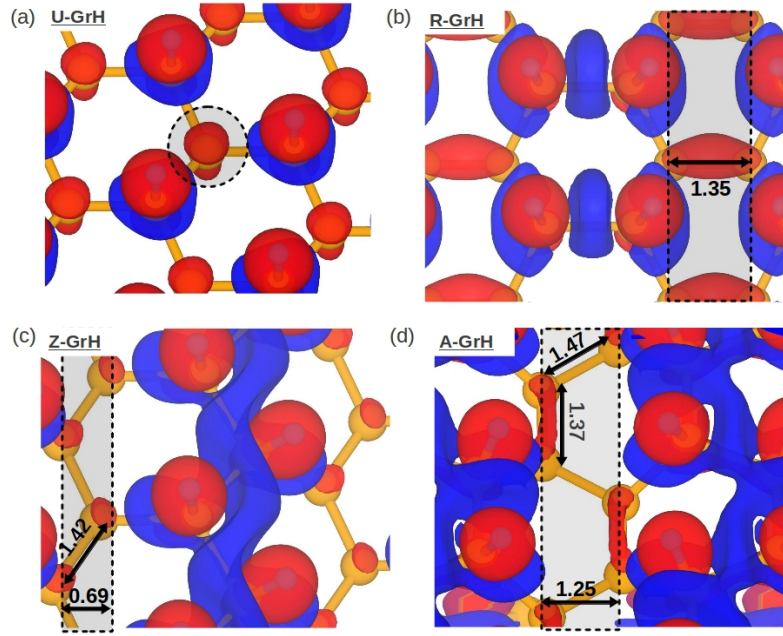


FIGURE 4.5: (a)-(d) Charge transfer plots for U-GrH, R-GrH, Z-GrH and A-GrH, respectively. The charge transfer is evaluated as:  $\Delta n(r) = n_{GrH} - n_{Gr} - n_{4H}$ , where,  $n_{GrH}$  is the charge density of semihydrogenated graphene in different H-patterns,  $n_{Gr}$  charge density of clean graphene in the same geometry as in the presence of H and  $n_{4H}$  is the charge density of four H atoms in the same geometry as they are in the semihydrogenated graphene structures. The C-C bond lengths (in Å) between the unhydrogenated C atoms are also shown.

Å (figure 4.5(d)). This distance between the two dimers are still large enough to allow the localized electrons to hop. However, because of the connectivity between them, the band gap is reduced to 1.80 eV suggesting that much lower energy is required for the electrons to be excited from valence band to conduction band. In variance with all the other adsorption patterns described above, for the Z-GrH, the unhydrogenated C atoms not only form a connected network but also the distance between them is about 1.42 Å (figure 4.5(d)), which is same as that observed for graphene. Hence in this case the electrons can hop from one unhydrogenated C atom to another resulting in a metallic system.

### 4.3.2 Semihydrogenated graphene sheet on transition metal surfaces

We have next studied semihydrogenation of graphene sheet supported on three transition metal (TM) surfaces, namely Ni(111) and Co(111) surfaces, on which the epitaxial graphene sheet is found to be chemisorbed and Cu(111) surface which physisorbs the epitaxial graphene sheet. From Ni(111) to Co(111) to Cu(111) surfaces the strain on the epitaxial graphene increases as 1.2%, 2.0% and 5.7%, respectively. By comparing



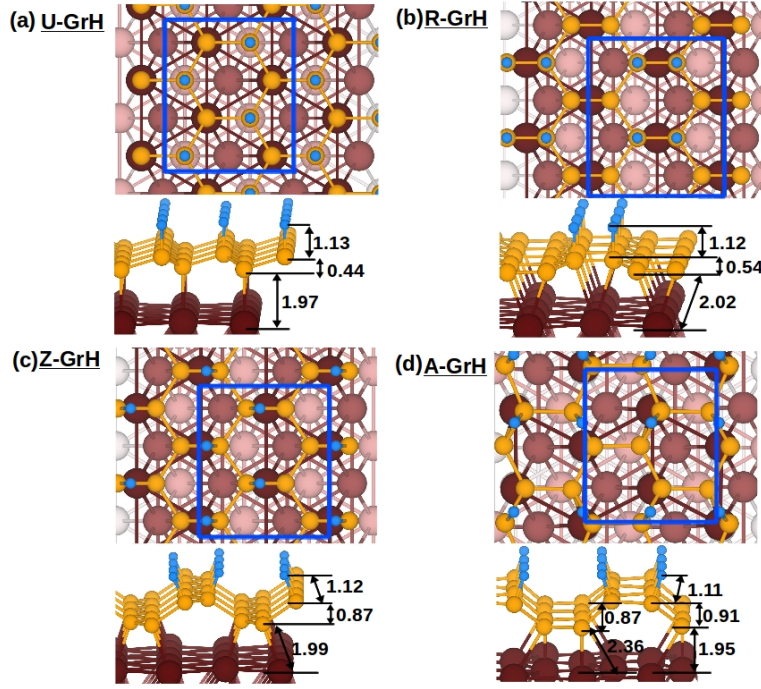


FIGURE 4.6: Topview (in top panel) and side-view (in bottom panel) of configurations of uniformly hydrogenated graphone (UGrH) (a), rectangular graphone (RGrH) (b), zigzag graphone (c) and armchair graphone (d) on Ni(111) surface. In top-view the bigger dark (brown) colored atoms are surface Ni atoms and lighter ones are the Ni atoms that resides below the surface. The blue rectangular box denotes the unit cell. The distances shown in side-view figures are in angstrom units.

the lattice parameters of semihydrogenated graphene in different H adsorption patterns and the three TM surfaces we find that the strain on semihydrogenated graphene remains trifling when supported on Ni(111) and Co(111) surfaces while it is significant when on Cu(111) surface. The lattice parameters of the four freestanding semihydrogenated graphene and the three transition metal surfaces are given in Table 4.1. On Ni(111) surface we find that all four H patterns are equally stable with binding energy of H ( $\Delta E_H^{supp}$ ) around  $-0.39 \text{ eV}/\text{\AA}^2$ . On Co(111) surface AGrH and ZGrH are equally stable with  $\Delta E_H^{supp}$  of around  $-0.37 \text{ eV}/\text{\AA}^2$ . RGrH on Co(111) is slightly more stable with  $\Delta E_H^{supp}$  around  $-0.38 \text{ eV}/\text{\AA}^2$  while UGrH shows less stability with  $\Delta E_H^{supp}$  around  $-0.36 \text{ eV}/\text{\AA}^2$ . Similarly on Cu(111) surface AGrH and ZGrH again show equal stability ( $\Delta E_H^{supp} = -0.34 \text{ eV}/\text{\AA}^2$ ); RGrH is most stable ( $\Delta E_H^{supp}$  around  $-0.37 \text{ eV}/\text{\AA}^2$ ) and UGrH is least stable ( $\Delta E_H^{supp} = -0.33 \text{ eV}/\text{\AA}^2$ ).  $\Delta E_H^{supp}$  is determined using an equation analogous to that of equation 4.4 where  $E_{Gr/H}$  and  $E_{Gr}$  on the RHS are replaced with total energies of semihydrogenated graphene ( $E_{TM/Gr/H}$ ) and pristine graphene ( $E_{TM/Gr}$ ) on TM surface, respectively. Even though the stability of all four structures on Ni(111) surface are equal the sites occupied by the C atoms in each structure are different. Similarly different configurations of semihydrogenated graphene for different H adsorption

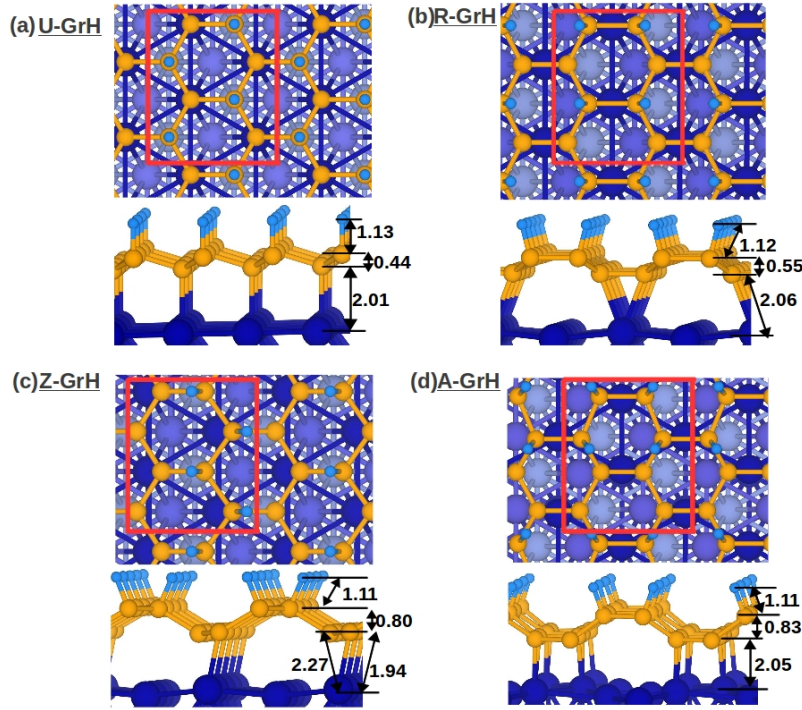


FIGURE 4.7: Topview (in top panel) and side-view (in bottom panel) of configurations of uniformly hydrogenated graphone (UGrH) (a), rectangular graphone (RGrH) (b), zigzag graphone (c) and armchair graphone (d) on Co(111) surface. In top-view the bigger dark (blue) colored atoms are surface Co atoms and lighter ones are the Co atoms that resides below the surface. The red rectangular box denotes the unit cell. The distances shown in side-view figures are in angstrom units.

patterns are observed on Co(111) and Cu(111) surfaces. The top and side view of the relaxed structures of the semihydrogenated graphene on Ni(111), Co(111) and Cu(111) are shown in figures 4.6, 4.7 and 4.8, respectively. The UGrH on all three TM surfaces takes the top-fcc configuration in which the hydrogenated (unhydrogenated) C is at the fcc (top) site. This is consistent with our earlier study on uniform graphone supported on Ni(111) and Co(111). [92], [48] Next RGrH takes the bridge-top configuration on all the three TM surfaces. The bridge-top configuration is formed when one C is at the bridge between fcc and top sites while the other one is at the bridge between hcp and top sites. Thus the C-C bonds lie above the surface TM atom. Bridge-top configuration is found to be equally stable to top-fcc configuration for clean graphene sheet on Ni(111).[98] In RGrH the C-C bond over the top-site is between the same kind of carbon atoms, i.e. both are either unhydrogenated or hydrogenated. Next, ZGrH on Ni(111) surface takes the bridge-top configuration such that the C-C bond over the top-site is between one unhydrogenated C and one hydrogenated C. A different structure is obtained for ZGrH on Co(111) and Cu(111) where the carbon atoms are laterally shifted by 0.4-0.5 Å from the top sites and 0.3-0.4 Å from fcc sites. Hence we have named the configuration as shifted-top-fcc configuration. AGrH on Co(111) takes bridge-top configuration while

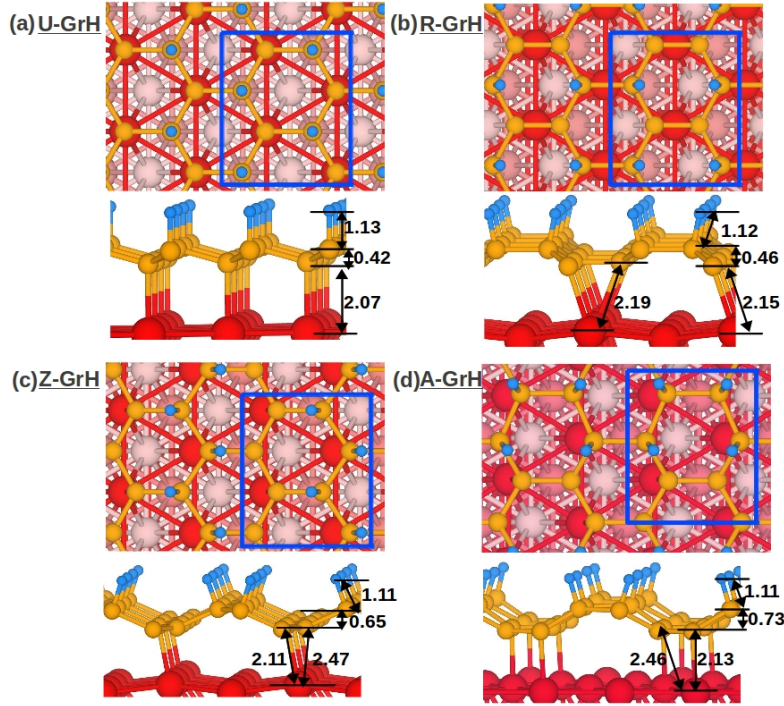


FIGURE 4.8: Topview (in top panel) and side-view (in bottom panel) of configurations of uniformly hydrogenated graphone (UGrH) (a), rectangular graphone (RGrH) (b), zigzag graphone (c) and armchair graphone (d) on Cu(111) surface. In top-view the bigger dark (red) colored atoms are surface Cu atoms and lighter ones are the Cu atoms that resides below the surface. The blue rectangular box denotes the unit cell. The distances shown in side-view figures are in angstrom units.

on Ni(111) and Cu(111) the C atoms are present in shifted-top-fcc configuration. The lateral shift in the C atoms with respect to Ni (Cu) atoms at the top-sites is around 0.3 (0.3-0.4) Å while at fcc-sites is around 0.3-0.4 (0.5-0.6) Å in AGrH on Ni(111) (Cu(111)) surface.

At this point few questions arise: (a) First question is how is it that on Ni(111) surface alone all the hydrogenation patterns on the semihydrogenated graphene, including UGrH, are equally stable? (b) Next question is why are the four semihydrogenated graphene structures present in different configurations on the TM surfaces? (c) Further among the four stable patterns only UGrH structure on Ni(111) surface was recognised experimentally using XPS measurements. Why were there no signatures of other H adsorption pattern in the XPS studies? [1] To answer the first question we have decomposed  $\Delta E_H^{supp}$  into its constituent energy terms, in the following equations. The competing energy terms are (1) interaction energy ( $E_{int}$ ) which is the sum of C-H interaction energy ( $E_{Gr-H}^{int}$ ) and H-H interaction energy ( $E_{H-H}^{int}$ ) and (2) strain energy ( $E_{Gr}^{strain}$ ).  $E_{Gr-H}^{int}$ ,  $E_{H-H}^{int}$  and  $E_{Gr}^{strain}$  calculated for the semihydrogenated structures on transition metal surfaces by using equations 4.6, 4.7 and 4.8, respectively, with the only

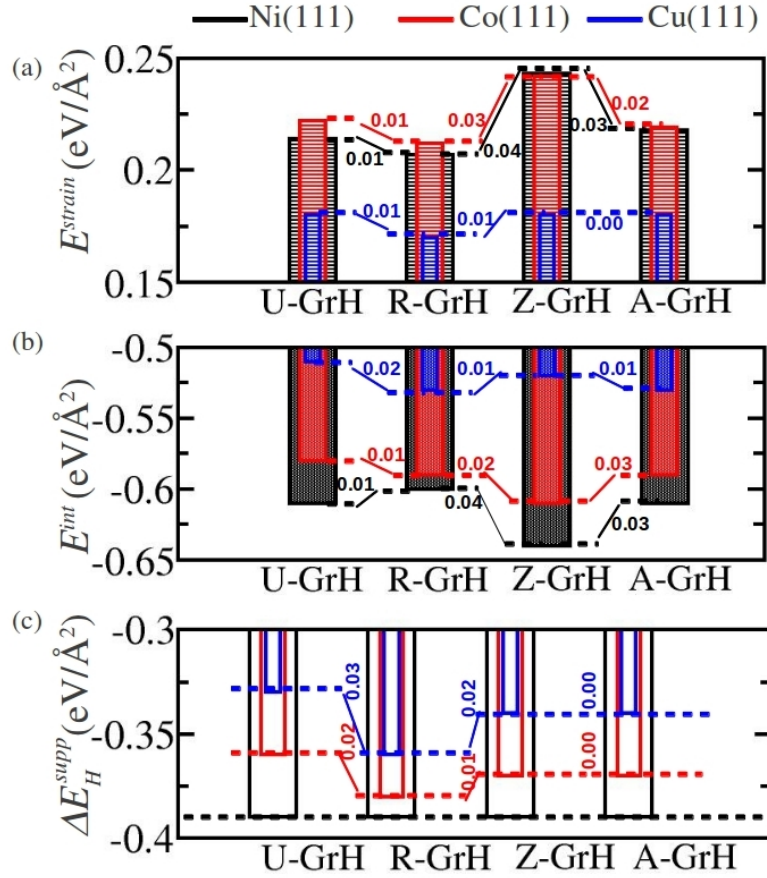


FIGURE 4.9: (a) Strain energy, (b) interaction energy and (c) binding energy of H on graphene supported on Ni(111) (black), Co(111) (red) and Cu(111) (blue) surfaces.

difference that the graphene sheet is supported on transition metal surface and  $A$  is the area of the cell defined with lattice parameters of transition metal surfaces. Figure 4.9 shows bar plot of  $\Delta E_H^{\text{supp}}$  for different semihydrogenated structures on the three TM surfaces along with the contribution of the two competing energy terms. We note that  $E^{\text{int}}$  is highly dominating over  $E_{\text{Gr}}^{\text{strain}}$  and thus semihydrogenated graphene is stable on all three TM surfaces. On Ni(111) surface both  $E^{\text{int}}$  and  $E_{\text{Gr}}^{\text{strain}}$  shows the following trend among the four semihydrogenated structures: ZGrH > UGrH = AGrH > RGrH. Moreover we note that the difference in the net energy gain by system (ie. change in  $E^{\text{int}}$ ) is compensated exactly by the difference in the energy cost by the system (change in  $E_{\text{Gr}}^{\text{strain}}$ ) as we move from one structure to other on Ni(111) surface, thereby making all the patterns equally favorable. On Co(111) as well as on Cu(111) surfaces the trends observed for  $E_{\text{Gr}}^{\text{strain}}$  are different from that for  $E^{\text{int}}$ . On Co(111) surface trends in  $E^{\text{int}}$  and  $E_{\text{Gr}}^{\text{strain}}$  are ZGrH > RGrH = AGrH > UGrH and ZGrH > AGrH = UGrH > RGrH, respectively. ZGrH on Co(111) surface shows largest  $E^{\text{int}}$  ( $-0.61 \text{ eV}/\text{\AA}^2$ ) while UGrH has the least ( $-0.58 \text{ eV}/\text{\AA}^2$ ). RGrH and AGrH has equal  $E^{\text{int}}$  of around  $-0.59 \text{ eV}/\text{\AA}^2$ .

Substrate	Gr	UGrH	RGrH	ZGrH	AGrH
Ni(111)	-0.06	-0.34	-0.20	-0.22	-0.19
Co(111)	-0.08	-0.32	-0.20	-0.19	-0.17
Cu(111)	-0.03	-0.21	-0.11	-0.09	-0.09

TABLE 4.2: Interaction energy of graphene (column 2) and semihydrogenated graphene in different H patterns (column 3-6) with its transition metal substrate in eV/Å<sup>2</sup>

Though ZGrH on Co(111) surface has largest  $E^{int}$  but it also has largest  $E_{Gr}^{strain}$  of around 0.24 eV/Å<sup>2</sup> resulting in  $\Delta E_H^{supp}$  of around -0.37 eV/Å<sup>2</sup> which is equal to that in AGrH on Co(111).  $E_{Gr}^{strain}$  in AGrH and UGrH on Co(111) surface are equal and 0.02 eV/Å<sup>2</sup> smaller than that in ZGrH. However UGrH shows weaker  $E^{int}$  than AGrH on Co(111) surface by about 0.01 eV/Å<sup>2</sup>. Therefore  $\Delta E_H^{supp}$  is stronger in AGrH (-0.37 eV/Å<sup>2</sup>) than in UGrH (-0.36 eV/Å<sup>2</sup>) on Co(111) surface. The least strain energy is observed in RGrH among other semihydrogenated structures on Co(111) surface which is about 0.21 eV/Å<sup>2</sup>. Hence  $\Delta E_H^{supp}$  of -0.38 eV/Å<sup>2</sup> is strongest in RGrH among other structures on Co(111) surface. On Cu(111) surface we find the trend in  $E^{int}$  as RGrH = AGrH > ZGrH > UGrH and that in  $E_{Gr}^{strain}$  as UGrH = ZGrH = AGrH > RGrH. RGrH shows largest  $E^{int}$  of about -0.53 eV/Å<sup>2</sup> and smallest  $E_{Gr}^{strain}$  of about 0.17 eV/Å<sup>2</sup> which makes it the most stable structure. The remaining three structures shows equal strain energy of around 0.18 eV/Å<sup>2</sup>. Thus their relative stability is decided by  $E^{int}$ . AGrH has equal  $E^{int}$  as in RGrH and thus it shows second strongest  $\Delta E_H^{supp}$  of around -0.35 eV/Å<sup>2</sup>.  $E^{int}$  for ZGrH and UGrH are around -0.52 eV/Å<sup>2</sup> and -0.51 eV/Å<sup>2</sup> which results in  $\Delta E_H^{supp}$  of around -0.34 eV/Å<sup>2</sup> and -0.33 eV/Å<sup>2</sup>, respectively.

For addressing the second question we have evaluated interaction energy between TM surface and epitaxial graphene sheet when it is clean and when it is semihydrogenated in different H adsorption patterns. The TM-Gr interaction energy ( $E_{TM-Gr}^{int}$ ) is determined using the following equation 4.9:

$$E_{TM-Gr}^{int} = \frac{E'_{TM/Gr/H} - E'_{TM} - E'_{Gr/H}}{A} \quad (4.9)$$

where, the terms in the RHS are the total energies of semihydrogenated graphene on TM surface, the clean TM surface and the freestanding semihydrogenated graphene sheet, all calculated using their respective geometries as in the semihydrogenated graphene supported on TM surfaces. For the system of clean graphene on TM surface the first and third terms in equation 4.9 are replaced with total energies of clean graphene on TM surface and freestanding graphene.  $E_{TM-Gr}^{int}$  for different systems are listed in Table 4.2. As freestanding UGrH (AGrH) is highly unstable (stable) we find that  $E_{TM-Gr}^{int}$

is stronger (weaker) for UGrH (AGrH) on all three TM surface.  $\Delta E_H^{supp}$  has direct dependence on  $E_{TM-Gr}^{int}$  which is expressed in equation 4.10.

$$\Delta E_H^{supp} = \frac{[E_{TM-Gr}^{int} + \Delta E'_H - E_{TM-Gr}^{int}] - E_{Gr}^{strain} - E_{H-H}^{int}}{A} \quad (4.10)$$

$\Delta E'_H$  and  $E_{TM-Gr}^{int}$  are binding energy of H in freestanding semihydrogenated graphene when it has the same geometry as on TM surface and interaction energy of clean graphene sheet and TM surface when the system of epitaxial graphene on TM surface is in the same geometry as when semihydrogenated. The rest of the terms are defined earlier in this chapter:  $E_{Gr}^{strain}$  in equation 4.7 and  $E_{H-H}^{int}$  in equation 4.8. Note that the first three terms in equation 4.10, included within square brackets, equals  $E_{Gr-H}^{int}$  which is defined in equation 4.6. Thus stronger  $E_{TM-Gr}^{int}$  stronger is  $E_{Gr-H}^{int}$  and more is the stability of semihydrogenated structure, ie. stronger  $\Delta E_H^{supp}$ . Hence the direct dependence of stability of semihydrogenated graphene on TM surface on  $E_{TM-Gr}^{int}$  suggests that the role of substrate is to stabilise the unhydrogenated C. The C-H interaction energy in freestanding semihydrogenated graphene, given in figure 4.3, is weaker than that when the semihydrogenated graphene sheet is supported on TM surfaces. In order to achieve maximum stability of the unhydrogenated C the semihydrogenated graphene sheet chooses different configurations on the TM surfaces. Thus the semihydrogenated graphene with uniform H pattern stabilises in top-fcc configuration even when we start with bridge-top configuration on Ni(111) surface. Similarly ZGrH and AGrH on Ni(111) moves to bridge-top and shifted-top-fcc configuration from the initial top-fcc configuration. We were able to optimise AGrH on Ni(111) in bridge-top configuration however, it shows higher total energy than shifted-top-fcc configuration by 108 meV. RGrH also chooses bridge-top configuration over top-fcc configuration by about 72 meV of energy. In the same manner we obtain different configurations of different semihydrogenated graphene sheet on Co(111) and Cu(111) surfaces. We further note that unlike UGrH and RGrH structures, AGrH and ZGrH structures does not show same configuration as we change the underlying substrate. For explaining this observation we have calculated strain energy in the semihydrogenated graphene sheet when it is freestanding but in the same geometry as it is on the TM surfaces. The strain energy is calculated by taking the difference between total energies of freestanding semihydrogenated graphene when it is in the same geometry as on TM surface and when it is completely relaxed. We find that for both, UGrH and RGrH, the strain energy remains more or less constant on all three TM surfaces to  $0.03 \text{ eV}/\text{\AA}^2$  and  $0.04 \text{ eV}/\text{\AA}^2$ , respectively. Therefore for these two H patterns we do not observe change in their configurations with different metal substrates. For ZGrH the strain energy on Co(111) and Cu(111) surfaces are equal and around  $0.03 \text{ eV}/\text{\AA}^2$  while it is higher on Ni(111) surface which is around  $0.05 \text{ eV}/\text{\AA}^2$ . Thus on

Co(111) and Cu(111) surfaces ZGrH chooses same configuration (shifted-top-fcc) while on Ni(111) surface it settles in a different configuration (bridge-top). Similarly for AGrH strain energy is higher when placed on Ni(111) surface ( $0.04 \text{ eV}/\text{\AA}^2$ ) and Cu(111) surface ( $0.05 \text{ eV}/\text{\AA}^2$ ) than when placed on Co(111) surface ( $0.02 \text{ eV}/\text{\AA}^2$ ). Therefore on Ni(111) and Cu(111) surfaces AGrH is present in shifted-top-fcc configuration while on Co(111) surface it is present in bridge-top configuration.

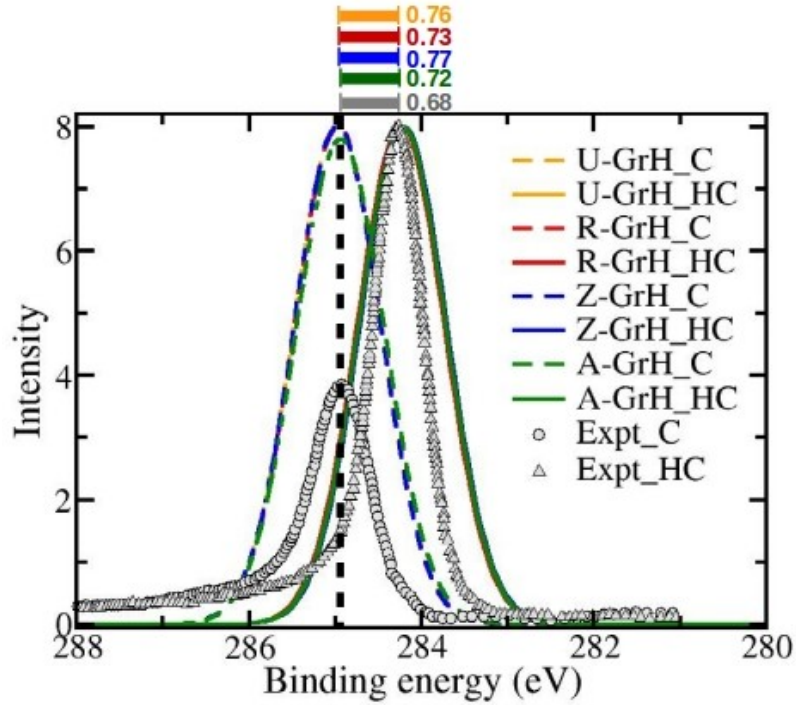


FIGURE 4.10: Corelevel shifts of C 1s of the unhydrogenated carbon (C) and hydrogenated carbon (HC) in the semihydrogenated graphene sheet supported on Ni(111) surface. The dotted and solid curves corresponds to C and HC, respectively. The peaks are shifted with respect to the experimental peak of the unhydrogenated C atom at 284.96 eV. The experimental data is obtained from the XPS studies performed by Zhao *et al.* [1]. The difference in the binding energy are noted above the plot.

In order to address the last question we have computationally determined the core-level shifts for C 1s of unhydrogenated and hydrogenated C in all the Ni(111) surface-supported structures and have compared with the experimental C 1s spectra reported by Zhao *et al.* [1] for semihydrogenated graphene on Ni(111) surface. In figure 4.10 we have shown the C 1s spectra of hydrogenated and unhydrogenated carbon atoms with dashed and continuous lines, respectively. The plots for all the four structures are shifted so as to align the peaks corresponding to the unhydrogenated carbon atoms obtained from our study with the peak for unhydrogenated carbon atoms obtained from the experimental measurement at 284.96 eV by Zhao *et al.* [1] The spectra obtained for all the four structures from our calculations match quite well with the experimental one. The area under the peaks corresponding to the unhydrogenated carbon atom and

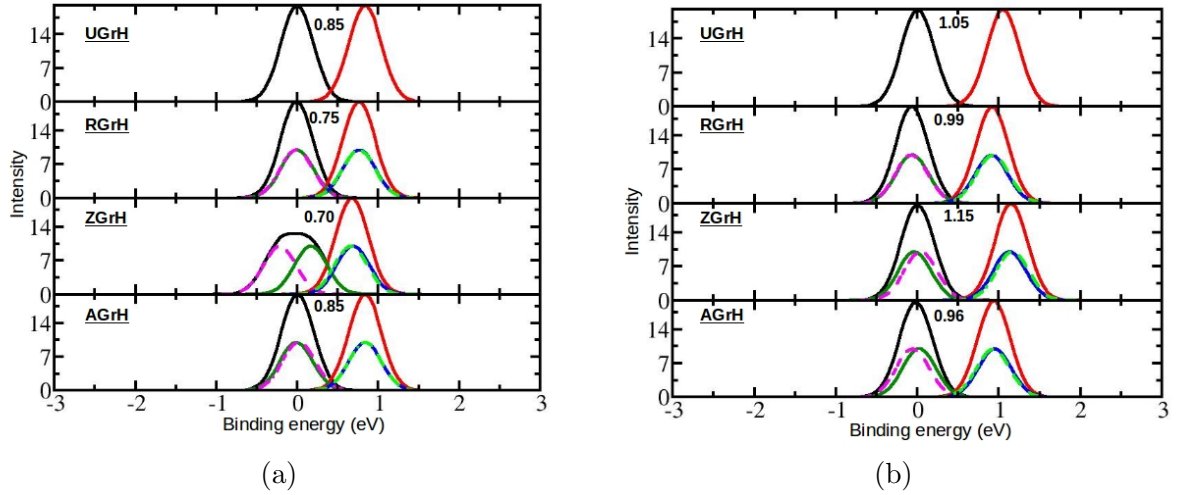


FIGURE 4.11: Corelevel shifts of C 1s of the unhydrogenated carbon (C) and hydrogenated carbon (HC) in the semihydrogenated graphene sheet supported on (a) Co(111) surface and (b) Cu(111) surface. C and HC are denoted by dotted and solid curves, respectively. The peaks are shifted with respect to the peak of unhydrogenated carbon atom at 0 eV. The differences in the binding energies are noted above the plot.

hydrogenated carbon atom are equal implying that the hydrogen coverage is 0.5 ML. Also the spectra for all four Ni(111)/HGr structures closely follow each other which is consistent with our result that the four semihydrogenated structures on Ni(111) surface are equally favourable. The small differences in the corelevel shifts (0.01-0.05 eV) due to change in the H adsorption patterns of the semihydrogenated graphene are quite smaller than the experimental resolution (0.2 eV) and hence probably are not detected. Similar corelevel shifts were determined for structures on Co(111) and Cu(111) surfaces in figure 4.11. However since XPS studies on semihydrogenated graphene supported on Co(111) and Cu(111) surfaces has not been reported we are unable to make any comparisons of our results on these surfaces with those from experiments. Where for the Ni surface we find that CLS vary between 0.72-0.77 eV, for Co(111) they vary between 0.7 to 0.85 eV and for Cu(111) they vary between 0.96 to 1.15 eV. Thus again we believe that it would be difficult to discern different H adsorption patterns on Co(111) as well as Cu(111) surfaces if the resolution is set to 0.2 eV or greater in the XPS measurements.

Though not discernible from XPS measurements our study shows that each structure displays different interfacial electronic and magnetic properties. From figure 4.6, 4.7 and 4.8 we observe variation in the TM-C bondlength suggesting variation in TM-C interaction ( $E_{TM-Gr}^{int}$ ) among different structures. This variation in TM-C interaction in turn results in variation of magnetic moments on surface TM and graphene sheet. In figure 4.12 (a) we have plotted the average magnetic moment on surface TM and graphene sheet for the four semihydrogenated structures supported on TM surfaces, respectively. Weaker (stronger) is the TM-C bondlength larger is the magnetic moment



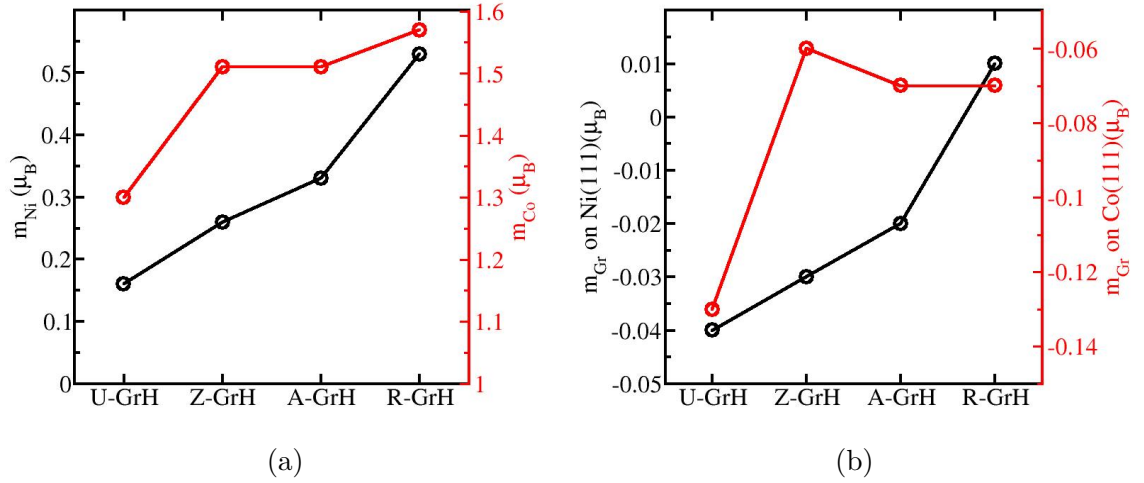


FIGURE 4.12: Net magnetic moment on (a) surface Ni (black) and Co (red) atoms and (b) on graphene sheet in four semihydrogenated structures supported on Ni(111) (black) and Co(111) (red) surfaces.

on surface TM (C) atoms. In UGrH on Ni(111) surface the Ni-C bond length is around  $1.96 \text{ \AA}$  which slightly increases to  $1.99 \text{ \AA}$  in ZGrH. As a consequence the magnetic moment on surface Ni in UGrH on Ni(111) surface is around  $0.16 \mu_B$  which is less compared to  $0.26 \mu_B$  in ZGrH on Ni(111) surface. In case of AGrH on Ni(111) surface there are two kind of Ni-C bondlengths: (i) one where the unhydrogenated C is in shifted top site and the Ni-C bondlength is stronger of around  $1.94 \text{ \AA}$  and (ii) the other where the unhydrogenated C is in the shifted fcc site with weaker Ni-C bondlength of around  $2.15 \text{ \AA}$ . Thus the stronger of the two interactions result in  $0.26 \mu_B$  while the weaker results in  $0.40 \mu_B$  magnetic moment on the surface Ni. Finally in RGrH only half of the Ni atoms interact with pairs of unhydrogenated C (Ni-C bondlength =  $2.03 \text{ \AA}$ ) while the other half has pairs of hydrogenated C above them. Therefore, those Ni atoms interacting with unhydrogenated C have quenched magnetic moment of  $0.42 \mu_B$  while the rest of the Ni atoms have a magnetic moment of  $0.64 \mu_B$  that is closely comparable in magnitude with what is observed for the clean Ni(111) surface ( $0.71 \mu_B$ ). The interaction with surface Ni atoms induces magnetic moment on unhydrogenated C of the graphene sheet giving rise to small net magnetic moment which is an order of magnitude smaller than that of surface Ni atom as shown in figure 4.12 (b). On Co(111) surface UGrH again shows stronger Co-Gr interaction which results in quenched magnetic moment on surface Co of around  $1.30 \mu_B$  with respect to  $1.78 \mu_B$  in clean Co(111) surface. In shifted-top-fcc configuration of ZGrH structure we find that only half of the surface Co interacts with the unhydrogenated C resulting in Co-C bondlength of around  $1.94 \text{ \AA}$ . Therefore half of the surface Co show quenched magnetic moment of around  $1.15 \mu_B$  while the remaining Co show larger magnetic moment of around  $1.87 \mu_B$ . Thus the net magnetic moment of surface Co in ZGrH on Co(111) is around  $1.51 \mu_B$ . Like on Ni(111) surface,

RGrH on Co(111) is present in bridge-top configuration such that half of the surface Co atoms interact with the pair of unhydrogenated C making Co-C bondlength of around 2.07 Å. Thus half of the surface Co have quenched magnetic moment ( $1.32 \mu_B$ ) while the remaining half have larger magnetic moment ( $1.82 \mu_B$ ) making the net magnetic moment on surface Co to be around  $1.57 \mu_B$ . Similar to RGrH, AGrH on Co(111) is present in bridge-top configuration with only half Co atoms interacting with the pair of unhydrogenated C (Co-C bondlength = 2.05 Å) which results in quenched magnetic moment on surface Co of around  $1.18 \mu_B$ . The remaining half surface Co have magnetic moment of around  $1.84 \mu_B$  which results in the net magnetic moment on surface Co of around  $1.51 \mu_B$ . As in the case on Ni(111) we find weak net magnetic moment on graphene when the semihydrogenated graphene sheets are supported on Co(111). However on Co(111) surface the induced moment on graphene is larger than on Ni(111) as also seen from figure 4.12 (a). Unlike Ni and Co surfaces, Cu(111) is non-magnetic. Hence the three non-magnetic semihydrogenated graphene structures, namely AGrH, ZGrH and RGrH remains non-magnetic on Cu(111) while the ferromagnetic structure, UGrH show magnetic moment of around  $0.22 \mu_B$  on each unhydrogenated C in the graphene sheet. The surface Cu atoms in UGrH on Cu(111) also show weak magnetic moment of around  $0.08 \mu_B$ .

Next we have studied the contribution to the DOS from atoms at the interface of semihydrogenated graphene and TM surfaces. In figure 4.13 we have shown the DOS projected on the *d*-orbitals of the surface TM and on both hydrogenated and unhydrogenated C for all the four structures. We notice that the supported semihydrogenated graphene in all four H adsorption patterns show non-zero DOS at Fermi level, which arise primarily from the interaction of unhydrogenated C atoms with the TM substrate. The interaction at the interface causes variation in the density of states of surface TM atoms with H adsorption patterns. We have quantified this variation by calculating spin polarization (*S*) of TM-*d* using equation 4.11.

$$S = \frac{D^\uparrow(\epsilon_F) - D^\downarrow(\epsilon_F)}{D^\uparrow(\epsilon_F) + D^\downarrow(\epsilon_F)} \times 100 \quad (4.11)$$

where,  $D^{\uparrow/\downarrow}(\epsilon_F)$  is the density of state of spin up/down at the Fermi energy. The positive (negative) *S* suggests that there is density of states from spin up (down) electrons. The spin polarization of Ni-*d* in UGrH, RGrH and AGrH are 67.7%, 78.8% and 56.4%, respectively while that in ZGrH is only 9.9%, where we notice both the spin channels heavily contribute in conduction. The interaction with Ni(111) induces smaller spin polarization, relative to that in Ni-*d*, in semihydrogenated graphene sheet which are around 6.3%, 7.8%, -2.5% and 19.7% for UGrH, RGrH, ZGrH and AGrH, respectively. Similarly spin polarization of Co-*d* in UGrH (-68.8%), RGrH (-79.5%), ZGrH (-78.4%) and AGrH

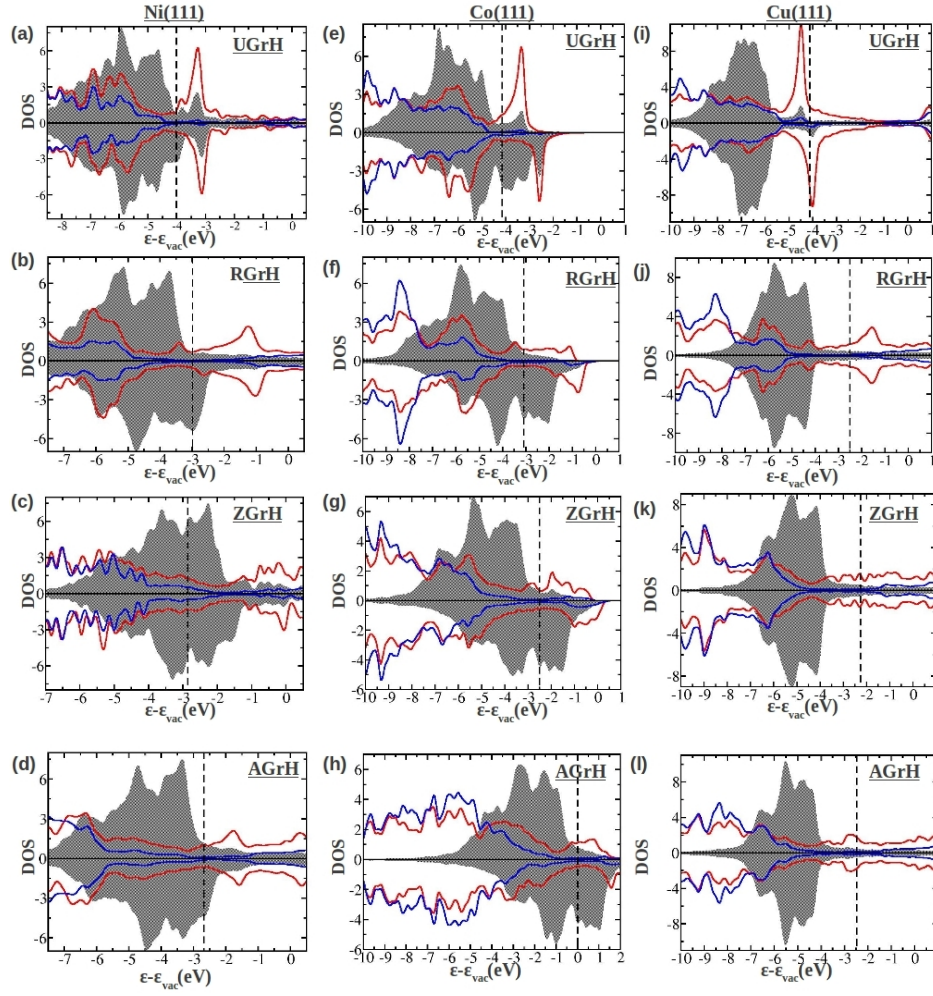


FIGURE 4.13: Projected DOS of surface TM atom (shaded grey), unhydrogenated C (red) and hydrogenated C (blue) in (a, e, i) UGrH, (b, f, j) RGrH, (c, g, k) ZGrH and (d, h, l) AGrH supported on TM(111) surface. The energies are shifted with respect to vacuum energy. The vertical dashed line denotes Fermi energy.

(-71.2%) induces spin polarization in the semihydrogenated graphene which are around 31.1%, 24.6%, 4.8% and 29.2%. The spin polarization of semihydrogenated graphene supported on Co(111) are greater than that of those supported on Ni(111) surface. However the spin polarization in Co-*d* and graphene have opposite sign. Thus interfaces with Ni(111) and Co(111) surfaces with different semihydrogenated graphene structures will give rise to weak or non-spin polarized conduction. On Cu(111) structure with uniform hydrogen pattern show spin polarization of Cu-*d* (-60.2%) and semihydrogenated graphene sheet (-61.1%) suggesting much higher possibility of spin polarised conduction than in structures on Ni(111) and Co(111) surfaces. The states of the interfacial atoms at remaining three structures on Cu(111) are non-spin-polarised.

## 4.4 Summary

We have carried out detailed investigations of semihydrogenated graphene sheet when freestanding and when supported on a (111) surfaces of Ni, Co and Cu. Our calculations suggest that the preferred H adsorption pattern on freestanding graphene is determined by two factors: (a) minimization of sublattice imbalance and (b) packing of the H atoms. Based on these two factors we have identified the armchair graphone as the most stable configuration for the semihydrogenated freestanding graphene. Further, upon semihydrogenating the graphene sheet on a Ni(111) support alone we find that all the different adsorption patterns are equally favorable. The reason for this is attributed to the fact that the energy gained is balanced equally with energy loss as we move from one structure to other which is observed neither on Co(111) surface nor on Cu(111) surface. Further importantly we note from core-level shifts in semihydrogenated graphene supported on (111) surface of Ni, Co and Cu that the four H adsorption patterns can be distinguished in XPS measurements if and only if the resolution less than 0.2 eV. For structures on Ni(111), Co(111) and Cu(111) surface the required minimum resolution is around 0.05 eV, 0.1 eV and 0.19 eV so that at least two structures are discerned. However such small resolution is extremely difficult in current setup for XPS measurements. We further investigated interfacial properties at different structures on the three TM surfaces. We find that though the stability of different semihydrogenated graphene structures are similar they show varied structural, electronic and magnetic properties. The interface with the ferromagnetic Ni(111) and Co(111) surfaces induces small magnetic moment in the non-magnetic semihydrogenated graphene structure, namely RGrH, ZGrH and AGrH. However magnetic moment in ferromagnetic UGrH is highly quenched. On Cu(111) surface RGrH, ZGrH and AGrH retain their non-magnetic behaviour while UGrH show larger magnetic moment that observed on Ni(111) and Co(111) surfaces. Furthermore we find the magnetic moment on surface Ni and Co atoms are quenched with stronger interaction with unhydrogenated C in semihydrogenated graphene. The TM-C interaction in UGrH on Cu(111) surface induces small magnetic moment on surface Cu atoms. Moreover, this interface, of UGrH and Cu(111) surface show high possibility for spin polarised conduction than any other interface studied in this paper. Hence in our opinion to realistically model these interfaces and throw light on their properties, it is important to consider all the H adsorption patterns reported in this work.

## Chapter 5

# Investigation of vacancy-Co adatom complex in freestanding graphene and graphene supported on Ni(111) surface

### 5.1 Introduction

In the last two chapters we have discussed how one can control the electronic and magnetic properties of graphene by chemical functionalization and by choosing appropriate substrate. These studies were performed by assuming that the graphene sheet is defect-free. However in reality fabrication of defect-free or impurity-free material, especially in nanoscale regime is highly unavoidable. Due to the reduced dimensionality even atomic-scale defects play a crucial role in determining the properties of nanoscale materials. It is also observed that defects not only degrade the material properties but they can also induce new properties into the material. For example, vacancy defects in graphene induces local magnetic moment in the lattice making graphene more accessible for spintronic device applications. [106–108] Hence investigation of structural defects can be a route for varying properties by which one can enhance the utility of the material in different applications.

Additionally, defects are also designed in the material, which is known as defect-engineering, for application-specific investigations. S. Jafri *et al.* [109] have demonstrated that conductivity increases with increasing the concentration of vacancy defects in graphene. Pristine graphene shows high mobility of electrons but has no conduction electrons

which results in zero density of states at the Fermi energy. Creation of single vacancy decreases mobility but produces carriers in graphene which induces metallic behaviour and hence increases conductivity. Studies have also shown that point defects (like vacancy or impurity defects) in two-dimensional materials act as active sites for various catalytic reactions providing better and noble-metal-free catalysts. [110, 111] In this chapter we will be discussing one such application-specific study of graphene with defect. To clearly state we have investigated adsorption of magnetic atom at single vacancy in graphene sheet. Such studies of magnetic nanostructure (like adatoms, molecules, cluster of atoms) supported on non-magnetic substrate are important for high density magnetic data storage device applications. The magnetic nanostructure is intended to act as a magnetic bit and hence it is required to show large magnetic moment as well as magnetization stability.

The major concern in such studies is obtaining high enough magnetic anisotropy energy (MAE), which provides directionality and stability to the magnetization. The magnetic anisotropy in lower dimensional systems arises as a result of spin-orbit interaction. [112, 113] The magnetic anisotropy due to spin-orbit interaction arises due to the combined effect of orbital angular momentum ( $\mathbf{L}$ ) and its interaction with spin angular momentum ( $\mathbf{S}$ ). Depending upon the ligand field strength  $\mathbf{L}$  tries to align along a particular symmetry direction of the system. The coupling between spin of an electron and its orbital motion around the nucleus, known as the spin-orbit coupling, tends to align the magnetization vector of the atom along the same symmetry direction. Thus energy is required by the system to change the orientation of the magnetization vector in a direction other than the preferred one, when no external field is applied. This required energy is the magnetic anisotropy energy (MAE). Greater the MAE greater is the stability of the magnetization vector under the influence of external factors like thermal fluctuations.

Previous theoretical as well as experimental studies have reported large MAEs determined for metal adatoms adsorbed on MgO and Pt(111) surfaces. [112, 114, 115] M. Sargolzaei *et al.* [116], using first principles calculations, have reported significantly high MAEs for a range of transition metal (TM) atoms adsorbed on pristine graphene and benzene molecule. Graphene being a flat surface with weak spin-orbit coupling proves to be an ideal substrate for adsorption of magnetic adatoms. However, later studies show that adatoms on pristine graphene surface are highly mobile resulting in lower stability and hence a high risk of losing data. [117] A possible solution is adsorbing the adatoms at the vacancy sites in graphene sheet. [118, 119] Vacancies in graphene sheet show higher reactivity due to creation of dangling bonds. As a consequence, they form trapping centres which reduces mobility of the adsorbed magnetic adatoms. Even so, according to the first principles calculations by H. Kandpal *et al.* [117], the MAE of the TM atom at the single vacancy in graphene are weak due to strong interaction

of the adatom with the host carbon atoms surrounding the vacancy. Further, the authors have performed calculations with Co dimer at the vacancy. They found that the anchoring Co atom establishes strong bonding with graphene sheet while the Co atom away from the graphene sheet has large orbital magnetic moment. Therefore, unlike single Co adatom at the vacancy in graphene, Co dimer shows large MAE. K. Zhang *et al.* [120] performed calculations by adsorbing single rare-earth (RE) metals at the single and double carbon vacancy in graphene sheet. Since rare-earth metals does not bind strongly to the undercoordinated carbon atoms at the vacancy, the carbon atoms surrounding the vacancy were replaced with carbonyl group. Not only is the adsorption of RE metals strong at vacancy decorated with carbonyl group but the MAEs are also large; around 40-70 meV for single vacancy structures and 12-20 meV for double vacancy structures. Along with RE metals the authors have also performed calculations for Co adatom adsorbed at vacancies enclosed by carbonyl group in graphene and found the MAEs to be about 2-4 meV, which are much larger than those obtained without the carbonyl group substitution around the vacancy. The study thus gives us a general idea of functionalizing the vacancy in order to achieve enhanced magnetic properties and large MAE.

In this study we have investigated N-decoration and B-decoration of vacancy in graphene for tuning MAE of vacancy-Co adatom complex. N has one electron more than C, which forms lone pair with the dangling bond at the vacancy site. B has one electron less and thus shows no dangling bonds at the vacancy site. As a result N and B decoration stabilizes the vacancy in graphene. Such structures with transition metal atoms adsorbed on N and B decorated vacancy in graphene sheet have already been computationally explored by X. Zhang *et al.* [121] and S. Kattel *et al.* [122]. However these studies were restricted in scalar relativistic regime and thus their study lacked the knowledge of MAE. Another study by L. Wang *et al.* [123] showed that supporting the graphene sheet with vacancy on transition metal surface also stabilises the vacancy.

In our work we have studied and compared magnetic properties of three vacancy-Co adatom complexes namely, i) undecorated vacancy-adatom complex in which Co is adsorbed at a C vacancy in graphene sheet (Co-SVG), ii) N-decorated vacancy-adatom complex, in which Co adatom is adsorbed at a C vacancy in graphene sheet where the C atoms surrounding the vacancy are replaced with N atoms (Co-SVNG) iii) B-decorated vacancy complex, in which Co is adsorbed at a C vacancy in graphene sheet where the C atoms surrounding the vacancy are replaced with B atoms (Co-SVBG). Since Co has the largest orbital as well spin magnetic moment we have chosen Co adatom in this study. Further, we have explored the effects of substrate on the magnetic properties on these vacancy-adatom complex structures by placing the graphene sheet containing the vacancy-Co-adatom complex on Ni(111) surface.

The chapter is organised as follows: The computational details are given in Section 5.2. In Section 5.3 we present and discuss our results. Finally in Section 5.4, we have summarised our work.

## 5.2 Computational Details

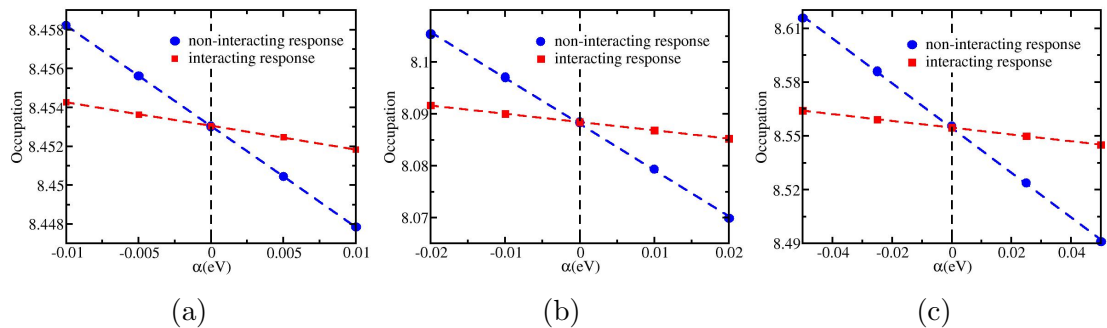


FIGURE 5.1: Linear response of Co-*d* occupation with respect to varying perturbing potential ( $\alpha$ ) in (a) Co-SVG, (b) Co-SVNG and (c) Co-SVBG

Using Quantum ESPRESSO software package [68] we have performed plane-wave based density functional theory calculations for geometry optimization and further determining the electronic and magnetic properties of the defect-adatom complex structures in graphene. The exchange and correlation are described using Perdew, Burke and Ernzerhoff (PBE) parametrization of the generalized gradient approximation (GGA).[70] We have used scalar relativistic ultrasoft pseudopotentials for describing the electron-ion interaction [69]. Only for determining the magnetic anisotropy energy we have used fully-relativistic pseudopotentials for the adatoms as well as for C atoms in the graphene sheet. The kinetic energy cutoffs for wavefunction and charge density used are 40 Ry and 320 Ry (360 Ry for calculations on Ni(111) surface) with scalar-relativistic ultrasoft pseudopotentials and 40 Ry and 420 Ry with fully-relativistic ultrasoft pseudopotentials.

We have used Hubbard U correction which accounts for the on-site Coulomb interaction in *d* orbitals of Co adatom using the implementation of M. Cococcioni and S. Gironcoli as discussed in chapter 2.[57] The value of U for Co in the three different systems has been determined using equation 2.28. The corresponding interacting and non-interacting responses of Co-*d* occupations as a function of the perturbing potential ( $\alpha$ ) are shown in figure 5.1. The determined values of U to be applied on the Co-*d* states are 6.14 eV, 4.46 eV and 5.19 eV for Co-SVG, Co-SVBG and Co-SVNG, respectively.

We have modeled the single vacancy in freestanding graphene and graphene supported on Ni(111) surface in a  $6 \times 6$  hexagonal supercell of graphene ( $|\mathbf{a}| = |\mathbf{b}| = 14.77 \text{ \AA}$ ) and Ni(111)



( $|\mathbf{a}|=|\mathbf{b}|=14.95\text{\AA}$ ), respectively, by removing a single C atom from the graphene sheet. The Ni(111) slab is modelled by taking four Ni(111) layers out of which the bottom two layers are fixed at the bulk interplanar distance of around  $2.03\text{\AA}$ . A vacuum of around  $15\text{\AA}$  thick is introduced along the normal to the plane of the surface in order to minimize the spurious interaction between the periodic images. The Brillouin zone integrations are carried out with a  $9 \times 9 \times 1$  ( $54 \times 54 \times 1$ ) unshifted Monkhorst-Pack k-point mesh [71] for a  $6 \times 6$  ( $1 \times 1$ ) supercell (unit cell) of freestanding graphene while  $3 \times 3 \times 1$  ( $18 \times 18 \times 1$ ) for structures on Ni(111) surface. For faster convergence of electronic iterations we have used Marzari-Vanderbilt smearing [72] of width  $0.005\text{ Ry}$  for both, structures in freestanding as well as structures supported on Ni(111) surface. When the structures are supported on Ni(111) surface we have used semiempirical dispersion correction to include van der Waals interaction [95, 96], known to be vital for Ni(111)/graphene interface [47], which otherwise is missing within the GGA formalism.

For comparing stability of structures we have computed the following quantities:

1. Formation energy of vacancy ( $E_f$ )

$$E_f = E_D + N_C \times \mu_C + N_X \times \mu_X - E_{Gr} \quad (5.1)$$

where,  $E_D$  and  $E_{Gr}$  are the total energies of graphene sheet (either freestanding or supported on Ni(111)) with and without defect, respectively, in the same supercell size.  $N_C$  is the number of missing C atom in the graphene sheet and  $\mu_C$  is chemical potential of C which is determined as:  $\mu_C = \frac{E_{Gr}}{N}$ , where  $N$  is number of C atoms in the cell which is 72 in our study.  $N_X$  is the number of atoms of other elements which replace C atoms around the vacancy, like N and B atoms in our study.  $\mu_X$  is the chemical potential of  $X$ , where  $X$  is N or B.  $\mu_N = \frac{E_{N_2}}{2}$ , where  $E_{N_2}$  is total energy of gas phase nitrogen molecule.  $\mu_B = \frac{E_B}{N_B}$ , where  $E_B$  is the total energy of bulk boron and  $N_B$  is the number of B atoms in the unit cell of bulk boron.

2. Binding energy of graphene with vacancy on Ni(111) surface ( $E_b$ )

$$E_b = \frac{E_D^s - E'_D - E^s}{A} \quad (5.2)$$

where,  $E_D^s$ ,  $E'_D$  and  $E^s$  are total energies of graphene sheet with single vacancy supported on Ni(111) surface, freestanding graphene sheet with single vacancy in the supercell of Ni(111) surface and the Ni(111) surface, respectively.  $A$  is the area of the supercell.

3. Binding energy of Co adatom ( $E_b^{Co}$ )

$$E_b^{Co} = E_{D-Co} - E_D - E_{Co} \quad (5.3)$$

where,  $E_{D-Co}$ ,  $E_D$  and  $E_{Co}$  are the total energies of graphene sheet with vacancy-Co adatom complex structures, graphene sheet with just the vacancy and the isolated Co atom, respectively, where the graphene sheet is either freestanding or supported on Ni(111) surface.

Further the magnetic anisotropy energy is calculated using the following equation:

$$MAE = E_X^{FR} - E_Z^{FR} \quad (5.4)$$

where,  $E^{FR}$  denotes the total energy obtained from fully relativistic calculations when the magnetization orientation is fixed to X (along zigzag direction) and Z (perpendicular to the surface of graphene) axes. For Co-SVG we have determined  $E^{FR}$  by fixing the magnetization orientation along another in-plane axis, Y (along armchair direction), and found that MAE differs by 0.003 meV from the MAE calculated using X as the in-plane direction. The calculated MAEs for the systems studied in this chapter are larger by atleast an order of magnitude and so in all cases we have calculated MAE using only one in-plane direction, X. The relaxed geometries from the scalar relativistic calculations are used in these fully relativistic calculations. In order to check whether geometry optimization with fully relativistic potentials causes any changes in the calculated values of MAE we have relaxed the geometry for Co-SVG in fully relativistic regime when the magnetization orientation was fixed along X and Z axes. We found that MAEs calculated without and with geometry optimization in fully relativistic regime differs by 0.001 meV which is again smaller by atleast an order of magnitude of MAEs of all systems studied in the present study. In systems with the vacancy-Co complexes supported on Ni(111) surface we have used fully relativistic pseudopotentials only for atoms in the graphene sheet and Co adatom while for Ni atoms we have used scalar relativistic pseudopotentials. This is because Ni atoms are coordinated with atoms in all the three dimensions which will result in weaker orbital moment and hence a weaker spin-orbit coupling. Convergence of fully relativistic calculation along with Hubbard U correction is computationally very expensive. Thus the total energy convergence in fully relativistic calculations is relaxed from  $10^{-4}$  meV (during geometry optimization with scalar relativistic pseudopotential) to  $10^{-2}$  meV for the SCF calculations with relativistic pseudopotentials. We note that except for the freestanding Co-SVG, all the other structures show MAEs that are of the order of meV. For freestanding Co-SVG the total energy convergence is made stricter by one order of magnitude ( $10^{-3}$

meV). Therefore, this gives us confidence that the computed values of MAEs reported in this chapter are significantly larger than the error bars of our calculations and hence trustworthy.

## 5.3 Results and discussions

### 5.3.1 Single C vacancy in freestanding graphene and graphene supported on Ni(111) surface

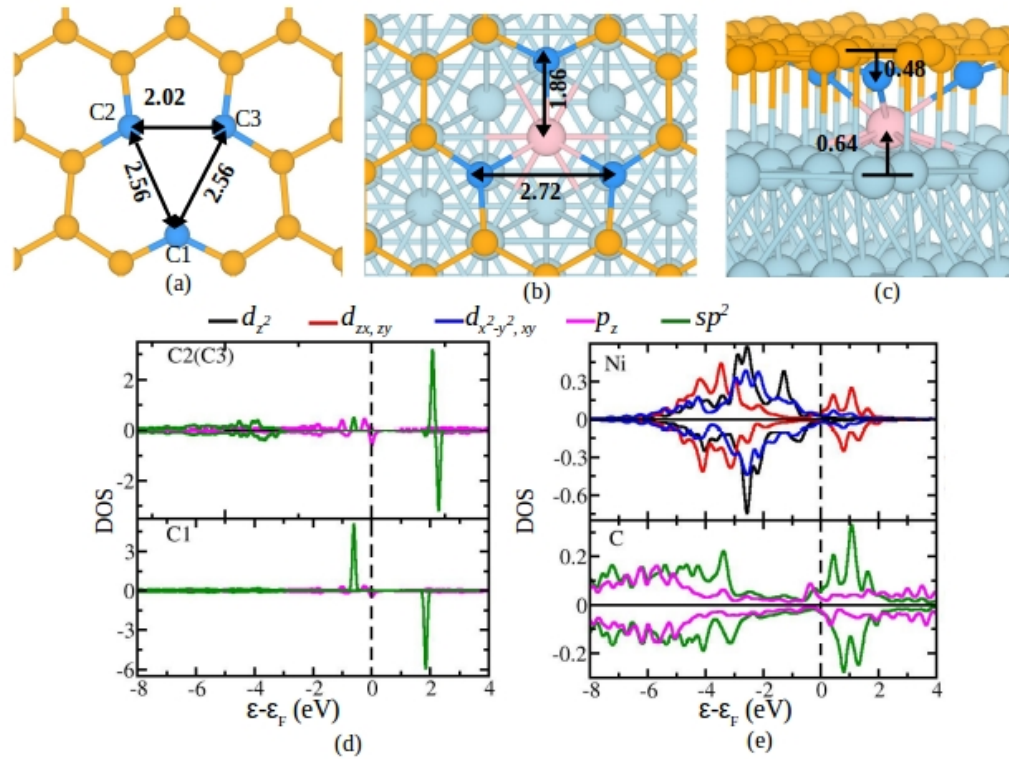


FIGURE 5.2: Structure of a single C vacancy in (a) freestanding graphene (SVG) and (b, c) graphene with single vacancy supported on Ni(111) surface (Ni/SVG). (b) and (c) shows top-view and side-view of Ni/SVG, respectively. Golden and pale blue colored atoms denote C and Ni atoms, respectively. The C atoms around the vacancy and the displaced Ni atom below the vacancy are marked differently with blue and pink color, respectively. (d) and (e) show projected density of states (PDOS), projected on the atomic orbitals of the C atoms and Ni atom at the vacancy site in SVG and Ni/SVG, respectively. The states are shifted with respect to Fermi energy.

Creation of a single vacancy in freestanding graphene (SVG) leads to dangling bonds on the three carbon atoms surrounding the vacancy (highlighted in blue in figure 5.2(a)), which destabilises the graphene lattice. For reducing this instability the graphene sheet undergoes Jahn-Teller distortion where two of the carbon atoms (marked as C2 and C3 in figure 5.2 (a)) surrounding the vacancy move closer and form a weak bond. The third

carbon atom (marked as C1 in figure 5.2 (a)) is however left alone with a dangling bond. Within a  $6 \times 6$  supercell of graphene we find that the bond length between C2 and C3 is about 2.02 Å and that between C1 and C2 (or C1 and C3) is elongated to 2.56 Å. Unlike few reports, we find the graphene sheet is planar with no out-of-plane displacement of C1. [124, 125] We have checked the planarity of the graphene sheet with single vacancy by performing geometry optimization by initially displacing C1 in the out-of-plane direction. We find that for these cases, after geometry optimization, C1 comes back in the plane of the graphene sheet. The formation energy of a SV in freestanding graphene is found to be around 7.66 eV. The structure and formation energy obtained from our calculations agree with the earlier reports where the level of DFT calculations used is similar to that used in our calculations. [124], [126], [127] However, A. Robertson *et al.* [128] could visualise both, reconstructed as well as unreconstructed, single vacancy in the graphene sheet from their HR-TEM studies. They explained this observation as a possibility that the captured unreconstructed image is actually the reconstructed vacancy image which is oscillating between the three stable structures of reconstructed vacancy where bond formation between any two C atoms is possible. Similar observation and explanation is also reported by A. El-Barbary *et al.* [125].

In addition to the structural changes, the presence of C-vacancy also alters the electronic properties of the graphene sheet. We find that the dangling bond on C1 in freestanding SVG give rise to magnetic moment of  $0.96 \mu_B$  on C1 while the weak bond between the other two C atoms quenches the magnetic moment to  $0.12 \mu_B$  on each of the two atoms which amounts to the total magnetisation of around  $1.63 \mu_B/\text{cell}$ . In figure 5.2(d) we have plotted the density of states projected on to C- $p_z$  and C- $sp^2$  states for the three C atoms surrounding the single vacancy. The DOS of C- $sp^2$  is sum of the DOS of C- $p_x$ , C- $p_y$  and C- $s$ . The formation of vacancy breaks the  $\pi$ -network of graphene locally, which destroys the Dirac cone such that  $p_z$  of all three carbon atoms at the Fermi energy contribute to the DOS. Additionally in the spin-up channel we find C- $sp^2$  state of C1 localised around -0.70 eV while the corresponding spin down state is unoccupied. This is consistent with the Löwdin charge analysis, which suggested the magnetic moment on C1 to be close to  $1 \mu_B$ . The  $sp^2$  characteristic of C2 and C3 is lost due to the reconstruction where they form a 5-membered ring through a weak bond. These electronic and magnetic properties of SV in freestanding graphene match well with the literature reports. [123, 126, 128, 129]

Further single C vacancy in the graphene sheet on Ni(111) surface in top-fcc configuration can either be created at fcc site or at top site. Consistent with previous reports [123] we find that structure with the C vacancy at the top site is more stable by about 2.76 eV. Figure 5.2 (b) and (c) shows the top and side view of the structure of single C vacancy at the top site in graphene on Ni(111) surface. We observe that the Jahn-Teller

distortion is lifted such that the three C atoms around the vacancy form an equilateral triangle. In this structure the three C atoms surrounding the vacancy are at the fcc sites. To stabilise the dangling bonds at the carbon atoms around the vacancy, the Ni atom, placed right below the vacancy site, moves 0.64 Å away from the Ni surface and towards the graphene sheet. Simultaneously, the C atoms around the vacancy are also observed to move down from the plane of the graphene sheet by around 0.48 Å. This results in the formation of Ni-C bonds with bond lengths of around 1.86 Å. We note that away from the vacancy Ni-C bond length is maintained to be around 2.10 Å as seen for defect-free graphene sheet placed over Ni(111) surface. The interaction of displaced Ni atom with the three C atoms surrounding the vacancy stabilises graphene sheet. The formation energy computed for SVG on Ni(111) surface is around 2.89 eV. We note that the formation energy is much lower than that of freestanding graphene sheet (7.66 eV). This suggests that it is more convenient to form a single vacancy when graphene is supported on Ni(111) surface. Moreover, we find that the binding energy of SVG on Ni(111) of about -0.09 eV/Å<sup>2</sup> is stronger than that of the pristine graphene on Ni(111) surface by -0.08 eV/Å<sup>2</sup>.

The three C atoms at the vacancy show similar PDOS when graphene is placed on Ni(111). We observe stronger interaction of C-*sp*<sup>2</sup> state with *d*<sub>zx,zy</sub> states of displaced Ni at vacancy than of C-*p*<sub>z</sub>, which give rise to hybridized states between -2 eV to -4.5 eV and between 0 eV to 2 eV in both the spin channels. Hybridization between other Ni-*d* orbitals are relatively weak. Due to the strong interaction we find that the magnetic moment on displaced Ni atom is completely quenched and that on the C atoms at the vacancy are around 0.03 μ<sub>B</sub>. However, away from the vacancy the magnetic moment on surface Ni atoms and on C atoms are maintained to the values observed when defect-free graphene is placed over Ni(111) surface which are around 0.55 μ<sub>B</sub> on Ni, 0.03 μ<sub>B</sub> on C at fcc site and -0.02 μ<sub>B</sub> on C at top site. [47, 130]

### 5.3.2 B-decorated and N-decorated single vacancy in freestanding graphene and graphene supported on Ni(111) surface

TABLE 5.1: Formation energy of single C vacancy in graphene ( $E_f$ ) and binding energy of graphene with vacancy on Ni(111) surface ( $E_b$ ).  $V_{top/fcc}$  stands for vacancy at the top/fcc site.

System	SVG	SVNG	SVBG	Ni/SVG		Ni/SVNG		Ni/SVBG	
				$V_{top}$	$V_{fcc}$	$V_{top}$	$V_{fcc}$	$V_{top}$	$V_{fcc}$
$E_f$ (eV)	7.66	3.64	4.45	2.89	5.65	2.59	2.21	-0.82	0.54
$E_b$ (eV/Å <sup>2</sup> )	-	-	-	-0.088	-0.074	-0.067	-0.069	-0.088	-0.081

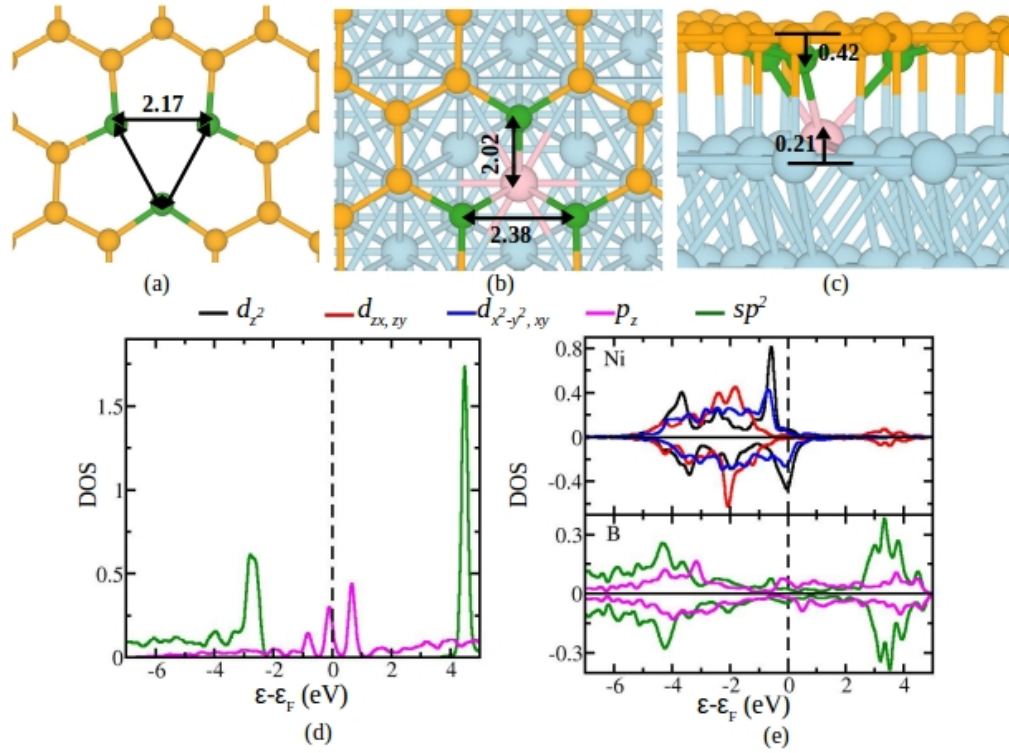


FIGURE 5.3: Structure of (a) freestanding graphene with B-decorated single vacancy (SVBG). (b, c) top-view and side-view of B-decorated single vacancy in graphene supported on Ni(111) surface (Ni/SVBG). Golden and pale blue colored atoms denote C and Ni atoms, respectively. The B atoms around the vacancy and the displaced Ni atom below the vacancy are denoted with green and pink color, respectively. (d) and (e) show PDOS of states of atoms at the vacancy site in SVBG and Ni/SVBG, respectively. The states are shifted with respect to Fermi energy.

The substitution of B and N around the vacancy removes the dangling bonds and increases the stability of the vacancy structure. Table 5.1 notes the formation energies and binding energies of graphene sheet with different single C vacancy. The formation energy of freestanding B-decorated single vacancy graphene (SVBG) is 4.45 eV which is lower by 3.21 eV than that of freestanding SVG. The Jahn-Teller distortion is lifted in freestanding SVBG such that the three B atoms at the vacancy forms an equilateral triangle with B-B distances of 2.17 Å, which is similar to that observed in the first principles study by X. Zhang *et al.* [121].

On Ni(111), similar to SVG on Ni(111) surface, we find that single C vacancy decorated by B atom is more stable at top site than at fcc site by around 1.36 eV. The formation energy is found to further decreases to -0.82 eV when SVBG is placed on Ni(111) surface with vacancy at the top site. The three B atoms are placed at the fcc site such that the B-B distances are around 2.38 Å. Similar to SVG on Ni(111) the top Ni atom at the vacancy is pulled up by the B atoms. However, the out-of-plane displacement of the top

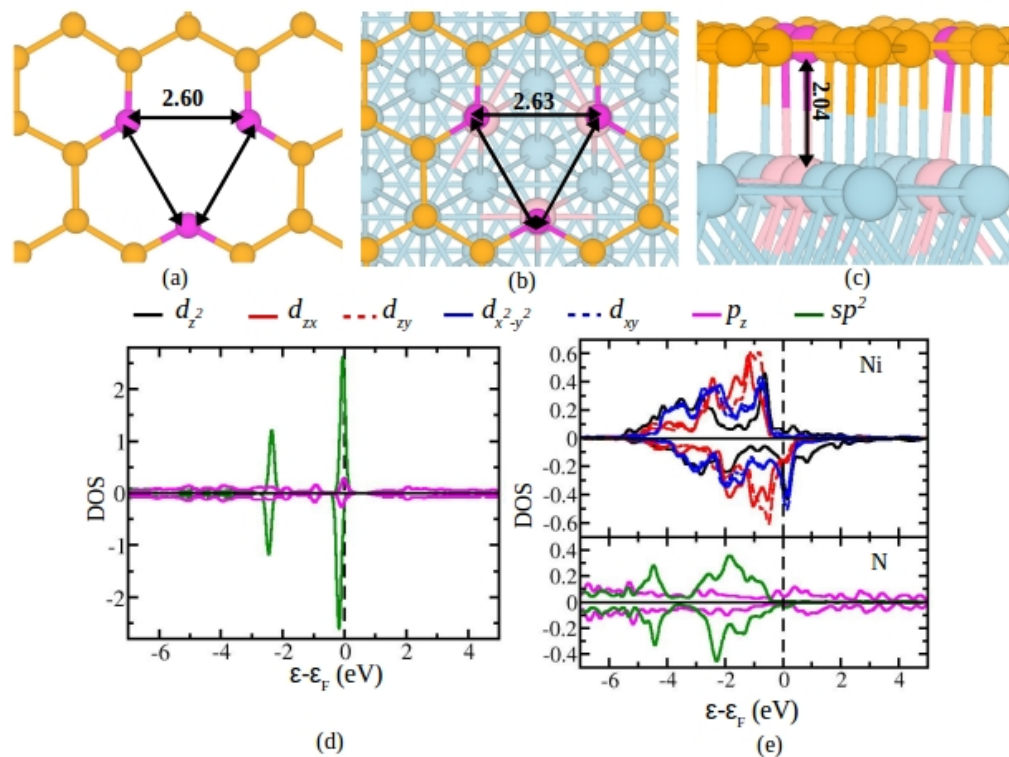


FIGURE 5.4: Structure of (a) freestanding graphene with N-decorated single vacancy (SVNG). (b, c) top-view and side-view of N-decorated single vacancy in graphene supported on Ni(111) surface (Ni/SVNG) after removing C atom from fcc site. Golden and pale blue colored atoms denote C and Ni atoms, respectively. The N atoms around the vacancy and surface Ni atoms that interact with N atoms are denoted with magenta and pink color, respectively. (d) and (e) show PDOS of states of atoms at the vacancy site in SVNG and Ni/SVNG. The states are shifted with respect to Fermi energy.

Ni atom is smaller ( $0.21 \text{ \AA}$ ) than in SVG on Ni(111) ( $0.64 \text{ \AA}$ ). The Ni-B bond length is around  $2.02 \text{ \AA}$ . The B atoms also move down towards the top Ni atom by about  $0.42 \text{ \AA}$ . The resulting binding energy of SVBG on Ni(111) surface is calculated to be  $-0.09 \text{ eV/\AA}^2$  atom which is equal to the binding energy of SVG on Ni(111) surface. J. Gerbhardt *et al.* [131] have reported results on B-doped graphene sheet on Ni(111) obtained using XPS and ARPES along with DFT calculations. However B-doping at single vacancy in graphene supported on Ni(111) by far our knowledge has not been reported.

Doping of N in graphene lattice can lead to different N-doped structures, namely structures with i) pyridinic N, ii) pyrrolic N and iii) graphitic N. However, only pyrrolic and pyridinic structures are possible at the single C vacancy in graphene. In this study we have considered only pyridinic N which from first principles calculation is found to be more stable. [122] The three pyridinic N atoms surrounding the vacancy also forms an equilateral triangle, as shown in figure 5.4(a), with the N-N distances of about  $2.60 \text{ \AA}$ . Substitution of N reduces the formation energy to  $3.64 \text{ eV}$  in freestanding SVNG from

7.66 eV in freestanding SVG. On Ni(111) surface, we observe that unlike for SVG and SVBG, SVNG is more stable when vacancy is formed at the fcc site than at top site by 0.38 eV. We find that the formation energy of SVNG reduces to 2.21 eV, when placed on Ni(111) surface with vacancy at fcc site. G. Carraro *et al.* [132] and R. Koch *et al.* [133] have synthesised N-doped graphene on Ni(111) where the N atoms are present in pyridinic form.  $N^{2+}$  are bombarded on graphene supported on Ni(111) followed by annealing. Annealing at higher temperatures are avoided so as to obtain major concentration of pyridinic N. In ref. [133] authors have synthesised N-doped graphene by using pyridine precursors during CVD growth of graphene on Ni(111) surface. The authors saw signatures of graphitic as well as pyridinic N in their samples. Thus pyridinic N in graphene supported on Ni(111) surface are stable. Figure 5.4(b) and (c) shows the structure of SVNG on Ni(111) surface with vacancy at fcc site and N atoms at the top sites. The N-N distances are found to be equal and slightly increased to 2.63 Å with respect to that in freestanding SVNG (2.60Å). The pyridinic N atoms surrounding the single vacancy binds to the surface Ni atoms with a bond length of around 2.04 Å. The N atoms do not shift downwards like the C and B atoms surrounding the single vacancy in SVG and SVBG on Ni(111), respectively. Moreover the surface Ni atom interacting with the N atoms also does not shifts towards the graphene sheet like in SVG on Ni(111) and SVBG on Ni(111). The binding energy of SVN on Ni(111) surface is found to be around  $-0.07 \text{ eV}/\text{Å}^2$  which is weaker than that of SVG and SVB on Ni(111) surface.

After discussing similarities and difference between the geometries of undecorated structure and decorated structures, we now compare their electronic properties. Figure 5.3(d) and 5.4 (d) shows DOS plots for  $sp^2$  and  $p_z$  of B and N in freestanding SVBG and freestanding SVNG, respectively. As compared to the  $sp^2$  hybridized state in SVG we find that in SVBG the  $sp^2$  hybridised state is more unoccupied while in SVNG the  $sp^2$  hybridized states is almost completely occupied. Hence this is consistent with our earlier assertion that the decoration with B and N atoms around vacancy removes the  $sp^2$  dangling state that is created due to the missing C atom. The small shift between the N states in spin-up and spin-down channels correspond to the small magnetic moment on N atoms of around  $0.07 \mu_B/\text{atom}$ . In ref [121] the authors have reported SVNG to be non-magnetic however, in ref. [122] the authors similarly find that SVNG shows weak magnetic behaviour. The total magnetisation of around  $0.46 \mu_B/\text{cell}$  reported in ref [122] is close with the value obtained from our calculations ( $0.4 \mu_B/\text{cell}$ ). The authors in ref [122] attribute this small but finite magnetism to the non-zero overlap of N wavefunction. B- $p_z$  and N- $p_z$  in SVBG and SVNG, respectively, are seen to be delocalised around the Fermi energy like C- $p_z$  in SVG.

The delocalisation of  $p_z$  states of B and N in SVBG and SVNG, respectively, is retained even on Ni(111) surface. Similar behaviour is also observed for C- $p_z$  in SVG on Ni(111).



In SVBG on Ni(111) the void created by the missing C atom is smaller than that in SVG on Ni(111). Thus we find B- $sp^2$  interacts not only with Ni- $d_{zx,zy}$  but also with Ni- $d_{z^2}$  states of the displaced surface Ni atom. The interaction with Ni(111) induces small magnetic moment of about  $0.01 \mu_B/B$  atoms at the single vacancy. However the magnetic moment on the surface Ni atom which interacts with the vacancy decreases to  $0.22 \mu_B$  from  $0.56 \mu_B$  which is the magnetic moment on the Ni atoms elsewhere on the top layer of Ni(111) surface. In SVNG on Ni(111) surface the hybridization of N- $sp^2$  is observed with  $d_{zx,zy}$  as well as  $d_{z^2}$  states of surface Ni atoms. Ni-N interaction results in slight enhanced magnetic moment on each of the three surface Ni atoms of around  $0.66 \mu_B$  than  $0.56 \mu_B$  on rest of the surface Ni atoms. The magnetic moments on N atoms are almost completely quenched.

### 5.3.3 Co adsorption at undecorated single vacancy in freestanding graphene and graphene supported on Ni(111) surface

Addition of Co adatom into the system increases computational complexity which arises due to the strong correlation between Co- $d$  electrons. In order to handle well the strongly correlated Co- $d$  electrons we have included Hubbard U parameter in our calculations, which corresponds to the onsite-Coulomb interaction, as also mentioned earlier in section 5.2. Adsorption of Co adatom at the undecorated single vacancy in freestanding graphene sheet breaks the weaker C-C bond formed due to the Jahn-Teller distortion resulting in a  $C_{3v}$  symmetry with each of the Co-C bond length to be around  $1.76 \text{ \AA}$ . The atomic radius of Co atom is much larger than that of C atom. Thus a single carbon vacancy cannot accommodate the Co adatom within the lattice of graphene. Hence, Co adatom stays elevated to a distance of around  $0.89 \text{ \AA}$  above the three C atoms surrounding the vacancy. The three C atoms at the vacancy are also elevated with respect to the C atom away from the vacancy by around  $0.44 \text{ \AA}$  (fig.5.5 (a) and (b)). Hence elevation of Co with respect to C atoms away from vacancy site is around  $1.33 \text{ \AA}$ . The three C-C distances between the surrounding C atoms to the Co adatom are about  $2.63 \text{ \AA}$ . The binding energy of Co adatom to the graphene sheet at the single vacancy is computed to be around  $-4.67 \text{ eV}$  which is much stronger than the binding energy of Co on pristine graphene sheet. [116],[134]. This suggests stronger interaction of Co with C atoms around the single C vacancy than interaction of Co adsorbed away from the vacancy in the graphene sheet. This is consistent with the assertion that the vacancy in the graphene sheet acts as a trapping center for the metal adatoms. Next we have discussed the density of states of Co-SVG which elucidates this strong interaction.

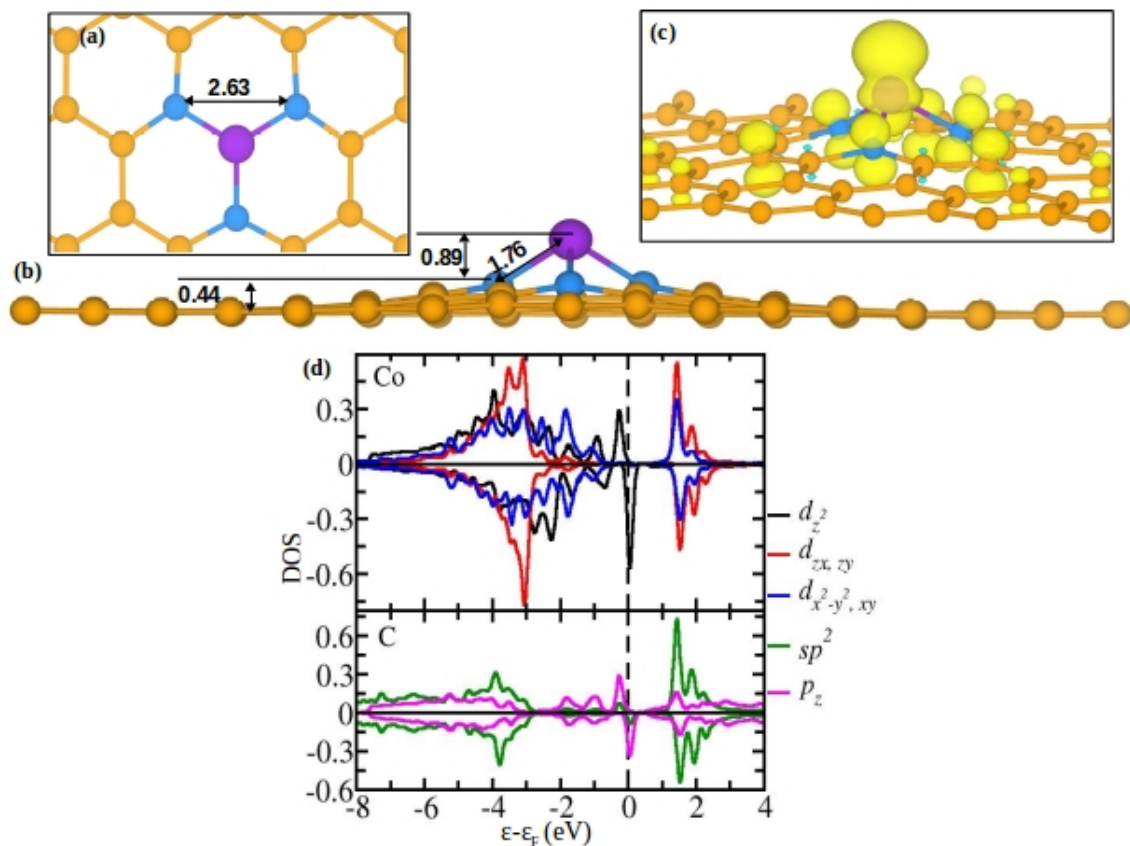


FIGURE 5.5: (a) Top-view and (b) side-view of single vacancy-Co complex in freestanding graphene sheet. C and Co atoms are denoted with golden and purple color while the C atoms around the vacancy are highlighted with blue color. The distance mentioned in the figures are in Å. (c) shows the magnetization density plot in which the yellow and cyan colored surfaces denote spin-up and spin-down magnetic moment, respectively. (d) DOS plots for Co (top panel) and C (bottom panel) states. The dashed vertical line represents Fermi energy.

The  $C_{3V}$  symmetry with principle axis passing through Co adatom is reflected in the DOS plot Co-SVG where we find degeneracy between i) Co- $d_{zx}$ , and Co- $d_{zy}$  and ii) Co- $d_{x^2-y^2}$  and Co- $d_{xy}$ . Due to elevation of Co adatom in Co-SVG the interaction of C- $p_z$  states of C at the single vacancy with Co- $d_{z^2}$  is much stronger than that with other Co- $d$  orbital. We observe overlap of Co- $d_{z^2}$  states with C- $p_z$  state between the energy range of -2 to 0 eV. Below -3 eV we notice weak interaction of Co- $d_{zx,zy}$  and Co- $d_{x^2-y^2,xy}$  with C- $sp^2$  states. The stronger hybridization with the C- $p_z$  results in stronger exchange splitting in Co- $d_{z^2}$  compared to that in other Co- $d$  orbitals. Thus magnetic moment on Co has larger contribution from Co- $d_{z^2}$  which can also be seen from the magnetization plot shown in figure 5.5(c). The magnetization density plot also shows wide spread of magnetization in the graphene lattice which amounts to about  $0.94 \mu_B/6 \times 6$  supercell. However we note that the magnetic moment on Co is highly quenched to around 0.26

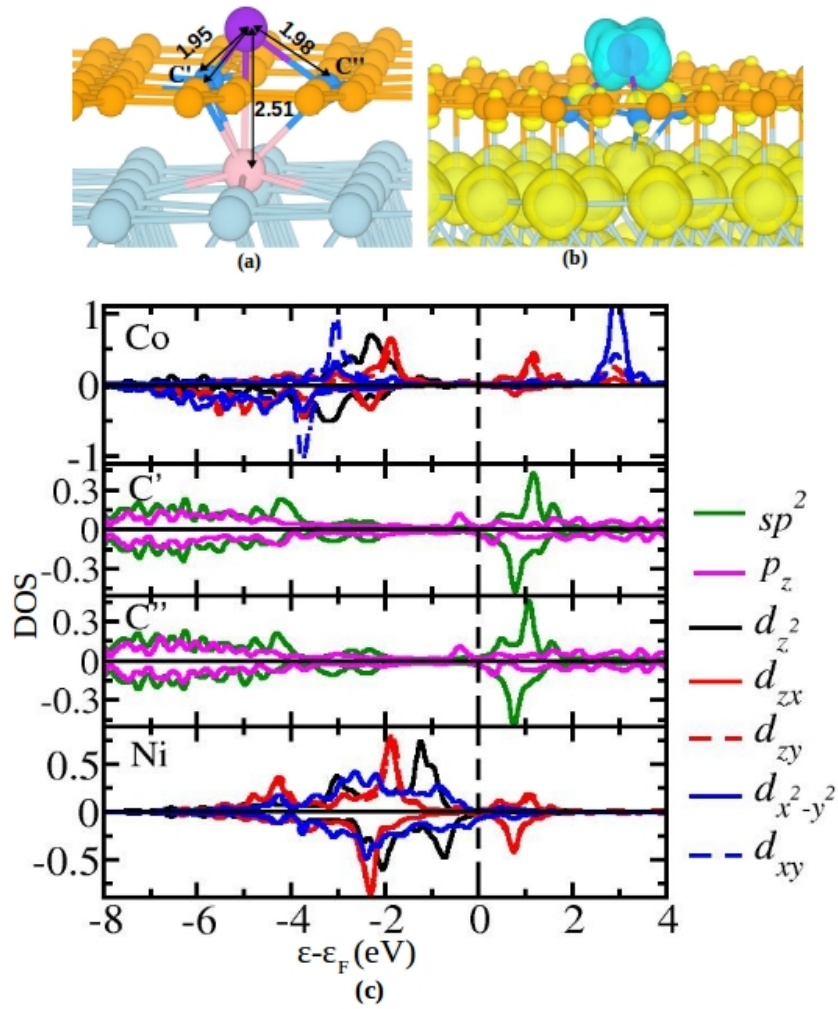


FIGURE 5.6: (a) Side-view geometry of Ni/Co-SVG. The distance marked are in Å. C atoms away from vacancy, C atoms surrounding vacancy, Ni and Co atoms are denoted with golden, blue, pale blue and purple colored spheres. (b) Magnetization density plot with yellow and cyan colored isosurface representing spin-up and spin-down magnetic moment. The isovalue is 0.02 (No. of electron)/(bohr<sup>3</sup>). (c) Density of states for Co (top panel), C atoms around the vacancy (middle panel) and Ni atom below the vacancy (bottom panel). The vertical dotted line represents Fermi energy.

$\mu_B$  compared to the magnetic moment on Co in isolated Co atom ( $3 \mu_B$ ). Our results are consistent with those in ref. [135].

On Ni(111) surface, Co adatom is found more stable at the single C vacancy at top site than at fcc site by 0.65 eV. The vacancy in graphene at top-site exposes a surface Ni atom. We thus observe significant interaction between the adsorbed Co adatom at the vacancy and the exposed surface Ni atom. From our GGA+U calculations we find that the Ni-Co bond length is around 2.51 Å which is elongated with respect to the Ni-Co bond length in Ni-Co dimer in its free state (2.07 Å). The structure of the vacancy-Co adatom complex in graphene supported on Ni(111) surface is shown in figure 5.6 (a).

The Co adatom is slightly shifted away from the center of the vacancy site leading to small difference in Co-C bond lengths. Two of the three Co-C bond lengths are 1.95 Å while the third is around 1.98 Å. These bond lengths are larger than 1.76 Å found in the freestanding structure. Therefore, the binding energy of Co in Co-SVG supported on Ni(111) (Ni/Co-SVG) of around -2.80 eV, is weaker than in freestanding condition (-4.67 eV).

Further in the DOS plot we observe that all Co-*d* states are non-degenerate (figure 5.6(c)). The in-plane Co-*d* states (Co- $d_{x^2-y^2}$  and Co- $d_{xy}$ ) shows largest crystal field splitting in comparison with the out-of-plane Co-*d* states (Co- $d_{zx}$  and Co- $d_{zy}$ ). Moreover, large exchange splitting in Co- $d_{x^2-y^2}$  majorily contributes to the enhanced magnetic moment on Co, around 1.35  $\mu_B$ , which is significantly larger with respect to that on Co in freestanding structure (0.26  $\mu_B$ ). The magnetization density plot obtained from our calculation is shown in figure 5.6 (b). The magnetic moment on Ni atom interacting with the Co adatom is about 0.22  $\mu_B$ . Within GGA+U formalism we find that the magnetic moment on Co prefers to stay antiferromagnetically coupled with that of Ni(111) substrate. Moreover, we find that even the initial ferromagnetic configuration changes to antiferromagnetic configuration after relaxation. The coupling between Co adatom on pristine graphene sheet and ferromagnetic Ni(111) substrate is also found to be antiferromagnetic.[130]

### 5.3.4 Co adsorption at B-decorated and N-decorated single vacancy in freestanding graphene and graphene supported on Ni(111) surface

The absence of dangling bonds at the vacancy decorated with N and B results in weaker binding energy of Co at the single vacancy in freestanding graphene. Co at N-decorated single vacancy (Co-SVNG) shows binding energy of around -3.84 eV while at B-decorated single vacancy (Co-SVBG) the binding energy is still weaker, around -1.90 eV. The elevation of Co increases from 1.33 Å in Co-SVG to 1.78 Å in Co-SVNG (figure 5.7 (b)) to 1.89 Å in Co-SVBG (figure 5.8(b)), which is consistent with the decrease in binding energy in the same order.

From the DOS plots we notice that in Co-SVNG (figure 5.7(d)) and Co-SVBG (figure 5.8(d)) the interaction primarily takes place between the out-of-plane Co-*d* states, Co- $d_{zx,zy}$  and Co- $d_{z^2}$ , with N- $sp^2$  and B- $sp^2$  states, respectively. The DOS plots and magnetization density plots in figures 5.7(c) and 5.8 (c), suggests that in Co-SVNG the exchange splitting in Co- $d_{zx,zy}$  and in Co-SVBG the exchange splitting in Co- $d_{z^2}$  and Co- $d_{x^2-y^2,xy}$  contributes majorily to the magnetic moment on Co, respectively. The

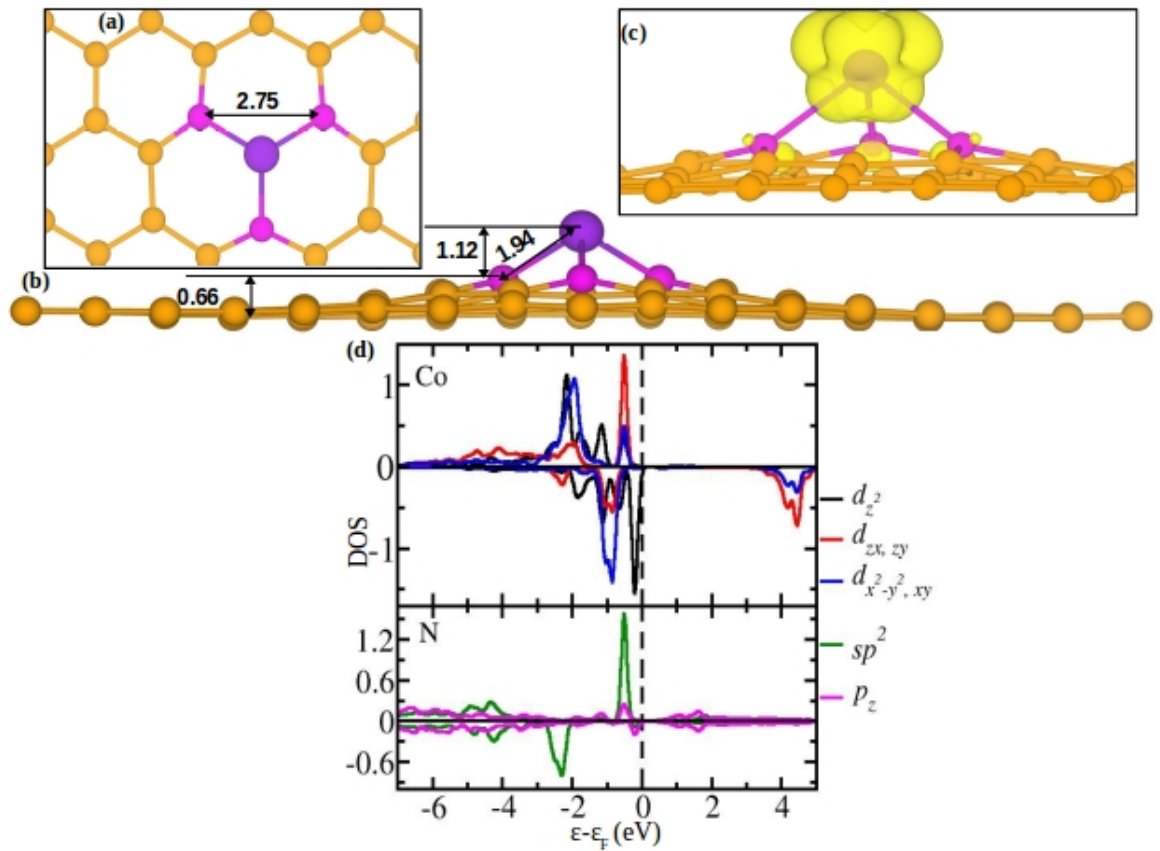


FIGURE 5.7: (a) Top-view and (b) side-view of single vacancy-Co complex with N-decoration in freestanding graphene sheet. C, N and Co atoms are denoted with golden, magenta and purple color. The distance mentioned in the figures are in Å. (c) shows the magnetization density plot in which the yellow and cyan colored surfaces denote spin-up and spin-down magnetic moment, respectively. (d) DOS plots for Co (top panel) and N (bottom panel) states. The dashed vertical line represents Fermi energy.

magnetic moment on Co in Co-SVNG is around  $1.85 \mu_B$  while in Co-SVBG is around  $0.99 \mu_B$ . Thus we note that N-decoration and B-decoration increases magnetic moment on Co at single vacancy in graphene. Moreover, we notice different magnetization features in all three vacancy-adatom structures. In Co-SVG the magnetization spreads away from the vacancy while in Co-SVNG it is localised around the vacancy site. In Co-SVBG the magnetic moment on Co shows antiferromagnetic coupling with the small magnetic moment on B atoms ( $0.06 \mu_B$ / B atom).

Similar to Ni/Co-SVG, in Ni/Co-SVNG as well as in Ni/Co-SVBG we find that the Co adatom prefers to bind with N-decorated and B-decorated single C vacancy at top site than fcc site by 0.84 eV and 1.04 eV, respectively. In Ni/Co-SVNG we observe that the vacancy-Co complex (Co adatom along with N atoms) moves away from the Ni(111) surface such that Ni-Co distance is around 3.71 Å (figure 5.9 (a)). The binding energy of Co is determined to be around -1.92 eV. Hence, the interaction of Co with N atoms

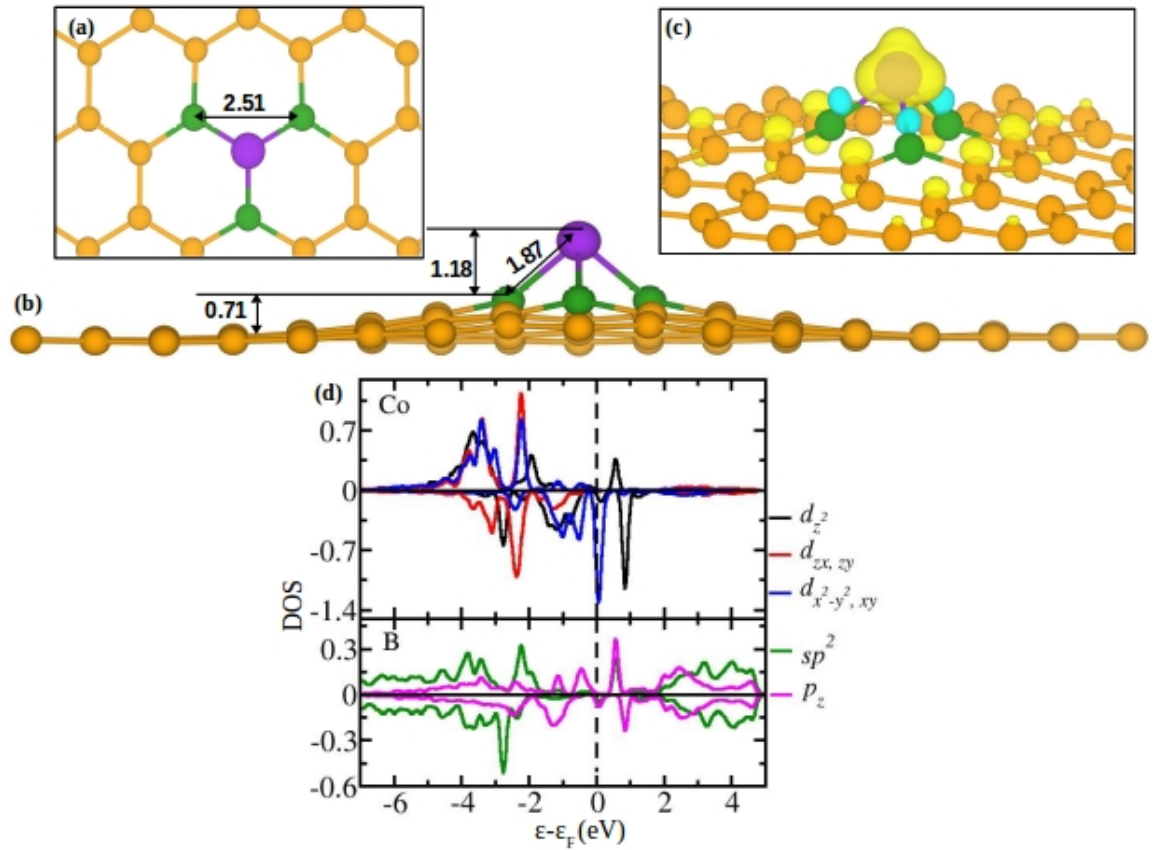


FIGURE 5.8: (a) Top-view and (b) side-view of single vacancy-Co complex with B-decoration in freestanding graphene sheet. C, B and Co atoms are denoted with golden, green and purple color. The distance mentioned in the figures are in Å. (c) shows the magnetization density plot in which the yellow and cyan colored surfaces denote spin-up and spin-down magnetic moment, respectively. (d) DOS plots for Co (top panel) and B (bottom panel) states. The dashed vertical line represents Fermi energy.

in Ni/Co-SVNG, shown in figure 5.9 (c), is similar to that in freestanding Co-SVNG (figure 5.7(d)) except that the peaks for Ni/Co-SVNG are broadened with respect to Co-SVNG. As a result, the magnetic moment on Co in Ni/Co-SVNG ( $1.86 \mu_B$ ) is also close to that obtained in freestanding Co-SVNG ( $1.85 \mu_B$ ). The magnetic moment on Ni atom below the vacancy reduces to around  $0.77 \mu_B$  from  $0.91 \mu_B$  before adsorption of Co. In Ni/Co-SVBG Co adatom is relatively closer to the Ni(111) surface such that the Ni-Co distance is around  $2.88 \text{ \AA}$ , which is however elongated with respect to the Ni-Co distance in Ni/Co-SVG. The binding energy of Co in Ni/Co-SVBG is around  $-3.07 \text{ eV}$ . We note that in DOS for Ni/Co-SVBG, Co- $d_z^2$  is unoccupied in minority spin channel, as shown in figure 5.10 (c). The in-plane states (Co- $d_{x^2-y^2,xy}$ ) are quite localised which suggests negligible interaction with B or surface Ni atoms. These interactions results in magnetic moment of  $1.33 \mu_B$  on Co adatom. The magnetic on Ni atom below the vacancy is around  $0.19 \mu_B$  which is close to that obtained in Ni/SVBG ( $0.22 \mu_B$ ).

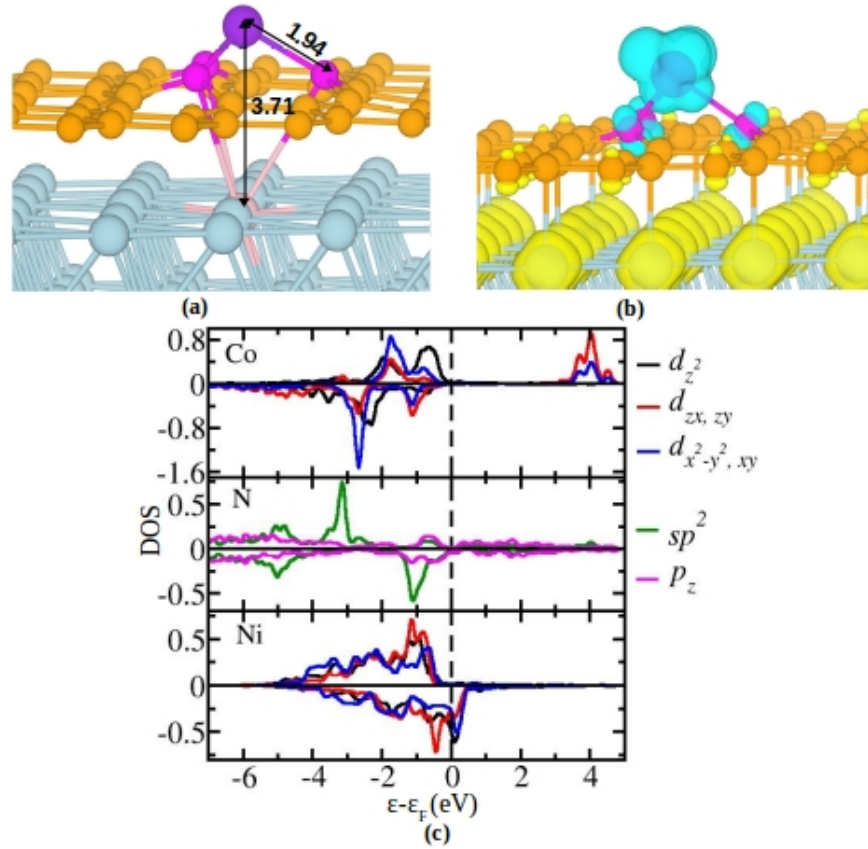


FIGURE 5.9: (a) Side-view geometry of Ni/Co-SVNG. The distance marked are in Å. C, N, Ni and Co atoms are denoted with golden, magenta, pale blue and purple colored spheres. (b) Magnetization density plot with yellow and cyan colored isosurface representing spin-up and spin-down magnetic moment. The isovalue is 0.02 (No. of electron)/(bohr<sup>3</sup>). (c) Density of states for Co (top panel), N atom (middle panel) and Ni atom below the vacancy (bottom panel). The vertical dotted line represents Fermi energy.

The antiferromagnetic coupling between Co adatom and Ni(111) surface observed in Ni/Co-SVG is retained in both, Ni/Co-SVNG and Ni/Co-SVBG. We could stabilize the geometry with ferromagnetic coupling in both the doped structures. However, we find that for Ni/Co-SVBG and Ni/Co-SVNG the ferromagnetic geometry is higher by 93 meV and 13 meV than the antiferromagnetic geometry, respectively.

### 5.3.5 Magnetic anisotropy energy of different vacancy-Co adatom structures

As discussed in the introduction, the aim of studying such vacancy-adatom complex structures is to understand their application in magnetic storage devices. Therefore understanding structural stability and magnetic moments on Co adatom in different

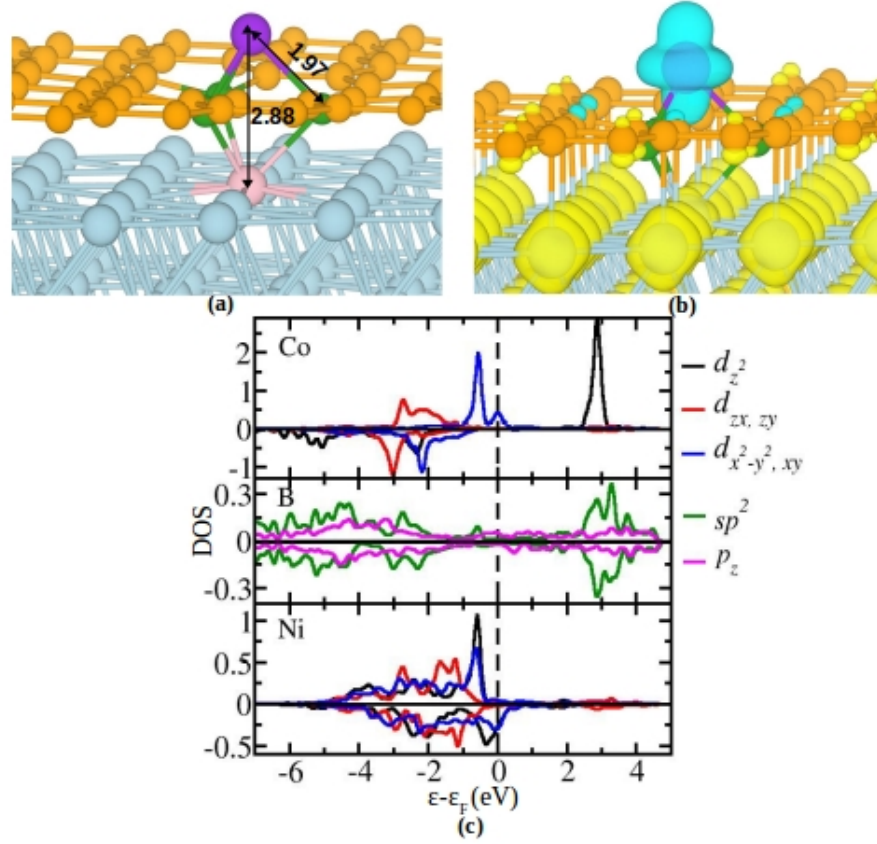


FIGURE 5.10: (a) Side-view geometry of Ni/Co-SVBG. The distance marked are in Å. C, B, Ni and Co atoms are denoted with golden, green, pale blue and purple colored spheres. (b) Magnetization density plot with yellow and cyan colored isosurface representing spin-up and spin-down magnetic moment. The isovalue is 0.02 (No. of electron)/(bohr<sup>3</sup>). (c) Density of states for Co (top panel), N atom (middle panel) and Ni atom below the vacancy (bottom panel). The vertical dotted line represents Fermi energy.

TABLE 5.2: Magnetic anisotropy energies (MAE) along easy axis of magnetization are listed for Co-vacancy complexes in freestanding graphene and graphene supported on Ni(111) surface.

System	MAE (meV)	Easy axis of magnetization
Co-SVG	0.03	Z
Co-SVNG	-1.49	X
Co-SVBG	-3.80	X
Ni/Co-SVG	39.73	Z
Ni/Co-SVNG	40.03	Z
Ni/Co-SVBG	42.30	Z



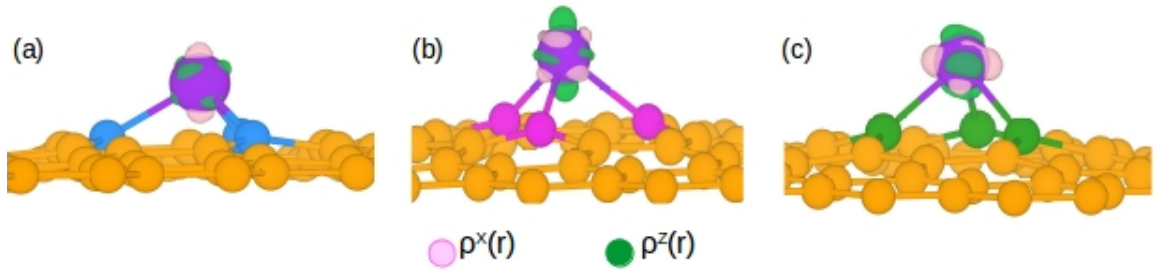


FIGURE 5.11: Isosurface showing difference between charge density when the magnetization axis is along X and Z direction for (a) Co-SVG, (b) Co-SVNG and (c) Co-SVBG, respectively. The isovalues are  $1 \times 10^{-5}$ ,  $1.5 \times 10^{-4}$  and  $1.5 \times 10^{-3}$  (No. of electrons/bohr<sup>3</sup>), respectively for Co-SVG, Co-SVNG and Co-SVBG.

structures is not enough. We should also have notion regarding the strength of the magnetic moment which can be obtained from magnetic anisotropy energy (MAE). The origin of magnetic anisotropy in a lower dimensional system is attributed to the in-plane and out-of-plane asymmetries. These asymmetries give rise to orbital moment anisotropy which account for magnetic anisotropy.[113] The orbital moment shows the following inverse dependence on the ligand field strength: The orbital moment of the in-plane (out-of-plane) orbitals will be relatively quenched if these orbitals are involved more in hybridization with ligands compared to the out-of-plane (in-plane) orbitals. Since the moment due to the orbit of electrons is generated in the perpendicular direction, we will obtain a net in-plane (out-of-plane) orbital moment. If the spin-orbit coupling is strong then the coupling between the spin angular momentum and orbital angular momentum will decide the stable orientation of the magnetization vector. Thus enhancement in MAE corresponds to (i) stronger spin-orbit coupling, (ii) large orbital moment and (iii) strong ligand field strength.[112]

The MAE and the easy axis of magnetization obtained using full relativistic pseudopotentials along with Hubbard U corrections are listed in table 5.2 for the three Co-graphene defect complexes in freestanding graphene and graphene supported on Ni(111) surface. The weaker magnetic moment on Co in Co-SVG shows a weak MAE of around 0.03 meV while in Co-SVNG and Co-SVBG the MAE is improved to 1.49 meV and 3.80 meV, respectively. Thus N and B decoration not only enhances the magnetic moment on Co adatom but also significantly strengthens the magnetization. Additionally we note two interesting observations: (i) For both, N and B decoration the easy magnetization axis is in-plane while in Co-SVG the easy magnetization axis is along the perpendicular axis and (ii) for all the complexes when supported on Ni(111) shows large enhanced MAE of around 40 meV with easy axis of magnetization along the perpendicular direction. Below we have tried to address these two intriguing observations.

To understand the change in the easy axis of magnetization upon N and B decoration in freestanding complexes we have plotted the difference of charge density when the magnetization axis is along X-direction (in-plane) and Z-direction (perpendicular). The charge density difference is shown in figure 5.11 for the three freestanding single vacancy structures. The green (pink) isosurface denotes excess charge when the magnetization axis is along Z (X) direction. The transformation of a vector along Z direction to a vector along X direction occurs by rotation around Y axis. In Co-SVG, we see that the excess charge is present along the XZ and YZ plane when magnetization is set along Z direction. Therefore in Co-SVG we see that the excess charge present along the XZ and YZ plane when the magnetization is set along Z axis (figure 5.11 (a)) accumulates along Z direction when magnetization axis is rotated parallel to X direction. Congruently we observe in Co-SVNG and Co-SVBG. The excess charge in Co-SVNG (Co-SVBG) is accumulated along Z direction, XZ and XY planes when the magnetization axis is fixed along Z axis and in XZ plane ( $X^2-Y^2$  and YZ planes) when the magnetization axis is along X direction. Thus consistently in all three plots we observe that when magnetization is along the hard axis (X for Co-SVG and Z for Co-SVNG and Co-SVBG) accumulation of excess charge takes place along Z direction where the effect of ligands is greater on Co due to its elevated above the graphene sheet. While when the magnetization is along the easy axis the excess charge is distributed away from Z direction so as to reduce the effect of the ligand field.

Out of the three factors which contribute in large MAE, spin-orbit coupling (SOC) is same in all system studied in this chapter as it depends only on the atomic species. The varying factors as we move from freestanding complex to a complex supported on Ni(111) surface is the ligand field which inturn modifies the orbital moment on Co atom. Therefore to account for of the large enhancement in MAE of the Co adatom complexes when supported on Ni(111) surface we have tried to estimate the orbital moment on the Co adatom when in freestanding complex and when in the complex supported on Ni(111). In freestanding Co-SVG the interaction of Co-*d* states are strong with the states of neighbouring C atom, as shown in figure 5.5(c). In figure 5.12(a) we have shown ILDOS for freestanding Co-SVG where the energy axis in the DOS plot is divided into three regions: (i) from -0.5 eV to Fermi energy is marked as region E1 within which Co- $d_{z^2}$  states are dominant, (ii) from -2.0 eV to -0.5 eV is marked as region E2, where in-plane degenerate states (Co- $d_{xy}$  and Co- $d_{x^2-y^2}$ ) are seen to contribute more and (iii) from -5.0 eV to -2.0 eV is marked as region E3 which consists of all Co-*d* states but the degenerate out-of-plane states (Co- $d_{xz}$  and Co- $d_{yz}$ ) show dominant contribution. In the ILDOS corresponding to all three energy regions show notable hybridization with the states of neighbouring C atoms. Hence we expect that the orbital moment along both,

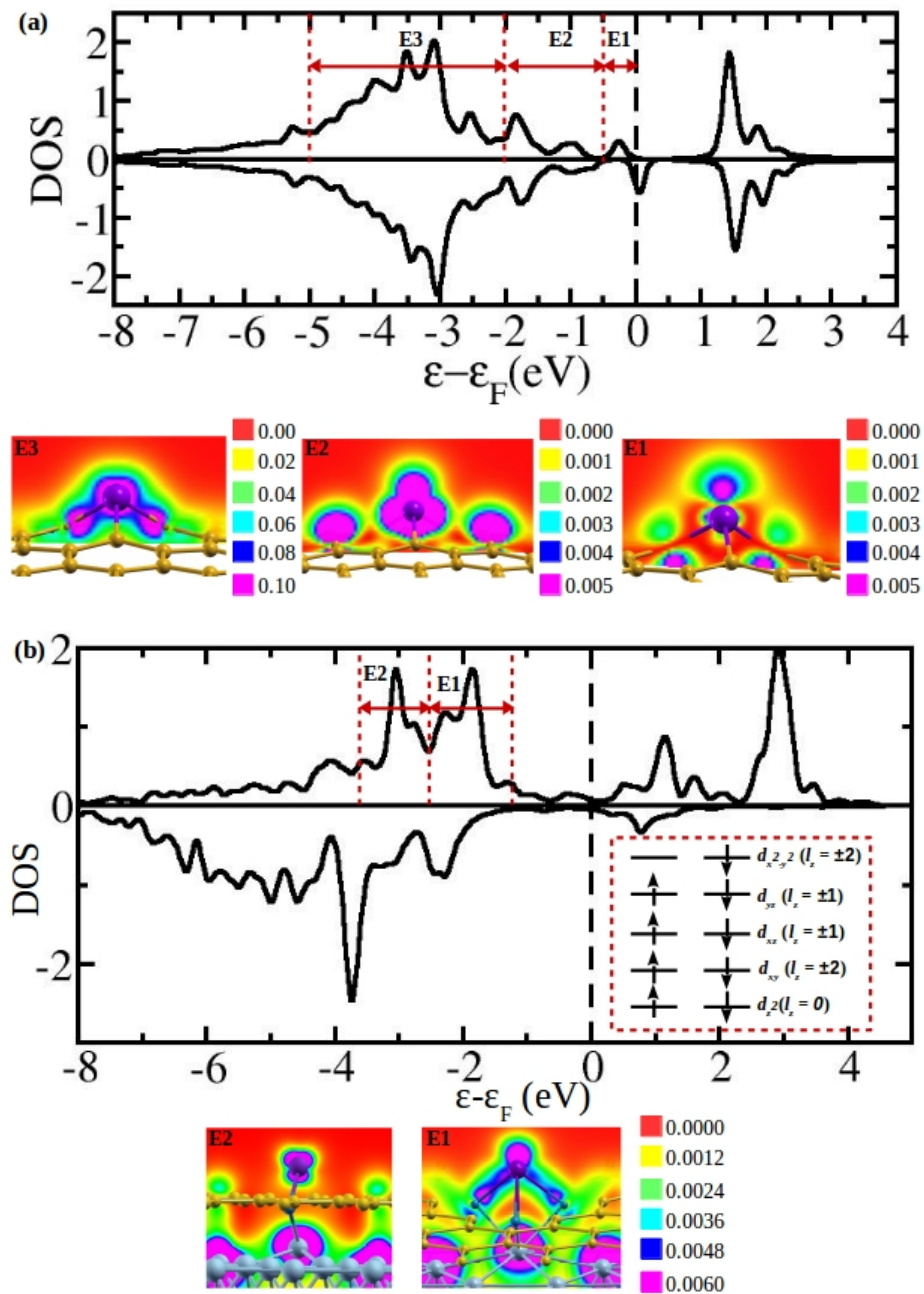


FIGURE 5.12: Total DOS of Co- $d$  in (a) Co-SVG and (b) Ni/Co-SVG. The bottom panel showing contour plots in each figure are ILDOS corresponding to the energy ranges marked as ‘E1’ and ‘E2’ and ‘E3’. In (b) the red dotted inset box at the right corner contains energy level diagram.

in-plane as well as out-of-plane, direction are highly quenched which results in small anisotropy in orbital moment and hence a small value of MAE.

From the DOS plot of Ni(111)/Co-SVG in figure 5.6(c) we have noted that unlike in

freestanding Co-SVG, all Co- $d$  states are non-degenerate due to the asymmetric geometry around Co adatom. Additionally, we observe that Co- $d_z^2$  is now completely occupied in both the spin channels and is shifted well below the Fermi energy. Another striking observation is that the majority spin channel (spin-down) is completely filled while in the minority spin channel (spin-up channel) we see that Co- $d_{x^2-y^2}$  is mostly unoccupied. This give rise to enhanced magnetic moment on Co. For the estimation of orbital moment we have only consider the minority spin-channel since the filled spin-down states result in zero orbital moment. We observe from the DOS shown in figure 5.6 (c) that Co- $d_{xz}$  and Co- $d_{zy}$  are mostly occupied. However these out-of-plane  $d$  states of Co adatom are seen to be involved more in the hybridization with C- $p$  than other  $d$  states. To clearly understand the involvement of Co- $d$  states in the hybridization we have plotted integrated local density of states (ILDOS) by dividing the energy axis into two parts, as shown in figure 5.12 (b): (i) From -2.5 eV to -1.0 eV is defined as region E1 where the out-of-plane states are dominating and (ii) from -3.5 eV to -2.5 eV is defined as region E2 which majorily consists of in-plane states. In region E1 we find that the dominating out-of-plane states shows strong overlap with C- $p$ . While in region E2 the in-plane Co- $d$  states show minimal interaction with C states. Thus the orbit of electrons is more (less) restricted in the out-of-plane (in-plane) states which results in quenched (unquenched) orbital moment. As a consequence we expect that the orbital moment along the plane of graphene sheet should be much less than the orbital moment directed along the normal to the plane of the graphene sheet. Quantitatively speaking,  $l_z \rightarrow 2$  as Co- $d_{x^2-y^2}$  is mostly empty while Co- $d_{xy}$  and other Co- $d$  states are almost completely filled. This can be easily visualized from the energy level diagram shown in figure 5.12 (b). The energy level diagram is build without taking into account the exchange splitting. The exchange splitting in different Co- $d$  is different and hence the order of energy levels in both the spin channels are not consistent. Therefore for convenience, in the energy level diagram we chose the order of energy levels as in miniority spin channel while representing states in both the spin channels. Thus the orbital moment along the out-of-plane direction can be expected to have a value close to  $2 \mu_B$  while that along the in-plane direction to be close to zero. This large anisotropy in orbital moment of Co adatom in Ni(111)/Co-SVG give rise to a large value of MAE.

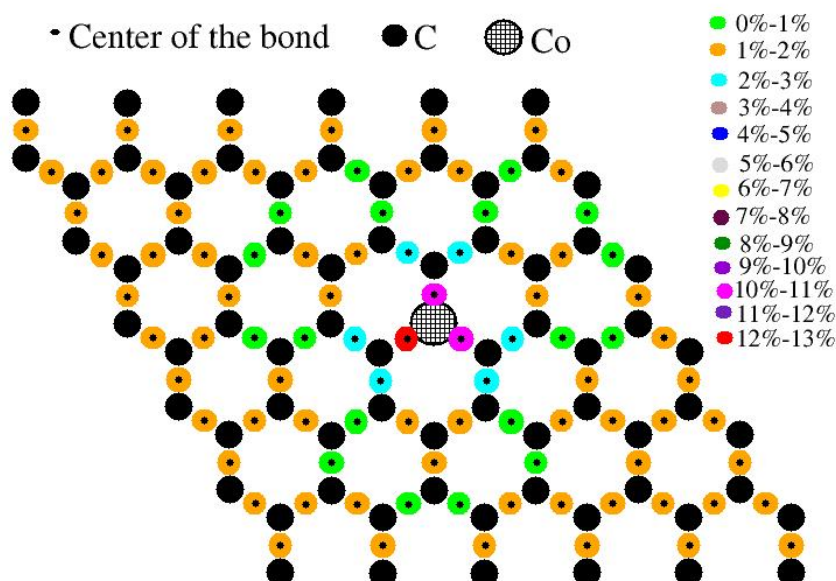


FIGURE 5.13: Color map of strain (in %) in bonds experienced by atoms in Co-SVG complex as it is placed on Ni(111) surface. The color codes for different amount of strain is displayed at the right-hand corner. The small filled black circle represents the center of the bond, the bigger filled black circle denote C atoms while the biggest circle filled with grid pattern denotes Co adatom.

The change in the ligand field and hence electronic structure of Co adatom that we observe in Co-SVG complex as it is placed on the Ni(111) surface is due to two factors. The first factor is change in the geometry of the complex. In figure 5.13 we have plotted the strain in the bond lengths when Co-SVG is placed on Ni(111) surface. As expected, minimum strain is experienced by those atoms which are away from the defect center while maximum strain is experienced by atoms in the closest vicinity of the defect. The least amount of strain is calculated to be around 0.62% while maximum strain is around 12.18%. The second factor is interaction of Co and C atoms surrounding the vacancy with surface Ni atom. To apprehend the effect of these two factors individually we have studied the electronic structure of (i) freestanding Co-SVG complex as it in the same geometry as on Ni(111) surface (Co-SVG $\rightarrow$ Ni(111)) and (ii) Co-SVG $\rightarrow$ Ni(111) with a Ni atom which is at the same position as the interacting surface Ni atom in Ni(111)/Co-SVG (Co-SVG-Ni). Not only the geometries of these two complexes are same as that of complex on Ni(111) surface but also the magnetic moment on Co are in close agreement.

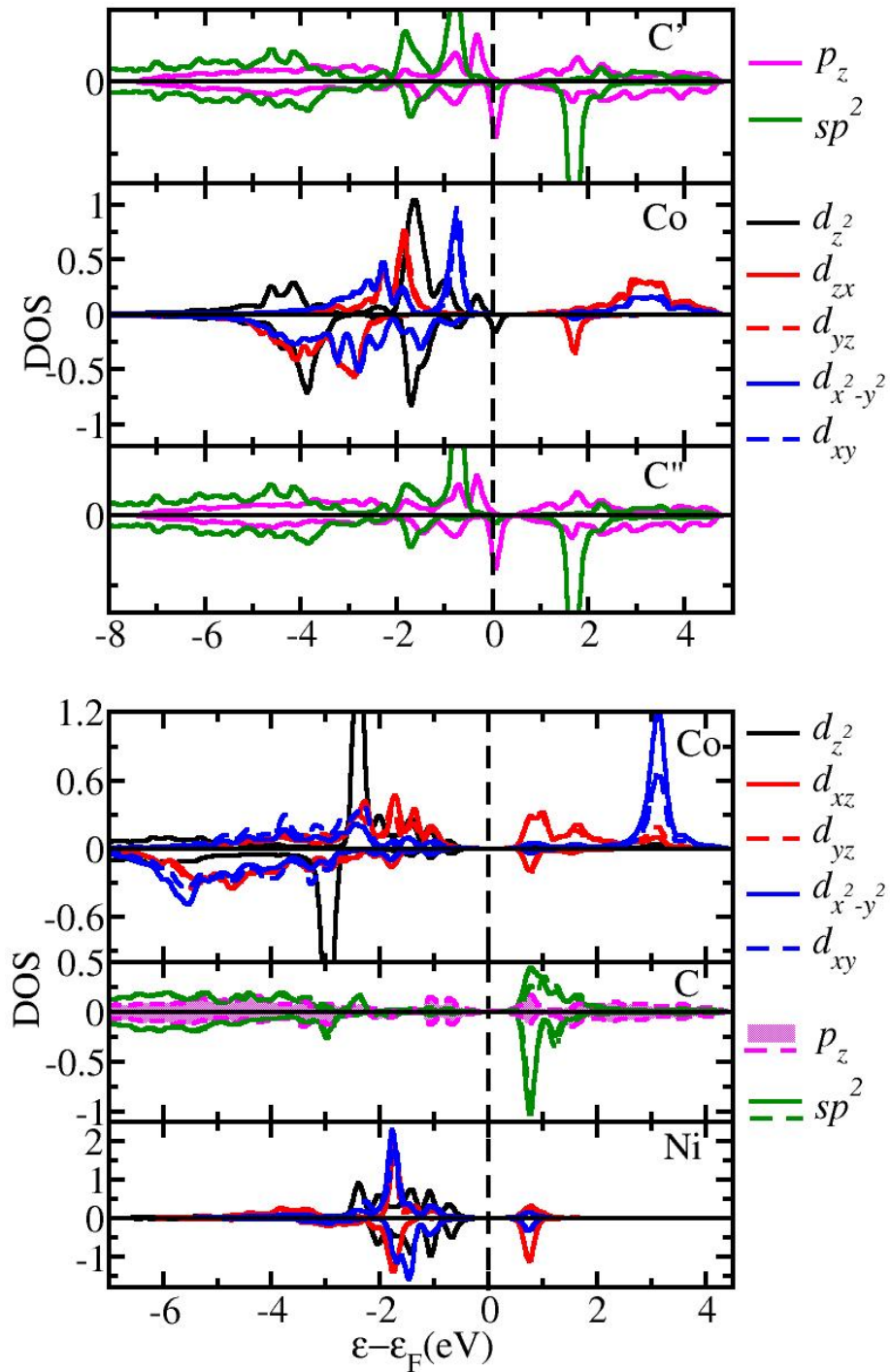


FIGURE 5.14: Density of states for (a)Co-SVG→Ni and (b)Co-SVG-Ni. In (a) top and bottom panel corresponds to C' atom (with shorter Co-C bond length) and C'' atom (with greater Co-C bond length), respectively and middle panel corresponds to Co. In (b) top and bottom panel corresponds to Co and Ni atoms while middle panel corresponds to C atoms. The magenta shaded region and bold green lines shows DOS of  $p_z$  and  $sp^2$  states of C' atom while the dotted line in magenta and green shows DOS of  $p_z$  and  $sp^2$  states of C'' atom. The vertical black dotted line represents Fermi energy.

The magnetic moment on Co in Co-SVG→Ni(111) is around  $1.24 \mu_B$  and that in Co-SVG-Ni is around  $1.49 \mu_B$  which are comparable to magnetic moment on Co of  $1.35 \mu_B$  in Ni(111)/Co-SVG. Furthermore similar to the orientations of magnetic moments in Ni(111)/Co-SVG we observe that in Co-SVG→Ni(111) the magnetic moment on Co is antiparallel with that on the neighbouring C atoms and in Co-SVG-Ni the magnetic moment on Co is antiparallel to that on Ni atom and neighbouring C atoms.

In figure 5.14 (a) and (b) we have shown DOS for Co-SVG→Ni(111) and Co-SVG-Ni, respectively. Similar to the DOS of Co- $d$  in Ni(111)/Co-SVG we observe that in both, Co-SVG→Ni(111) and Co-SVG-Ni, the  $d$  states in spin-down channel are almost completely occupied while there are unoccupied states in spin-up channel. Unlike in relaxed freestanding Co-SVG in Co-SVG→Ni(111) we observe that (i) Co- $d_{xz}$  and Co- $d_{yz}$  and (ii) Co- $d_{x^2-y^2}$  and Co- $d_{xy}$  states are non-degenerate, however we note that they are close in energy. The change in the geometry causes larger exchange splitting in  $d_{xz}$ ,  $d_{yz}$ ,  $d_{x^2-y^2}$  and  $d_{xy}$  states of Co in Co-SVG→Ni(111) than that observed in the relaxed structure of freestanding Co-SVG. The exchange splitting and interaction with C- $sp^2$  states results in partial occupation of Co- $d_{xz}$  and Co- $d_{yz}$  states.  $d_{x^2-y^2}$  and  $d_{xy}$  states of Co are seen to crowd more near the Fermi energy than in the relaxed freestanding Co-SVG. These in-plane  $d$  states (around -0.80 eV) are observed to interact with C- $sp^2$ . Though the DOS of Co- $d$  show significant changes as an effect of the change in the geometry, still there is enough hybridization between Co and graphene states to quench the orbital moment.

On adding a Ni atom in Co-SVG→Ni(111)(Co-SVG-Ni complex) we find that the C- $sp^2$  state at around -0.08 eV in Co-SVG→Ni(111) moves lower in energy to around -2.40 eV and interact with Ni- $d_z^2$ . Thus the interaction of Co- $d_{x^2-y^2}$  and Co- $d_{xy}$  with C- $sp^2$  are completely quenched. To minimize the energy, the non-interacting in-plane  $d$  states of Co in are exchange split such that  $d_{xy}$  is filled and shifts further below the Fermi energy while  $d_{x^2-y^2}$  is emptied and shifts above Fermi energy to around 3.0 eV.  $d_{xz}$  and  $d_{yz}$  states of Co interacts with C- $p_z$ . Thus Co- $d_{xz}$  and Co- $d_{yz}$  are filled more and are seen to move to lower energies with respect to those in Co-SVG→Ni(111). Hence we observe that the unoccupied states are primarily from Co- $d_{x^2-y^2}$ . As a consequence we

notice that the occupation of Co- $d$  states in Co-SVG-Ni are in close agreement to those obtained in Ni(111)/Co-SVG. Therefore we find that similar to Ni(111)/Co-SVG the orbital moment on Co atom in Co-SVG-Ni is close to  $2.0 \mu_B$ .

Thus from the above analysis is clear that the change in the electronic structure in Ni(111)/Co-SVG which leads to an enhanced orbital moment resulting in the huge increase in MAE is primarily due to the interaction of surface Ni atom with the vacancy-Co complex. Thus next we will discuss the possible reason or rather the role of Ni(111) surface for these changes in the electronic structure of Co adatom. Co in Co-SVG as well as in Ni(111)/Co-SVG is present in  $d^8$  configuration. In an ideal  $d^8$  configuration the  $d_z^2$  orbital is completely filled while one of the Co- $d_{xz}$  and Co- $d_{yz}$  is empty in the minority channel and one of the Co- $d_{x^2-y^2}$  and Co- $d_{xy}$  is empty in the minority channel. Thus the orbital moment in  $d^8$  configuration is  $3 m\mu_B$ . However, in Co-SVG due to the hybridization of with C- $p_z$  state we find all the Co- $d$  to be partially filled. In Ni(111)/Co-SVG the interaction of Co with C atoms is weakened due to the interaction of C atoms with surface Ni atoms. As a consequence, the hybridization between Co- $d_z^2$  and C- $p_z$  is highly quenched. Therefore Co- $d_z^2$  is occupied completely in Ni(111)/Co-SVG. Thus the electronic configuration of Co- $d$  state in Ni(111)/Co-SVG, filled  $d_z^2$  and large exchange split Co- $d_{x^2-y^2}$ , becomes almost similar to the ideal  $d^8$  configuration except for the filled  $d_{xz}$  and  $d_{yz}$  states which are actively involved in the hybridization. As a result the orbital moment is expected to be less than  $3m\mu_B$  but close to  $2 m\mu_B$  which is much greater than the negligible orbital moment in Co-SVG. Hence we find a large increase in MAE for the Co-SVG complex when supported on Ni(111) surface.

Similar investigations for decorated complexes, (Co-SVBG and Co-SVNG in freestanding condition and those supported on Ni(111) surface, are under progress and hence we have not reported those in the present chapter.

## 5.4 Summary

In this chapter we have presented detailed discussions regarding (i) underdecorated and decorated single vacancy in freestanding graphene and graphene supported on Ni(111)



surface and (ii) adsorption of magnetic adatom (Co) at these single vacancies in the graphene sheet. Consistent with previous studies we find that the stability of single vacancy in graphene sheet increases from undecorated structure to B-decorated structure to N-decorated structure. Therefore we find that the binding energy of Co adatom also decreases in the same order. Moreover we note that the magnetic moment on Co adatom again increases in the same order. However the MAE is largest for B-decorated vacancy-Co complex in freestanding graphene (3.89 meV) which has the easy axis of magnetization aligned in the in-plane direction. Further our calculation suggest that the binding of Co adatom becomes weaker for all the structures when the graphene sheet is supported on Ni(111) surface. Besides the trend of binding energy of Co also seen to change. For the supported structure the strongest binding energy of Co is obtained in Ni/Co-SVBG followed by Ni/Co-SVG and then Ni/Co-SVNG. Because of the asymmetric structure of Co-SVG on Ni(111) surface we feel that the binding energy of Co is obtained weaker than that in Ni/Co-SVBG. While weak binding energy of Co in Ni/Co-SVNG is expected due to greater elevation of Co adatom from the surface.

Further we note that the magnetic moment on Co adatom increases for undecorated structure when placed on Ni(111) surface from  $0.26 \mu_B$  in Co-SVG to  $1.35 \mu_B$  in Ni/Co-SVG. For B-decorated structure we find that the magnetic moment on Co shows a small increase from  $0.99 \mu_B$  in Co-SVBG to  $1.32 \mu_B$  in Ni/Co-SVBG. While for N-decorated structure the magnetic moment on Co is more or less the same in freestanding condition and when supported on Ni(111) surface. A more important effect of Ni(111) surface on the properties of vacancy-Co complexes is the large enhancement in MAE ( $\sim 40$  meV) with easy axis of magnetization aligned perpendicular to the surface. We attribute this large increase majorily to the anisotropy in orbital moment which presently is only discussed for the underdecorated systems. The increase in the anisotropy is the result of change in the ligand field which is caused due to change in the geometry of the complex and due to inclusion of additional interaction of Co and C atoms surrounding the vacancy with the surface Ni atoms. Comparing MAE of Co adsorbed on other metal surfaces like Pt(111), Pd(111) and Rh(111) surfaces we find that the MAE obtained in our system is higher by an order of magnitude. [115], [136] Additionally, in our system the surface around the Co adatom is flat and inert unlike the terminated transition metal surfaces.

Moreover, Co adatom is more stable at the vacancy than on pristine graphene sheet. Besides the presence of graphene, which shows weak spin-orbit coupling, also ensures efficient transportation of spin information over larger distance in the device. Our study thus highlights the vital role played by substrates in triggering and preserving useful properties of magnetic nanostructures from the point-of-view of magnetic storage device application.

# Effect of doping on the structure and electronic properties of GaSe(0001) surface

## 5.5 Introduction

The layered metal-chalcogenides (MC) have an inherent advantage over graphene in switching device applications. While chemical modifications are required to open bandgap in graphene, MCs are already semiconducting. As a consequence post-transition metal chalcogenides, III-VI semiconductors like GaSe, and transition metal dichalcogenides, like MoS<sub>2</sub>, attracted attention in the research and development of semiconducting devices. Moreover, upon doping with magnetic impurities these semiconducting materials form a new class of intriguing materials, two-dimensional dilute magnetic semiconductor (DMS).[137] Examples of typical DMS are transition metal doped II-VI compounds, such as GaAs, which are usually found in wurzite or zinc blende structures.[138] Studies including manipulation of spin in semiconducting material are more intriguing than in usual magnetic metals from the point-of-view of developing spintronic devices. This is because magnetism in doped semiconducting material is usually mediated by carriers. The magnetic coupling between the carriers and magnetic impurity can be easily altered under the influence of some external bias. Such easy control of the magnetism in conventional ferromagnetic metals is not possible. Carrier-induced ferromagnetism in Mn doped II-VI compounds hence initiated the thought of using DMS in non-volatile

memory devices with faster data processing and lower power consumption.[139, 140] Mn-doped II-VI compounds, especially GaAs, have been studied extensively which showcases interesting magneto-optical applications, like in spin-polarised light emitting diode. [141] However the device is realised to function only at low temperatures.

Studies of III-VI semiconductors have shown potentials in optoelectronic applications.[142] Their layered structure gives them additional variable characteristics such that their bandgaps are tuned by changing the number of layers.[143] Moreover, due to wide transparency range, GaSe attracted special attention. [144] GaSe is a layered material consisting of Se-Ga-Ga-Se sandwiches stacked along [0001] plane. In each sandwich Ga atom is covalently bonded with three Se atoms and one Ga atom thereby forming a tetrahedra with the Ga-Ga bond along the principal axis. The inter-sandwich interaction is van der Waals in nature. There are many possible ways for stacking the Se-Ga-Ga-Se sandwiches that result in several polytypes. Amongst these  $\epsilon$ -GaSe with 2H stacking sequence, reflected by two bilayer stacking periodicity and a hexagonal unit cell is the most common one (figure 5.15 (a) and (b)). [145, 146] This polytype lacks inversion symmetry. The layered structure makes GaSe highly cleavable and hence it shows weak mechanical properties such that the nonlinear optical properties shows notable variations from sample to sample making it difficult for device applications.[147, 148] It has however been proved that the structural strength of GaSe can be enhanced by doping with elements, like In, Ag,Te, without degrading its other properties.[147]-[149] Furthermore studies with magnetic impurities, like Mn, in III-VI have shown intriguing but complex magnetic properties which were not observed in doped II-VI compounds.[150, 151].

X-ray spectroscopy studies were performed to investigate the electronic properties of GaSe upon doping with magnetic (Mn) impurity. [2] XPS studies were performed by increasing the amount of deposited Mn atoms on the GaSe surface which suggested that initially at lower Mn coverage (less than 2 ML) a reacted interface is formed where Mn atom moves to the substitutional site rather than clustering on the surface. But what happens to the replaced Ga atoms is not clear from the experiments. Further at higher coverage of Mn (around 2.4 ML) agglomeration of Mn atoms starts on the surface which restricts further substitution of Ga atom. The substituted Mn atoms hybridises

with host atoms which is unlike Fe dopant in Fe-GaSe. But the negligible crystal-field splitting and +2 oxidation state of Mn, suggested from their XAS studies, implies weak hybridization between Mn-*d* and states of Ga and Se. Such behaviour of Mn is different from that in Mn-doped GaAs.

In order to understand these experimental observations it is imperative to have a microscopic understanding of how the Mn electronic states hybridizes with those of the host atoms. Further, in contrast with GaAs, in Mn-doped GaSe, there is a possibility of Mn ion to interact with both Se and Ga (due to layered structure). This might affect the mixing of the Mn electronic states with those of GaSe. To elucidate these aspects we have performed density functional theory calculations for Mn-doped GaSe(0001) surface.

The chapter is organised as follows: In Section 5.6 we have briefly discussed the computational methods used in our investigations and in Section 5.7 we have presented the results. In results we have first discussed the electronic properties of bulk GaSe and clean GaSe(0001) surface. Further in the subsequent subsections we have discussed structure, electronic and magnetic properties of Mn-doped GaSe(0001) surface and compared them with the experimental observations reported in Ref. [2]. In Section 5.8 we have summarised our results.

## 5.6 Computational details

We have performed spin polarized density functional theory (DFT) based calculations using the Quantum Espresso software [68] which is an implementation of the DFT in a plane wave pseudopotential framework. The electron-ion interactions were described using ultrasoft pseudopotentials. [69] We have used a kinetic energy cutoff of 35 Ry and 400 Ry for the wave function and charge density, respectively. The electron-electron exchange and correlation functional was described with the Perdew-Burke-Ernzerhof (PBE) parametrization of the generalized gradient approximation (GGA). [70] To speed up the convergence, we have used a Marzari-Vanderbilt smearing of 0.001 Ry. [72]

The Se-Ga-Ga-Se sandwiches interact through weak van der Waals dispersion. This interaction is not included in the conventional PBE exchange-correlation functional.

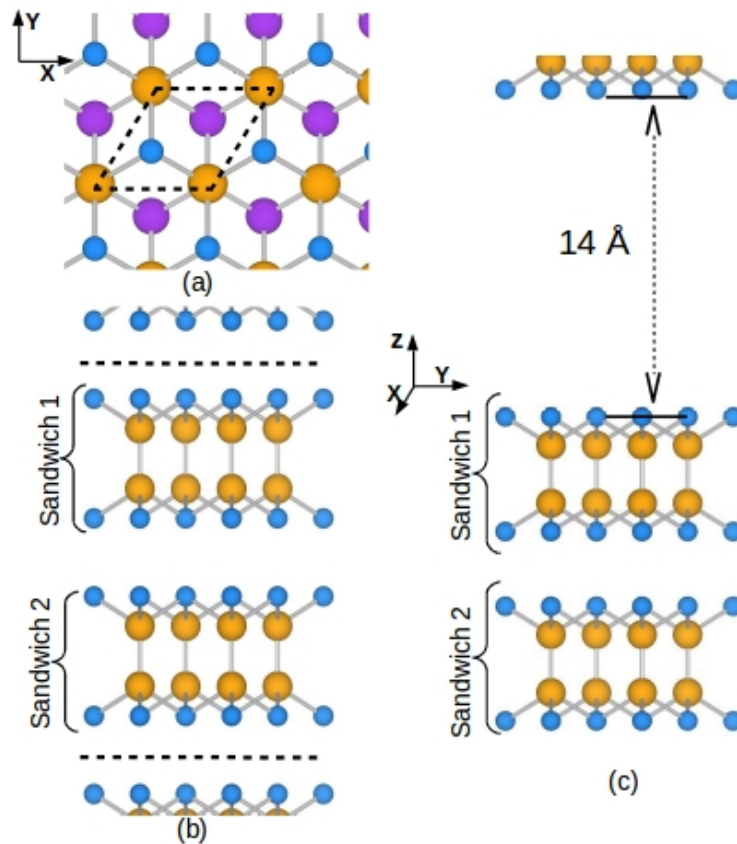


FIGURE 5.15: (a) Top and (b) side view of structure of bulk  $\epsilon$ -GaSe. The dashed parallelogram in (a) shows the unit cell of bulk  $\epsilon$ -GaSe. The dashed horizontal lines in (b) denote the periodically repeated unit along the  $z$  axis. The blue and orange spheres denote Se and Ga atoms, respectively. In (a) the purple spheres denotes Ga atoms from the bottom sandwich. (c) The slab model of GaSe(0001) surface.

Hence we have used an empirical van der Waals correction [95, 96] to the total energy. For the bulk structure Brillouin zone (BZ) integrations were done using a  $8 \times 8 \times 4$  shifted Monkhorst-Pack [71] k-point grid. Our calculations yield the bulk lattice parameters  $a$  and  $c$  of  $\epsilon$ -GaSe to be 3.74 and 15.88 Å, respectively. These are in excellent agreement with those reported in Ref. [145].

The (0001) surfaces are modeled using a slab where we have considered two sandwiches stacked along the (0001) direction and separated by vacuum along the (0001) direction (figure 5.15 (c)). Since the sandwiches interact through weak van der Waals interaction, when the (0001) surface is created through cleaving the crystal (as done in the experimental work reported in ref. [2]), the cleavage will take place in between two sandwiches, exposing the Se atoms to the surface. Therefore, in our model, the slab has

a Se-termination on both sides. This has an added computational advantage. Since we are using periodic boundary conditions in our calculations, there is spurious interaction between the slab and its periodic images, through the surface dipole. Having Se atoms on both the surfaces cancels this dipole and reduces the spurious interaction significantly. For our calculations we have used a vacuum of about 14 Å in the perpendicular direction to the surface. For the Mn-doped slabs, the symmetry of the surfaces on either side of the slab is broken. For these we incorporate a dipole correction to ensure that the electrostatic potential in the vacuum region is flat (for details refer figure 26 of Appendix 5.8). To study the effect of Mn doping in these systems, we have used a  $3 \times 3$  surface unit cell and put one Mn atom resulting in a doping concentration of about 5.5%, which is similar to the experimental doping concentrations at low doping in ref. [2]. The BZ integrations for the surface calculations were done using  $2 \times 2 \times 1$  shifted k-point grid.

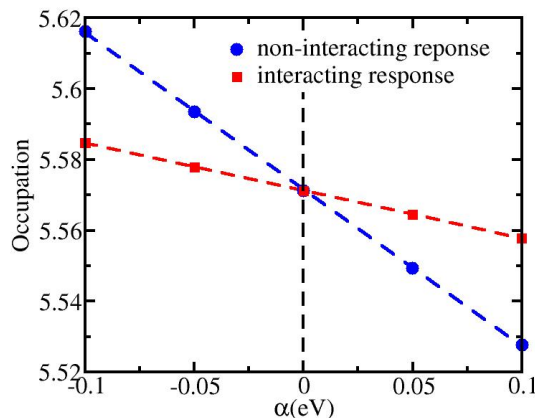


FIGURE 5.16: Linear response of Mn- $d$  occupation with respect to varying perturbing potential ( $\alpha$ )

To correctly account for the strong Coulomb and exchange interactions between the Mn- $d$  electrons we have used the DFT+U method as implemented by Cococcioni and Gironcoli. [57] The value of U for Mn is calculated to be around 5.84 eV using equation 2.28. The corresponding interacting and non-interacting responses of Mn- $d$  occupations to the perturbing potential ( $\alpha$ ) are shown in figure 5.16.

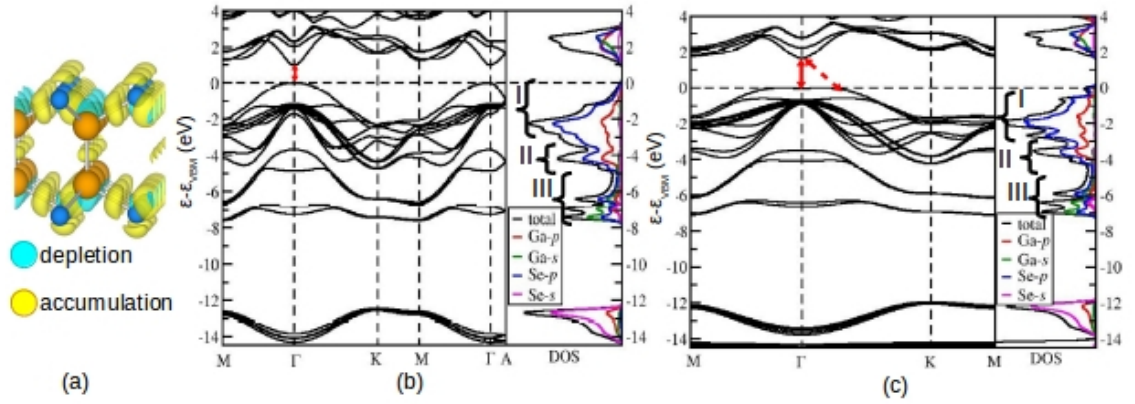


FIGURE 5.17: (a) The isosurfaces showing the difference between the computed charge density and that obtained from superposition of atomic charge density for bulk  $\epsilon$ -GaSe. The yellow (cyan) surfaces show accumulation (depletion) of charge. Bandstructure and density of states (total, Ga- $s,p$  and Se- $s,p$ ) for (b) bulk  $\epsilon$ -GaSe and (c) GaSe(0001) surface. The horizontal dashed line represents the valence band maxima while the vertical dashed lines marks the high symmetry points in the Brillouin zone. The red solid (dashed) arrow denotes the direct (indirect) bandgap.

## 5.7 Results

### 5.7.1 Properties of GaSe bulk and (0001) surface

In order to understand the electronic properties of Mn-doped GaSe surface it is important to study the electronic bandstructure of bulk GaSe and GaSe(0001) surface. Ga-Se bonds in bulk  $\epsilon$ -GaSe, of around 2.47 Å, are covalent in nature. This covalent bonding is demonstrated by the charge density difference plotted in figure 5.17 (a). The difference is calculated between the charge density for the interacting system and that obtained from superposition of atomic charge density for bulk. The yellow and cyan color represents accumulation and depletion of charge, respectively. Since the accumulation of charge is between the atoms while depletion is at the atoms, the Se-Ga bond is covalent in nature. The Ga-Ga-Se bond angle and Ga-Se-surface normal bond angle are 118.8° suggesting that there is a mixture of  $sp^2$  and  $sp^3$  type of hybridization in this material. This is in contrast to GaAs where it is purely  $sp^3$  hybridization.

To elucidate the hybridization we have computed bandstructure and density of states (DOS) for bulk  $\epsilon$ -GaSe which is shown in figure 5.17 (b). We note that both, the bandstructure and the DOS, are in good agreement with the previous calculations.



[145, 146] The direct bandgap at  $\Gamma$  point of the BZ obtained from our calculations for  $\epsilon$ -GaSe is around 0.98 eV. The valence band can be divided into three regions, I, II and III, as marked in figure 5.17 (a). From orbital-resolved DOS of Ga and Se atoms we find that region I and II primarily comprise of hybrid states of Se- $p$  and Ga- $p$  with Se- $p$  having a larger contribution. In region III the majority of states are from Ga- $s$  that hybridises with Se- $p$ , while contribution from Se- $s$  and Ga- $p$  is relatively small.

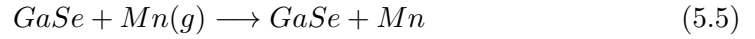
The band structure and DOS of the (0001) surface is shown figure 5.17 (c). We find that the overall electronic structure of the GaSe(0001) surface with two sandwiches is similar to that of the bulk. However the dispersion of bands in region I and II are more flat for the slab than that of bulk. Additionally we observe a new peak, corresponding to the valence-band maxima (VBM), which is mostly contributed by  $p$  states of surface Se atoms. In the bandstructure this increased density of states at VBM is represented by flat states along the  $M \rightarrow \Gamma \rightarrow K$  direction of the BZ. Furthermore, we note that the VBM for slab shifts to a k-point between  $\Gamma$  and K while the conduction band minima is retained at  $\Gamma$ . Thus, unlike its bulk counterpart, GaSe(0001) surface has an indirect bandgap. Also there is a notable enhancement in the bandgap to around 1.66 eV from 0.98 eV in bulk. We find these results in good agreement with those reported in [143].

### 5.7.2 Structure and stability of Mn-doped GaSe(0001) surface

Typically the magnetic impurity in semiconductors like GaAs or InAs, is observed to either substitute a host cation or is present at the interstitial site within the host lattice. However, unlike these semiconductors, GaSe has a layered structure which give rise to one more possibility of doping site, which is intercalation of impurity atom between the two weakly interacting GaSe sandwiches. In our study we have considered the following different doping cases which can be broadly classified into two types: (1) type I: Adsorption and (2) type II: Substitution. In type I doping the Mn atom can either (a) stay on the surface of host material or (b) move to an interstitial site or (c) intercalate between two sandwiches. For type II structures Mn can either substitute Ga atom from the (a) top Ga layer or (b) bottom Ga layer.

The stability of structures in these five doping cases are compared by calculating formation energy. Depending on the type of doping following two reactions are considered to determine the formation energy:

- I. For type I structures the reactants are Mn atom in the gas phase (Mn(g)) and GaSe(0001) slab while the product is Mn-doped GaSe(0001) slab. In the experimental studies, reported in ref. [2], Mn atoms are deposited on the GaSe(0001) surface by electron beam evaporation of Mn metal flakes. Therefore, formation energy is calculated with respect to energy of gas phase Mn atom rather than Mn atom in bulk.

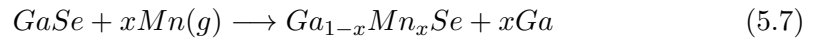


Thus the formation energy is determined as:

$$E^f = \frac{E(GaSe + Mn) - E(GaSe) - N_{Mn} \times E(Mn)}{N_{Mn}} \quad (5.6)$$

where  $E(GaSe + Mn)$ ,  $E(GaSe)$  and  $E(Mn)$  are total energies of Mn-doped GaSe(0001), clean GaSe(0001) slab and gas phase Mn atom. The energy for clean GaSe(0001) is obtained for the same cell size as used for Mn-doped GaSe(0001).  $N_{Mn}$  are the number of Mn atoms doped in GaSe(0001) slab.

- II. For type II structures, where Ga atoms are replaced with Mn atoms, the reactants are same as in the above reaction while the product contains Mn-doped GaSe(0001) along with replaced Ga atoms.



The formation energy is formulated as:

$$E^f = \frac{E(Ga_{1-x}Mn_xSe + Ga) - E(GaSe) - x \times E(Mn)}{x} \quad (5.8)$$

where  $E(Ga_{1-x}Mn_xSe + Ga)$  is the total energy of Mn-doped GaSe(0001) slab which includes the replaced Ga atoms.  $E(GaSe)$ ,  $E(Mn)$  and  $N_{Mn}$  are same as defined above.  $x$  is the number of replaced Ga atoms.

## 5.7.2.1 Structures of type I Mn-doped GaSe(0001) surface

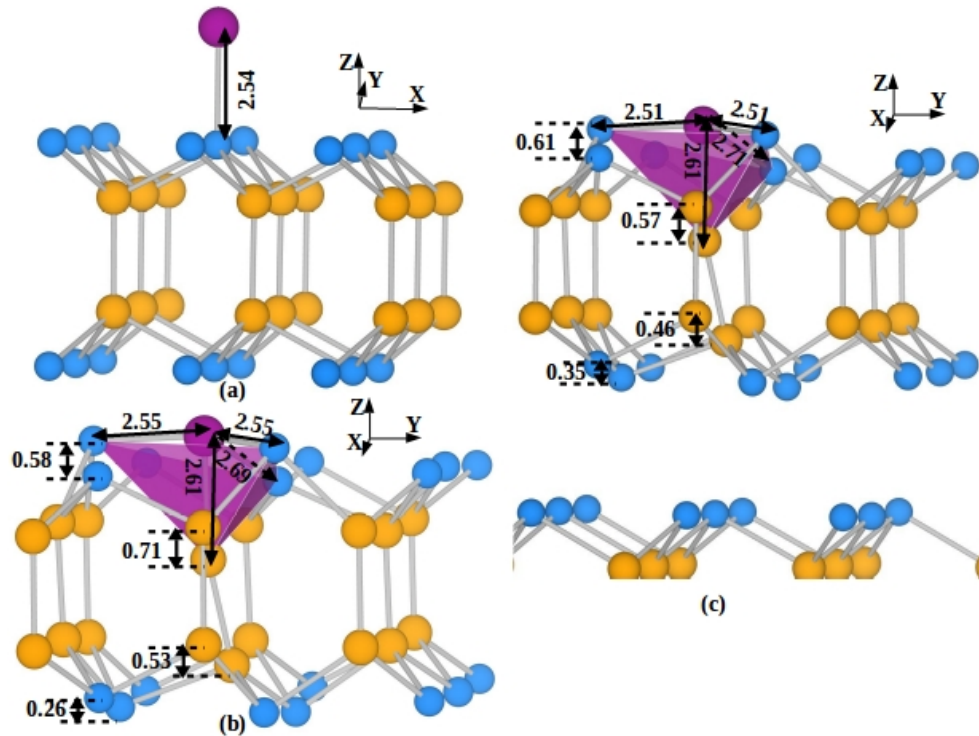


FIGURE 5.18: Two adsorption geometries of Mn atom on GaSe(0001) surface: (a) Mn atop surface Se atom in monolayer GaSe(0001) and Mn at Se-Se bridge site in (b) monolayer GaSe(0001) and (c) bilayer GaSe(0001) slab. The distances shown in the figures are in Å. The purple closed surface denotes the distorted tetrahedra around the Mn dopant. Se, Ga and Mn are denoted with blue, orange and purple colored spheres.

We will first discuss type I(a) structure where Mn stays on GaSe(0001) surface. The Mn atom on the surface can either be (i) atop surface Se atom or (ii) at the bridge site between two surface Se atoms. These two possible adsorption structures are shown in figure 5.18 (a) and (b, c), respectively. In order to save computational time the two adsorption geometries are initially explored on monolayer GaSe(0001). The calculated formation energies suggest that the two adsorption structures are formed through an endothermic reaction. The formation energy for Mn atop Se is 3.75 eV/Mn atom while that for Mn at Se-Se bridge site is around 0.50 eV/Mn atom. The energetics can be understood from the charge density difference plot shown in figure 5.17(a) where we observe accumulation of charge at Se atoms in clean GaSe(0001). The accumulated charges on Se atoms strongly repels Mn atom which is adsorbed exactly above it while the repulsion is relatively reduced if the Mn atom is present at the bridge site of two

Se atoms. In the structure for Mn atop surface Se we notice that the GaSe(0001) has no significant distortion suggesting negligible interaction. However we observe that the adsorbed Mn atom present at the Se-Se bridge distorts the local geometry significantly.

In order to achieve experimental concentration of dopant (5.5 %) we added one more GaSe sandwich below. We find that there are only minor changes, of around 0.02-0.04 Å, in the bond lengths between atoms. But the local distortions around the doping site shows notable changes, as illustrated in figures 5.18 (b) and (c). The Ga atom in top (bottom) layer is pushed down by 0.71 (0.53) Å and 0.57 (0.46) Å in the case of Mn adsorption on monolayer and bilayer GaSe(0001), respectively. The upward displacement of surface Se atoms which forms bridge site for Mn atom is however only slightly modified for the two thickness of the GaSe(0001) slab. Thus the decrease in local distortion around Mn atom on bilayer GaSe(0001) slab results in a more stable structure such that the formation energy reduces to 0.42 eV/Mn atom from 0.50 eV/Mn atom.

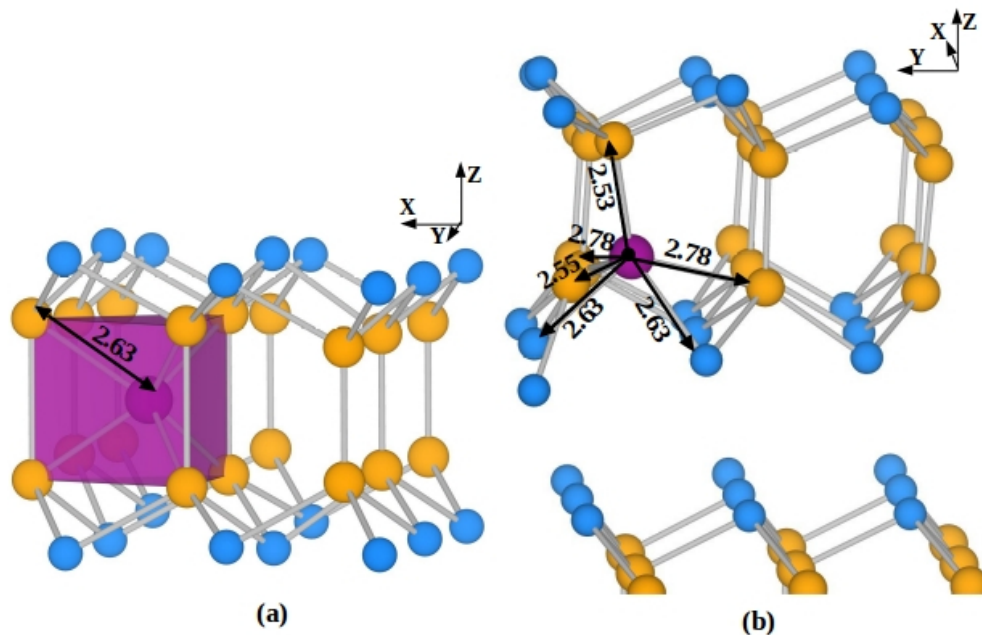


FIGURE 5.19: Geometries of Mn-doped (a) monolayer and (b) bilayer GaSe(0001) surface with Mn present at the interstitial site. The distances shown in the figures are in Å. The purple closed surface in the monolayer structure denotes the trigonal prism around the Mn dopant. Se, Ga and Mn are denoted with blue, orange and purple colored spheres.

The next doped structure in type I is where Mn is present interstitially within the surface sandwich of GaSe(0001) surface. Initially within a monolayer of GaSe(0001),

the interstitially present Mn atom binds symmetrically to three Ga atoms from each top and bottom Ga layer forming a trigonal prism with a Mn-Ga bond length around 2.63 Å (figure 5.19 (a)). We have obtained the formation energy corresponding to this structure to be around 1.83 eV/Mn atom which again suggests that energy is needed to push Mn in the interstitial site of the GaSe monolayer.

Further by adding one more sandwich below the surface sandwich we find that Mn atom introduces local distortion such that the dopant atom moves closer to bottom layer of the sandwich from where it pushes one pair of Ga and Se atoms away from other Ga and Se atoms, as shown in figure 5.19 (b). Mn binds to the displaced Ga atom with a bond length of around 2.55 Å. The bond length of Mn with two other Ga atoms of the bottom layer is relatively stretched (2.78 Å). Additionally the dopant also binds with two neighbouring Se atoms of the displaced Ga atom from bottom layer with a bond length of around 2.63 Å. Lastly the Mn atom binds with the Ga atom from the top layer, which was originally above the displaced Ga, with a bond length of around 2.53 Å. The distorted structure shows stronger binding of Mn with not only Ga atoms but also with Se atoms as compared to the symmetric structure. Thus the formation energy decreases to 0.87 eV/Mn atom. Nonetheless the reaction is still endothermic and less stable than adsorption geometry.

The last structure in type I is formed when Mn moves deeper into the slab and intercalates between two GaSe(0001) sandwiches. The intercalated Mn can take two possible sites: (i) atop surface Se of the bottom sandwich (figure 5.20 (a)) and (ii) atop Ga atom of the bottom sandwich (figure 5.20 (b)). In the first structure the intercalated Mn atom is much closer to top sandwich than to the bottom sandwich such that Mn is only 0.88 Å below the top sandwich while 2.38 Å above the bottom sandwich. The dopant atom forms a distorted tetrahedra such that it binds to three Se atom from the top sandwich and one Se atom from the bottom sandwich as shown in figure 5.20 (a). In the other structure where Mn is atop Ga of the bottom sandwich, it forms a distorted octahedra. The Mn atom is found to be again slightly closer to the top sandwich such that Mn is away by 1.57 Å from the top sandwich and 1.83 Å away from the bottom sandwich. We note from figure 5.20 (b) that three Se atoms from top as well as from bottom sandwich

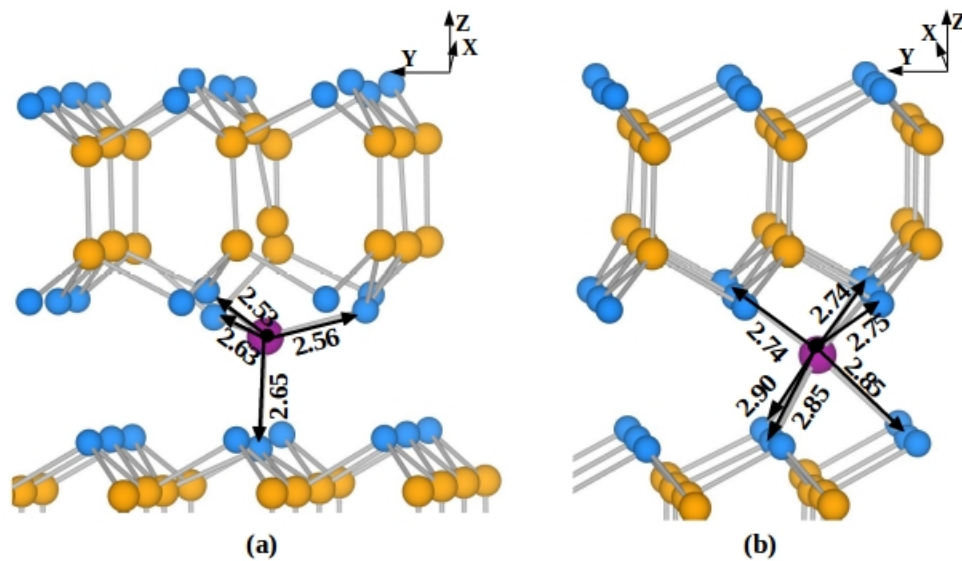


FIGURE 5.20: Geometries of Mn intercalated between two GaSe(0001) sandwiches. (a) Mn is atop Se atom and (b) atop Ga atom of the bottom sandwich. Se, Ga and Mn are denoted with blue, orange and purple colored spheres. The distances shown in the figures are in Å.

bind weakly with Mn atom which is atop Ga atom of the bottom sandwich than when Mn is atop Se of the bottom sandwich. Compared to other two structures in type I, structure with intercalated Mn is relatively more stable. The formation energy of the structure when Mn is present atop Ga (Se) atom of the bottom is around -0.01 (0.15) eV/Mn atom.

### 5.7.2.2 Structures of type II Mn-doped GaSe(0001) surface

The last two doping structures belong to type II where Ga atom is replaced by Mn atom; Ga either from top Ga layer or from the bottom Ga layer. If Mn replaces top layer Ga atom, the replaced Ga can either be present interstitially (figure 5.21 (a)) or pushed to the surface (figure 5.21 (b)). The interstitially present Ga atom ( $Ga_i$ ) does not distort the lattice significantly.  $Ga_i$  remains closer to the doped site such that the Mn- $Ga_i$  bond length is around 2.65 Å while Ga- $Ga_i$  bond length with the Ga atom below Mn atom is around 2.55 Å. The dopant form a distorted tetrahedra with three surface Se atoms and one Ga atom from bottom layer. Among the three Se atoms, two Se atoms are closer to  $Ga_i$  than the third Se atom. Thus two Mn-Se bond lengths are longer, around 2.63 Å,

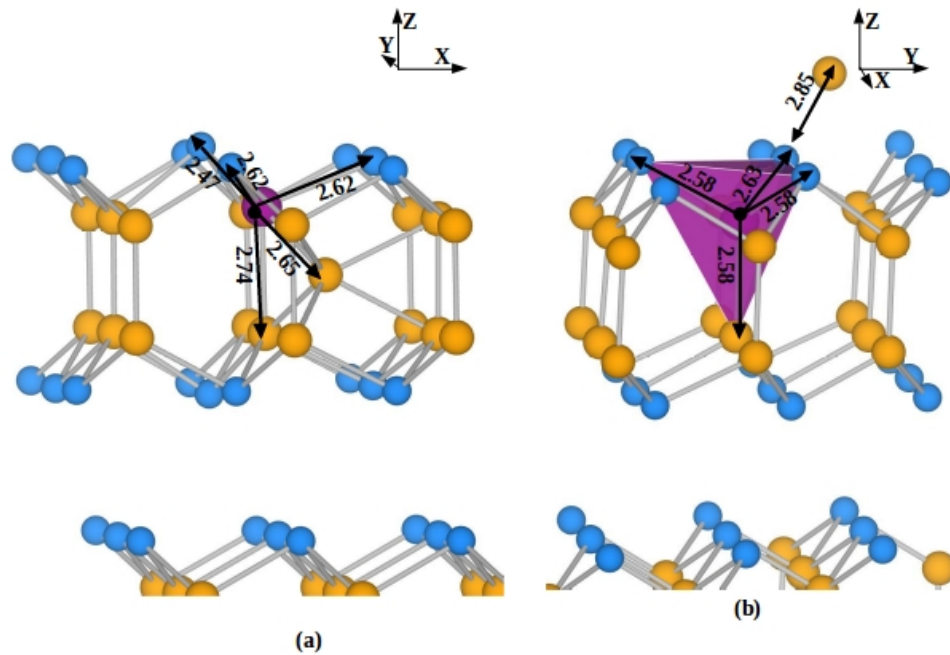


FIGURE 5.21: Structures of Mn substituting Ga atom from 1st layer where in (a) the replaced Ga is pushed to an interstitial site and in (b) the replaced Ga atom is moved to the surface. Se, Ga and Mn are denoted with blue, orange and purple colored spheres. The distances shown in the figures are in Å.

than the third one which is around 2.47 Å. The Mn-Ga bond length within the distorted tetrahedra is around 2.74 Å, which is significantly stretched with respect to Ga-Ga bond length of 2.43 Å that is away from the doping site.

When the replaced Ga is pushed to the surface the distortion in the tetrahedra formed around the Mn atom is significantly reduced. In this structure there are two Se atoms which are away (by 6.25 Å) from the replaced Ga atom and the corresponding Mn-Se bond lengths are around 2.58 Å. The third Se atom, which is relatively closer (2.85 Å) to the replaced Ga atom, forms a stretched Mn-Se bond length of around 2.63 Å. The Mn-Ga bond length within the tetrahedra is around 2.58 Å which is still stretched with respect to Ga-Ga bond length (2.43 Å) away from doping site. However, it is shorter than when the replaced Ga is present interstitially (2.74 Å). The formation energy calculation, using equation 5.8, suggests that both the structures for Mn replacing the Ga atom from top layer are exothermic. However moving Ga atom to the surface is significantly more preferable than pushing it to an interstitial site. The formation

energy when the replaced Ga atom moves to the surface is around  $-0.97$  eV/Mn atom while that when the replaced Ga atom goes to the interstitial site is around  $-0.06$  eV/Mn atom.

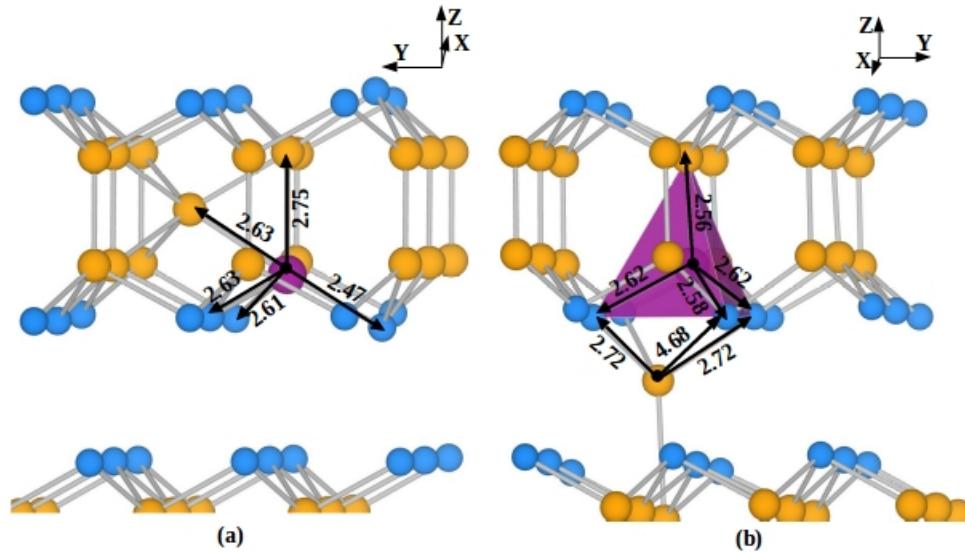


FIGURE 5.22: Structures of Mn substituting Ga atom from II<sub>nd</sub> layer where in (a) the replaced Ga is pushed to a interstitial site and in (b) the replaced Ga atom is moved deeper to intercalate between the two sandwiches. Se, Ga and Mn are denoted with blue, orange and purple colored spheres. The distances shown in the figures are in Å.

In the last doping case where Mn replaces Ga from the second layer, the replaced Ga atom can again either move to an interstitial site (figure 5.22 (a)) or can go deeper and intercalate between the two sandwiches (figures 5.22 (b)). For the first structure with interstitial Ga atom,  $Ga_i$ , we again find that those bond length around Mn are stretched which are closer to the interstitially present Ga atom. As a result a distorted tetrahedra is formed with principle axis passing through Mn atom. The three Mn-Se bond length in the tetrahedra are around  $2.46$  Å,  $2.61$  Å and  $2.63$  Å while Mn-Ga bond length is around  $2.75$  Å. In the second structure the intercalated Ga, similar to the intercalated Mn atom in type I, stays atop Ga of the bottom sandwich. The intercalated Ga is around  $1.51$  Å below the top sandwich and  $2.02$  Å above the bottom sandwich. The tetrahedra around Mn is again slightly distorted due to the presence of intercalating Ga atom. Two out of the three Se atom which binds to Mn are in closer to the intercalated Ga, at a distance of around  $2.73$  Å. Thus the corresponding Mn-Se bond lengths are stretched to  $2.62$  Å while the third bond length is around  $2.58$  Å. The Mn-Ga bond length within



the tetrahedra is around 2.56 Å. The substitution of Ga by Mn in the second layer is also an exothermic reaction, however less stable than replacing Ga from first layer. The formation energy for Mn in the second layer with intercalated (interstitially present) Ga atom is around -0.64 (-0.03) eV/Mn atom.

TABLE 5.3: Formation energy for Mn-doped GaSe(0001) bilayer surface in different configurations. Formation energy of adsorption and interstitial configuration for monolayer GaSe(0001) are also included. FM and AFM represents structures where Mn-Mn coupling is ferromagnetic and antiferromagnetic, respectively.

Type of doping	Doping site	Configuration	Formation energy (eV/Mn atom)
Type I	adsorption on surface	atop Se (1S)[FM]	3.75
		Se-Se bridge (1S)[FM]	0.50
		Se-Se bridge (2S) [FM]	0.42
		Se-Se bridge (2S) [AFM]	0.39
	interstitial	1S [FM]	1.83
		2S [FM]	0.89
		2S [AFM]	0.97
	intercalating between sandwiches	atop Se of lower sandwich (2S)[FM]	0.15
		atop Ga of lower sandwich (2S) [FM]	-0.01
atop Ga of lower sandwich (2S) [AFM]		-0.21	
Type II	substituting Ga from 1st layer	replaced Ga at interstitial site (2S) [FM]	-0.06
		replaced Ga at the surface (2S) [FM]	-0.94
		replaced Ga at the surface (2S) [AFM]	-0.95
	substituting Ga from 2nd layer	replaced Ga at interstitial site (2S) [FM]	-0.03
		replaced Ga intercalating between sandwiches (2S) [FM]	-0.64
		replaced Ga intercalating between sandwiches (2S) [AFM]	-0.63

The formation energy corresponding to different doping structures are listed in table 5.3. From the table and the discussions in the previous paragraphs we conclude that Mn prefers the substitutional site where it replaces Ga atom from top layer of the GaSe(0001) surface and the substituted Ga moves to the surface. In experimental investigations a comparison between Mn-2p XPS spectra in doped GaSe and metallic Mn

is made from where similar conclusion are drawn that Mn moves to the substitutional site of the host lattice where it replaces Ga atom from the top layer.[2]

In the subsequent subsections we have discussed the electronic and magnetic properties of the Mn-doped GaSe(0001) slab consisting of two GaSe sandwiches in the five structures that are stable than the other configurations of same type of doping, namely, (1) Mn adsorbed at Se-Se bridge site on the surface, (2) Mn in the interstitial site within the sandwich, (3) intercalated Mn placed above Ga atom of the bottom sandwich, (4) Mn substituting Ga from 1st layer with replaced Ga atom on the surface and (5) Mn substituting Ga from 2nd layer with the replaced Ga intercalating between two sandwiches.

### 5.7.3 Electronic properties of Mn-doped GaSe(0001) surface: Elucidating interaction between Mn dopant and host atoms

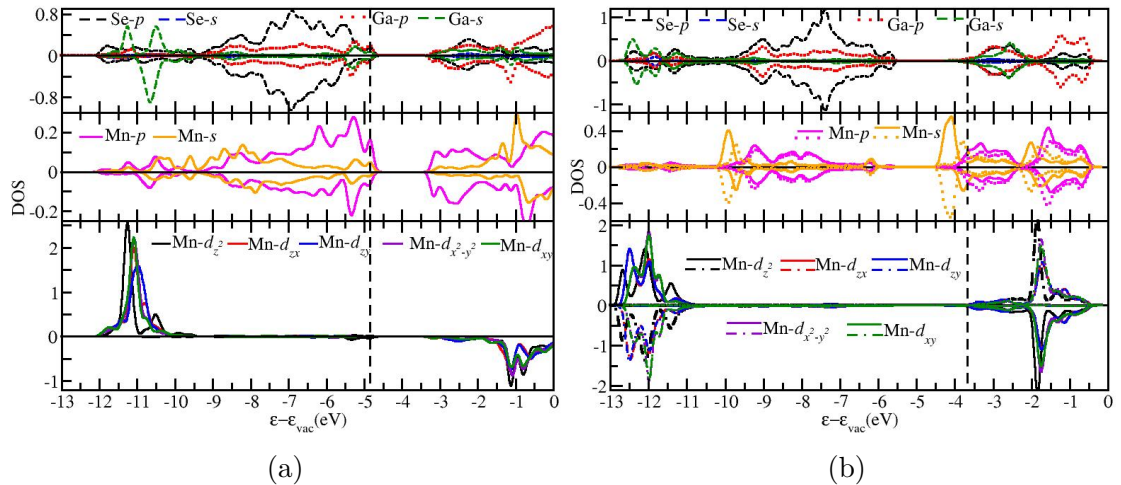


FIGURE 5.23: Density of states of  $s$  and  $p$  states of Ga and Se (top panel),  $s$  and  $p$  states of Mn (middle panel) and  $d$  states of Mn (bottom panel) for Mn-doped GaSe(0001) where (a) Mn replaces Ga atom from 1st layer and (b) Mn intercalates between two sandwiches.

In the conventional DMS, the  $3d$  states of the transition metal impurity atom are found to hybridize strongly with the  $s$  and  $p$  states of the ligand. The relative position of  $p$  states of the ligands and  $3d$  states of the impurity decides the strength of  $p - d$  hybridization. For instance, it is shown in ref. [152] that Cr- $d$  bands are present within the bandgap of GaN host while they almost merge in the valence band of GaAs. Mn- $d$  are also reported

to merge into the valence band of GaAs. However there are earlier reports of Mn- $d$  states being below the valence band with only a small peak around the Fermi level. The  $p-d$  hybridization results into crystal-field splitting in  $d$  states of transition metal impurity atom. The competition between crystal-field splitting and exchange splitting in  $3d$  states of impurity atom decides the spin ground state for the DMS. A high-spin ground state is obtained for magnetic impurity atom if the exchange splitting in  $3d$  is larger than crystal-field splitting. Thus to elucidate the interaction in Mn-doped GaSe and to understand the magnetic behaviour we have plotted DOS of Mn- $d$ ,  $p$  and  $s$  along with DOS of  $s$  and  $p$  states of the host atoms for all the five Mn-doped GaSe structures.

From the DOS we find that the distribution of states is similar in all five structures. Except for one structure where Mn intercalates between the two sandwiches, we find all others are semiconducting. Figure 5.23(a) shows DOS for the most stable configuration where Mn replaces Ga from 1st layer. The structure where Mn is present in the intercalating site between two sandwiches is metallic which is seen from the DOS plot in figure 5.23 (b). The DOS for the remaining three structures (Mn adsorbed on the surface, Mn present in the interstitial site and Mn substituting Ga from second layer) are included in figure 27 of Appendix 5.8. The occupied region in the DOS plot can be split into two regions based on the involvement of Mn-states in hybridization with the states of host atoms: (i) between -13 and -10 eV and (ii) between -10 eV to the highest occupied state. The occupied Mn- $d$  states are primarily localized in region (i) which is much below the valence band. The distortions around Mn result in a reduced symmetry of  $C_s$  and hence all the five  $d$  orbitals are nondegenerate. However, unlike in Mn-doped GaAs the effect of crystal-field splitting is negligible here, as also observed from the experimental X-ray absorption spectra and resonant photoemission spectra. [2] This is because in Mn-doped GaSe, Mn atom are not only surrounded by ligand (Se) but also by Ga atoms. The electronegativity difference between Mn and Ga is much less than that between Mn and Se which results in less ionicity of the bonds. Moreover, in typical DMS the dopant  $d$  orbitals hybridize primarily with the anion (ligand)  $s$  and  $p$  orbitals. However, in the case of Mn-doped GaSe, we find that the hybridization of Mn- $d$  with the Se- $s$  and  $p$  orbitals is weaker than the hybridization of Mn- $d$  (specifically, Mn- $d_{z^2}$ ) with Ga- $s$  at the bottom of the valence band, in region (i). As a consequence

of negligible crystal-field splitting, a high spin state is observed for Mn atom in GaSe in all five structures, which is discussed in more details in the following subsection. In region (ii), the contributions to the states in both the spin up and down channels are primarily from  $p$  states of Se and Ga hybridized with the Mn- $p$  and  $s$  states.

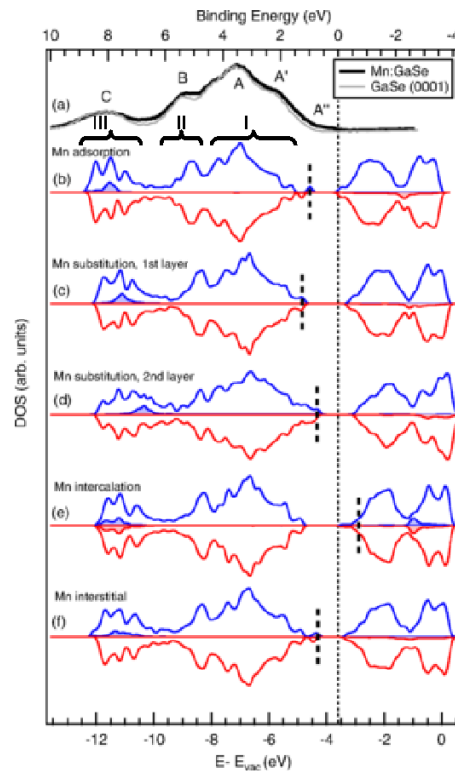


FIGURE 5.24: Valence-band spectra of the clean GaSe (thin line) and the reacted Mn-GaSe surface (thick line) (a). Spin-projected DOS calculated for Mn adsorbed on the surface (b), Mn replacing Ga in the first Ga layer below the surface (c), Mn replacing Ga in the second Ga layer below the surface (d), Mn intercalated between the two Se layers (e), and Mn interstitial (f). The Mn partial DOS is represented by shaded areas. The vertical dashed lines represent the calculated highest occupied states. Reprinted with permission from ref.[2] Copyright2016, APS

In figure 5.24 we have shown the valence-band spectra, which is reproduced from Ref. [2], of clean GaSe surface and Mn-doped GaSe surface along with the DOS of the five Mn-doped structures. The spectra consists of four main features, namely  $A'$ ,  $A$ ,  $B$  and  $C$ . An additional feature,  $A''$  is observed in spectra obtained for Mn-doped GaSe surface. We can identify such similar features in the computed DOS plots as well: From the DOS plots of undoped GaSe (figure 5.17 (c)) and Mn-doped GaSe (figure 5.24), region I can be associated to feature  $A'$  and  $A$  while region II to peak  $B$  and region III to peak

C. Thus the increase in spectral weight between peak A and B and B and C can be correlated with the hybridization of Mn-states with Se- $p$  and Ga- $s, p$  states. We note that for the doped system, the valence band edge states result from the mixing of the Mn- $p$  and  $s$  with  $p$  states of Se and  $s$  and  $p$  states of Ga. This results in an increase in the density of states appearing at the Fermi edge compared to the undoped case which can be associated to peak A'' in the valence band spectra. Therefore with change in doping site, which brings in a change in the hybridization near valence band maxima, we observe changes in the bandgap, as noted in table 5.4. For the intercalated structure we notice the conduction band, comprising of Mn- $s, p$  states, moves down and crosses the Fermi energy, making it metallic. In the intercalated Mn structure, Mn is present in the void space between the two sandwiches. Thus unlike in other structures the dopant atom interacts (weakly though) with the host atoms of both the sandwiches. Therefore the interaction between the two sandwiches is no longer just weak van der Waals interaction but also includes weak chemical interactions which give rise to the metallic behaviour in its electronic structure.

#### 5.7.4 Magnetism in Mn-doped GaSe(0001)

In the preceding subsection we observed from the DOS plots that the exchange splitting is very large while the crystal-field splitting is extremely weak. The Mn in Mn-doped GaSe is an open-shell atom with Mn- $d$  occupied states are only in one spin channel while all the unoccupied Mn- $d$  states are in other spin channel. Thus for all the five different doped structures we find that the magnetic moment on Mn are close to  $5 \mu_B$  (from Löwdin charge analysis), as noted in table 5.4. This implies that Mn is in the +2 oxidation state which agrees with the XAS spectra where the XAS profile of Mn in Mn-doped GaSe(0001) is found to be closer to Mn<sup>+2</sup> profile obtained from the following allowed transition:  $2p^63d^5 \rightarrow 2p^53d^6$  [2]. The magnetic moments on the Ga and Se atoms interacting with the impurity atom are less than  $0.10 \mu_B$  and it further decreases for other host atoms as one moves away from the doping site. The magnetization density plot for all five structures are shown in figure 5.25.

TABLE 5.4: Magnetic moment on Mn and bandgap obtained each of the five Mn-doped GaSe(0001) structures. The magnetic moment values in the paranthesis are contribution from Mn-*d* orbital.

Sr.No.	Structure	Magnetic moment on Mn ( $\mu_B$ )	Bandgap (eV)
1	Mn adsorbed on surface at Se-Se bridge site (FM)	5.00 (4.72)	1.11
2	Mn in the interstitial site (FM)	4.94 (4.68)	1.11
3	Intercalated Mn atop Ga of lower sandwich (AFM)	5.15 (4.83)	0.00
4	Mn substituting Ga from 1st layer with replaced Ga on the surface (FM)	5.04 (4.77)	1.68
5	Mn substituting Ga from 2nd layer with replaced Ga intercalated between sandwiches (FM)	5.05 (4.78)	1.52

So far our discussion was restricted to structures where we have considered only ferromagnetic coupling between the magnetic moments on the adjacent dopants. However the large magnetic moment on Mn atom insists on investigating other magnetic coupling where the magnetic moment on the adjacent Mn atoms are antiferromagnetically coupled. Thus we increased the size of the supercell to  $6 \times 6$  to incorporate antiferromagnetic coupling between Mn atoms. The formation energy for stable structures in each of five doping cases with antiferromagnetic coupling between Mn atoms are also included in table 5.3. We notice that the structure where Mn is intercalated between two sandwiches shows largest change in formation energy, of around 0.2 eV/Mn atom with the change in the magnetic coupling. In type I structure in which the adsorbed Mn stays on the surface and type II structures show negligible magnetic coupling at the present concentration of doping. For type I structure where the adsorbed Mn moves to interstitial site we find a small change in formation energy of around 0.08 eV/Mn atom such that the ferromagnetic coupling is more stable.

The ferromagnetic coupling between the adjacent dopant atoms in Mn-doped GaAs was observed to be mediated by the holes produced in vicinity of the Mn atom which substitutes the Ga atom. [139] However in Mn-doped GaSe we do not find any charge doping. Additionally magnetic moments induced on the host atoms are very weak

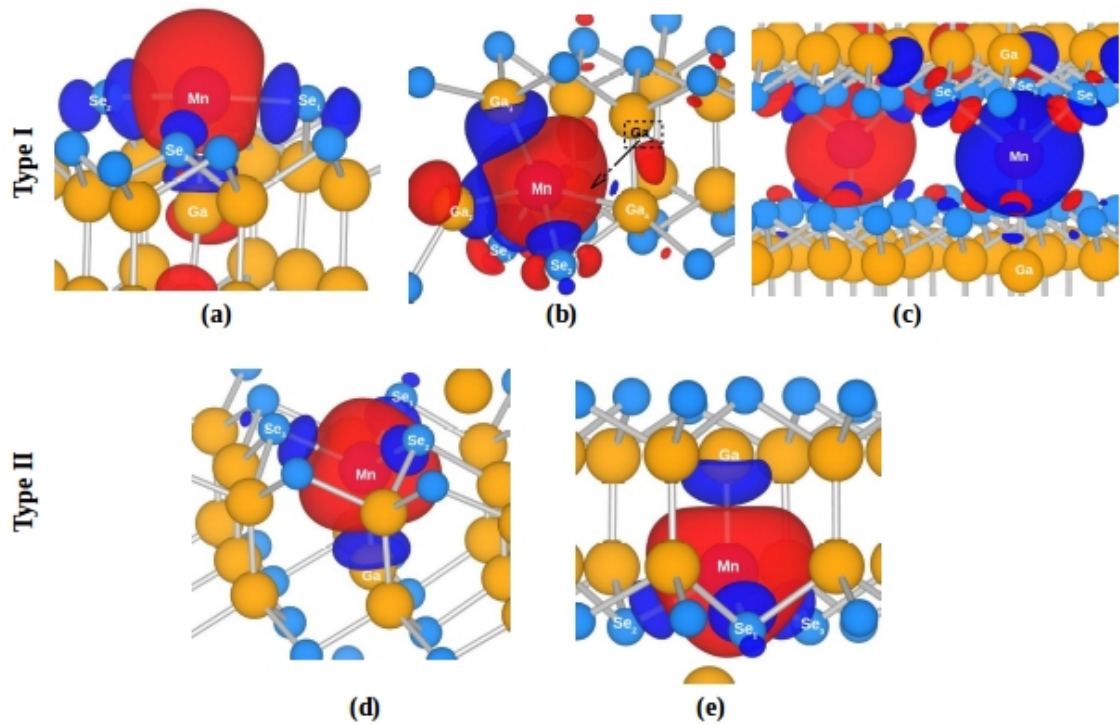


FIGURE 5.25: Magnetization density plot for Mn-doped GaSe(0001) bilayer structure of (a)-(c) type I and (d)-(e) type II. (a), (b) and (c) corresponds to structures where Mn is adsorbed, Mn is present interstitially and Mn is intercalated, respectively, while (b) and (c) corresponds to structures where Mn replaces Ga from 1st and 2nd layers, respectively. The red and blue isosurface denotes spin-up and spin-down magnetization, respectively. In each figures atoms interacting with Mn are marked with their atomic symbol.

and grow weaker quickly as one moves away from the doping site. Hence in Mn-doped GaSe, host atoms do not participate in building magnetic coupling between the adjacent Mn atoms. The local magnetic moment on the dopant atom in Mn-doped GaSe thus couples with adjacent local moments only through dipole-dipole interaction which is restricted by the surrounding host atoms. In intercalated Mn structure however the dopant is present in the void space between the two weakly interacting GaSe(0001) sandwiches. Moreover, from the geometries discussed in the earlier subsection we observe that interaction between Mn and host atoms is relatively weaker in intercalated Mn structure than in other doped structures. Thus in this structure the magnetic dipole-dipole interactions are less restricted and we observe a relatively stronger magnetic coupling than in other Mn-doped GaSe structures.

## 5.8 Summary

From the experimental studies reported in ref.[2] and from our density functional theory calculations we are able to conclude that Mn impurity atom substitutes Ga atom in Mn-doped GaSe(0001) surface from the top layer of the surface GaSe sandwich. The states of Mn atom are involved in the hybridization with the  $s$  and  $p$  states of Ga and Se atoms. More specifically, from the computed density of states we could observe hybridization between (i) Mn- $d_{z^2}$  and Ga- $s$  and (ii) Mn- $s, p$  and Se- $p$  and Ga- $p$ . The highest occupied level in Mn-doped GaSe(0001) corresponds to the hybrid states of Mn- $s, p$  and Se- $p$  and Ga- $s, p$  whereas that in undoped GaSe(0001) surface corresponds to only Se- $p$  and Ga- $p$ . Thus a new feature is observed in valence band spectra which directly corresponds to the increased density of states at the valence band edge in Mn-doped GaSe surface. Additionally since Mn states contribute to the highest occupied level we observe change in bandgap with the change in the doping site in Mn-doped GaSe(0001) surface. Interestingly for structure in which Mn intercalates between two GaSe sandwiches we find that the Mn- $s, p$  states cross Fermi energy making the structure metallic. Consistent with the experimental studies we find that the effect of crystal-field splitting is negligible for Mn atom. This is because only the spherically symmetric  $s$  state of Ga interacts with Mn- $d$ . Due to weak hybridization, Mn in Mn-doped GaSe(0001) retains its  $d^5$  configuration similar to Mn in gas phase. Thus from Löwdin charge analysis we obtain magnetic moment which is close  $5 \mu_B$  for Mn in different Mn-doped GaSe(0001) structures. Moreover we find that Mn-doped GaSe(0001) structure where Mn intercalates between two sandwiches shows largest magnetic coupling of around 0.2 eV/Mn atom such that the magnetic moment on Mn atoms prefer antiferromagnetic coupling. Magnetic coupling in other structures are either negligible or weak where ferromagnetic coupling is preferred.



# Summary and outlook

The present thesis has focussed on two of the many routes to tune and modify the electronic and magnetic properties of layered materials. The first route is chemical functionalization where through adsorption or intercalation of foreign species we were able to achieve modulation in the properties at the interface of epitaxial graphene and its transition metal substrates. The second route is defects which locally alters the properties of the material. The results from first route has been discussed in chapters 3 and 4 while those from second route are discussed in chapters 5 and 5.4.

Ni(111) surface is known to be as an ideal substrate for graphene for two reasons: (i) The lattice parameter of Ni(111) surface closely matches with that of graphene and hence it experiences least amount of stress when placed over Ni(111) surface. (ii) The interaction with surface Ni atoms induces small bandgap changing the semimetallic graphene to semiconducting. Moreover, small magnetic moment is also induced making the epitaxial graphene ferrimagnetic. This is important from the point of view of semiconducting device applications. Further tuning of magnetic and electronic properties was achieved by hydrogenating the epitaxial graphene sheet. [47] It was observed that for the highest hydrogen coverage the graphene sheet turns from a ferrimagnetic to a ferromagnetic semiconductor such that the band gaps in two spin channels are notably different. At the highest hydrogen coverage each alternate carbon atom in the epitaxial graphene sheet is hydrogenated. Such hydrogenated structure in freestanding condition was studied by Zhou *et al.*[60]. The structure is named as graphone. It was observed that the freestanding graphone is also ferromagnetic semiconductor. However, the magnetic moment on freestanding graphone is around  $1.0 \mu_B$  while that on the epitaxial graphone (on Ni(111))

surface) is around  $0.04 \mu_B$ . Additionally hydrogenating the epitaxial graphene also significantly quenches the magnetic moment on surface Ni atoms. Retaining large magnetic moment at the interface is important for spin transport and hence for spintronic applications. Thus as an effort to improve interfacial magnetic properties at the interface of Ni(111) surface and graphone, in chapter 3 we investigated intercalation of atomic oxygen at the Ni(111)/graphone interface at three different O coverages. From our DFT+U calculations we find that the stability of Ni(111)/O/graphone interface increases as the coverage of the intercalating O is increased with respect to Ni(111)/graphone interface. The stability of the epitaxial graphone sheet depends on the interplay between energy gained due to O intercalation and the sublattice imbalance existing in the graphone sheet due to hydrogenation of C atoms of one sublattice. Further, we find that the magnetic moment on graphone remains weak for 1 ML and 0.25 ML of O coverage, while enhances for 0.5 ML of O coverage by eight times with respect to the magnetic moment on graphone in the absence of the intercalating O atomic layer. Furthermore, the magnetic moment on surface Ni atoms increases notably with increase in the O coverage. We observe that the enhancement in magnetic moment on surface Ni atoms with 1 ML O coverage is about seven-fold, with 0.5 ML O coverage is about six-fold and with 0.25 ML O coverage is about five-fold. We attribute this enhancement of magnetic moment to spin-dependent charge transfer between graphone and Ni(111) surface via intercalating O atoms. From density of states and integrated local density of states we find that at the interface with 1 ML O coverage higher preference is shown for the conduction of charge of one spin type. Thus the interface of Ni(111)/O-1ML/graphone can be used in a spin filter device. These results lead to a new set of questions for instance, whether similar behavior will be seen with other transition metal substrates or what happens if instead of the electronegative O atoms other electronegative atoms or electropositive atoms than C atoms are intercalated. In other words are the intriguing properties discussed in this chapter restricted to the Ni(111)/O/GrH interface?

Ferromagnetic and semiconducting behaviour of graphone makes it a special material for spintronic applications. However, graphone or uniformly semihydrogenated graphene sheet (UGrH), is the least stable structure compared to other semihydrogenated graphene structures which are non-magnetic. This is because UGrH has large

sublattice imbalance due to hydrogenation of carbon atoms belonging to only one sublattice. However the large sublattice imbalance is reduced when UGrH is supported on Ni(111) surface such that the unhydrogenated carbon atoms on the other sublattice interacts with the surface Ni atoms. In chapter 4 we have studied four different structures, including UGrH, of the semihydrogenated graphene on Ni(111) surface and as well as on other transition metal surfaces like Co(111) and Cu(111), whose lattice parameters are close to that of the graphene sheet. The study aims at understanding whether other structures, which are more stable than UGrH in freestanding condition, are attainable on transition metal surfaces so as to consider them during the synthesis of hydrogenated graphene on transition metal surfaces. Additionally we aimed at finding different signatures that distinguish the different H patterns on the metal surfaces. Apart from UGrH the three structures studied in this chapter are rectangular graphone (RGrH) [85], zigzag graphone (ZGrH) [86] and armchair graphone (AGrH). On Ni(111) surface we find that all the four semihydrogenated graphene structures are equally favourable. Additionally, the difference between core-level shifts of unhydrogenated and hydrogenated carbon atoms show minor variation ( 0.05 eV) with different semihydrogenated structures on Ni(111) surface. This suggests that it is highly difficult to distinguish different semihydrogenated structures of graphene on Ni(111) experimentally using XPS measurements. However, we find that magnetic moment on surface Ni atoms as well as spin-polarization of Ni-*d* states shows noticeable variation with the change in the structure of the epitaxial semihydrogenated graphene. Similar results are obtained on Co(111) and Cu(111) surface with a difference that the four semihydrogenated structures shows small differences in the stability unlike on Ni(111) surface. Also the difference in the core-level shifts are larger than that obtained on Ni(111) surface. Nonetheless, they are small in comparison to the experimental resolution (0.20 meV). Further for structures on Ni(111) surface and Co(111) surface we find that the spin polarization of graphone states is either weak or opposite to that of metal states. Thus these interfaces will need additional effort to make them good candidates for spin conduction, like O intercalation which was discussed in the earlier chapter. On Cu(111) surface only UGrH is magnetic and it induces small magnetism in the otherwise non-magnetic surface Cu atoms. Additionally we find impressive spin polarization in UGrH

states as well as Cu-*d* states with same polarity. Hence the interface of Cu(111)/UGrH can be considered for devices which requires conduction of spin-polarised current.

In the above two studies we have investigated interfaces with graphene which allows passage of spin-polarised current. The chemical modification performed on graphene, to attain improved or device application based properties, were uniform throughout the graphene sheet. However now in further two chapters we focus on obtaining localised variation in the properties, specifically magnetic properties, for application in data storage devices. Local modifications can be achieved on surfaces by creating point defects, such as vacancy or adsorption of foreign species like molecules, adatoms or even both such that the foreign specie is adsorbed at the vacancy site. Vacancies in graphene are known to host metal adatoms better than the pristine graphene sheet. This is because the mobilities of metal atoms on pristine graphene sheet are high. Therefore to obtain high local magnetic moment it is proposed that magnetic atoms like Co, Fe, Mn, should be adsorbed at the vacancies in the graphene sheet. This local moment acts as a data unit which is processed for reading or writing data in storage devices. Hence for functioning of the device atleast at temperatures close to room temperature the stability of the local magnetic moment is most important. The stability of magnetic moment depends on the magnetic anisotropies in the system such that higher the magnetic anisotropy energy (MAE), higher is the stability of the magnetic moment. MAE is determined as the total energy difference between two orientations of the magnetization vector. Large MAE in lower dimensional system can be achieved from (i) strong spin-orbit coupling, (ii) large orbital moment and (iii) strong ligand field.[112] For single C vacancy in graphene, the atoms surrounding the vacancy have dangling bonds and hence these C atoms interact strongly with the adsorbed magnetic atom. The strong interaction results in weak orbital moments and hence results in weak MAE of around 0.03 meV. Additionally the magnetic moment on Co adatom is also highly quenched ( $0.26 \mu_B$ ). Therefore, in chapter 5 in order to achieve better magnetic properties for the adsorbed magnetic atom (Co) we decorated the vacancy in the graphene sheet with N and B atoms so as to remove the dangling bonds. N and B decoration of single C vacancy resulted in improved magnetic moment on Co adatom as well as magnetic anisotropy energies; magnetic moment on

Co is around 1.92 (0.99)  $\mu_B$  while MAE 1.49 (3.80 meV) meV in N(B)-decorated structure. However we notice that N and B decoration results in change in the easy axis of magnetization along the in-plane direction from the out-of-plane direction obtained in freestanding undecorated vacancy-Co adatom complex. Further, we placed the graphene sheet containing Co adatom adsorbed at the single C vacancy site (decorated and undecorated) on the ferromagnetic Ni(111) surface to understand the effect of substrate on the magnetic properties of the vacancy-Co complexes. Interestingly, we observed that there is a huge enhancement in the MAEs for all three vacancy-Co complexes on Ni(111) surface. The MAE obtained from our full relativistic calculations with GGA+U formalism is around 40 meV for Co adatom adsorbed either at undecorated or decorated single C vacancy in graphene sheet supported on Ni(111) surface. We apprehend from our density of states and integrated local density states analysis that the orbital moment anisotropy in undecorated vacancy-Co complex supported on Ni(111) surface (Ni/Co-SVG) is much larger than in freestanding undecorated vacancy-Co complex(Co-SVG). The large change in the orbital moment anisotropy is contributed by the strain on the Co-SVG on Ni(111) surface and interaction of surface Ni atom with Co and C atoms surrounding the vacancy. This gives an account to enhanced MAE for vacancy-Co complex supported on Ni(111) surface. Similar investigation for decorated vacancy-Co complexes are in progress.

In the last chapter we have dealt with another two-dimensional material, gallium selenide, which belongs to III-VI semiconductor group. Like the known III-V and II-VI semiconductor groups, these newer III-VI group of semiconductors also form dilute magnetic semiconductors (DMS) upon doping with magnetic impurities. Magnetism in semiconducting material is vital for spintronic devices because the functioning of the device depends on spin of the electrons rather than charge as in the current working electronic devices. Due to carrier-induced ferromagnetism in DMS derived from III-V semiconductors, these materials were found to be suitable for magneto-optic devices like spin-polarised light emitting diodes. The III-VI class of semiconductors like GaSe or GaS or GaTe, differ from the conventional bulk DMS materials because of their layered structures. Moreover, the same reason make these materials more interesting as it fits into the current demand of reduced dimensional semiconducting materials for device

applications. The monolayer of gallium selenide is four atomic layer thick with two Se layers sandwiching two Ga layers. Thus due to greater availability of space there are various possible sites for doping of magnetic impurity, such as substitutional, interstitial within a monolayer, within the void space between two monolayer of the slab, or simply on surface sites. In chapter 5.4 we have considered all possible doping sites for Mn impurity in GaSe slab of two monolayer thickness and found that Mn prefers to substitute surface Ga atom which is consistent with the experimental observation reported in [2]. From our calculation we find that the replaced Ga atom moves to the GaSe(0001) surface and adsorbs at the Se-Se bridge site. Further our calculations suggested that the dopant atom has half-filled  $d$  states which contributes to the magnetic moment on Mn, determined to be close to  $5 \mu_B$ . The  $d$  states of Mn are observed to interact weakly only with Ga- $s$  states. Thus we do not observe notable crystal-field effects on Mn atom, as also noted in the experimental studies. From our density of states plots we find that the Mn- $d$  states are well localised and much below the valence band level. Interestingly we find that the empty Mn- $s, p$  states participate in the hybridization with the ligand states as well as with Ga- $p$  states. Since the interaction of dopant with the ligands is weak we observe weak (or negligible in some cases) magnetic coupling between the magnetic moments on adjacent Mn atoms as was observed in conventional DMS like Mn-doped GaAs. These electronic and magnetic properties show only small quantitative variation with change in the doping site of Mn. Our calculation was dedicated to a single concentration value of Mn of around 5.5% of the number of Ga atoms in GaSe(0001) which is close to the experimental concentration. However, we feel one should also look into other concentrations of the Mn atom and check whether the above induced properties hold true. In the popular DMS, Mn-doped GaAs, it is observed that the most preferred doping type is substituting Ga atom. Mn at the substituted site acts as an acceptor which results in hole doping in the host material which is the origin of carrier-mediated ferromagnetism. To increase the carrier density it is hence required to increase concentration of Mn atoms. For this purpose a low growth temperature is preferred which increases the possibility of interstitially present Mn atoms which are donor in nature. The interstitial Mn atoms thus compensate significant amount of free holes generated due to substitution of Mn which quenches the ferromagnetic coupling. Thus we feel that

an investigation of structures and their properties where more than one type of doped Mn atoms co-exist in the host material should also be included in further studies.

# Appendix A

## .1 Dipole-corrected electrostatic potential for different Mn-doped GaSe(0001) structures

Since we are using periodic boundary conditions in our calculations and we are modeling surfaces (the periodicity is broken in the direction perpendicular to the surface), one needs to have sufficient vacuum to avoid the spurious interactions between the periodic images in the direction normal to the surface. For the undoped GaSe, since both sides of the slab is same, the dipole moments are cancelled resulting in a constant value of the planar average of the electrostatic potential ( $V(z)$ ) in the vacuum region. For the Mn-doped systems, we have used dipole corrections for the cases where  $V(z)$  is not planar. Below are the plots of the eplanar average of the lectrostatic potential as a function of  $z$  for the different configurations:



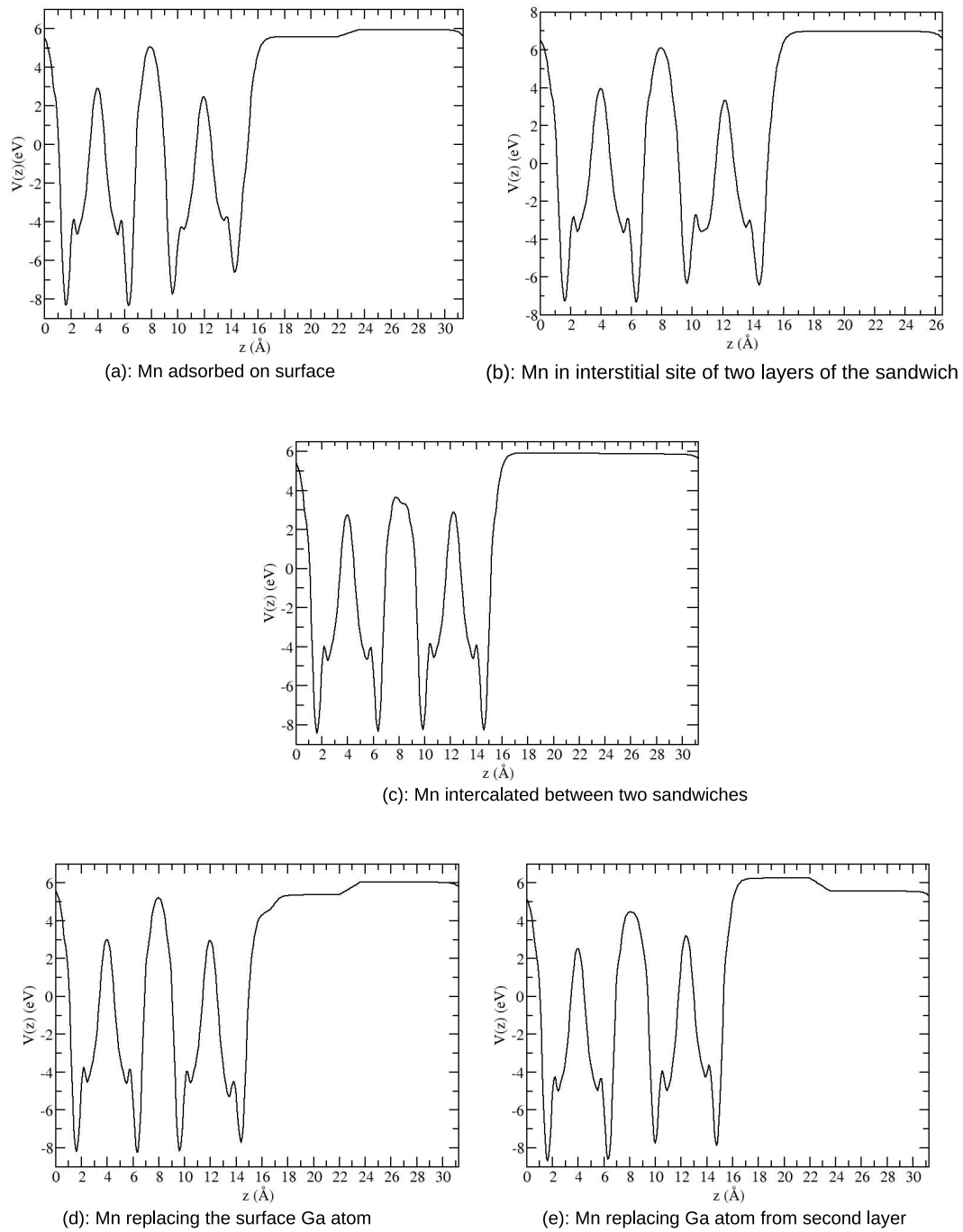
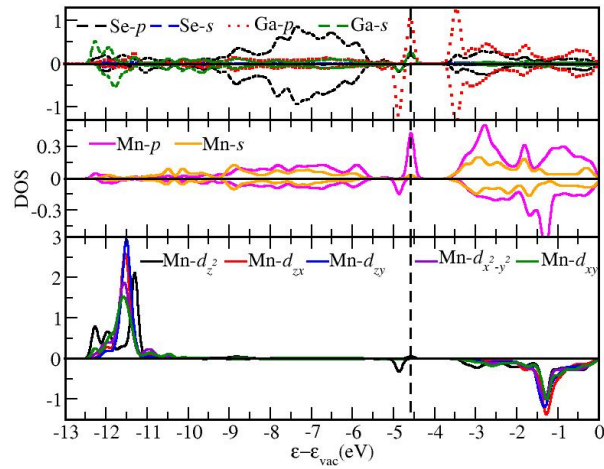


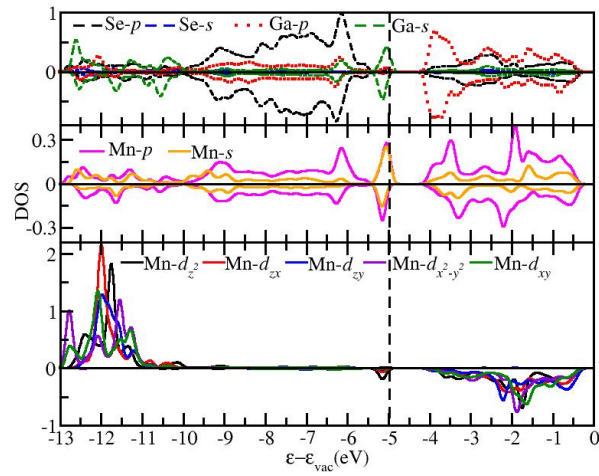
FIGURE 26: Dipole corrected electrostatic potential for all the Mn-doped GaSe(0001) surfaces

## .2 Density of states of Mn-doped GaSe(0001) surface

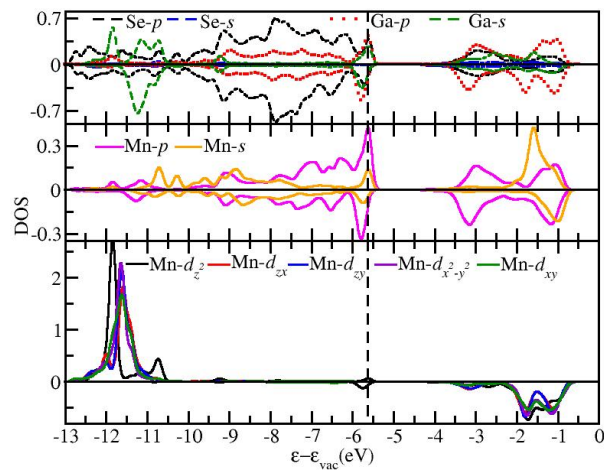
Following are the DOS plots of the three Mn-doped GaSe(0001) structures where Mn is adsorbed at the surface, Mn is present interstitially and Mn replaces Ga atom from the 2nd layer. Similar to the DOS for structure where Mn substitutes Ga from the 1st layer (figure 5.23) we find that the occupied region in the following DOS plots can be divided in two regions. First region can be from -13 eV to -10 eV which consists of localised Mn- $d$  interacting weakly with Ga- $s$  state. The second region, from -10 eV to valence band maxima, comprises of  $s, p$  states of Se, Ga and Mn. In structures where Mn substitutes Ga from 2nd (or even 1st) layer and Mn adsorbs on the surface, the dopant atom has a Ga atom right above and below its position. Hence we find greater contribution from  $p$ , specifically  $p_z$ , of Ga and Mn at the valence band edge for these two structures than in other structures.



(a)



(b)



(c)

FIGURE 27: Density of states of  $s$  and  $p$  states of Ga and Se (top panel),  $s$  and  $p$  states of Mn (middle panel) and  $d$  states of Mn (bottom panel) for Mn-doped GaSe(0001) where (a) Mn is adsorbed on the surface at Se-Se bridge site, (b) Mn is present interstitially and (c) Mn replaces Ga atom from 2st layer with the replaced Ga intercalating between two sandwiches.

# Bibliography

- [1] Wei Zhao, Julian Gebhardt, Florian Späth, Karin Gotterbarm, Christoph Gleichweit, Hans-Peter Steinrück, Andreas Görling, and Christian Papp. Reversible hydrogenation of graphene on ni(111)—synthesis of “graphone”. *Chemistry – A European Journal*, 21(8):3347–3358, 2015.
- [2] S. Dash, N. Joshi, G. Drera, P. Ghosh, E. Magnano, F. Bondino, P. Galinetto, M. C. Mozzati, G. Salvinelli, V. Aguekian, and L. Sangaletti. Cation diffusion and hybridization effects at the mn-gase(0001) reacted interface: Ab initio calculations and soft x-ray electron spectroscopy studies. *Phys. Rev. B*, 93:115304, Mar 2016.
- [3] A. K. Geim and K. S. Novoselov. The rise of graphene. *Nature Materials*, 6(3):183–191, 2007.
- [4] D. C. Elias, R. R. Nair, T. M. G. Mohiuddin, S. V. Morozov, P. Blake, M. P. Halsall, A. C. Ferrari, D. W. Boukhvalov, M. I. Katsnelson, A. K. Geim, and K. S. Novoselov. Control of graphene’s properties by reversible hydrogenation: Evidence for graphane. *Science*, 323(5914):610–613, 2009.
- [5] Akhtar Hussain, Saif Ullah, and M. Arshad Farhan. Fine tuning the band-gap of graphene by atomic and molecular doping: a density functional theory study. *RSC Adv.*, 6:55990–56003, 2016.
- [6] Lin Du, Tam N. Nguyen, Ari Gilman, André R. Muniz, and Dimitrios Maroudas. Tuning the band structure of graphene nanoribbons through defect-interaction-driven edge patterning. *Phys. Rev. B*, 96:245422, Dec 2017.
- [7] A. A. Avetisyan, B. Partoens, and F. M. Peeters. Electric field tuning of the band gap in graphene multilayers. *Phys. Rev. B*, 79:035421, Jan 2009.

- [8] A. Avetisyan, Bart Partoens, and F. Peeters. Electric-field control of the band gap and fermi energy in graphene multilayers by top and back gates. *Phys. Rev. B*, 80, 11 2009.
- [9] Hamid Oughaddou, Hanna Enriquez, Mohammed Rachid Tchalala, Handan Yildirim, Andrew J. Mayne, Azzedine Bendounan, Gérald Dujardin, Mustapha Ait Ali, and Abdelkader Kara. Silicene, a promising new 2d material. *Progress in Surface Science*, 90(1):46 – 83, 2015. Special Issue on Silicene.
- [10] A Acun, L Zhang, P Bampoulis, M Farmanbar, A van Houselt, A N Rudenko, M Lingenfelder, G Brocks, B Poelsema, M I Katsnelson, and H J W Zandvliet. Germanene: the germanium analogue of graphene. *Journal of Physics: Condensed Matter*, 27(44):443002, oct 2015.
- [11] Apratim Khandelwal, Karthick Mani, Manohar Harsha Karigerasi, and Indranil Lahiri. Phosphorene – the two-dimensional black phosphorous: Properties, synthesis and applications. *Materials Science and Engineering: B*, 221:17 – 34, 2017.
- [12] P. Beilstein Vogt. Silicene, germanene and other group iv 2d materials. *J. Nanotechnol.*, 9:2665–2667, 09 2018.
- [13] Botao Fu, M Abid, and Cheng-Cheng Liu. Systematic study on stanene bulk states and the edge states of its zigzag nanoribbon. *New Journal of Physics*, 19(10):103040, nov 2017.
- [14] Dinh Loc Duong, Seok Joon Yun, and Young Hee Lee. van der waals layered materials: Opportunities and challenges. *ACS Nano*, 11(12):11803–11830, 2017. PMID: 29219304.
- [15] G.R. Bhimanapati, N.R. Glavin, and J.A. Robinson. Chapter three - 2d boron nitride: Synthesis and applications. In Francesca Iacopi, John J. Boeckl, and Chennupati Jagadish, editors, *2D Materials*, volume 95 of *Semiconductors and Semimetals*, pages 101 – 147. Elsevier, 2016.
- [16] Juan Xia, Jin Wang, Dongliang Chao, Zhen Chen, Zheng Liu, Jer-Lai Kuo, Jiayu Yan, and Ze Xiang Shen. Phase evolution of lithium intercalation dynamics in 2h-mos<sub>2</sub>. *Nanoscale*, 9:7533–7540, 2017.

- [17] Julia C. E. Rasch, Torsten Stemmler, Beate Müller, Lenart Dudy, and Recardo Manzke.  $1t-tiSe_2$ : Semimetal or semiconductor? *Phys. Rev. Lett.*, 101:237602, Dec 2008.
- [18] Bao Liu, Jie Yang, Yonghao Han, Tingjing Hu, Wanbin Ren, Cailong Liu, Yanzhang Ma, and Chunxiao Gao. Electronic structure of  $tiSe_2$  and its electric transport properties under high pressure. *Journal of Applied Physics*, 109(5):053717, 2011.
- [19] Seok Joon Yun, Gang Hee Han, Hyun Kim, Dinh Loc Duong, Bong Gyu Shin, Jiong Zhao, Quoc An Vu, Jubok Lee, Seung Mi Lee, and Young Hee Lee. Telluriding monolayer  $MoS_2$  and  $WS_2$  via alkali metal sinter. *Nature Communications*, 8(1):2163, 2017.
- [20] Ming-Wei Lin, Houlong L. Zhuang, Jiaqiang Yan, Thomas Zac Ward, Alexander A. Puretzy, Christopher M. Rouleau, Zheng Gai, Liangbo Liang, Vincent Meunier, Bobby G. Sumpter, Panchapakesan Ganesh, Paul R. C. Kent, David B. Geohegan, David G. Mandrus, and Kai Xiao. Ultrathin nanosheets of  $CrSiTe_3$ : a semiconducting two-dimensional ferromagnetic material. *J. Mater. Chem. C*, 4:315–322, 2016.
- [21] Houlong L. Zhuang, Yu Xie, P. R. C. Kent, and P. Ganesh. Computational discovery of ferromagnetic semiconducting single-layer  $CrSiTe_3$ . *Phys. Rev. B*, 92:035407, Jul 2015.
- [22] Manish Chhowalla, Debdeep Jena, and Hua Zhang. Two-dimensional semiconductors for transistors. *Nature Reviews Materials*, 1(11):16052, 2016.
- [23] W. Cao, J. Kang, S. Bertolazzi, A. Kis, and K. Banerjee. Can 2d-nanocrystals extend the lifetime of floating-gate transistor based nonvolatile memory? *IEEE Transactions on Electron Devices*, 61(10):3456–3464, Oct 2014.
- [24] Jun Kang, Sefaattin Tongay, Jian Zhou, Jingbo Li, and Junqiao Wu. Band offsets and heterostructures of two-dimensional semiconductors. *Applied Physics Letters*, 102(1):012111, 2013.

- [25] Xiaoping Hong, Jonghwan Kim, Su-Fei Shi, Yu Zhang, Chenhao Jin, Yinghui Sun, Sefaattin Tongay, Junqiao Wu, Yanfeng Zhang, and Feng Wang. Ultrafast charge transfer in atomically thin mos<sub>2</sub>/ws<sub>2</sub> heterostructures. *Nature Nanotechnology*, 9(9):682–686, 2014.
- [26] K. S. Novoselov, A. Mishchenko, A. Carvalho, and A. H. Castro Neto. 2d materials and van der waals heterostructures. *Science*, 353(6298), 2016.
- [27] Yanping Liu, Siyu Zhang, Jun He, Zhiming M. Wang, and Zongwen Liu. Recent progress in the fabrication, properties, and devices of heterostructures based on 2d materials. *Nano-Micro Letters*, 11(1):13, 2019.
- [28] Xing Zhou, Xiaozong Hu, Jing Yu, Shiyuan Liu, Zhaowei Shu, Qi Zhang, Huiqiao Li, Ying Ma, Hua Xu, and Tianyou Zhai. 2d layered material-based van der waals heterostructures for optoelectronics. *Advanced Functional Materials*, 28(14):1706587, 2018.
- [29] N.H. Al-Hardan, M.J. Abdullah, N.M. Ahmed, F.K. Yam, and A. Abdul Aziz. Uv photodetector behavior of 2d zno plates prepared by electrochemical deposition. *Superlattices and Microstructures*, 51(6):765 – 771, 2012.
- [30] Young Duck Kim, Hakseong Kim, Yujin Cho, Ji Hoon Ryoo, Cheol-Hwan Park, Pilkwang Kim, Yong Seung Kim, Sunwoo Lee, Yilei Li, Seung-Nam Park, Yong Shim Yoo, Duhee Yoon, Vincent E. Dorgan, Eric Pop, Tony F. Heinz, James Hone, Seung-Hyun Chun, Hyeonsik Cheong, Sang Wook Lee, Myung-Ho Bae, and Yun Daniel Park. Bright visible light emission from graphene. *Nature Nanotechnology*, 10(8):676–681, 2015.
- [31] Lukas Dobusch, Simone Schuler, Vasili Perebeinos, and Thomas Mueller. Thermal light emission from monolayer mos<sub>2</sub>. *Advanced Materials*, 29(31):1701304, 2017.
- [32] Keith E. Whitener. Review article: Hydrogenated graphene: A user’s guide. *Journal of Vacuum Science & Technology A*, 36(5):05G401, 2018.
- [33] T. O. Wehling, K. S. Novoselov, S. V. Morozov, E. E. Vdovin, M. I. Katsnelson, A. K. Geim, and A. I. Lichtenstein. Molecular doping of graphene. *Nano Letters*, 8(1):173–177, 2008. PMID: 18085811.

- [34] Aurélien Lherbier, X. Blase, Yann-Michel Niquet, François Triozon, and Stephan Roche. Charge transport in chemically doped 2d graphene. *Phys. Rev. Lett.*, 101:036808, Jul 2008.
- [35] Dacheng Wei, Yunqi Liu, Yu Wang, Hongliang Zhang, Liping Huang, and Gui Yu. Synthesis of n-doped graphene by chemical vapor deposition and its electrical properties. *Nano Letters*, 9(5):1752–1758, 2009. PMID: 19326921.
- [36] Peitao Liu, Yonggang Liu, Weichun Ye, Ji Ma, and Daqiang Gao. Flower-like n-doped MoS<sub>2</sub> for photocatalytic degradation of RhB by visible light irradiation. *Nanotechnology*, 27(22):225403, apr 2016.
- [37] Yafei Zhao, Jiai Ning, Xiaoying Hu, Jian Tu, Wenqin Zou, Xuezhong Ruan, Yao Li, Yongbing Xu, and Liang He. Adjustable electronic, optical and photocatalytic properties of black phosphorene by nonmetal doping. *Applied Surface Science*, page 144488, 2019.
- [38] Xiaojia Liu, Liping Li, Yuanjie Wei, Yizhi Zheng, Qian Xiao, and Bo Feng. Facile synthesis of boron- and nitride-doped mos<sub>2</sub> nanosheets as fluorescent probes for the ultrafast, sensitive, and label-free detection of hg<sup>2+</sup>. *Analyst*, 140:4654–4661, 2015.
- [39] Hakkim Vovusha, Tanveer Hussain, Muhammad Sajjad, Hoonkyung Lee, Amir Karton, Rajeev Ahuja, and Udo Schwingenschlögl. Sensitivity enhancement of stanene towards toxic so<sub>2</sub> and h<sub>2</sub>s. *Applied Surface Science*, 495:143622, 2019.
- [40] Mohammad Asadi, Bijandra Kumar, Amirhossein Behranginia, Brian A. Rosen, Artem Baskin, Nikita Replin, Davide Pisasale, Patrick Phillips, Wei Zhu, Richard Haasch, Robert F. Klie, Petr Král, Jeremiah Abiade, and Amin Salehi-Khojin. Robust carbon dioxide reduction on molybdenum disulphide edges. *Nature Communications*, 5(1):4470, 2014.
- [41] Mohammad Asadi, Kibum Kim, Cong Liu, Aditya Venkata Addepalli, Pedram Abbasi, Poya Yasaei, Patrick Phillips, Amirhossein Behranginia, José M. Cer-rato, Richard Haasch, Peter Zapol, Bijandra Kumar, Robert F. Klie, Jeremiah Abiade, Larry A. Curtiss, and Amin Salehi-Khojin. Nanostructured transition



- metal dichalcogenide electrocatalysts for co2 reduction in ionic liquid. *Science*, 353(6298):467–470, 2016.
- [42] Marcus Freitag, Hsin-Ying Chiu, Mathias Steiner, Vasili Perebeinos, and Phaedon Avouris. Thermal infrared emission from biased graphene. *Nature Nanotechnology*, 5(7):497–501, 2010.
- [43] C. R. Woods, L. Britnell, A. Eckmann, R. S. Ma, J. C. Lu, H. M. Guo, X. Lin, G. L. Yu, Y. Cao, R. V. Gorbachev, A. V. Kretinin, J. Park, L. A. Ponomarenko, M. I. Katsnelson, Yu N Gornostyrev, K. Watanabe, T. Taniguchi, C. Casiraghi, H.-J. Gao, A. K. Geim, and K. S. Novoselov. Commensurate-incommensurate transition in graphene on hexagonal boron nitride. *Nature Physics*, 10(6):451–456, 2014.
- [44] Min Gao, Yi Pan, Chendong Zhang, Hao Hu, Rong Yang, Hongliang Lu, Jinming Cai, Shixuan Du, Feng Liu, and H.-J. Gao. Tunable interfacial properties of epitaxial graphene on metal substrates. *Applied Physics Letters*, 96(5):053109, 2010.
- [45] Liqin Su, Yifei Yu, Linyou Cao, and Yong Zhang. Effects of substrate type and material-substrate bonding on high-temperature behavior of monolayer ws2. *Nano Research*, 8(8):2686–2697, Aug 2015.
- [46] R. Yakimova, T. Iakimov, G. R. Yazdi, C. Bouhafs, J. Eriksson, A. Zakharov, A. Boosalis, M. Schubert, and V. Darakchieva. Morphological and electronic properties of epitaxial graphene on SiC. *Physica B Condensed Matter*, 439:54–59, Apr 2014.
- [47] Niharika Joshi, Nirmalya Ballav, and Prasenjit Ghosh. Hydrogen-induced reversal of spin alignment in graphene supported on ni(111) surface. *Phys. Rev. B*, 86:121411, Sep 2012.
- [48] Niharika Joshi, Indu Kaul, Nirmalya Ballav, and Prasenjit Ghosh. Spin enhancement and band gap opening of ferrimagnetic graphene on fcc-co(111) surface upon hydrogenation. *AIP Conference Proceedings*, 1512(1):694–695, 2013.

- [49] M. C. Payne, M. P. Teter, D. C. Allan, T. A. Arias, and J. D. Joannopoulos. Iterative minimization techniques for ab initio total-energy calculations: molecular dynamics and conjugate gradients. *Rev. Mod. Phys.*, 64:1045–1097, Oct 1992.
- [50] Jos Thijsen. *Computational Physics*. Cambridge University Press, 2 edition, 2007.
- [51] R.G. Parr and W. Yang. *Density-Functional theory of atoms and molecules*. Oxford University Press, 1989.
- [52] R.M. Martin. *Electronic Structure: Basic Theory and Practical Methods*. Cambridge University Press, 2008.
- [53] Vladimir I. Anisimov, Jan Zaanen, and Ole K. Andersen. Band theory and mott insulators: Hubbard u instead of stoner i. *Phys. Rev. B*, 44:943–954, Jul 1991.
- [54] V. I. Anisimov, I. V. Solovyev, M. A. Korotin, M. T. Czyżyk, and G. A. Sawatzky. Density-functional theory and nio photoemission spectra. *Phys. Rev. B*, 48:16929–16934, Dec 1993.
- [55] W. E. Pickett, S. C. Erwin, and E. C. Ethridge. Reformulation of the LDA +  $u$  method for a local-orbital basis. *Phys. Rev. B*, 58:1201–1209, Jul 1998.
- [56] Vladimir I Anisimov, F Aryasetiawan, and A I Lichtenstein. First-principles calculations of the electronic structure and spectra of strongly correlated systems: theLDA umethod. *Journal of Physics: Condensed Matter*, 9(4):767–808, jan 1997.
- [57] Matteo Cococcioni and Stefano de Gironcoli. Linear response approach to the calculation of the effective interaction parameters in the LDA + U method. *Phys. Rev. B*, 71:035105, Jan 2005.
- [58] N.W. Ashcroft and N.D. Mermin. *Solid state physics*. Science: Physics. Saunders College, 1976.
- [59] Jorge O. Sofo, Ajay S. Chaudhari, and Greg D. Barber. Graphane: A two-dimensional hydrocarbon. *Phys. Rev. B*, 75:153401, Apr 2007.
- [60] J. Zhou, Q. Wang, Q. Sun, X. S. Chen, Y. Kawazoe, and P. Jena. Ferromagnetism in semihydrogenated graphene sheet. *Nano Letters*, 9(11):3867–3870, 2009. PMID: 19719081.

- [61] L. Feng and W. X. Zhang. The structure and magnetism of graphone. *AIP Advances*, 2(4):042138, 2012.
- [62] Željko Šljivančanin, Richard Balog, and Liv Hornekær. Magnetism in graphene induced by hydrogen adsorbates. *Chemical Physics Letters*, 541:70 – 74, 2012.
- [63] Wei Zhao, Julian Gebhardt, Florian Späth, Karin Gotterbarm, Christoph Gleichweit, Hans-Peter Steinrück, Andreas Görling, and Christian Papp. Reversible hydrogenation of graphene on ni(111)—synthesis of “graphone”. *Chemistry – A European Journal*, 21(8):3347–3358, 2015.
- [64] M. Bernien, J. Miguel, C. Weis, Md. E. Ali, J. Kurde, B. Krumme, P. M. Panchmatia, B. Sanyal, M. Piantek, P. Srivastava, K. Baberschke, P. M. Oppeneer, O. Eriksson, W. Kuch, and H. Wende. Tailoring the nature of magnetic coupling of fe-porphyrin molecules to ferromagnetic substrates. *Phys. Rev. Lett.*, 102:047202, Jan 2009.
- [65] Liang Ma, Xiao Cheng Zeng, and Jinlan Wang. Oxygen intercalation of graphene on transition metal substrate: An edge-limited mechanism. *The Journal of Physical Chemistry Letters*, 6(20):4099–4105, 2015. PMID: 26722784.
- [66] Stefano Gottardi, Kathrin Müller, Luca Bignardi, Juan Carlos Moreno-López, Tuan Anh Pham, Oleksii Ivashenko, Mikhail Yablonskikh, Alexei Barinov, Jonas Björk, Petra Rudolf, and Meike Stöhr. Comparing graphene growth on cu(111) versus oxidized cu(111). *Nano Letters*, 15(2):917–922, 2015. PMID: 25611528.
- [67] Elin Grånäs, Jan Knudsen, Ulrike A. Schröder, Timm Gerber, Carsten Busse, Mohammad A. Arman, Karina Schulte, Jesper N. Andersen, and Thomas Michely. Oxygen intercalation under graphene on ir(111): Energetics, kinetics, and the role of graphene edges. *ACS Nano*, 6(11):9951–9963, 2012. PMID: 23039853.
- [68] Paolo Giannozzi, Stefano Baroni, Nicola Bonini, Matteo Calandra, Roberto Car, Carlo Cavazzoni, Davide Ceresoli, Guido L Chiarotti, Matteo Cococcioni, Ismaila Dabo, Andrea Dal Corso, Stefano de Gironcoli, Stefano Fabris, Guido Fratesi, Ralph Gebauer, Uwe Gerstmann, Christos Gougoussis, Anton Kokalj, Michele

- Lazzeri, Layla Martin-Samos, Nicola Marzari, Francesco Mauri, Riccardo Mazzarello, Stefano Paolini, Alfredo Pasquarello, Lorenzo Paulatto, Carlo Sbraccia, Sandro Scandolo, Gabriele Sclauzero, Ari P Seitsonen, Alexander Smogunov, Paolo Umari, and Renata M Wentzcovitch. Quantum espresso: a modular and open-source software project for quantum simulations of materials. *J. Phys.: Condens. Matter*, 21:395502, 2009.
- [69] David Vanderbilt. Soft self-consistent pseudopotentials in a generalized eigenvalue formalism. *Phys. Rev. B*, 41(11):7892–7895, 1990.
- [70] John P. Perdew, Kieron Burke, and Matthias Ernzerhof. Generalized gradient approximation made simple. *Phys. Rev. Lett.*, 77(18):3865–3868, 1996.
- [71] Hendrik J. Monkhorst and James D. Pack. Special points for brillonin-zone integrations. *Phys. Rev. B*, 13(12):5188–5192, 1976.
- [72] Nicola Marzari, David Vanderbilt, Alessandro De Vita, and M. C. Payne. Thermal contraction and disordering of the al(110) surface. *Phys. Rev. Lett.*, 82(16):3296–3299, 1999.
- [73] P. B. Balbuena and V. R Subramanian. *Theory and Experiment in Electrocatalysis*. Modern Aspects of Electrochemistry. Springer-Verlag New York, 2010.
- [74] S. López-Moreno and A. H. Romero. Atomic and molecular oxygen adsorbed on (111) transition metal surfaces: Cu and ni. *The Journal of Chemical Physics*, 142(15):154702, 2015.
- [75] Tao Li, Bhawna Bhatia, and David S. Sholl. First-principles study of c adsorption, o adsorption, and co dissociation on flat and stepped ni surfaces. *The Journal of Chemical Physics*, 121(20):10241–10249, 2004.
- [76] Marek Gajdo, Andreas Eichler, and Jürgen Hafner. CO adsorption on close-packed transition and noble metal surfaces: trends from ab initio calculations. *Journal of Physics: Condensed Matter*, 16(8):1141–1164, feb 2004.
- [77] Christian F. Hermanns, Kartick Tarafder, Matthias Bernien, Alex Krüger, Yin-Ming Chang, Peter M. Oppeneer, and Wolfgang Kuch. Magnetic coupling of

- porphyrin molecules through graphene. *Advanced Materials*, 25(25):3473–3477, 2013.
- [78] C. Sorg, N. Ponpandian, M. Bernien, K. Baberschke, H. Wende, and R. Q. Wu. Induced magnetism of oxygen in surfactant-grown fe, co, and ni monolayers. *Phys. Rev. B*, 73:064409, Feb 2006.
- [79] Dorota Chylarecka, Christian Wäckerlin, Timur K. Kim, Kathrin Müller, Frithjof Nolting, Armin Kleibert, Nirmalya Ballav, and Thomas A. Jung. Self-assembly and superexchange coupling of magnetic molecules on oxygen-reconstructed ferromagnetic thin film. *The Journal of Physical Chemistry Letters*, 1(9):1408–1413, 2010.
- [80] Christian Wäckerlin, Jan Nowakowski, Shi-Xia Liu, Michael Jaggi, Dorota Siewert, Jan Girovsky, Aneliia Shchyrba, Tatjana Hählen, Armin Kleibert, Peter M. Oppeneer, Frithjof Nolting, Silvio Decurtins, Thomas A. Jung, and Nirmalya Ballav. Two-dimensional supramolecular electron spin arrays. *Advanced Materials*, 25(17):2404–2408, 2013.
- [81] J. Zhou, Q. Wang, Q. Sun, X. S. Chen, Y. Kawazoe, and P. Jena. Ferromagnetism in semihydrogenated graphene sheet. *Nano Letters*, 9(11):3867–3870, 2009. PMID: 19719081.
- [82] . Šljivančanin, E. Rauls, L. Hornekær, W. Xu, F. Besenbacher, and B. Hammer. Extended atomic hydrogen dimer configurations on the graphite(0001) surface. *The Journal of Chemical Physics*, 131(8):084706, 2009.
- [83] Željko Šljivančanin, Mie Andersen, Liv Hornekær, and Bjørk Hammer. Structure and stability of small h clusters on graphene. *Phys. Rev. B*, 83:205426, May 2011.
- [84] Richard Balog, Bjarke Jørgensen, Justin Wells, Erik Lægsgaard, Philip Hofmann, Flemming Besenbacher, and Liv Hornekær. Atomic hydrogen adsorbate structures on graphene. *Journal of the American Chemical Society*, 131(25):8744–8745, 2009. PMID: 19496562.
- [85] L. Feng and W. X. Zhang. The structure and magnetism of graphone. *AIP Advances*, 2(4):042138, 2012.

- [86] Željko Šljivančanin, Richard Balog, and Liv Hornekær. Magnetism in graphene induced by hydrogen adsorbates. *Chemical Physics Letters*, 541:70 – 74, 2012.
- [87] P. A. Khomyakov, G. Giovannetti, P. C. Rusu, G. Brocks, J. van den Brink, and P. J. Kelly. First-principles study of the interaction and charge transfer between graphene and metals. *Phys. Rev. B*, 79:195425, May 2009.
- [88] Sergey M. Kozlov, Francesc Viñes, and Andreas Görling. Bonding mechanisms of graphene on metal surfaces. *The Journal of Physical Chemistry C*, 116(13):7360–7366, 2012.
- [89] Line Kyhl, Richard Balog, Thierry Angot, Liv Hornekær, and Régis Bisson. Hydrogenated graphene on ir(111): A high-resolution electron energy loss spectroscopy study of the vibrational spectrum. *Phys. Rev. B*, 93:115403, Mar 2016.
- [90] S. Son, C. Holroyd, J. Clough, A. Horn, S. P. K. Koehler, and C. Casiraghi. Substrate dependence of graphene reactivity towards hydrogenation. *Applied Physics Letters*, 109(24):243103, 2016.
- [91] M. L. Ng, R. Balog, L. Hornekær, A. B. Preobrajenski, N. A. Vinogradov, N. Mårtensson, and K. Schulte. Controlling hydrogenation of graphene on transition metals. *The Journal of Physical Chemistry C*, 114(43):18559–18565, 2010.
- [92] Niharika Joshi, Nirmalya Ballav, and Prasenjit Ghosh. Hydrogen-induced reversal of spin alignment in graphene supported on ni(111) surface. *Phys. Rev. B*, 86:121411, Sep 2012.
- [93] Thomas Olsen and Kristian S. Thygesen. Random phase approximation applied to solids, molecules, and graphene-metal interfaces: From van der waals to covalent bonding. *Phys. Rev. B*, 87:075111, Feb 2013.
- [94] Andrew M. Rappe, Karin M. Rabe, Efthimios Kaxiras, and J. D. Joannopoulos. Optimized pseudopotentials. *Phys. Rev. B*, 41:1227–1230, Jan 1990.
- [95] Stefan Grimme. Semiempirical gga-type density functional constructed with a long-range dispersion correction. *Journal of Computational Chemistry*, 27(15):1787–1799, 2006.

- [96] Vincenzo Barone, Maurizio Casarin, Daniel Forrer, Michele Pavone, Mauro Sambi, and Andrea Vittadini. Role and effective treatment of dispersive forces in materials: Polyethylene and graphite crystals as test cases. *Journal of Computational Chemistry*, 30(6):934–939, 2009.
- [97] Y. Gamo, A. Nagashima, M. Wakabayashi, M. Terai, and C. Oshima. Atomic structure of monolayer graphite formed on ni(111). *Surface Science*, 374(1):61 – 64, 1997.
- [98] Wei Zhao, Sergey M. Kozlov, Oliver Höfert, Karin Gotterbarm, Michael P. A. Lorenz, Francesc Viñes, Christian Papp, Andreas Görling, and Hans-Peter Steinrück. Graphene on ni(111): Coexistence of different surface structures. *The Journal of Physical Chemistry Letters*, 2(7):759–764, 2011.
- [99] F. Ortmann, F. Bechstedt, and W. G. Schmidt. Semiempirical van der waals correction to the density functional description of solids and molecular structures. *Phys. Rev. B*, 73:205101, May 2006.
- [100] Ikutaro Hamada and Minoru Otani. Comparative van der waals density-functional study of graphene on metal surfaces. *Phys. Rev. B*, 82:153412, Oct 2010.
- [101] M. Dion, H. Rydberg, E. Schröder, D. C. Langreth, and B. I. Lundqvist. Van der waals density functional for general geometries. *Phys. Rev. Lett.*, 92:246401, Jun 2004.
- [102] Kyuho Lee, Éamonn D. Murray, Lingzhu Kong, Bengt I. Lundqvist, and David C. Langreth. Higher-accuracy van der waals density functional. *Phys. Rev. B*, 82:081101, Aug 2010.
- [103] Valentino R. Cooper. Van der waals density functional: An appropriate exchange functional. *Phys. Rev. B*, 81:161104, Apr 2010.
- [104] N. Troullier and José Luís Martins. Efficient pseudopotentials for plane-wave calculations. *Phys. Rev. B*, 43:1993–2006, Jan 1991.
- [105] A. H. Castro Neto, F. Guinea, N. M. R. Peres, K. S. Novoselov, and A. K. Geim. The electronic properties of graphene. *Rev. Mod. Phys.*, 81:109–162, Jan 2009.

- [106] P. O. Lehtinen, A. S. Foster, Yuchen Ma, A. V. Krasheninnikov, and R. M. Nieminen. Irradiation-induced magnetism in graphite: A density functional study. *Phys. Rev. Lett.*, 93:187202, Oct 2004.
- [107] Oleg V. Yazyev and Lothar Helm. Defect-induced magnetism in graphene. *Phys. Rev. B*, 75:125408, Mar 2007.
- [108] Wei Han, Roland K. Kawakami, Martin Gmitra, and Jaroslav Fabian. Graphene spintronics. *Nature Nanotechnology*, 9(10):794–807, 2014.
- [109] S H M Jafri, K Carva, E Widenkvist, T Blom, B Sanyal, J Fransson, O Eriksson, U Jansson, H Grennberg, O Karis, R A Quinlan, B C Holloway, and K Leifer. Conductivity engineering of graphene by defect formation. *Journal of Physics D: Applied Physics*, 43(4):045404, jan 2010.
- [110] Igor A. Pašti, Aleksandar Jovanović, Ana S. Dobrota, Slavko V. Mentus, Börje Johansson, and Natalia V. Skorodumova. Atomic adsorption on graphene with a single vacancy: systematic dft study through the periodic table of elements. *Phys. Chem. Chem. Phys.*, 20:858–865, 2018.
- [111] Hongwei Zhang and Ruitao Lv. Defect engineering of two-dimensional materials for efficient electrocatalysis. *Journal of Materiomics*, 4(2):95 – 107, 2018. Two Dimensional Materials.
- [112] Ileana G. Rau, Susanne Baumann, Stefano Rusponi, Fabio Donati, Sebastian Stepanow, Luca Gragnaniello, Jan Dreiser, Cinthia Piamonteze, Frithjof Nolting, Shruha Gangopadhyay, Oliver R. Albertini, Roger M. Macfarlane, Christopher P. Lutz, Barbara A. Jones, Pietro Gambardella, Andreas J. Heinrich, and Harald Brune. Reaching the magnetic anisotropy limit of a 3d metal atom. *Science*, 344(6187):988–992, 2014.
- [113] Patrick Bruno. Tight-binding approach to the orbital magnetic moment and magnetocrystalline anisotropy of transition-metal monolayers. *Physical Review B*, 39(1):865, 1989.



- [114] Bin Shao, Wu-Jun Shi, Min Feng, and Xu Zuo. Large perpendicular magnetic anisotropy of single co atom on mgo monolayer: A first-principles study. *Journal of Applied Physics*, 117(17):17B316, 2015.
- [115] P. Gambardella, S. Rusponi, M. Veronese, S. S. Dhesi, C. Grazioli, A. Dallmeyer, I. Cabria, R. Zeller, P. H. Dederichs, K. Kern, C. Carbone, and H. Brune. Giant magnetic anisotropy of single cobalt atoms and nanoparticles. *Science*, 300(5622):1130–1133, 2003.
- [116] Mahdi Sargolzaei and Farideh Gudarzi. Magnetic properties of single 3d transition metals adsorbed on graphene and benzene: A density functional theory study. *Journal of Applied Physics*, 110(6):064303, 2011.
- [117] Hem C. Kandpal, Klaus Koepnik, and Manuel Richter. Strong magnetic anisotropy of chemically bound co dimers in a graphene sheet. *Phys. Rev. B*, 86:235430, Dec 2012.
- [118] E. J. G. Santos, D. Sánchez-Portal, and A. Ayuela. Magnetism of substitutional co impurities in graphene: Realization of single  $\pi$  vacancies. *Phys. Rev. B*, 81:125433, Mar 2010.
- [119] A. V. Krasheninnikov, P. O. Lehtinen, A. S. Foster, P. Pyykkö, and R. M. Nieminen. Embedding transition-metal atoms in graphene: Structure, bonding, and magnetism. *Phys. Rev. Lett.*, 102:126807, Mar 2009.
- [120] K Zhang, Y Li, Y Liu, and L Shi. Giant magnetic anisotropy of rare-earth adatoms and dimers adsorbed by graphene oxide. *Phys. Chem. Chem. Phys.*, 19:13245, Apr 2017.
- [121] X Zhang, S Yu, H Cheng, and W Zheng. Tm atoms on b/n doped defective graphene as a catalyst for oxygen reduction reaction: a theoretical study. *RSC Adv.*, 5:82804, September 2015.
- [122] Shyam Kattel, Plamen Atanassov, and Boris Kiefer. Stability, electronic and magnetic properties of in-plane defects in graphene: A first-principles study. *The Journal of Physical Chemistry C*, 116(14):8161–8166, 2012.

- [123] Lu Wang, Xiuyun Zhang, Helen L.W. Chan, Feng Yan, and Feng Ding. Formation and healing of vacancies in graphene chemical vapor deposition (cvd) growth. *Journal of the American Chemical Society*, 135(11):4476–4482, 2013. PMID: 23444843.
- [124] Wendel S. Paz, Wanderlã L. Scopel, and Jair C.C. Freitas. On the connection between structural distortion and magnetism in graphene with a single vacancy. *Solid State Communications*, 175-176:71 – 75, 2013. Special Issue: Graphene V: Recent Advances in Studies of Graphene and Graphene analogues.
- [125] A. A. El-Barbary, R. H. Telling, C. P. Ewels, M. I. Heggie, and P. R. Briddon. Structure and energetics of the vacancy in graphite. *Phys. Rev. B*, 68:144107, Oct 2003.
- [126] Stephen T Skowron, Irina V Lebedeva, Andrey M Popov, and Elena Bichoutskaia. Energetics of atomic scale structure changes in graphene. *Chemical Society Reviews*, 44(10):3143–3176, 2015.
- [127] AV Krasheninnikov, PO Lehtinen, AS Foster, and RM Nieminen. Bending the rules: contrasting vacancy energetics and migration in graphite and carbon nanotubes. *Chemical Physics Letters*, 418(1-3):132–136, 2006.
- [128] Alex W Robertson, Barbara Montanari, Kuang He, Christopher S Allen, Yimin A Wu, Nicholas M Harrison, Angus I Kirkland, and Jamie H Warner. Structural reconstruction of the graphene monovacancy. *ACS nano*, 7(5):4495–4502, 2013.
- [129] JJ Palacios and F Ynduráin. Critical analysis of vacancy-induced magnetism in monolayer and bilayer graphene. *Physical Review B*, 85(24):245443, 2012.
- [130] Alessandro Barla and other. Complex magnetic exchange coupling between co nanostructures and ni (111) across epitaxial graphene.
- [131] J Gebhardt, RJ Koch, W Zhao, O Höfert, K Gotterbarm, S Mammadov, C Papp, A Görling, H-P Steinrück, and Th Seyller. Growth and electronic structure of boron-doped graphene. *Physical Review B*, 87(15):155437, 2013.

- [132] Giovanni Carraro, Edvige Celasco, Marco Smerieri, Letizia Savio, Gianangelo Bracco, Mario Rocca, and Luca Vattuone. Chemisorption of co on n-doped graphene on ni (111). *Applied Surface Science*, 428:775–780, 2018.
- [133] RJ Koch, Martin Weser, W Zhao, F Viñes, K Gotterbarm, SM Kozlov, O Höfert, M Ostler, C Papp, J Gebhardt, et al. Growth and electronic structure of nitrogen-doped graphene on ni (111). *Physical Review B*, 86(7):075401, 2012.
- [134] Yuliang Mao, Jianmei Yuan, and Jianxin Zhong. Density functional calculation of transition metal adatom adsorption on graphene. *Journal of Physics: Condensed Matter*, 20(11):115209, 2008.
- [135] Abdulrafiu T Raji and Enrico B Lombardi. Stability, magnetic and electronic properties of cobalt–vacancy defect pairs in graphene: A first-principles study. *Physica B: Condensed Matter*, 464:28–37, 2015.
- [136] Piotr Błoński, Anne Lehnert, Samuel Dennler, Stefano Rusponi, Markus Etzkorn, Géraud Moulas, Peter Bencok, Pietro Gambardella, Harald Brune, and Jürgen Hafner. Magnetocrystalline anisotropy energy of co and fe adatoms on the (111) surfaces of pd and rh. *Physical Review B*, 81(10):104426, 2010.
- [137] K. Sato, L. Bergqvist, J. Kudrnovský, P. H. Dederichs, O. Eriksson, I. Turek, B. Sanyal, G. Bouzerar, H. Katayama-Yoshida, V. A. Dinh, T. Fukushima, H. Kizaki, and R. Zeller. First-principles theory of dilute magnetic semiconductors. *Rev. Mod. Phys.*, 82:1633–1690, May 2010.
- [138] H. Ohno, A. Shen, F. Matsukura, A. Oiwa, A. Endo, S. Katsumoto, and Y. Iye. (ga,mn)as: A new diluted magnetic semiconductor based on gaas. *Applied Physics Letters*, 69(3):363–365, 1996.
- [139] H. Ohno, A. Shen, F. Matsukura, A. Oiwa, A. Endo, S. Katsumoto, and Y. Iye. (ga,mn)as: A new diluted magnetic semiconductor based on gaas. *Applied Physics Letters*, 69(3):363–365, 1996.
- [140] S. A. Wolf, D. D. Awschalom, R. A. Buhrman, J. M. Daughton, S. von Molnár, M. L. Roukes, A. Y. Chtchelkanova, and D. M. Treger. Spintronics: A spin-based electronics vision for the future. *Science*, 294(5546):1488–1495, 2001.

- [141] Y. Ohno, D. K. Young, B. Beschoten, F. Matsukura, H. Ohno, and D. D. Awschalom. Electrical spin injection in a ferromagnetic semiconductor heterostructure. *Nature*, 402(6763):790–792, 1999.
- [142] A. Segura, J. Bouvier, M. V. Andrés, F. J. Manjón, and V. Muñoz. Strong optical nonlinearities in gallium and indium selenides related to inter-valence-band transitions induced by light pulses. *Phys. Rev. B*, 56:4075–4084, Aug 1997.
- [143] Yandong Ma, Ying Dai, Meng Guo, Lin Yu, and Baibiao Huang. Tunable electronic and dielectric behavior of gas and gase monolayers. *Phys. Chem. Chem. Phys.*, 15:7098–7105, 2013.
- [144] Wei Shi, Yujie J. Ding, Nils Fernelius, and Konstantin Vodopyanov. Efficient, tunable, and coherent 0.18–5.27-thz source based on gase crystal. *Opt. Lett.*, 27(16):1454–1456, Aug 2002.
- [145] S Nagel, A Baldereschi, and K Maschke. Tight-binding study of the electronic states in GaSe polytypes. *Journal of Physics C: Solid State Physics*, 12(9):1625–1639, may 1979.
- [146] Zhiyong Zhu, Yingchun Cheng, and Udo Schwingenschlögl. Topological phase transition in layered gas and gase. *Phys. Rev. Lett.*, 108:266805, Jun 2012.
- [147] Zhi-Shu Feng, Zhi-Hui Kang, Feng-Guang Wu, Jin-Yue Gao, Yun Jiang, Hong-Zhi Zhang, Yury M. Andreev, Grigory V. Lanskii, Viktor V. Atuchin, and Tatyana A. Gavrilova. Shg in doped gase:in crystals. *Opt. Express*, 16(13):9978–9985, Jun 2008.
- [148] N.C. Fernelius. Properties of gallium selenide single crystal. *Progress in Crystal Growth and Characterization of Materials*, 28(4):275 – 353, 1994.
- [149] N.B. Singh, D.R. Suhre, W. Rosch, R. Meyer, M. Marable, N.C. Fernelius, F.K. Hopkins, D.E. Zelmon, and R. Narayanan. Modified gase crystals for mid-ir applications. *Journal of Crystal Growth*, 198-199:588 – 592, 1999.

- 
- [150] T. M. Pekarek, B. C. Crooker, I. Miotkowski, and A. K. Ramdas. Magnetic measurements on the iii-vi diluted magnetic semiconductor  $\text{ga}_{1-x}\text{mn}_x\text{se}$ . *Journal of Applied Physics*, 83(11):6557–6559, 1998.
- [151] T. M. Pekarek, P. S. Edwards, T. L. Olejniczak, C. Lampropoulos, I. Miotkowski, and A. K. Ramdas. Magnetic properties of the layered iii-vi diluted magnetic semiconductor  $\text{ga}_{1-x}\text{fex}_{1-x}\text{te}$ . *AIP Advances*, 6(5):056222, 2016.
- [152] K Sato and H Katayama-Yoshida. First principles materials design for semiconductor spintronics. *Semiconductor Science and Technology*, 17(4):367–376, mar 2002.

---

## Publications

### Published

- N. Joshi and P. Ghosh, “Does semihydrogenated graphene on lattice matched transition metal substrates has a uniform hydrogen adsorption pattern?”, *J. Indian Chem. Soc.*, **96**,1-15 (2019). (Chapter 4)
- S. Dash, N. Joshi, G. Drera, P. Ghosh, E. Magnano, *et al.* “Cation diffusion and hybridization effects at Mn-GaSe(0001)reacted interface: ab-initio calculations and soft x-ray electron spectroscopy studies”, *Phys. Rev. B*, **93**,115304 (2016). (Chapter 5.4)

### Under communication

- N. Joshi, C. Gaurav, N. Ballav and P. Ghosh, “Tuning electronic and magnetic properties of graphone/Ni(111) interface by oxygen intercalation: A first principles prediction”, *under review in Phys. Rev. B*. (Chapter 3)

### Manuscript under preparation

- N. Joshi, and P. Ghosh, ”Strong magnetic anisotropy energy of Co adatom and single vacancy complex in graphene sheet supported on Ni(111) surface: A first principles prediction” (Chapter 5)

### Others

- V. Kumar, N. Joshi, B. Dhara, P. Jha, P. Ghosh, N. Ballav, “Stable Red Emission from nanosheets of molecularly doped hexagonal boron nitride”, *J. Phys. Chem. C*, **122**, 21076 (2018).
- V. Kumar Ravi, P. Santra, N. Joshi, J. Chugh, S. Kumar Singh,H. Rensmo,P .Ghosh,and A. Nag, “Origin of the Substitution Mechanism for the Binding of Organic Ligands on the Surface of CsPbBr<sub>3</sub> Perovskite Nanocubes”, *J. Phys. Chem. Lett.*, **8**, 4988-4994 (2017).

- 
- G. Drera, C. Cepek, L. L. Patera, F. Bondino, E. Magnano, S. Nappini, C. Africh, A. Lodi-Rizzini, N. Joshi, P. Ghosh, A. Barla, S. K. Mahatha, S. Pagliara, A. Giampietri, C. Pintossi and L. Sangaletti, “Identification of Ni<sub>2</sub>C electronic states in graphene-Ni(111) growth through resonant and dichroic angle-resolved photoemission at the C K-edge”, *Phys. Rev. B*, **96**, 165442 (2017).
  - N. Joshi and P. Ghosh, “Substrate induced changes in the magnetic and electronic properties of hexagonal boron nitride”, *Phys. Rev. B*, **87**, 235440 (2013).
  - N. Joshi, I. Kaul, N. Ballav and P. Ghosh, “Spin enhancement and band gap opening of ferrimagnetic graphene on fcc-Co(111) surface upon hydrogenation”, *AIP Conf. Proc.*, **1512**, 694 (2013).
  - N. Joshi, N. Ballav and P. Ghosh, “Hydrogen-induced reversal of spin alignment in graphene supported on Ni(111) surface”, *Phys. Rev. B*, **86**, 121411(R) (2012).
  - I. Kaul, N. Joshi, N. Ballav and P. Ghosh, “Hydrogenation of ferrimagnetic graphene on a Co surface: Significant enhancement of spin moments by C-H functionality”, *J. Phys. Chem. Lett.*, **3**, 2852 (2012).